SOLAR-WIND FLOW PAST THE PLANETS EARTH, MARS, AND VENUS

A DISSERTATION

SUBMITTED TO THE DEPARTMENT OF APPLIED MECHANICS

AND THE COMMITTEE ON GRADUATE STUDIES

OF STANFORD UNIVERSITY

NGR-05-020-330

IN PARTIAL FULFILLMENT OF THE REQUIREMENTS

FOR THE DEGREE OF

DOCTOR OF PHILOSOPHY

By

Arthur William Rizzi

May 1971

I certify that I have read this thesis and that in my opinion it is fully adequate, in scope and quality, as a dissertation for the degree of Doctor of Philosophy.

John G. P. Spreiter
(Principal Adviser)

I certify that I have read this thesis and that in my opinion it is fully adequate, in scope and quality, as a dissertation for the degree of Doctor of Philosophy.

Ira Hellwell
(Electrical Engineering)

I certify that I have read this thesis and that in my opinion it is fully adequate, in scope and quality, as a dissertation for the degree of Doctor of Philosophy.

Harold Lomax
(Aeronautics & Astronautics)

Approved for the University Committee on Graduate Studies:

Dean of Graduate Studies

ACKNOWLEDGMENTS

The author is indebted to Professor John Spreiter for suggesting this topic and for his guidance throughout its investigation. Thanks are also due to Messrs. Harvard Lomax, John Rakich, Mamoru Inouye, and Mrs. Audrey Summers of Ames Research Center for their valuable advice in matters related to the numerical computations.

The author also wishes to express thanks to Dr. Charles Sonett and Mr. Ray Reynolds for making facilities available at Ames Research Center.

A note of thanks is given to Mrs. Elsie Hirscher for her final preparation of this manuscript.

This research was partially supported by the National Aeronautics and Space Administration under contract NAS2-5535 administered by Ames Research Center and under Grant NGR 05-020-330 administered by NASA Headquarters as part of their Physics and Astronomy program.

TABLE OF CONTENTS

TABLE OF CONTENTS (cont.)

LIST OF ILLUSTRATIONS

LIST OF ILLUSTRATIONS (cont.)

LIST OF ILLUSTRATIONS (cont.)

LIST OF ILLUSTRATIONS (cont.)

CHAPTER I

INTRODUCTION

It is remarkable that interplanetary space provides simultaneously one of the best vacuums available to man, a marvelous laboratory for the study of collisionless plasma, and phenomena that can be represented by a continuum model. The reason for the latter is that the solar wind, a tenuous high-speed outflow of fully ionized and magnetized gas from the Sun, pervades interplanetary space and behaves in many ways in conformity with the equations of ordinary continuum magnetohydrodynamics and gasdynamics. This is true with respect to both large-scale irregularities in the solar wind itself and to the interaction of the solar wind with planetary or lunar-sized objects. This thesis will be concerned primarily with the development of an appropriate theory based on fluid concepts that accurately represents the large-scale features of the interaction between the solar wind and the planets Earth, Mars, and Venus and that advances the present understanding of such phenomena. The basic approach of the presentation followed throughout will be first to review and discuss observed phenomena that are pertinent to this topic, and then to formulate and develop a mathematical model that will adequately represent the observations.

Extensive theoretical studies, specific calculations, and detailed comparisons with observations have shown that the interaction of the solar wind and the Earth may be represented satisfactorily, insofar as gross features of the flow such as density, velocity, temperature, and magnetic field are concerned, by the standard continuum equations of magnetohydrodynamics (see Spreiter et al. [1968] or Spreiter and Alksne [1969, 1970] for recent summaries). This thesis extends the same line of analysis to objects in the solar system which have no significant intrinsic magnetic field, but a sufficiently dense and electrically conducting ionosphere to stop and deflect the solar wind before it is absorbed by the planetary surface or atmosphere.

Mars and Venus are known examples of such objects. It is the plan of the present investigation to base the mathematical analysis of these interaction phenomena with nonmagnetic planets on the equations of magnetohydrodynamics representing the steady flow of a perfect gas having infinite electrical conductivity as well as both zero viscosity and thermal conductivity and then to proceed to an approximate solution through simplifications that are well known and tested in previous applications to the interaction of the solar wind with the Earth. Modifications are introduced only as required because it is the ionosphere rather than the geomagnetic field through which the pressure of the planet is communicated to the solar wind.

In broad outline, the elements of the theory are as follows. The incident solar wind is considered to be steady and supersonic, and to flow in accordance with the equations of magnetohydrodynamics for a perfect gas in which all dissipative processes, such as those associated with shock waves and boundary layers, take place in the interior of thin layers idealized as magnetohydrodynamic discontinuity surfaces of zero thickness. The ionosphere, or at least the outer part of it that participates in the interaction with the solar wind, is idealized as spherically symmetric and hydrostatically supported plasma having infinite electrical conductivity. Since the two bodies of plasma are of different origin, and have different properties, they must be considered to be mutually impenetrable in the idealized hydromagnetic representation, and to be separated by a tangential discontinuity surface. This surface is called the ionopause, since it marks the outer boundary of the ionosphere. Once the problem is formulated, the solution proceeds in two steps, just as in the analogous problem for the Earth. First the shape and location of the ionopause is calculated for selected values of the parameters characterizing the solar wind and the ionosphere. Following that, the location of the bow wave and the properties of the flow field are determined from the equations of gasdynamics to which those of magnetohydrodynamics have been simplified. It is found that the results for a wide range of ionospheric parameters may be brought into close correspondence with those for solar-wind flow past the Earth's magnetosphere by

application of a simple geometric transformation of the coordinates. Finally, these theoretical results based on gasdynamic theory are compared with the observations made by Mariner 5 as it flew by Venus and Mariners 4, 6, and 7 as they flew past Mars, and implications of the points of agreement and disagreement are discussed.

A more refined analysis of this interaction of the solar wind with the Earth, Mars, and Venus in which the complete equations of magnetohydrodynamics are solved without any simplification is then carried out for the case of the magnetic field aligned with the flow direction. Furthermore, for Mars and Venus the exact shape and location of the ionopause is calculated using the hydromagnetic theory without introducing any approximations. Solutions of this improved theory are computed, and the location of the bow wave and the properties of the flow field are determined. For high Alfvén Mach number this refined hydromagnetic solution shows that the bow-wave location and the flow-field properties are very similar to those of the simpler gasdynamic theory, but for low Alfvén Mach numbers they are strikingly different. This unusual bow-wave position for flow past the Earth has recently been confirmed by spacecraft measurements. A detailed comparison of these two models is carried out to determine the accuracy and usefulness of the simpler gasdynamic theory. Lastly, the results of the hydromagnetic solution are shown to be in very good accordance with the observations made by Mariner 5 as it flew past Venus although certain differences near the theoretical location of the ionopause suggest the presence of a thick boundary layer.

The present version of the gasdynamic model for the interaction with Mars and Venus is based on a preliminary analysis originally reported by Spreiter, Summers, and Rizzi (1970b). In addition, because of the similarity of the flow past Mars and Venus with that past the Earth as indicated by the correspondence rule and also because our more accurate hydromagnetic solution has direct application to the interaction with the Earth, we choose, for the sake of unity, to parallel our gasdynamic analysis for the interaction with Mars and Venus with the gasdynamic investigations already carried out in the past years for the case of the Earth. For this purpose we borrow

heavily from the work of Spreiter et al. (1966a, 1968) and Spreiter and Alksne (1969, 1970).

However, before embarking on the major topic of this thesis, let us review the basic properties and idealizations of the solar wind itself in order to provide a background knowledge of the interplanetary medium and also to illustrate the basic coherence of the entire theoretical description of the solar wind and its interaction with the planets. Much of this is repeated from Spreiter et al. (1968).

CHAPTER II

THE SOLAR WIND

Although geomagnetic evidence (Chapman and Ferraro, 1931) had long before led to the belief that ionized gas was projected all the way from the Sun to the Earth and beyond, both occasionally from flares and more steadily in localized 'M-region' beams, the modern discussion of the solar plasma begins with Biermann's (1951, 1957) analysis of the behavior of ionized comet tails. An outstanding photograph of a more recent comet, Ikeya-Seki, taken at the Mojave Tracking Station is shown in figure 2-1. Clearly visible are the

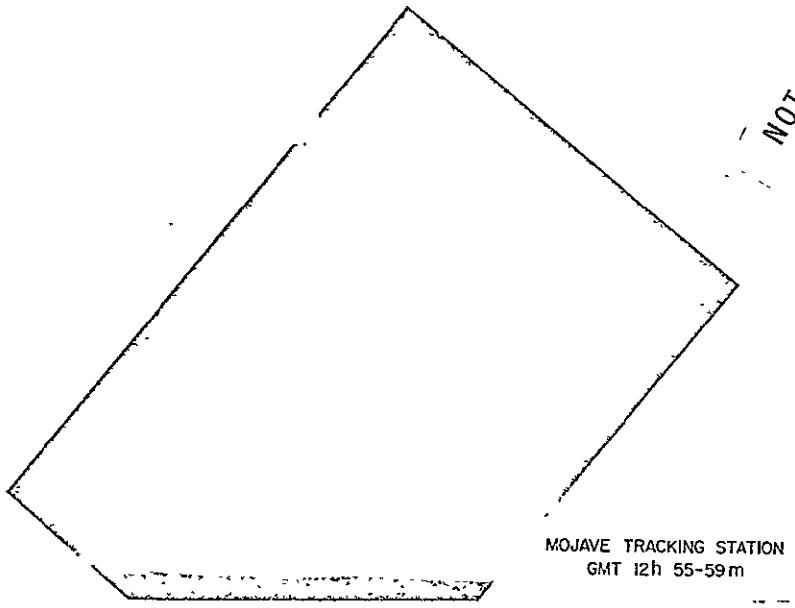

Figure 2-1. Comet Ikeya-Seki, October 29, 1965 (Spreiter et al., 1968).

head of the comet near the horizon at the bottom of the photograph and the extremely elongated tail. Although it had become customary to ascribe the antisolar direction of cometary tails to radiation pressure of sunlight, Biermann showed this explanation to be inadequate in many respects, and proposed in its place the concept of an approximately radial high-speed flow of ionized gas from all parts

the Sun at all times. It is not difficult to accept this explanation of a photograph like that of figure 2-1, since the general effect is very remindful of smoke from a smudge pot or of a wind sock in a strong and steady wind.

Although the solar corona is not normally visible because of the overwhelming brilliance of the light from the photosphere, it is clearly visible, even to the unaided eye, at the time of a total eclipse of the Sun by the Moon. As a result, much of what is known about the solar corona has been learned from observations made during the few-minutes duration of such events. In more recent years, such observations, particularly of the parts closer to the Sun, have been augmented by those taken at other times with the aid of a coronagraph, a telescope system fitted with special obscuring equipment invented by Lyot in 1937. Figure 2-2 shows a photograph of the corona taken

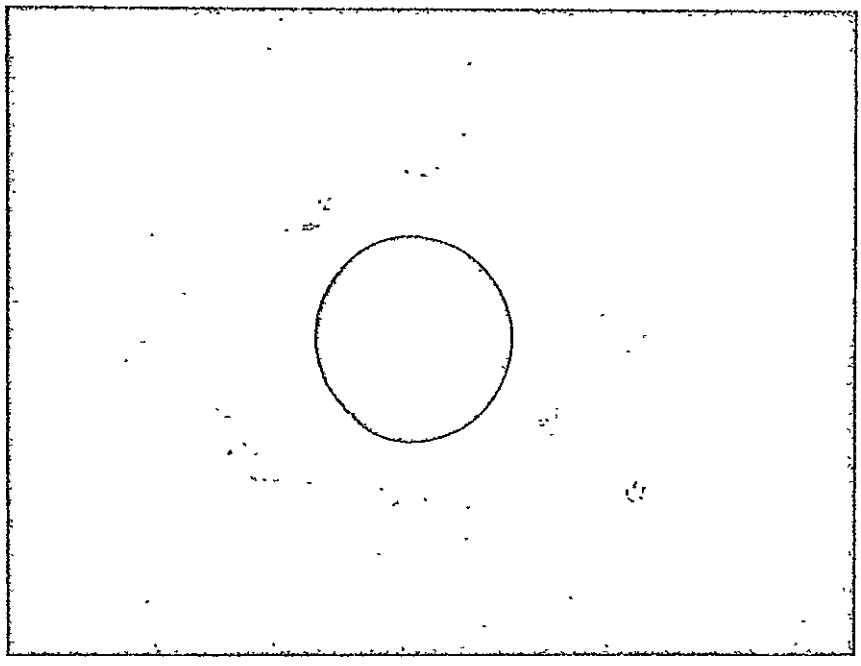

Figure 2-2. Solar corona during eclipse of May 30, 1965, from NASA CV-990 aircraft at 38,000 feet (Spreiter et al., 1968).

during the eclipse of May 30, 1965, from a NASA Convair 990 jet airliner at 38,000 feet altitude (Smith et al, 1967). Clearly visible

beyond the disk of the Moon are the polar rays, similar in shape to the magnetic lines of force at the poles of a magnetized sphere. More interesting from the present point of view is the large outward extension of the corona from the equatorial and middle latitudes. Although these plumes appear to extend only a few solar radii in this photograph, other photographs taken during other eclipses have shown rather similar features visible to distances as much as five or ten times farther from the Sun. Observations indicate that the coronal gas in these plumes is both somewhat hotter and many times denser than over the poles.

Beginning effectively with the flight of Mariner 2 to Venus in 1962, direct measurements between 0.7 and 1.5 astronomical units (a.u.) have demonstrated beyond all doubt the existence of a continuous flux of magnetized plasma from the Sun, essentially as predicted theoretically by Parker (1958) and termed by him the solar wind. However even this detailed information from the spacecrafts characteristically possesses substantially greater uncertainties than would usually be experienced in laboratory measurements of the same properties of a plasma. In particular, the rather low resolution of directional, temporal, and energy aspects of the plasma measurements resulting from weight, space, power, and telemetry limitations imposed by the spacecraft tends to limit the quality of the determination of the velocity distribution of the particles and ultimately, therefore, the knowledge of the bulk properties, such as density, velocity, and temperature, of the plasma. Further uncertainties arise from the non-Maxwellian and anisotropic character of the velocity distribution of the random motion of the particles. Nevertheless, a good understanding of the broad features of the properties of the solar wind is now in hand, and further refinements can be anticipated in the near future.

As a review, some of the basic properties and idealizations of the solar wind pertinent to our study are summarized in figure 2-3, which was originally presented by Spreiter et al. (1968). First of all it should be recognized that it is the velocity of the solar wind and not the planet's motion in its orbit around the Sun, that provides the dominant contribution to the relative motion of the planet and the

interplanetary plasma. In many ways we may think of the solar wind as a hypersonic gale that blows through interplanetary space. From an overall point of view, the solar wind may be considered to result from forces in the interior of the Sun which are too large to be constrained by the feeble pressure that can be imposed by the tenuous cool gas of the interstellar medium. As the immediate source of the solar wind, we may look to the unsteady conditions in the relatively cool visible surface, or photosphere, of the Sun. Here are to be found a wide spectrum of acoustical, hydromagnetic, and internal gravity waves which grow tremendously in amplitude as they propogate upward into an atmosphere of diminishing density. The dissipation of these waves, either directly or indirectly after their culmination in shock waves, results in a substantial deposition of energy generally believed to be sufficient to account for the high temperature of the solar corona relative to the photosphere. Since the energy is being deposited in the form of heat at a greater rate than can be transported away by radiation or thermal conduction, convection in the form of the solar wind ensues. This process is believed to account for both the 2×10^6 °K temperature of the corona, compared with the 5800 °K temperature of the photosphere, and the outward convection that leads ultimately to the supersonic solar wind at greater distances from the Sun. The average flow starts gradually with insignificant velocities of the order of 1 km/sec or less in the lower corona, and increases steadily with increasing distance from the Sun until its ultimate velocity is attained beyond a few tens of solar radii. The expanding coronal gas carries with it the solar magnetic field, stretching the lines of force outward through the solar system and enhancing the strength of the interplanetary magnetic field there while generally maintaining direct connection to the Sun. Because of the rotation of the Sun, the magnetic lines of force wind in spirals in the plane of the ecliptic making, on the average, an angle of about 45° with the direction from the Sun at the orbit of the Earth.

Representative values for the observed properties of the solar wind in the vicinity of the Earth's orbit are outlined in the box in the center of figure 2-3. The bulk velocity V of the solar wind has

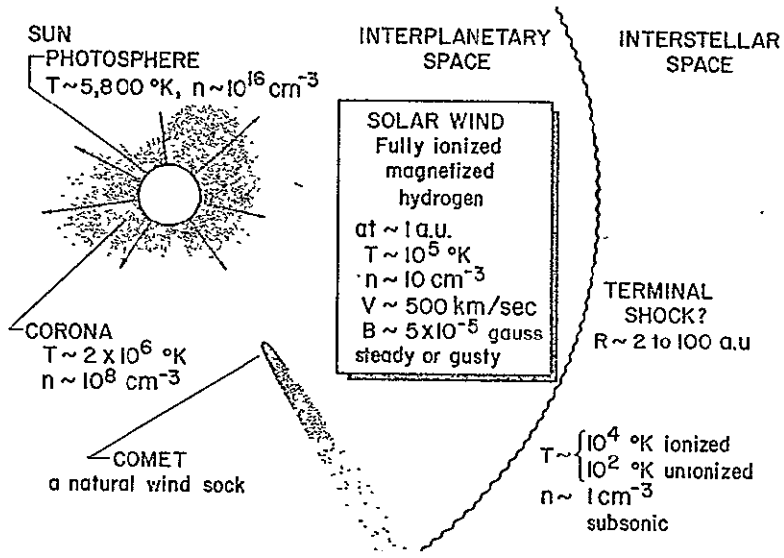

Figure 2-3. The solar wind, a hypersonic gale in interplanetary space (Spreiter et al, 1968).

been observed to vary between about 275 and 850 cm/sec, with the lower values usually associated with the quiet solar wind and the higher values with disturbed conditions in space. The number density n of the protons in the solar wind, which is substantially more difficult to determine from the plasma-probe data than V, is usually found to be between 1 and 10 cm^{-3} in the quiet solar wind and as much as an order of magnitude greater during disturbed times. The intensity of the magnetic field B is usually between about 3 and 7 γ ($1\gamma = 10^{-5}$ gauss), but may also be substantially greater during disturbed times. All of these quantities have been monitored with varying degrees of exactness and completeness for several years, and are known to display substantial variations with time and location. The chemical composition is principally ionized hydrogen with a small mixture, usually about 4 percent, but sometimes more than 20 percent, of helium nuclei (Hirshberg et al., 1970).

At great distances from the Sun, the solar wind must merge somehow into the interstellar medium. Although the spatial distribution of interstellar gas, and its degree of ionization, is both very non-uniform and uncertainly determined, temperatures and densities of

the order of those indicated in figure 2-3 are frequently quoted (see, e.g. Kaplan, [1966]). It is generally presumed that the region of supersonic solar-wind flow terminates with a shock wave and that the flow beyond is subsonic. The location of this terminal shock wave is usually estimated to be between 50 and 100 a.u., although Brandt (1962) has suggested, on the basis of an analysis of the directions of comet tails, that it may be as near as 2 a.u. (see Betton et al. [1963] and Brandt [1967] for later comments). One aspect of this terminal shock wave that does not appear to have been adequately considered in these discussions is that the temperature attained by the gas behind the terminal shock wave is far in excess of the temperatures quoted above for the interstellar medium. Whether the gas cools gradually as it continues to flow subsonically away from the Sun by means of some process such as radiation not normally included in the analysis of the solar wind or remains at high temperature throughout a spherical shell terminated at still greater heliocentric distances by a second shock advancing through the interstellar medium or behaves in some other manner altogether remains essentially unknown. It may be, on the other hand, that the supersonic solar wind terminates without the intervention of a shock wave in the manner suggested by Faus (1966) through the action of non-adiabatic transfer of kinetic energy to the interstellar medium in a roughly constant-pressure process that takes place between about 1 and 3.5 a.u. Corresponding uncertainties plague any discussion of the interaction of the solar wind with objects beyond the orbit of Mars.

Ultimately, at greater distances from the Sun, the subsonic solar wind must interact in some way with the interstellar gas. Although non-uniformities in the spatial distribution and uncertainties in the measurements are great, fluid considerations suggest the development of an interface, the heliopause, separating the solar and interstellar plasma. However, so little is known about the nature of the interaction and the properties of the gases involved that even the existence of the heliopause must be regarded as hypothetical.

In spite of the obvious deviations from spherical symmetry in the solar corona, and presumably in the solar wind as well, the theory of the solar wind is generally based for reasons of mathematical

tractability on the assumption of radially symmetric flow. This theory was initially presented by Parker (1958) and summarized in more developed form by Parker (1963, 1965), Lüst (1963, 1965), Scarf (1964, 1970), Dessler (1967), Hundhausen (1968, 1970), and others. Perhaps the most fundamental concept is that of treating the solar wind, even as it becomes extremely rarefied far beyond the orbit of the Earth, as an ordinary continuum gas. Thus to a theoretician, a very significant finding of plasma and magnetic-field measurements in space is the degree to which not only the broad features of the solar-wind flow, but also much of the small-scale features, can be represented by the continuum equations of fluid dynamics. Although it is apparent that not all matters of significance can be treated in this way (for example the anisotropy of the velocity distribution), the amount of understanding that is possible is truly astonishing, particularly in view of the fact that the solar-wind plasma is one of the most rarefied gases now accessible to direct measurement. However, it was always known that the fluid description could not be justified in terms of ordinary Coulomb-collision effects alone. In his earliest papers Parker pointed out that as the gas streams away from the Sun into the supersonic region, the collisional mean free path must rapidly increase so that near the Earth it is on the order of 1 a.u. Nevertheless, in these initial discussions Parker also provided a general justification for the use of fluid equations beyond the dense collisional region. He pointed out that some microscopic plasma instabilities must naturally develop and that associated wave-particle scattering then produces a thermalization mechanism leading to a finite mean free path and effective fluid transport characteristics. It is now quite clear that plasma turbulence generates partial thermalization at 1 a.u. Apparently the microscopic scattering mechanism produces randomizing and isotropizing effects so that the gasdynamic equations for conservation of mass and momentum remain appropriate for descriptions of the main flow properties, at least out to 1 or 2 a.u. However, microscopic interactions may play a significant role in energy transport and energy balance (see Scarf [1970]for a review of microscopic phenomena in the solar wind). Clearly these phenomena are important

in the study of the microscopic structure, but the equations of fluid dynamics appear to be appropriate for the description of the macroscopic features of the solar wind and its interaction with the planets Earth, Mars, and Venus.

CHAPTER III

BROAD FEATURES OF THE OBSERVATIONS

Data acquired in recent years in the vicinity of the Earth, Moon, Mars, and Venus have disclosed three essentially different types of interaction with the solar wind as illustrated in figure 3-1. For the Earth (Ness et al, 1966; Spreiter et al., 1968; Binsack, 1968), the geomagnetic field prohibits the solar wind from approaching nearer than about 10 Earth radii under ordinary circumstances. The shielded region, the magnetosphere, acts as an obstacle in the supersonic flow of the solar wind, and a bow wave forms a few Earth radii upstream of the magnetosphere boundary, or magnetopause. Neither Venus nor Mars has a significant magnetic field, but the electrical conductivity and density of the upper ionosphere of both Mars and Venus are sufficiently great that the solar wind is prevented from flowing directly into either the planetary surface or the lower absorbing levels of the atmosphere (Fjeldbo and Eshleman, 1968, 1969). The solar wind is thus deflected around the ionosphere, and a bow wave is formed upstream of the planet, similar in many ways to that associated with the Earth. Aside from evident differences in the underlying physical processes at the boundary surface between the ionosphere and the solar wind, the ionopause, the principal difference between the flow fields around Mars or Venus and Earth is the size of the cavity. As illustrated in figure 3-1, the ionopause is wrapped much closer around Mars and Venus than the magnetopause is around the Earth, the nose being at an altitude of about 500 km for Venus and probably about 155 to 175 km for Mars, compared with about 60,000 km for the Earth.

Interaction of the solar wind and the Moon is very different because of the lack of either a sensible magnetic field or ionosphere to deflect the incident flow (Lyon et al., 1967; Ness et al., 1967; Spreiter et al., 1970a). The particles of the solar wind thus proceed unchecked until they contact the lunar surface, where they are effectively removed from the flow. As a consequence, no bow wave forms, and the

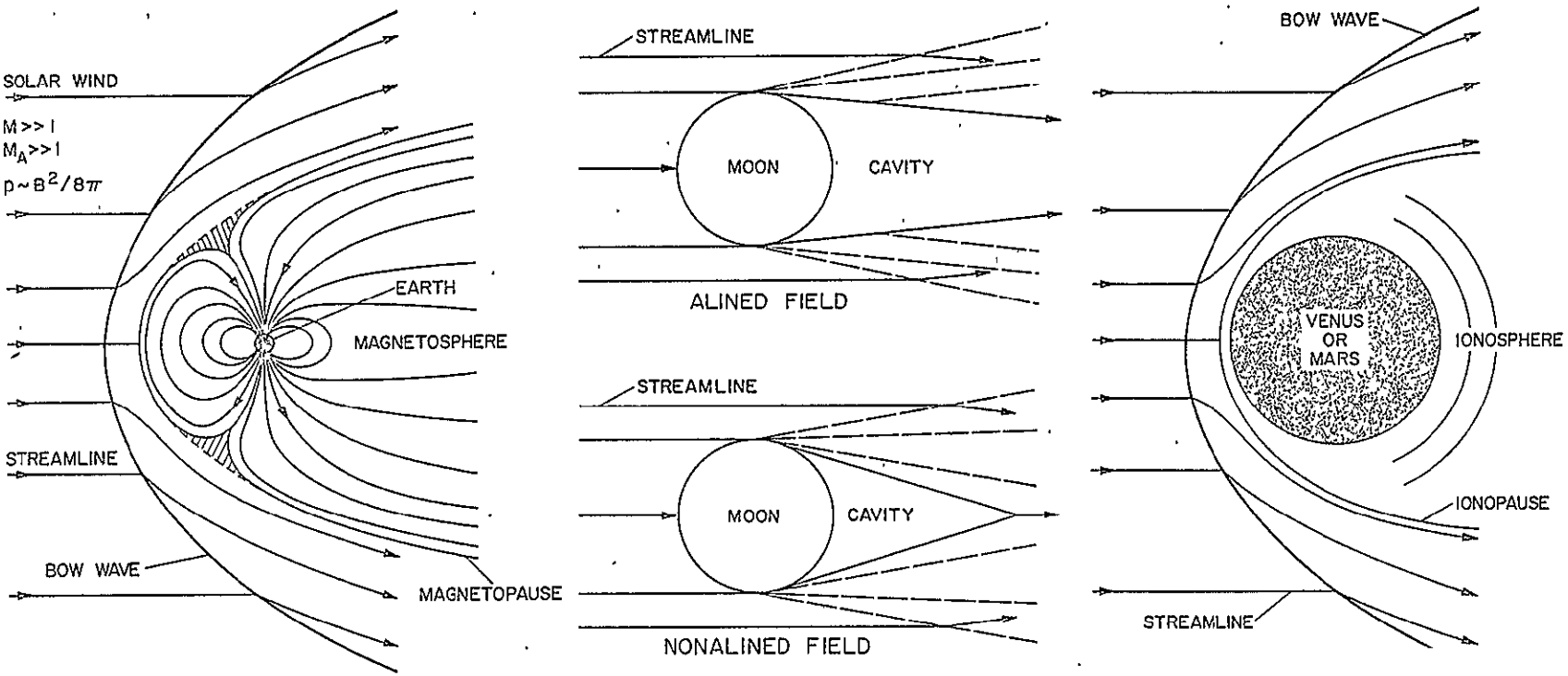

Figure 3-1. Principal features of solar-wind flow past the Earth, the Moon, and Mars or Venus (Spreiter, Summers, and Rizzi, 1970b).

principal features of the flow field are associated with the closure of the lunar wake, or cavity in the solar wind (Colburn et al., 1967), that extends downstream from the Moon as illustrated.

CHAPTER IV

FORMULATION OF FLUID REPRESENTATION

Just as in the theory of the solar wind itself, the fundamental assumption underlying nearly all theoretical analyses of large-scale features of the interaction of the solar wind with the planets is that the average bulk properties of the flow can be described adequately by the continuum equations of fluid dynamics. That this should be so is not at all obvious since the mean free path of the particles, based on Coulomb interactions, is of the order of half the distance to the Sun at the orbit of the Earth. Indeed, theoretical justification is essentially qualitative at the present time, and usually consists of referring to randomizing and isotropizing effects of small irregularities, much like a form of plasma turbulence, which are always present in the solar wind. The details of these processes are not well understood at this time, and it is fair to state that the real support for the use of the continuum-fluid model is provided by the outstanding agreement between results calculated in this way and those actually measured in space. Moreover, the difficulties in solving the nonlinear continuum equations and the richness of the phenomena contained within this theory are sufficiently great so that it is worthwhile to explore the consequences of this model before introducing additional complications.

If an ionized gas like the solar wind moves in a magnetic field, electric fields are induced in it and electric currents flow. The magnetic field exerts forces on these currents which may considerably modify the flow. In turn the currents themselves modify the magnetic field. Thus the interaction between the magnetic and fluid dynamic phenomena is complex, and the flow must be examined by combining the magnetic-field equations with those of fluid dynamics. Hence the appropriate mathematical model capable of description of this phenomena is provided by the standard equations of magnetohydrodynamics (see, e.g. Landau and Lifshitz [1960]).

For explicit application to the study of the solar wind's interaction with planets, these equations can be simplified by treating the flowing plasma as a steady, calorically perfect, and dissipationless conducting gas. The wind is known to fluctuate in time, but very few theoretical analyses of these effects have been carried out as yet. There is little doubt that such studies must be made if many important dynamical properties of the interaction are to be understood. However, in at least some instances, observations (Spreiter and Alksne, 1969; Binsack and Vasyliunas, 1968) and theory (Spreiter and Summers, 1965) suggest that many features of the flow are able to respond rapidly enough to achieve an essentially steady-state equilibrium within a few minutes after a sudden change in the solar wind. Consequently, the steady-state solution for conditions existing at a given time should adequately represent the flow properties of the wind at that time. Similarly, the assumption that the solar wind is perfectly conducting, inviscid, and nonheat conducting is also not strictly valid, but the full dissipative equations are much more complicated, and as yet a solution cannot be achieved. Hence, in order to fully develop and examine the fluid theory, our model is restricted to the ideal equations in which all dissipative processes, such as those associated with shock waves, boundary layers, and current sheets, take place in the interior of thin layers idealized as magnetohydrodynamic discontinuity surfaces of zero thickness. Finally, even though some of its properties are known to be anisotropic, the solar wind is taken to be a calorically perfect isotropic gas primarily because its high temperature and low pressure satisfy the conditions for a perfect gas, but also because a more detailed theory of the thermodynamic equation of state for a two-species ionized gas embedded with a magnetic field has not been developed yet. The theoretical justification for these three assumptions is essentially heuristic in nature, and, like the original postulate of representing the solar wind by a fluid model, the real support derives from the fact that extensive theoretical studies, specific calculations, and detailed comparisons with observations have shown that the interaction of the solar wind and the Earth has been represented satisfactorily, insofar as gross features of the

flow are concerned, by this model (see Spreiter et al. [1968] or Spreiter and Alksne [1969] for recent summaries). Moreover, recent investigations (see Spreiter et al. [1970a]for an extensive account) have shown that the same is true for the Moon, provided that boundary conditions are applied at the lunar surface that correspond to the Moon absorbing or neutralizing all particles of the solar wind on impact.

CHAPTER V

FUNDAMENTAL EQUATIONS

The following fundamental differential equations of magnetohydrodynamics for the steady flow of an isotropic and calorically perfect gas having infinite electrical conductivity as well as both zero viscosity and thermal conductivity (Spreiter et al., 1966a)

$$\nabla \cdot \rho \underset{\sim}{V} = 0$$

$$\rho(\underset{\sim}{V} \cdot \nabla)\underset{\sim}{V} + \nabla p = -\frac{1}{4\pi} \underset{\sim}{B} \times \operatorname{curl} \underset{\sim}{B}$$

$$\operatorname{curl}(\underset{\sim}{B} \times \underset{\sim}{V}) = 0 \qquad \operatorname{div} \underset{\sim}{B} = 0 \tag{5-1}$$

$$(\underset{\sim}{V} \cdot \nabla) S = 0 \qquad S - S_0 = c_v \ln \frac{p/p_0}{(\rho/\rho_0)^{\gamma}}$$

provide the basis for all theoretical matters to be discussed in thi thesis. In these and the equations to follow, the symbols ρ , p S , and $\underset{\sim}{V}$ refer to the density, pressure, entropy, and velocity of the gas; and $\underset{\sim}{B}$ refers to the magnetic field expressed in terms gaussian units.[1] c_p and c_v are constants representing the specif heats at constant pressure and constant volume. The quantity $\gamma = c_p/c_v$ is the ratio of specific heats and is equal to N / (N + 2)

---

[1] The use of this standard notation contrasts with the practice in the much older science of geomagnetism of using the symbol $\underset{\sim}{H}$ to represent the Earth's magnetic intensity. Discussion of this property does appear in some space-research papers but causes no confusion because the magnetic permeability of the solar wind is very nearly unity and hence in gaussian units $\underset{\sim}{B} = \underset{\sim}{H}$. These two quantities will be used interchangeably in this thesis in order to avoid making any alteration of original sources.

where N is the number of degrees of freedom of the gas particles. On first thought the choice of the value 2 for the ratio γ of specific heats may seem justified in a variety of ways, generally centering around the presumed two-degrees-of-freedom nature of the interactions of charged particles in a magnetic field. This argument weakens, however, when consideration is given to the extremely irregular character of the magnetic fields observed in space, particularly downstream of the bow shock wave. In fact, the supposition of applying hydromagnetic theory to the flow of solar plasma around the planets involves the assumption of an isotropic pressure, and the whole concept appears more internally consistent if the particles are considered to behave as if they have three rather than two degrees of freedom. Thus for a monatomic gas, such as either of the two leading constituents of the solar wind, atomic hydrogen and helium, $N = 3$ and $\gamma = 5/3$. The subscript o refers to conditions at an arbitrary reference location in the flow field.

Important auxiliary relations for the temperature T, speed of sound a, internal energy e, and enthalpy h are as follows:

$$p = \rho RT/\bar{m} = nkT$$

$$a = \sqrt{\partial p/\partial \rho} = \sqrt{\gamma p/\rho} = \sqrt{\gamma RT/\bar{m}} \qquad (5\text{-}2)$$

$$e = c_v T \qquad h = c_p T = e + p/\rho$$

where $R \doteq (c_p - c_v)\bar{m} = 8.314 \times 10^7$ erg/°K is the universal gas constant, and $\bar{m}$ is the mean molecular weight nondimensionalized so that $\bar{m} = 16$ for atomic oxygen. For fully ionized hydrogen plasma, $\bar{m}$ is thus 1/2, and n = number of particles/cm^3 = $2n_p$ where n_p is the number of protons/cm^3, and k = Boltzmann's constant = 1.38×10^{-16} erg / °K. The relationship between ρ and n is easily seen to be

$\rho = m_p n_p$ where $m_p = 1.67 \times 10^{-24}$ gm is the mass of a proton. It is also fully equivalent and convenient for some purposes to replace the entropy equation $(\underset{\sim}{V} \cdot \underset{\sim}{\nabla}) S = 0$ in equations (5-1) by the following energy equation:

$$\operatorname{div}\left[\rho \underset{\sim}{V}\left(\tfrac{1}{2}V^2 + h\right) + \frac{\underset{\sim}{V}}{4\pi} B^2 - \frac{1}{4\pi}(\underset{\sim}{B} \cdot \underset{\sim}{V})\underset{\sim}{B}\right] = 0 \qquad (5\text{-}3)$$

Implicit in the relations of equations (5-1) are two important nondimensional parameters that characterize the flow at any point, the Mach number M and the Alfvén Mach number M_A defined by

$$M = \frac{V}{a} = \frac{V}{\sqrt{\gamma p/\rho}} \qquad M_A = \frac{V}{A} = \frac{V}{\sqrt{B^2/4\pi\rho}} \qquad (5\text{-}4)$$

where a represents the speed of sound defined in equations (5-2), A the speed of an Alfvén wave which will be discussed later, and $V = |\underset{\sim}{V}|$ represents the speed of the gas.

Although only first derivatives appear in the system of differential equations (5-1), the neglected dissipative terms are described by second derivatives. Their neglect requires that the gradients be small. In magnetohydrodynamics, as in gasdynamics, however, compressions tend to coalesce and steepen into shock waves of such small thickness that they can be considered virtual discontinuities for many purposes. In this way gradients tend to become very large, and continuous motions tend to break down some place if they involve compressions. In addition, attraction between like electric currents tends to cause distributed currents to collapse into thin sheaths, across which the magnetic field changes nearly discontinuously. Mathematically, continuous solutions of the dissipationless equations cease to exist beyond the point of breakdown, and the flow is no longer governed solely by the differential equations (5-1). Mass, momentum, magnetic flux, and energy must still be conserved, however, and conservation relations provided by integrals of equations (5-1) and (5-3)

must hold between quantities on the two sides of any such discontinuity. The conservation equations for magnetohydrodynamic discontinuity surfaces are (see, e.g. Landau and Lifshitz [1960])

$$
\begin{aligned}
&\left[\rho V_n\right] = 0 \\
&\left[\rho V_n \underset{\sim}{V} + (p + B^2/8\pi)\hat{n} - B_n \underset{\sim}{B}_t/4\pi\right] = 0 \\
&\left[B_n \underset{\sim}{V}_t - \underset{\sim}{B}_t V_n\right] = 0 \qquad \left[B_n\right] = 0 \\
&\left[\rho V_n\left(h + V^2/2\right) + V_n B^2/4\pi - B_n \underset{\sim}{V}\cdot\underset{\sim}{B}/4\pi\right] = 0
\end{aligned}
\tag{5-5}
$$

Unit vectors normal and tangential to the discontinuity surface are designated by $\hat{n}$ and $\hat{t}$, and components of $\underset{\sim}{V}$ and $\underset{\sim}{B}$ in these directions are indicated by subscripts n and t. The square brackets are used to indicate the difference between the enclosed quantities on the two sides of the discontinuity, as in $[Q] = Q_1 - Q_0$ where subscripts 0 and 1 refer to conditions on the upstream and downstream sides of the discontinuity. These relations are frequently supplemented by the statement that there is a current sheet flowing along the discontinuity surface and that the value $\underset{\sim}{J}^*$ of this current per unit width is given by

$$
\underset{\sim}{J}^* = \frac{1}{4\pi}\,\underset{\sim}{\mathrm{curl}}\,\underset{\sim}{B} \tag{5-6}
$$

It is now well known (Landau and Lifshitz, 1960; Jeffrey and Taniuti, 1964; Jeffrey, 1966) that five classes of discontinuities are described by the conservation equations (5-5), but for the sake of completeness and unity we repeat some of the mathematical development establishing the basis for the existence of these different classes. The particular

version presented closely follows that of Spreiter et al. (1966a).

Friedrichs and Kranzer (1958) originally developed an alternative form for the conservation equations that affords a quick survey of the possible types of discontinuities and some of their properties, and is particularly useful in the determination of asymptotic properties of weak discontinuities. It is based on extensive use of mean values $\langle Q \rangle = (Q_0 + Q_1)/2$, and the new variables $W = 1/\rho$ and $m = \rho V_n$ representing the specific volume and the mass flux across the discontinuity. In terms of these variables, the relations given in equations (5-5) become

$$
\begin{aligned}
& m[W] - [V] = 0 \\
& m[\underset{\sim}{V}] + [p]\hat{n} + \frac{1}{4\pi}\langle B \rangle \cdot [\underset{\sim}{B}]\hat{n} - \frac{1}{4\pi} B_n [\underset{\sim}{B}] = 0 \\
& m\langle W \rangle [\underset{\sim}{B}] + \langle B \rangle [V_n] - B_n [\underset{\sim}{V}] = 0 \qquad [B_n] = 0 \\
& m\left(\left[e + \frac{W}{8\pi} B^2 \right] + [W]\left(\langle p \rangle + \frac{1}{8\pi}\langle B_t^2 \rangle - B_n^2/8\pi \right) - \frac{1}{4\pi}[W \underset{\sim}{B}_t] \cdot \langle \underset{\sim}{B}_t \rangle \right) = 0
\end{aligned}
\tag{5-7}
$$

The last of these can be replaced by

$$
m\left(\left[e + \langle p \rangle W \right] + \frac{1}{16\pi}[W][B_t]^2 \right) = 0 \tag{5-8}
$$

If the mean quantities are considered known, there are thus eight equations in eight scalar variables $[W]$, $[p]$, $[V]$, $[B]$, and $[e]$ since the condition $[B_n] = 0$ always holds.

Since e appears in only the last relation of equations (5-7), we can consider alternatively the seven scalar equations in seven variables defined by the first three relations of equations (5-7). They are all linear homogeneous equations, and solutions exist only if

their determinant vanishes. Equating the determinant to zero yields the following equation for the mass flux m

$$\langle W\rangle m\left(\langle W\rangle m^2-\frac{B_n^2}{4\pi}\right)\left\{\langle W\rangle m^4+\left(\frac{\langle W\rangle}{[W]}[p]-\frac{\langle B\rangle^2}{4\pi}\right)m^2-\frac{[p]B_n^2}{[W]4\pi}\right\}=0 \qquad (5\text{-}9)$$

With the density ρ_o upstream of the discontinuity given, this equation can also be considered as an equation for the normal component of the incident velocity V_{n_o}.

Immediately we see that $m=0$ is a solution to equation (5-9) and that three additional plus-minus pairs of real roots exist for which $m \neq 0$. To follow Landau and Lifshitz (1960) and Spreiter et al. (1966a), discontinuities that lie along streamlines ($m=\rho V_n=0$) are called tangential discontinuities or contact discontinuities according to whether or not the normal component of the magnetic field B_n vanishes. Discontinuities across which there is flow ($m \neq 0$) are divided into categories. Those associated with the roots $m=\pm B_n/(4\pi\langle W\rangle)^{1/2}$ are called rotational discontinuities, although they are frequently termed transverse or intermediate shock waves by many authors. The term shock wave is reserved here, however, for the discontinuities associated with the four remaining roots.

A. Tangential Discontinuities

Tangential discontinuities are defined as those in which both m and B_n vanish. For these conditions, equations (5-5) and (5-7) yield the following relations between the quantities on the two sides of the discontinuity surface

$$V_n=B_n=0 \qquad [\underset{\sim}{V}_t]=0 \qquad [\underset{\sim}{B}_t]=0$$
$$[\rho]\neq 0 \qquad \left[p+B^2/8\pi\right]=0 \qquad (5\text{-}10)$$

Although the velocity and magnetic field are required to be parallel to a tangential discontinuity, these relations show that the density and the tangential components of the velocity and magnetic field may have jumps of any magnitude. The other thermodynamic quantities, such as temperature, entropy etc., are also discontinuous in accordance with their definitions provided in equations (5-2). The sum of fluid pressure p and magnetic pressure $B^2/8\pi$ must, however, be continuous across a tangential discontinuity.

B. Contact Discontinuities

The properties of contact discontinuities are given by solving equations (5-5) and (5-7) with $m = 0$ and $B_n \neq 0$. They are as follows:

$$V_n = 0 \qquad B_n \neq 0 \qquad [V] = [B] = [p] = 0 \qquad [\rho] \neq 0 \tag{5-11}$$

These relations show that the fluid not only flows parallel to the contact discontinuity in a steady flow, but that the velocity, pressure, and magnetic field must be continuous. The density, and therefore the temperature, entropy, and other thermodynamic variables, may have any discontinuity however.

C. Rotational Discontinuities

The properties of rotational discontinuities are determined by solving equations (5-5) or (5-7) with $m = m_r = \pm B_n/(4\pi \langle w \rangle)^{1/2}$. They are

$$V_n = \pm B_n/(4\pi\rho)^{1/2} \qquad [\underset{\sim}{V}_t] = [\underset{\sim}{B}_t]/(4\pi\rho)^{1/2}$$

$$[\rho] = [p] = [V_n] = [B_n] = [B^2] = 0 \tag{5-12}$$

These relations show that only the tangential component of the velocity

and the direction of the magnetic-field vector change across a rotational discontinuity. The flow-velocity component V_n normal to a rotational discontinuity is equal to the phase velocity of an Alfvén wave in the direction of the wave normal, and is moreover independent of the strength of the discontinuity. There is thus no tendency for a series of weak rotational discontinuities in a homogeneous medium either to overtake one another and coalesce into a shock wave or to spread out as in an expansion fan. Although there has been considerable discussion of possible effects of traveling rotational or Alfvén waves in the magnetosphere and in space (see, e.g. MacDonald [1964] for a review), and it has been suggested (Levy et al., 1964) that the magnetosphere boundary may be resolved into a rotational discontinuity and a slow expansion fan, the role and importance of stationary rotational discontinuities in the steady-state flow of solar plasma past the planets has not been established.

D. Shock Waves

The mass flux m through magnetohydrodynamic shock waves satisfies the equation

$$\langle W\rangle m^4 + \left(\langle W\rangle [p]/[W] - \langle B\rangle^2/4\pi\right) m^2 - [p] B_n^2/4\pi [W] = 0 \qquad (5\text{-}13)$$

obtained by setting to zero the last factor of equation (5-9). Spreiter et al. (1966a) showed that equations (5-7), together with the further requirement stemming from the entropy considerations that all shock waves are compression waves, yields the following relations between the quantities on the two sides of such a shock wave

$$[\underset{\sim}{B}_t] = [\underset{\sim}{B}] = \frac{-m^2[W]\langle \underset{\sim}{B}_t\rangle}{\langle W\rangle m^2 - B_n^2/4\pi} \qquad [B_n] = 0$$

$$[\underset{\sim}{B}]^2 = 2\langle \underset{\sim}{B}\rangle\cdot[\underset{\sim}{B}] \qquad [\underset{\sim}{V}_t] = -\frac{m[W]B_n\langle \underset{\sim}{B}_t\rangle/4\pi}{\langle W\rangle m^2 - B_n^2/4\pi}$$

$$[V_n] = -[W]m \qquad [W] < 0 \qquad [p] > 0 \tag{5-14}$$

where m represents any of the four roots of equation (5-13). The first of these, they pointed out, indicates that the sum $2\langle \underset{\sim}{B}_t \rangle$ and difference $[\underset{\sim}{B}_t]$ of the tangential components of the magnetic fields on the two sides of the shock wave lie in either the same or opposite directions. This requires the shock normal $\hat{n}$ and the magnetic-field vectors on the two sides of the discontinuity to be coplanar. The velocity relations also show that the tangential component of the velocity discontinuity $[\underset{\sim}{V}_t] = \underset{\sim}{V}_{t_1} - \underset{\sim}{V}_{t_0}$ is in the same or opposite directions as $\langle \underset{\sim}{B}_t \rangle$ and therefore in the same plane as $\underset{\sim}{B}_1$ and $\underset{\sim}{B}_0$.

Spreiter et al. (1966a) discussed the properties of shock waves characterized by the various roots for m by rewriting equation (5-13) to read

$$\left(m + [p]/[W]\right)\left(\langle W \rangle m^2 - B_n^2/4\pi\right) = m^2 \langle \underset{\sim}{B}_t \rangle^2 / 4\pi \tag{5-15}$$

Since the roots $m = m_r = \pm B_n/(4\pi\langle W \rangle)^{1/2}$ were considered before, it follows that $m_f^2 > -[p]/[W]$ if $m^2 = m_f^2 > m_r^2$, and conversely that $m_s^2 < -[p]/[W]$ if $m^2 = m_s^2 < m_r^2$. Shock waves characterized by the larger value m_f for the mass flux are called fast, and those by the smaller value m_s slow. The mass flux across either class of shock wave must therefore satisfy the inequalities

$$m_f \geq m_r \geq m_s \qquad m_f \geq -[p]/[W] \geq m_s \tag{5-16}$$

It follows immediately from equations (5-14) and (5-16) that $\underset{\sim}{B}_t$ and B^2 increase through a fast shock wave and decrease through a slow shock wave.

Solutions of equations (5-5) or (5-7) are determined by straightforward but lengthy algebraic manipulations, details of which

are available in several books (see, e.g. Anderson [1963] or Jeffrey and Taniuti [1964] for extensive accounts). It is important to recognize, however, that these equations possess extraneous solutions that cannot occur in nature. These solutions were originally referred to as unstable, but this term has now been generally abandoned since it has become known that this is not an ordinary instability growing exponentially with time, but rather a sudden disintegration of the shock wave. Alternatively, as noted by Spreiter et al. (1966a), a solution containing an extraneous shock wave does not have neighboring solutions corresponding to a small change in the boundary condition which requires an arbitrarily small angle or rotation of the plane containing the magnetic field. Identification of the physically relevant solutions cannot be made on the basis of entropy considerations alone, as in ordinary gasdynamics. It is necessary in magnetohydrodynamics to consider how a shock wave could evolve through waves of small amplitude overtaking one another and coalescing. The appropriate requirements for a physically relevant solution can be stated in general mathematical terms by a pair of evolutionary conditions (see e.g. Jeffrey and Taniuti [1964]). A more physical description that leads to the same conclusions has been given by Kantrowitz and Petschek (1964). From either point of view, it is found that no additional conditions need be imposed for fast shock waves and that the conservation equations (5-5) possess extraneous solutions only for slow shock waves. Fortunately, the extraneous solutions can be easily recognized by the fact that they indicate the tangential component of the magnetic field to be directed oppositely on the two sides of the discontinuity, a physical impossibility in all but certain degenerate cases. Since the first of equations (5-14) shows that the tangential component of the magnetic field cannot reverse direction through a fast shock wave, one has the general result that the tangential components of the magnetic field on the two sides of any physically relevant shock wave must always lie in the same direction. Spreiter et al. (1966a) pointed out the further consequence that the flow velocity must be greater than the rotational wave speed on both sides of a fast shock wave and less than the rotational wave speed on both sides of a slow shock wave.

Thus a fast shock wave overtakes a slow shock wave, and conversely a slow shock wave cannot overtake a fast shock wave. In application to the supersonic flow of the solar wind past either the Earth or Mars or Venus, we therefore anticipate that the bow wave would be a fast magnetohydrodynamic shock wave. However, slow shock waves, as well as additional fast shock saves, can be expected in the flow downstream of the bow wave.

E. Weak Shock Waves

The relations given in equations (5-13) and (5-14) simplify for weak shock waves to the point where they can be expressed explicitly in terms of the sound speed a, the Alfvén speed A, and its components A_n and A_t normal and tangential to the plane of the discontinuity surface. The latter are defined as

$$A = \sqrt{B^2/4\pi\rho}$$

$$A_n = \sqrt{B_n^2/4\pi\rho} = A\left|\cos\theta\right| \tag{5-17}$$

$$A_t = \sqrt{B_t^2/4\pi\rho} = A\left|\sin\theta\right|$$

where θ refers to the angle between the magnetic field B and the shock normal n. For such shock waves, the jump $[Q]$ in every quantity Q is much smaller than the quantity itself, and the desired simplification can be accomplished by simply removing the mean value brackets and replacing, for clarity of expression, the difference brackets with δ, i.e. $\langle Q\rangle = Q$ and $[Q] = \delta Q$. Equation (5-13) may then be solved to yield the following expression for the normal velocity component V_n of the incident stream:

$$V_n = \pm\left\{\frac{1}{2}\left[a^2 + A^2 \pm \sqrt{(a^2 + A^2)^2 - 4a^2A_n^2}\right]\right\}^{1/2} \tag{5-18}$$

With V_n taken positive, the larger of the two values obtained by using the plus sign before the inner radical pertains to the fast wave and the smaller to the slow wave.

Equation (5-18) coincides with the corresponding expression for the velocity component normal to the characteristic surfaces of equations (5-1) and can be recognized, upon changing to a reference frame fixed in the fluid upstream of the shock wave, as the appropriate expression for the phase velocities of fast and slow traveling hydromagnetic plane waves. The propagation of such waves is conveniently described graphically by the familiar normal-speed or Friedrichs I diagrams, examples of which are shown in figure 5-1 originally presented by Spreiter et al. (1966a) for $a = \sqrt{2}\,A$, $a = A$, and $a = A/\sqrt{2}$. In these diagrams V_n is plotted as a function of angle θ between the shock normal and the magnetic field $\underset{\sim}{H}$ (here taken parallel to the horizontal axis). The outer curve in each diagram represents the results for the fast wave, and the inner curves the results for the slow wave.

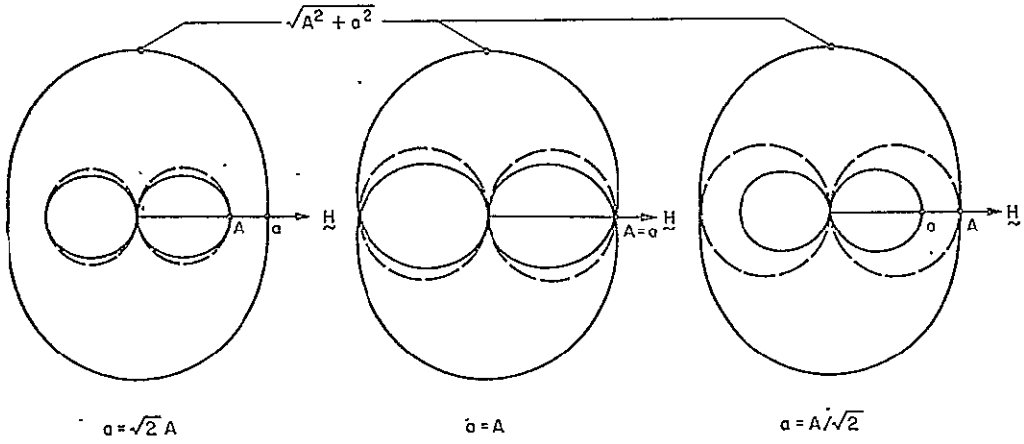

Figure 5-1. Normal speed or Friedrichs I diagrams for propagation velocity of weak plane waves (Spreiter et al., 1966a)

Also included are dotted curves representing the normal velocity of a rotational discontinuity defined by equation (5-12). For ease of illustration, the diagrams were drawn for the plane containing the

wave normal and the magnetic-field vectors. The corresponding results for more general orientations are represented by the corresponding three-dimensional surfaces formed by rotating the plane curves of figure 5-1 about the $\theta = 0$ axis. These plots illustrate that, for any direction θ, the speed of a rotational wave is intermediate between that of the fast and slow waves. Further, V_h for the fast wave is equal to the larger of a and A when the wave normal is parallel to $\underset{\sim}{H}$ ($\theta = 0$), and to $(a^2 + A^2)^{1/2}$ when the wave normal is perpendicular to $\underset{\sim}{H}$ ($\theta = \frac{\pi}{2}$). For the slow wave, V_h vanishes when $\theta = \pi/2$, and is equal to the smaller of a and A when $\theta = 0$. If A approaches zero while a remains finite, the surfaces representing the slow and rotational waves disappear and the surface representing the fast wave approaches a sphere of radius a. Under these circumstances, the equations of magnetohydrodynamics approach those of gasdynamics, and calculations based on aerodynamic methods should provide a good approximation for most applications. If, on the other hand, a approaches zero while A remains finite, the surfaces representing the slow wave disappear while the one representing the fast wave approaches a sphere of radius A, and those representing the rotational discontinuity remain spheres of radius $A/2$ as always. Although equation (5-18) clearly shows that the normal velocity of fast and slow waves are invariant with interchange of values for a and A and that the former become independent of direction θ as a vanishes, the rotational discontinuities retain a finite normal velocity, and neither the differential equations nor the shock relations of magnetohydrodynamics approach those of gasdynamics in this limit (except in a special and restricted sense for flows in which the velocity and magnetic-field vectors are parallel at all points [Kantrowitz and Petschek, 1964]).

Spreiter et al. (1966a) indicated that the jump relations given in equations (5-14) similarly reduce in the limit of weak shock waves to

$$\delta \underset{\sim}{B}_t = \frac{V_n^2 \underset{\sim}{B}_t}{V_n^2 - A_n^2} \frac{\delta\rho}{\rho} \qquad \delta B_n = 0 \qquad \delta B^2 = 2\underset{\sim}{B} \cdot \delta \underset{\sim}{B}$$

$$\delta \underset{\sim}{V}_t = \left(\frac{V_n A_t A_n}{V_n^2 - A_n^2}\right) \frac{\delta\rho}{\rho} \left[\frac{\underset{\sim}{B}_t \; B_n}{|\underset{\sim}{B}_t| \, |\underset{\sim}{B}_n|}\right] \qquad \delta V_n = V_n \, \delta\rho \tag{5-19}$$

where the quantity in the last bracket of the expression for $\delta \underset{\sim}{V}_t$ gives the direction and sign of that quantity. The corresponding expressions for the change in pressure p and entropy S across a weak shock wave are (see, e.g. Jeffrey and Taniuti [1964])

$$\frac{\delta p}{p} = \gamma \frac{\delta\rho}{\rho} + \gamma \frac{(\gamma-1)}{2} \left(\frac{\delta\rho}{\rho}\right)^2 + \left[\frac{\gamma(\gamma-1)^2}{4} + \frac{\gamma(\gamma-1) V_n^4}{4(a^2/A_t^2)(V_n^2 - A_n^2)^2}\right] \left(\frac{\delta\rho}{\rho}\right)^3 + \cdots \tag{5-20}$$

$$\delta S = c_v \frac{\gamma(\gamma-1)}{4} \left[\frac{\gamma+1}{3} + \frac{V_n^4}{(V_n^2 - A_n^2)^2 (a^2/A_t^2)}\right] \left(\frac{\delta\rho}{\rho}\right) + \cdots$$

The latter relation shows that the change in entropy through a weak shock wave is proportional to only the third power of $\delta\rho/\rho$, and hence it is vanishingly small for weak waves. Physically, this indicates that infinitesimal expansions, as well as compressions, can be considered without violation of the entropy requirement. Thus $\delta\rho$ can be either positive or negative. Moreover, equation (5-20) shows that although the change in pressure through a weak discontinuity is proportional to $\delta\rho/\rho$ the first term in which the magnetic field appears is proportional to $(\delta\rho/\rho)^3$. The changes in entropy and pressure through magnetohydrodynamic expansions or compressions are

thus the same as in gasdynamics until the strength of the discontinuity is sufficiently great that third-order terms must be retained. As indicated by equation (5-19), however, this statement does not extend to other quantities such as the velocity or the magnetic field.

These results for weak compression and expansion waves are useful for describing conditions at great distances from the Earth or other disturbing obstacles where it can be safely assumed that $\delta\rho/\rho << 1$. They are not sufficient for the discussion of the entire bow-wave problem, however, because typical conditions in the solar wind close by the Earth are such that $\delta\rho/\rho$ may easily exceed unity near the nose. The maximum value for the density ratio across a hydromagnetic shock is finite, however, and given simply by $\rho_1/\rho_0 = (\gamma + 1)/(\gamma - 1)$ just as in gasdynamics.

CHAPTER VI

APPLICATION TO PLANETARY INTERACTION

The concepts and equations of magnetohydrodynamics which were reviewed in the preceding chapter can now be applied to the specific study of the interaction of the steady solar wind and the planets Earth, Mars, and Venus.

Extensive theoretical investigations, specific calculations, and detailed comparisons with observations have been carried out in the past by many workers (see Spreiter et al. [1968] and Spreiter and Alksne [1969, 1970] for recent summaries) in the study of the gross features of the interaction of the solar wind with the Earth. We have recently extended and modified the hydromagnetic theory of the solar-wind flow past the Earth so that it is applicable to nonmagnetic planets, such as Mars and Venus, that have a sufficient ionosphere to deflect the solar plasma around the planet and its atmosphere. (A preliminary version of this work was reported by Spreiter et al. [1970b]). Here, because of the similarity of these two theoretical analyses, we choose next to review those elements of the theory of the interaction with the Earth which are necessary for comparison with and completeness of this more comprehensive account of solar-wind interaction with nonmagnetic planets.

Of the five classes of discontinuities described in the last chapter, only the tangential discontinuity has properties compatible with those found in space (Spreiter and Alksne, 1969, 1970) describing the boundary surface that separates the planet from the flowing solar plasma. Specifically, for the Earth the condition $B_n = 0$ complies with the finding that there is no connectivity between the geomagnetic and interplanetary fields (Behannon and Fairfield, 1969). For planets such as Mars and Venus that have no significant intrinsic magnetic field, but a sufficiently dense and electrically conducting ionosphere to stop and deflect the solar wind before it is absorbed by the planetary surface or atmosphere, $B_n = 0$ states that at the

boundary the interplanetary field is parallel to it. In both cases, the condition $V_h = 0$ prohibits flow across the surface, which thus can be identified as a streamline and therefore a boundary of the flow. Arbitrary differences in the density and the velocity and magnetic-field components parallel to the boundary are allowed, but the sum of the gas pressure p and magnetic pressure $B^2/8\pi$ must be the same on the two sides of this surface.

The properties of contact discontinuities appear to be appropriate for the boundary of the distant wake far downstream from the planets. There, any current system or velocity discontinuity, such as exists on the forward part of the Earth's magnetopause, has ample time to diffuse or decay no matter how slight the departures from perfect electrical conductivity or inviscid flow. Under these circumstances the external magnetic field penetrates the discontinuity and ultimately at great distances downstream may be expected to traverse the wake completely without distortion (Spreiter et al., 1966a). Thermodynamic properties of the wake remain different from those of the surrounding flow, however, because of the different previous histories of the gases.

As pointed out before, two important parameters that characterize the flow at any point are the Mach number M and the Alfvén Mach number M_A defined by equations (5-4). The former is the ratio of the flow velocity to the speed of sound a, and the latter is the corresponding ratio of velocity to the speed A of a rotational or Alfvén wave propagating along the direction of the magnetic field. Values for a and A for conditions typical of those encountered in the solar wind as it flows past Venus, Earth, and Mars are illustrated in figure 6-1. The solar wind is known to vary substantially with time, but number densities of the order of 2.5 to 25 protons/cm^3, magnetic fields of 3 to 10 γ, and temperatures of 50,000 to 100,000 °K may be considered representative. Since the velocity of the incident solar wind ranges from about 300 to 800 km/sec, it is evident that the free-stream Mach number M_∞ and Alfvén Mach number $M_{A\infty}$ are generally much greater than unity. And for normal conditions, the interaction of the solar wind and the planets is related to highly

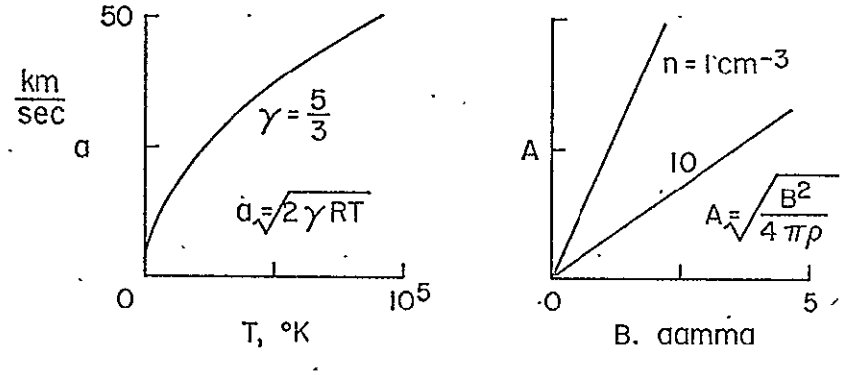

Figure 6-1. Speed of sound a and of Alfvén waves A in fully ionized hydrogen for conditions representative of those in the solar wind (Spreiter and Alksne, 1970).

supersonic and superAlfvénic magnetohydrodynamic flows in which M and M_A are of the order of 10.

Even though it is possible for weak disturbances to travel as fast as $(a^2 + A^2)^{1/2}$ in a direction normal to the magnetic field, the maximum propagation speed is much less than the flow speed. Consequently, it can be inferred that a standing shock wave must exist in the flow around these planets. Of the five classes of discontinuities outlined above, Spreiter et al. (1968) pointed out that only the fast shock wave can be used to represent this standing bow wave because the solar wind approaches these planets with a mass flux $\rho_\infty V_\infty$ that greatly exceeds that of a rotational discontinuity, and therefore also of a slow shock wave.

A. Asymptotic Directions of Shock Waves and Wakes

The Friedrichs I diagrams of figure 5-1 describe the propagation speeds of weak plane waves as viewed in a coordinate system in which the undisturbed plasma is at rest. In applications to steady flows, the corresponding diagram for the infinitesimal standing wave pattern of a point disturbance is often of greater interest. The directions of such waves are of significance for finite disturbances as well because they coincide with the asymptotic directions of the standing wave pattern at great distances from the obstacle. So when

M_∞ and $M_{A\infty}$ are given together with the directions of the velocity and magnetic-field vectors $\underset{\sim}{V}_\infty$ and $\underset{\sim}{B}_\infty$ in the undisturbed incident solar wind, the asymptotic directions of the planetary tail (or wake) and shock waves at great distances from an obstacle can be determined immediately by a simple geometrical construction based on these normal-wave-speed diagrams and originally devised by Spreiter et al. (1966a). The results apply equally whether the obstacle is in effect the confined geomagnetic field as in the case of the Earth's magnetosphere, or the highly conducting ionosphere of either Mars or Venus.

This construction is illustrated in figure 6-2(a) for a case

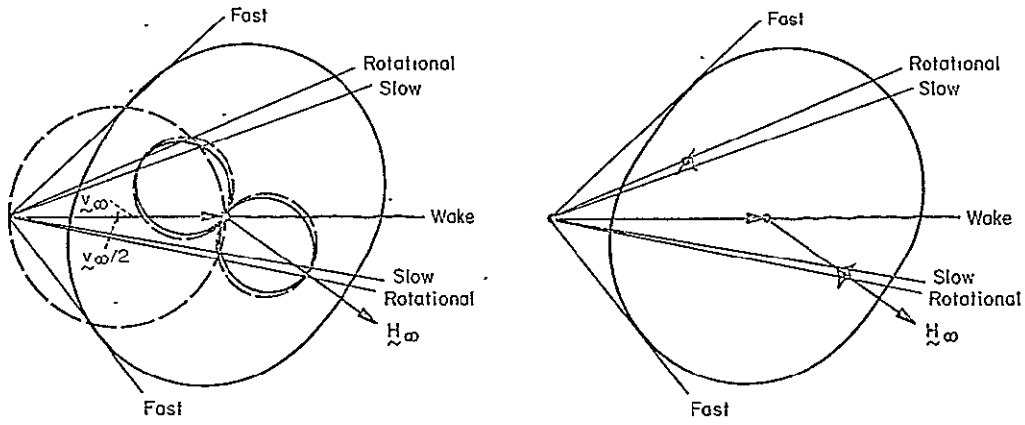

Figure 6-2. Sketches showing how asymptotic directions of shock waves, rotational discontinuities, and wakes can be determined by use of Friedrichs I or II diagrams. (a) Using Friedrichs I diagram for plane waves. (b) Using Friedrichs II diagram for waves from a point disturbance (Spreiter et al., 1966a).

in which the magnetic-field vector $\underset{\sim}{B}_\infty$ is inclined 45° from the free-stream-velocity vector $\underset{\sim}{V}_\infty$, and $M_{A\infty} = \sqrt{2}\, M_\infty$ and M_∞ is chosen to be 2, abnormally small values for the solar wind, in order to better show the construction details. For M_∞ and $M_{A\infty}$ of the order of 10, the $\underset{\sim}{V}_\infty$ vector would be much longer, and all waves would make much smaller angles with the direction of flow. For ease of illustration, only the traces of the various three-dimensional

surfaces in the plane containing the velocity and field vectors are shown. In this plot the flow is to the right and parallel to the horizontal axis. The obstacle is supposed stationary at the center of the Friedrichs diagram which has been rotated by the 45-degree angle between $\underset{\sim}{V}_\infty$ and $\underset{\sim}{B}_\infty$. With the center at the tip of the vector $\underset{\sim}{V}_\infty$ and θ measured from the direction of $\underset{\sim}{B}_\infty$, equation (5-18) is used to construct curves representing the normal velocities of weak shock waves and rotational discontinuities. Except for a translation of the origin and rotation of the axis, the latter are of course the same as shown in figure 5-1 for $a/A = \sqrt{2}$. The asymptotic directions of the various discontinuities at great distances from the obstacle can now be determined by application of the theorem that states that the two lines drawn from any point on a circle to the extremities of a diameter intersect at a right angle. The required construction is thus performed simply by drawing a circle of radius $\underset{\sim}{V}_\infty/2$ with center at $\underset{\sim}{V}_\infty/2$ and connecting the origin of $\underset{\sim}{V}_\infty$ to the various points of intersection with the normal speed curves by straight lines as indicated in figure 6-2(a). These lines are not tangent to the Friedrichs I diagram, as in the simpler isotropic case of gasdynamics, because this diagram represents the speed of plane waves and is very different from the Friedrichs II diagram for the speed of waves from a point source. The asymptotic directions can also be constructed by drawing straight lines from the origin of the vector $\underset{\sim}{V}_\infty$ tangent to the Friedrichs II diagram as illustrated in figure 6-2(b). This procedure often requires more effort because the expression describing the Friedrichs II diagram is much more complex than equation (5-18). The construction employed in figure 6-2(a) is more direct and fully equivalent for the present purposes.

Also indicated in figure 6-2 is the asymptotic direction of the wake or tail, which as noted previously would be represented by either a tangential discontinuity or a contact discontinuity depending upon whether or not the normal component of the magnetic field vanishes. In either case Spreiter *et al*. (1966a) noted that equations (5-10) and (5-11) state that $V_n = 0$ indicating that the wake must be aligned parallel to $\underset{\sim}{V}_\infty$ independently of the direction of the

magnetic field. The orientations of the other discontinuities illustrated in figure 6-2 change, however, as the direction of the magnetic-field vector is altered. The extent of these changes can be readily visualized, morover, since a change in the direction of the magnetic field leads to a rotation of the Friedrichs speed diagrams about the end of the fixed $\underset{\sim}{V}_\infty$ vector, and this in turn leads to associated changes in the intersection points of figure 6-2(a) or the tangency points of figure 6-2(b).

B. Relation Between Hydromagnetic and Gasdynamic Flows

Although the diagrams of figure 6-2 are drawn for the case in which the free-stream Mach number is 2 and the speed of sound is $\sqrt{2}$ times the Alfvén speed, that is for $(a/A)_\infty = (4\pi\gamma p_\infty/B_\infty^2)^{1/2} = \sqrt{2}$, the qualitative character of these diagrams remains the same for all Mach numbers and ratios $(a/A)_\infty$ greater than unity. If A_∞ should become small relative to a_∞, however, as might readily occur if the magnetic field should diminish in intensity, the inner loops representing the propagation speeds of rotational and slow waves become small relative to the outer ovals representing the fast waves. Finally, if the magnetic field approaches zero, the inner loops shrink toward a point at the end of the $\underset{\sim}{V}_\infty$ vector while the outer oval approaches a circle (or sphere in the corresponding three-dimensional representation) of radius a_∞. In this way Spreiter et al. (1966a) indicated that the fast hydromagnetic wave degenerates to the Mach wave of ordinary gasdynamics, and the rotational and slow waves lose their physical significance. The fluid and electromagnetic aspects of the flow thus decouple, and the fluid motion is described entirely by the equations of gasdynamics. The approach to the limiting case appears, moreover, to be free of singular behavior, and gasdynamic theory should thus provide a useful approximation to hydromagnetic flows when $(a/A)_\infty$ is substantially greater than unity. In such approximations the gasdynamic Mach number should be associated with the Mach number M of the corresponding hydromagnetic flow, rather than the Alfvén Mach number M_A as was done at times in the past.

If on the other hand the Alfvén speed is substantially greater

than the sound speed, as would occur if the magnetic field is sufficiently strong, the inner loops representing the slow wave speed again shrink toward a point at the end of the $\underset{\sim}{V}_\infty$ vector, while the outer oval representing the fast wave speed approaches a circle of radius A_∞ . The resulting asymptotic directions for fast waves in a hydromagnetic flow of Alfvén Mach number $M_{A\infty}$ thus approach those of gasdynamics for Mach number $M_\infty = M_{A\infty}$. As described by Sears (1960) and others, however, the flows about a given obstacle may be quite different. For certain combinations of M_∞ , $M_{A\infty}$, and angles between $\underset{\sim}{V}_\infty$ and $\underset{\sim}{B}_\infty$ the physically significant waves are those that extend upstream rather than downstream from the disturbance. When such conditions prevail, hydromagnetic flow about a given obstacle may tend to resemble gasdynamic flow about the same obstacle, but with the flow direction of the related incident stream reversed. For other combinations of these quantities, hydromagnetic flow about a given obstacle bears little, if any, resemblance to its gasdynamic counterpart.

C. Shape of the Boundary

In order to calculate the shape of the boundary for a given planet, the physical criterion that determines which of the three classes of interactions sketched in figure 3-1 occurs must be suitably expressed so that the jump conditions for a tangential discontinuity can be applied. To stop the solar wind above the subsolar point, as in the flows past the Earth, Mars, and Venus, the sum of the planetary gas pressure p and the magnetic pressure $B^2/8\pi$ must be sufficient to balance the stagnation pressure p_{st} of the solar wind at a height great enough so that the ionosphere gas can be considered to be effectively collisionless. For Earth, all estimates and observations of the magnitudes of the gas pressure p and the magnetic pressure $B^2/8\pi$ in the outer magnetosphere lead to the conclusion that $B^2/8\pi \gg p$, whereas for nonmagnetic planets like Mars and Venus, spacecraft measurements have shown that $B^2/8\pi \ll p$. However, for the Moon the solar wind was found to flow directly into the surface which indicates that $p + B^2/8\pi \ll p_{st}$. Intermediate cases are easily conceived, but observations have not yet indicated a need for their

consideration.

1. Location of the magnetopause

For the Earth, then, $B^2/8\pi$ far exceeds p throughout all the magnetosphere above a few hundred kilometers. So far as the flow outside the magnetosphere is concerned, the magnetosphere boundary may thus be represented by the limiting case of a tangential discontinuity in which there is a vacuum $(\rho = 0, p = 0)$ on one side, and across which the sum of the gas and magnetic pressure of the exterior flow must be balanced entirely by the magnetic pressure of the magnetosphere (Spreiter et al., 1966a). With the neglect of small effects of electrical currents in the ionosphere, the dominant features of the magnetic phenomena that the impinging solar wind produces in the outer magnetosphere are represented by the terms that remain in equations (5-1) when p and ρ are equated to zero, namely

$$\operatorname{div} \underset{\sim}{B} = 0 \qquad \underset{\sim\sim}{\operatorname{curl}}\ \underset{\sim}{B} = 0 \tag{6-1}$$

The form and size of the magnetosphere boundary are therefore effectively independent of the details of the flow within the magnetosphere and determined primarily by the interaction between the magnetic field within the outer magnetosphere and the hydromagnetic flow around the exterior. There is still flow to be expected within the magnetosphere, but it would be required to move about as if it were confined in a container described by the magnetopause.

To complete the analysis, a mathematical representation for the intrinsic magnetic field of the Earth is required. This is provided with sufficient accuracy for the present purposes by a magnetic dipole at the center of the Earth having a strength such that $\left|\underset{\sim}{B}_e\right| = B_{eq}$ = 0.312 gauss at the geomagnetic equator, and oriented so that the north geomagnetic pole is at 78.6° North latitude and 70.1° West longitude (Chapman and Bartels, 1940). Its extension into space according to equations (6-1) is described by

$$\underset{\sim}{B}_{\oplus} = -B_{eq}(a_e/r)^3(\hat{\theta}\sin\theta + \hat{r}2\cos\theta) \qquad (6\text{-}2)$$

in which $a_e = 6.37 \times 10^8$ cm is the radius of the Earth, r is the geocentric distance, and θ is the polar angle measured with respect to the north geomagnetic pole, and $\hat{r}$ and $\hat{\theta}$ are unit vectors in the r and θ directions. Thus, the mathematical problem of determining the shape of the magnetopause and the distortion of the geomagnetic field confined therein is now completely reduced to finding the solution to equations (6-1) that has a dipole singularity given by equation (6-2) at the origin and that simultaneously matches with the solution for the exterior flow through the tangential discontinuity conditions $B_n = 0$ and $(B^2/8\pi)_{int} = (p + B^2/8\pi)_{ext}$ at the unknown location of the magnetopause.

The resulting free-boundary problem is, however, extremely complex because the location and shape of the magnetosphere boundary is not known a priori, but must be determined as part of the solution much as in the classical theory of free-streamline flows in hydrodynamics. The problem as such is too difficult to solve, and reasonable approximations must be sought. At the magnetosphere boundary one simplification of great practical utility can be made by introducing an approximation to the tangential discontinuity conditions. The basis for this is that space observations and theoretical estimates indicate that the pressure p of the solar wind tends to be much larger than the magnetic pressure $B^2/8\pi$ in the exterior flow around the forward part of the magnetopause (Spreiter et al., 1966a). Consequently, as far as the flow exterior to the magnetosphere is concerned, the equations for the discontinuity at the magnetopause can be satisfactorily approximated by those of the limiting case of a tangential discontinuity in which there is a vacuum on one side and no magnetic field on the other side, i.e.,

$$B_n = 0 \qquad (B^2/8\pi)_{int} = (p)_{ext} \qquad (6\text{-}3)$$

However, since both p_{ext} and B_{int} remain unknown and must satisfy

equations (6-3) at an unknown location, the problem as such continues to be intractable.

Two additional approximations finally reduce the problem to amenable form. The first, used in all existing analyses, is the introduction of the Newtonian approximation for the pressure on the surface of an obstacle in a high-Mach-number flow. Thus p_{ext} is assumed given by

$$p_{ext} = p_{st}\cos^2\psi = K\rho_\infty V_\infty^2 \cos^2\psi \qquad (6\text{-}4)$$

in which ψ is the angle between the outward normal to the magnetopause and the incident free-stream-velocity vector $\underset{\sim}{V}_\infty$, subscript ∞ refers to conditions in the solar wind upstream of the bow wave, and K is a constant equal to 0.88 for high-Mach-number flow of a monatomic gas although usually taken as unity in most applications (Spreiter et al., 1966a). The Newtonian approximation greatly simplifies the problem because it decouples the calculation of the shape of the magnetosphere boundary from the detailed analysis of the surrounding flow. The final approximation assumes that the unknown magnetic field B_{int} at the magnetopause, which results from the distorting of the geomagnetic field by the solar wind, is simply equal to $2f$ times the tangential component of the Earth's dipole field, where f is a constant usually taken to be unity (Spreiter and Briggs, 1962). Its use, together with the Newtonian pressure approximation, in the discontinuity conditions (6-3) leads to a partial differential equation for the geocentric distance r to the magnetopause. Figure 6-3 illustrates the solution of that equation for the equatorial plane (Beard, 1960), the noon meridian plane (Spreiter and Briggs, 1962), and the remainder of the magnetosphere boundary (Briggs and Spreiter, 1963) for the case in which the dipole axis is perpendicular to the solar-wind flow. Higher-order solutions which do not make use of the last approximation for B_{int} have been given more recently (Mead and Beard, 1964; Olson, 1969), but the results differ from each other and from

those of the first-order solution by only about the width of the gray lines of figure 6-3. As may be seen by comparison with figure

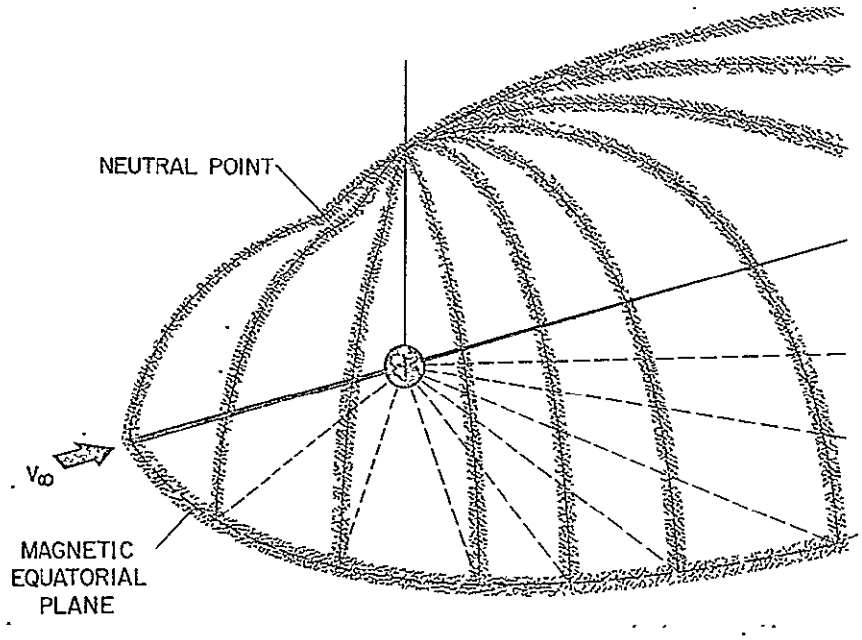

Figure 6-3. The boundary of the geomagnetic field (Spreiter et al., 1968).

3-1, the neutral points indicated on figure 6-3 have physical significance as the points on the magnetopause from which extend the only magnetic field lines to connect directly with the Earth.

2. Location of the ionopause

For Mars or Venus the magnetic field is weak or nonexistent $(B^2/8\pi \ll p)$, but the gas pressure p of the ionosphere is sufficient to stop the solar wind well above the planetary surface. So in this case, the ionosphere rather than the planetary magnetic field communicates the presence of the planet to the solar wind. The ionosphere, or at least the outer part of it that participates in the interaction with the flowing solar plasma, is idealized as spherically symmetric and hydrostatically supported plasma having infinite electrical conductivity. Since the two bodies of plasma are of different

origin and have different properties, they must be mutually impenetrable in the idealized hydromagnetic representation and be separated by a tangential discontinuity surface. This surface is called the ionopause because it marks the outer boundary of the ionosphere (Spreiter et al., 1970b).

More explicitly, the assumption of hydrostatic support is equivalent to assuming that all motions of the gas within the ionosphere are sufficiently small with respect to the planetary body that equilibrium exists between the pressure gradient and the force of gravity, thus

$$\frac{dp}{dr} = -\rho g \tag{6-5}$$

where p and ρ are the gas pressure and density, r is the radial distance from the center of the planet, and g is the acceleration of gravity. Values for the latter are inversely proportional to r^2. Thus $g = g_s (r_s/r)^2$, where subscript s refers to values at the surface of the planet. Values for g_s for Venus, Mars, and Earth are about 870, 375, and 982 cm/sec^2, and those for r_s are about 6.1, 3.4, and 6.4 x 10^8 cm, respectively. The pressure is assumed to be related to the density by the perfect gas law

$$p = nkT = \rho RT/\bar{m} \tag{6-6}$$

which was originally stated in equations (5-2). The mean molecular mass $\bar{m}$ is equal to 1/2 for fully ionized hydrogen plasma, and 1 and 2 for singly ionized molecular hydrogen and helium. The density may be eliminated from equation (6-5) by introduction of equation (6-6), and the result integrated to yield

$$p = p_R \exp\left(-\int_{r_R}^{r} \frac{dr}{H}\right) \tag{6-7}$$

in which p_R is the pressure at the reference radius r_R, and H, the local scale height of the atmosphere, is given by

$$H = \frac{kT}{mg} = \frac{RT}{\bar{m}g} \tag{6-8}$$

where $m = 1.67\bar{m} \times 10^{-24}$ gm is the mean molecular mass.

If H is constant, equation (6-7) may be integrated to obtain

$$p = p_R \exp\left(-\frac{r - r_R}{H}\right) \tag{6-9}$$

which shows that H represents the height interval in which the pressure decreases by a factor e. If the variation of g with r is disregarded over the range of application of equation (6-9), T is also constant, and the density varies with height in the same way as the pressure, thus

$$\frac{\rho}{\rho_R} = \frac{n}{n_R} = \frac{p}{p_R} = \exp\left(-\frac{r - r_R}{H}\right) \tag{6-10}$$

In the upper atmosphere, where little mixing would be presumed to occur, diffusive equilibrium may be considered to prevail among the various ionic constituents, at least in an idealized sense. As emphasized recently by Bauer (1969), however, this equilibrium is more complicated in an ionosphere than in a neutral atmosphere for which Dalton's law of partial pressures is customarily invoked. This is because an electric polarization field, dependent on the mean ionic mass and charged-particle temperatures, acts on all the ions and couples the diffusive equilibrium distribution of all of them. In most circumstances, however, the lightest ionic constituent, ionized atomic hydrogen, would emerge as dominant at great altitudes. At lower and intermediate attitudes, more specific knowledge, such as is now resulting from space experiments conducted by the USSR and USA, is

needed to specify the variation of pressure with radius with any degree of precision.

Figure 6-4 shows the variation with distance from the center of Venus of the electron number density, as deduced from the

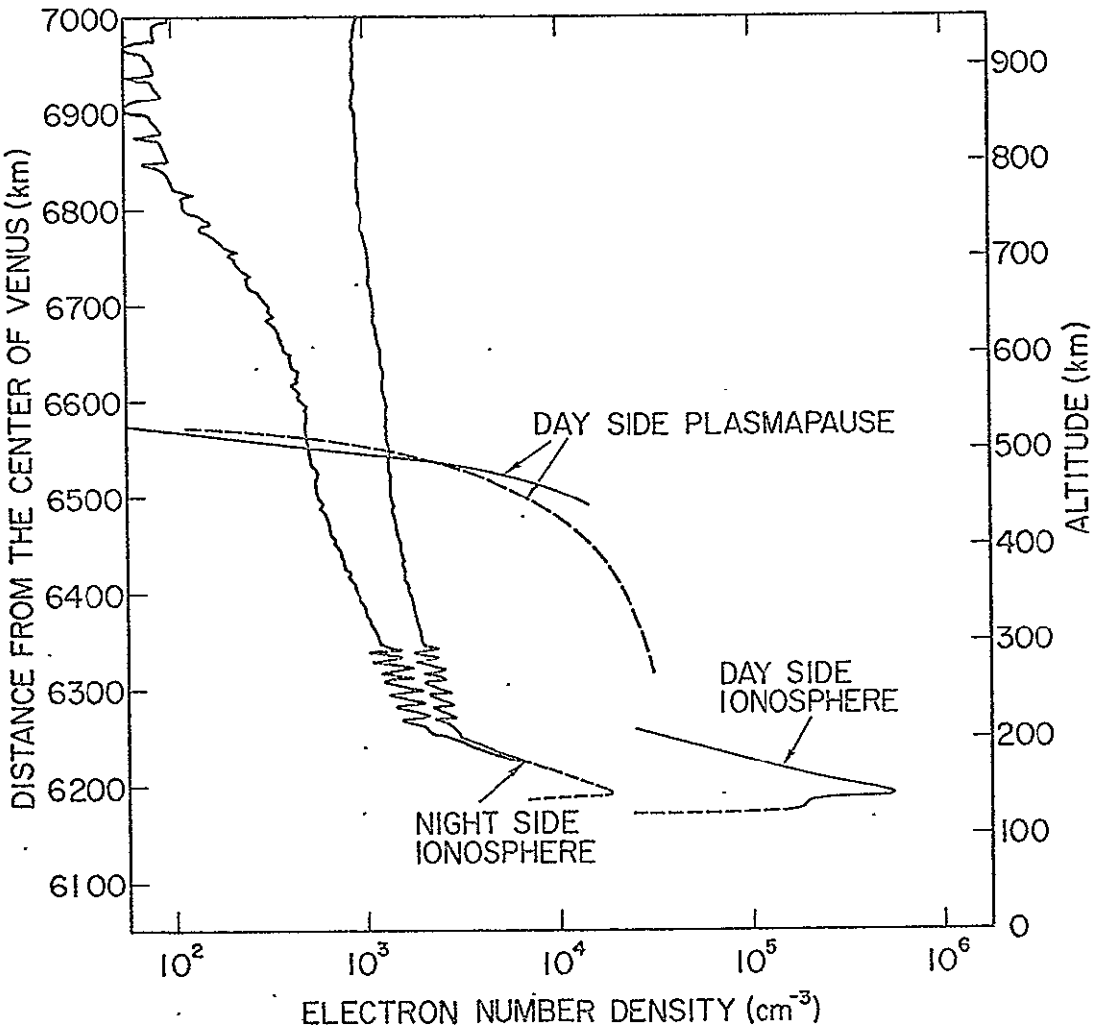

igure 6-4. Profiles of electron concentrations in the night and day ionospheres of Venus, as deduced from the dual-frequency-radio-occultation measurements by Fjeldbo and Eshleman (1969). The dashed lines represent the average profile independent of strong fluctuations in the data.

dual-frequency-radio-occultation measurements by Fjeldbo and Eshleman (1969). For a plasma with singly ionized ions, charge neutrality requires that these curves also describe the ion number density, summed over all constituents. These measurements indicate that the nose of the ionopause is at a distance of about 6500 km from the center of Venus, or about 450 km above the surface. At high altitudes, there is some uncertainty in the data associated with the reference level of interplanetary ionization so that the nightside profile may be somewhere between the two indicated curves. Between 6300 and 6600 km, however, the experimenters have reported that the nightside ionosphere probably consists of ionized helium at a temperature between 330 and 710 °K. And although there is some ambiguity in the data above 6600 km, they suggest that at high altitudes the dominant constituent may be either ionized atomic or molecular hydrogen with a plasma temperature of either 675 or 1350 °K.

The proper interpretation of these data, and also those from the Mariner-5-Lyman-alpha measurements of Barth et al. (1967), has, however, been the subject of considerable discussion. Barth (1968) and Barth et al. (1968) conclude that the entire upper atmosphere of Venus above about 6500 km can be represented best by an atmosphere consisting primarily of molecular hydrogen at 650 ± 50 °K. On the other hand, Wallace (1969) and Donahue (1969) have concluded from their analysis of the Mariner-5-Lyman-alpha data that the dominant constituent above 6500 km is deuterium at about 650 °K. McElroy and Strobel (1969) have compared results from a number of models of the topside nighttime ionosphere of Venus with observations of Mariner 5 and concluded that the primary ionized constituent is either helium or molecular hydrogen. More recently, Whitten (1970) has performed a similar study for a number of models of the upper daytime ionosphere and concluded that a dominant amount of ionized helium also provides a suitable explanation of the spacecraft's findings.

In view of these uncertainties, and even greater ones with respect to Mars at the time of this writing, we put aside any further discussion of refinements of the variation of H with altitude even though there are obvious violations of the conditions for spherical

symmetry, constant scale height, and hydrostatic pressure support, particularly near the dawn meridian of the planet and at great altitudes where H cannot possibly be constant because of diminishing g. However, one inadequate result of this is that equation (6-9) then predicts the implausible occurrence of the planetary pressure becoming vanishingly small at only a distance of several planetary radii on the nightside of the planet. This prediction directly conflicts with the analysis of the occultation data from Mariner 5 suggesting that there may be a wake of planetary ionization extending a great distance in the antisolar direction (Fjeldbo and Eshleman, 1969). To reconcile this difficulty equation (6-9) is slightly modified so that instead of approaching zero, the planetary pressure now varies exponentially to a small, finite value p_w that corresponds to the very low pressure in the tail of the ionosphere at great distances in the antisolar direction. Thus we alter equation (6-9) to read

$$p = (p_R - p_w)\exp\left(-\frac{r - r_R}{H}\right) + p_w \qquad (6\text{-}11)$$

Because nothing about the structure within the tail is known and also because at very great distances this tail must somehow merge with the solar wind, p_w is taken to be a constant equal to $p_\infty + B_\infty^2/8\pi$ the sum of the gas pressure and magnetic pressure in the undisturbed solar wind. The value of p_w is about two orders of magnitude smaller than the maximum pressure on the ionopause. If the constant p_R is taken to be the pressure at the subsolar point of the ionopause, where the maximum pressure occurs, then the coefficient of the exponential term differs from p_R by only about 1 percent. Therefore, the exponential variation of p with r is maintained on the daytime side of the ionosphere, and the small constant p_w does not bear effect in equation (6-11) until r reaches a value of a few planetary radii and the exponential becomes much smaller than p_w. Because the ionopause is located so near the dayside of the planet that r can only become this large in the antisolar direction, equation (6-11) satisfactorily predicts the approximate constant

pressure p_w for the ionized planetary wake, which ultimately balances the sum of the magnetic and gas pressure of the solar wind. Since equation (6-11) corresponds at least generally with the little amount of information so far obtained from spacecraft measurements, we adopt equation (6-11) as adequate to represent the variation of p with r in the upper atmosphere of either Venus or Mars.

Results will be presented for several values for H, however, in order to provide an indication of the variations to be expected between ionospheres of different chemical composition. For Venus, with r_R equated to 6500 km and T to 700 °K, H is approximately 1500, 760, 380, and 35 km for ionized atomic hydrogen, singly ionized molecular hydrogen, helium, and carbon dioxide. The corresponding values for the nondimensional ratio H/r_0, in which r_0, the distance from the center of the planet to the nose of the ionopause, is equated to 6500 km are 0.23, 0.115, 0.058, and 0.0052. For Mars, the smaller radius and acceleration of gravity and lower ionospheric temperature of about 200 °K (Kliore et al., 1965; Fjeldbo and Eshleman, 1968) lead to values that are about 1.2 times larger than for Venus, namely about 0.28, 0.138, 0.069, and 0.0062. The calculations of these values makes use of the result, indicated by the data from Mariners 4, 6, and 7 together with the present theory, that the nose of the ionopause is at an altitude between 155 and 175 km, and that r_0 therefore scales nearly in proportion to the planetary radius.

In a manner exactly analogous to the mathematical formulation of the Earth's magnetopause, the boundary of the ionosphere is represented, under the assumption that the upper ionosphere can be treated as a perfectly conducting fluid effectively bound to the planet and incapable of mixing with the solar-wind plasma, by a tangential discontinuity. For Mars and Venus the planetary magnetic field is weak or nonexistent, and as far as the flow around the ionosphere is concerned, the ionopause can be modeled by the limiting case of a tangential discontinuity in which there is a perfectly conducting ionosphere on the interior side, and across which the sum of the gas and magnetic pressure of the exterior flow must be balanced entirely by

the pressure of the upper ionosphere. For this situation the tangential discontinuity equations become

$$V_n = B_n = 0 \qquad (p)_{int} = (p + B^2/8\pi)_{ext} \qquad (6\text{-}12)$$

and relate conditions on the interior and exterior sides of the ionopause. Therefore the mathematical problem of calculating the shape of the ionopause is now completely reduced to finding the solution for the exterior flow that simultaneously matches with equation (6-11) through the tangential discontinuity conditions of equations (6-12) at the unknown location of the ionopause, which has to be determined as part of the solution.

This free-boundary problem, like that for the determination of the magnetopause, is too difficult to solve as stated. In order to proceed, we introduce, as in the corresponding application to the Earth's magnetosphere, two important simplifications in these relations. In the present application, p tends to be much larger than $B^2/8\pi$ on the exterior side of the ionopause. Therefore the pressure-balance relation of equations (6-12) may be reduced to

$$p_{int} = p_{ext} \qquad (6\text{-}13)$$

a simple balance between the ionosphere pressure, which is given with sufficient accuracy for the present purposes by equation (6-11), and the exterior pressure of the flowing solar plasma adjacent to the ionopause. However, p_{ext} still remains unknown until the exterior-flow solution is determined, but the problem can be reduced to tractable form, as was done for the corresponding determination of the Earth's magnetopause, by the introduction of the Newtonian approximation for the exterior pressure on the ionopause (see equation [6-4]). The Newtonian approximation $p_{ext} = p_{st} \cos^2 \psi$, however, can be improved because it underestimates the pressure on the flanks of the

ionopause (Spreiter et al., 1966a). Behind the planet where the boundary surface becomes parallel to the flow, ψ reaches 90 degrees, and the Newtonian expression indicates that the plasma pressure approaches zero which is physically implausible. A more reasonable limit for the exterior pressure on the flanks of the ionopause is the sum of the static magnetic and gas pressure of the solar plasma $p_\infty + B_\infty^2/8\pi$ because very far behind the planet the pressure must return to free-stream conditions. Therefore, a better approximation for the exterior pressure on the ionopause is

$$p_{ext} = (p_{st} - p_\infty - B_\infty^2 8\pi)\cos^2\psi + p_\infty + B_\infty^2/8\pi \qquad (6\text{-}14)$$

where $p_{st} = K \rho_\infty V_\infty^2$ is the stagnation pressure of the solar wind exerted on the nose of the ionopause (Spreiter et al., 1966a). This expression together with equation (6-11) and the relation $p_w = p_\infty + B_\infty^2/8\pi$ from above reduces equation (6-13) for the pressure balance to

$$(p_{st} - p_w)\cos^2\psi = (K\rho_\infty V_\infty^2 - p_w)\cos^2\psi$$

$$= (p_R - p_w)\exp\left(-\frac{r - r_R}{H}\right) \qquad (6\text{-}15)$$

So in exactly the same way as for flow past the Earth, use of the foregoing approximations greatly simplifies the problem because they decouple the calculation of the shape of the ionopause from the detailed solution of the surrounding flow and permit the coordinates of the ionopause to be computed without determining any further properties of the exterior flow field.

It is convenient in the calculation of the shape of the ionopause to let $r_R = r_0$, the distance from the center of the planet to the nose of the ionopause. Since $\cos^2\psi = 1$ at this point, equation (6-15) simplifies to

$$P_R = P_o = K\rho_\infty V_\infty^2 \qquad (6\text{-}16)$$

at the ionopause nose, and to

$$\cos^2\psi = e^{-(r-r_o)/H} \qquad (6\text{-}17)$$

elsewhere along the ionosphere boundary. If, for example, the solar wind is considered to approach Venus with a number density of 3 protons/cm^3 and a bulk velocity of 5 x 10^7 cm/sec, as the data reported by Bridge et al. (1967) show occurred at the time of the Mariner-5 measurements, equation (6-16) indicates that P_o = 1.1 x 10^{-8} dynes/cm^2. Equation (6-6) shows that such a value corresponds, assuming T = 700 °K, to an ion or electron number density $n_i = n_e = n/2$ at $r = r_o$ of about 5.7 x 10^4 particles/cm^3. This value is somewhat greater than that indicated by the data of figure 6-4 for r = 6500 km, but is not unreasonable if the averaged nature of the Mariner-5 data involved in the estimate and the uncertainties attendant with all plasma measurements in space are considered. In any case, it may be seen from figure 6-4 that the essential condition that the ion-electron number density required to stop the solar wind be exceeded at some altitude is satisfied by a considerable margin, since the peak daytime value of 6 x 10^5 electrons/cm^3 is larger than the required value by a factor of about 10. Similarly for Mars, the values V_∞ = 3.3 x 10^7 cm/sec, n_∞ = 0.8 protons/cm^3, and T = 200 °K inferred from the measurements of Mariner 4 (Lazarus et al., 1967; Kliore et al., 1965) indicate that an electron number density of 2.6 x 10^4 electrons/cm^3 is required at the subsolar point for the ionosphere to stop the solar wind. This value is exceeded by a factor of about 6 by the peak electron density of 1.5 x 10^5 electrons/cm^3 deduced by Kliore et al. (1965) from Mariner 4, and subsequently confirmed by similar experiments with Mariners 6 and 7 (Fjeldbo et al., 1970). On the basis of the further observations that the altitude of

the peak electron density is between 120 and 130 km above the Martian surface and that the electron scale height there is between 20 and 25 km, we may estimate from the above relations that the subsolar point of the ionopause is at an altitude between 155 and 175 km. For these reasons, we feel that the applicability of the theory to both Venus and Mars is supported by existing data, even though those for Mars are restricted in quantity and inferential in nature at the present time.

To proceed, we must express $\cos^2\psi$ in terms of r and θ, where $r(\theta)$ represents the coordinates of the boundary and θ is the angle measured at the center of the planet with respect to a line that extends directly upstream. Upon carrying out this step in the way made clear by the illustration in figure 6-5, and substituting the result into equation (6-17), we find

$$\cos^2\psi = \left(\frac{dy}{ds}\right)^2 = \frac{(r\,d\theta\cos\theta + dr\sin\theta)^2}{dr^2 + (r\,d\theta)^2}$$

$$= \exp\left(-\frac{r - r_o}{H}\right) = E \qquad (6\text{-}18)$$

The numerical solution of this differential equation is facilitated by solving for $dr/rd\theta$ to obtain

$$\frac{dr}{rd\theta} = \frac{\sin 2\theta \pm 2\sqrt{E - E^2}}{2(E - \sin^2\theta)} \qquad (6\text{-}19)$$

At the ionopause nose $\theta = 0$, $r = r_o$, and $dr/rd\theta = 0$ with either choice of sign. The proper choice of sign is dictated by the following considerations based on the assumption that r increases monotonically from r_o to ∞, and hence that E diminishes monotonically from 1 to 0, as θ increases from 0 to 180°. Since $\sin^2\theta = 0$ at $\theta = 0$, increases to unity at $\theta = 90°$, and then returns to 0 at 180°, the

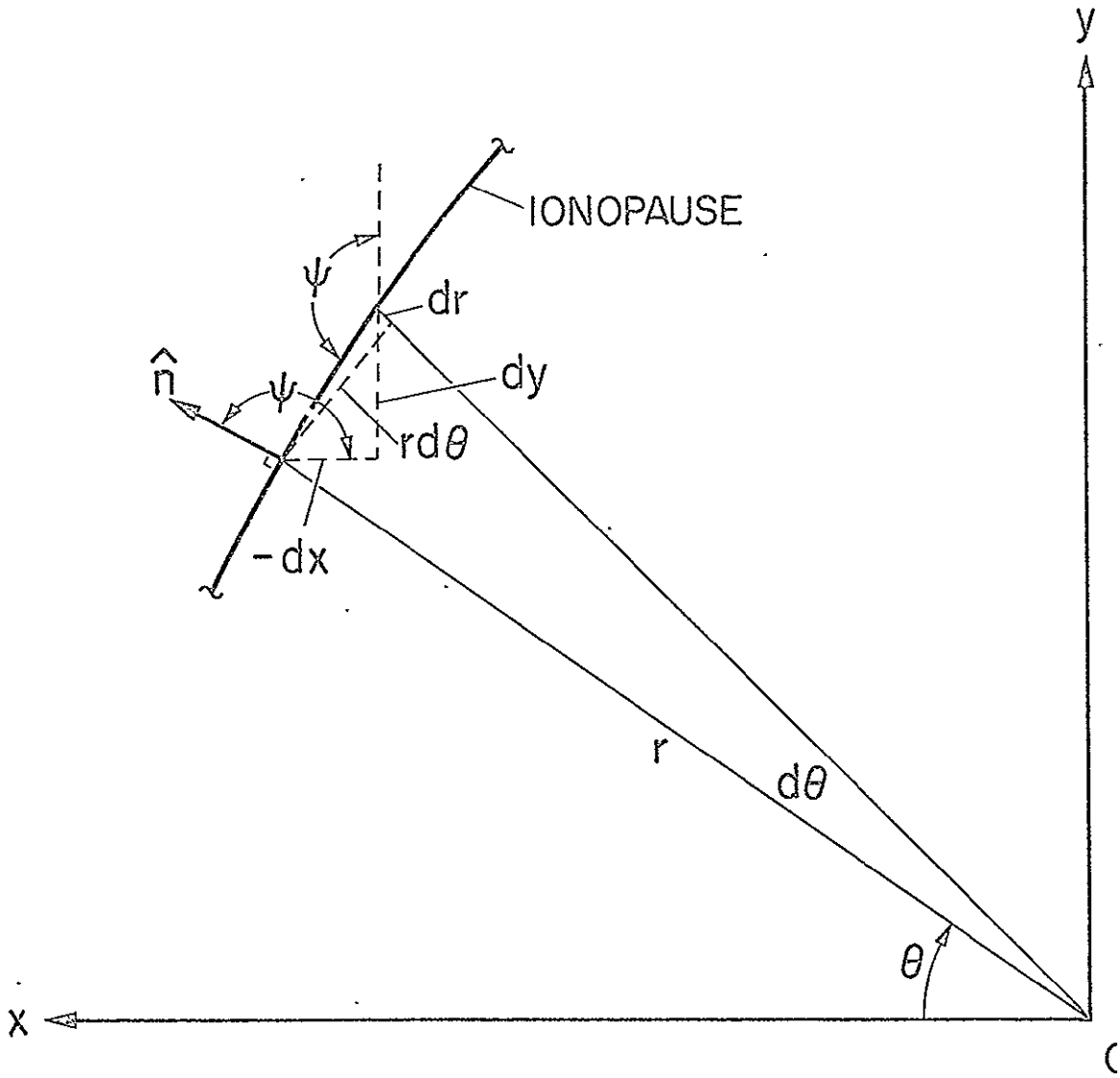

Figure 6-5. View of element of ionopause and coordinates used in equation (6-18) (Spreiter, Summers, and Rizzi, 1970b).

denominator of equation (6-19) must vanish at one or more values for Θ, and $dr/rd\Theta$ would be infinite unless the numerator vanishes simultaneously. If the critical values for Θ and E are designated by the subscript cr, we have

$$E_{cr} = \sin^2\theta_{cr} \tag{6-20}$$

and also that

$$\sin 2\theta_{cr} \pm 2\left(E_{cr} - E_{cr}^2\right)^{1/2} = 0 \tag{6-21}$$

Substitution of the former into the latter to obtain

$$\sin 2\theta_{cr} \pm 2\left(\sin^2\theta_{cr} - \sin^4\theta_{cr}\right)^{1/2} \tag{6-22}$$

$$= 2\sin\theta_{cr}\cos\theta_{cr} \pm 2\left|\sin\theta_{cr}\cos\theta_{cr}\right| = 0$$

shows that the minus sign must be used in equation (6-19). That the resulting indeterminate form actually leads to a finite value for $dr/d\theta$ at $\theta = \theta_{cr}$ may be confirmed by application of L'Hospital's rule. The shape of the ionopause may therefore be determined directly by integration starting from the boundary condition that $r = r_o$ at $\theta = 0$.

Results obtained by numerical integration are presented in terms of cylindrical coordinates $x = r\cos\theta$ and $\bar{r} = r\sin\theta$ for several values for H/r_o from 0.01 to 1 in figure 6-6. As noted previously, this range is ample to include all likely possibilities for both Venus and Mars.[1] Also included on figure 6-6 is a dotted

---

[1]Although the displayed results are independent of the altitude of the ionopause nose, a planet silhouette has been added to the plot to indicate the radius r_V of Venus for the ratio $r_V/r_o = 6050/6500 = 0.93$. The corresponding ratio r_M/r_o for Mars is not known so definitely, but the estimate given above indicates that it is about 0.95.

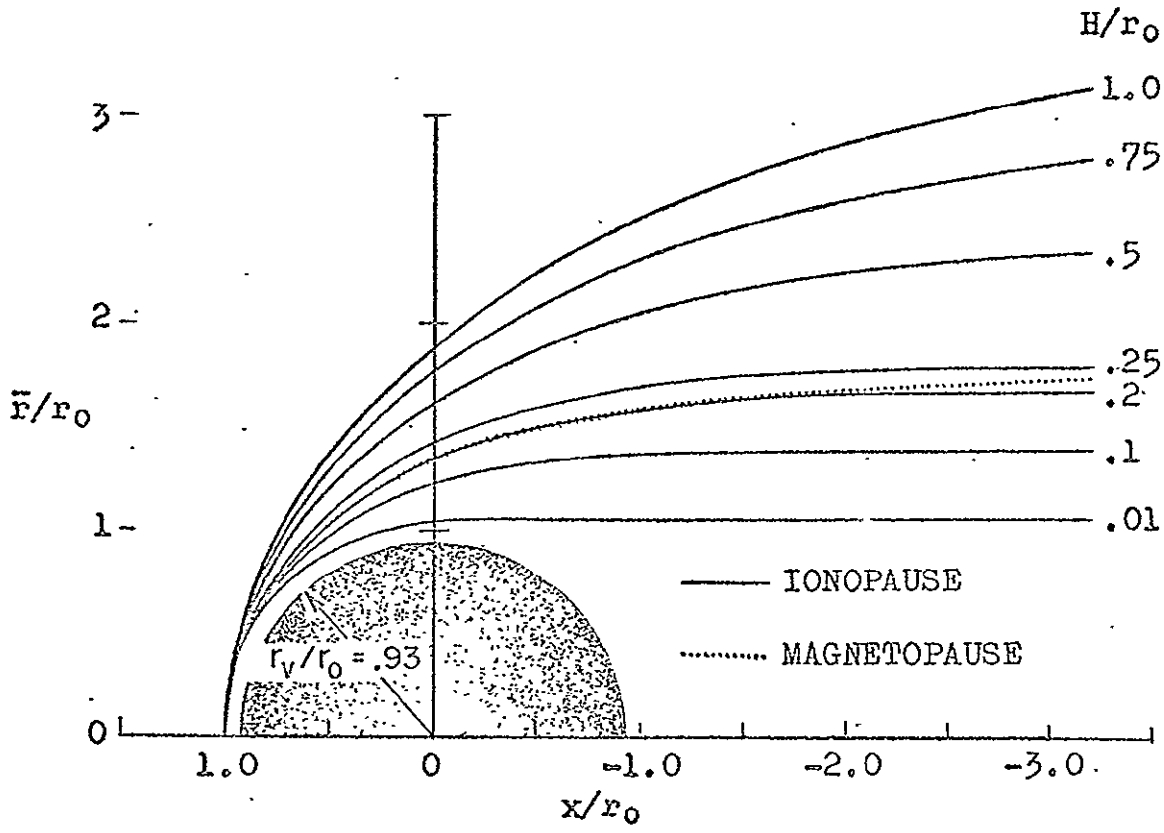

Figure 6-6. Calculated location of ionopause for various H/r_0 . The corresponding results for the shape of the Earth's magnetopause, nondimensionalized so that the magnetosphere nose is at $x/r_0 = 1$, is included for purposes of comparison.

line indicating the coordinates of the magnetic equatorial trace of the magnetosphere boundary, as determined by Beard (1960) and Spreiter and Briggs (1961, 1962), that has been used extensively in the calculation of solar-wind flow past the Earth. These coordinates have been nondimensionalized by dividing by the distance from the center of the Earth to the magnetosphere nose. We shall continue to call this distance r_o, even though it is much larger than for Venus or Mars, and evaluated differently using the expression $r_o = r_e(B_{eq}^2/2\pi K \rho_\infty V_\infty^2)^{1/6}$ in which $r_e = 6.37 \times 10^8$ cm is the radius of the Earth, and $B_{eq} = 0.312$ gauss is the average intensity of the geomagnetic field at the geomagnetic equator. It may be seen that this curve is very similar to that for the ionosphere boundary for $H/r_o = 0.2$. The size, with respect to the planet, of the cavity carved in the solar wind is very different in the two applications, however, since r_o is only a few percent greater than the planetary radius for Venus or Mars, whereas it is usually of the order of 10 Earth radii for the magnetosphere (see figure 6-3).

CHAPTER VII

NUMERICAL SOLUTION OF THE APPROXIMATE EXTERIOR FLOW

A. Simplification to Gasdynamics

We have just shown in the preceding chapter that the exterior and interior regions of the complex free-boundary problem representing the solar-wind interaction with planets can be disjoined and solved separately and that the interior boundary shape can be calculated independently of the exterior-flow solution. We have determined the shape and location of both the magnetopause and ionopause, and what remains is to solve the exterior-flow problem represented by equations (5-1) satisfying the remaining tangential discontinuity relations $V_n = B_n = 0$ of equations (6-12) at the location of the previously determined boundary. These reduced tangential discontinuity conditions are completely equivalent to the boundary conditions that must be satisfied on a solid body, and the problem may be thought of as a hypersonic, but weakly magnetized plasma streaming past a solid body having the shape of either the magnetopause or ionopause. In many ways it is very similar to the aerodynamic problem of a body in a supersonic stream.

However, this magnetohydrodynamic-flow problem is far too complicated to be solved exactly, and resort must be had to approximations. For Earth, Mars, and Venus, an important simplification of the magnetohydrodynamic equations (5-1) can be made on the basis of the combined effects of the large magnitude of the Alfvén Mach number and the strong interaction nature of the flow (Spreiter et al., 1966a). This is so because the order of magnitude of the inertia term $\rho(\underset{\sim}{V}\cdot\underset{\sim}{\nabla})\underset{\sim}{V}$ in the differential equation for the momentum is related to the magnetic term $(1/4\pi)\underset{\sim}{B}\times\underset{\sim\sim}{\text{curl}}\,\underset{\sim}{B}$ by the square of the Alfvén Mach number. When the latter is large, therefore, the magnetic term can usually be safely dropped from the equation with little loss of accuracy, just as discussed in section B of chapter VI. In order for this approximation to be valid, however, the square of the Alfvén Mach number must remain

large at all points in the exterior flow. For normal conditions of the solar wind upstream of the bow wave, this term is about 100, but observations made in space indicate that it decreases somewhat in the disturbed region of the flow downstream of the bow wave. Lees (1964) has suggested that a small region may exist near the stagnation point in which the magnetic field may become sufficiently enhanced under certain circumstances to produce a substantial reduction in the gas density. The region affected is very small for weak magnetic fields, however, and is anticipated to have little effect on the gross features of the flow so that the simplification is justifiable throughout the exterior-flow region. Although factors of 2 appear when similar comparisons are made of the magnetic and inertia terms in the conservation equations for the momentum and energy, the general conclusion that the magnetic terms may be dropped from these equations when the Alfvén Mach number is large still holds. An immediate consequence is that both the differential equations and the conservation equations defining the flow are decoupled from those involving the magnetic field. The differential equations (5-1) for the fluid motion thereby reduces to

$$\underset{\sim}{\nabla} \cdot \rho \underset{\sim}{V} = 0$$

$$\rho (\underset{\sim}{V} \cdot \underset{\sim}{\nabla}) \underset{\sim}{V} + \underset{\sim}{\nabla} p = 0 \qquad (7\text{-}1)$$

$$(V \cdot \nabla) S = 0 \qquad S - S_o = c_v \ln \frac{p/p_o}{(\rho/\rho_o)^{\gamma}}$$

and the conservation equations (5-5) to

$$[\rho V_n] = 0$$

$$\left[\rho V_n \underset{\sim}{V} + p\hat{n}\right] = 0$$

$$\left[\rho V_n \left(h + \tfrac{1}{2}V^2\right)\right] = 0 \qquad (7\text{-}2)$$

Thus, all the properties of the flow except the magnetic field $\underset{\sim}{B}$ can be determined by solving the equations of gasdynamics (7-1, 7-2). The properties of the magnetic field can then be determined subsequently by solving the remaining equations

$$\underset{\sim}{\text{curl}}\,(\underset{\sim}{V} \times \underset{\sim}{B}) = 0 \qquad \text{div}\,\underset{\sim}{B} = 0$$

$$\left[B_n \underset{\sim}{V}_t - \underset{\sim}{B}_t V_n\right] = 0 \qquad \left[B_n\right] = 0 \qquad (7\text{-}3)$$

using the values for $\underset{\sim}{V}$ already computed from the preceding step. These relations, or equivalently, the following equations derived from them

$$\frac{D}{D\tau}\int\int_{\Omega} \underset{\sim}{B}\cdot d\underset{\sim}{\Omega} = 0$$

$$\frac{D}{D\tau}\left(\frac{\underset{\sim}{B}}{\rho}\right) = \frac{1}{\rho}(\underset{\sim}{B}\cdot\underset{\sim}{\nabla})\underset{\sim}{V} \qquad (7\text{-}4)$$

in which Ω is an arbitrary surface moving with the fluid and $D/D\tau = \frac{\partial}{\partial\tau} + (\underset{\sim}{V}\cdot\underset{\sim}{\nabla})\underset{\sim}{V} = (\underset{\sim}{V}\cdot\underset{\sim}{\nabla})\,\underset{\sim}{V}$ is the substantial derivative for steady flow, indicate (Laudau and Lifshitz, 1960) that the magnetic flux passing through Ω is conserved and moves with the fluid. In more picturesque language, the magnetic field is frozen in the fluid, the general effect being essentially similar to that of a line of smoke or dye released at some instant into a medium flowing at speeds high relative to the diffusion rate of the contaminant.

B. Description of Numerical Method

The preceding discussion has shown how the nonmagnetic properties of the exterior flow described by equations (5-1) can be represented without undue loss of accuracy by purely gasdynamic equations. In this manner, the flow of the solar wind past the Earth, Mars, and Venus is exactly equivalent to the familiar, but complex, problem of the external aerodynamics of round-nosed bodies in a supersonic stream. Although this represents an enormous simplification, the mathematical complexity associated with the non-linear and mixed elliptic-hyperbolic character of the governing partial differential equations requires that the solution be sought by numerical methods. A variety of numerical procedures can be used to solve the equations of gasdynamics for flow about a given body in a supersonic stream, but the difficulties are sufficiently great that at the present time solutions can only be computed for round-nosed, axisymmetric bodies. This restriction poses no difficulty for the calculation of flow past the ionopause which is a surface of revolution, but it remains necessary to approximate the magnetopause with an axisymmetric shape. In nearly all cases for which calculations have been carried out, the shape selected is that obtained by rotating the magnetic equatorial trace of the boundary illustrated in figure 6-3 about its center line. Inspection of the magnetopause coordinates shows that this approximation is reasonable, except possibly where the boundary is dented inward near the neutral points. Even this exception may be of little importance, however, because these dents result from the use of the Newtonian pressure approximation and would disappear in a more accurate analysis based on fluid concepts (Spreiter and Summers, 1967). In our calculations we use the shape obtained by rotating the magnetic equatorial trace of the boundary given by Spreiter and Briggs (1961, 1962).

Several methods are available for the numerical solution of the equations of gasdynamics for flow about a given round-nosed body of revolution in a supersonic stream. The method employed in the calculations for our work here is that developed by Inouye and Lomax (1962) and Lomax and Inouye (1964) which is founded on the basic approach of Van Dyke (1958) and Van Dyke and Gordon (1959) as modified

by Fuller (1961). As a representative example, figure 7-1 illustrates the gasdynamic equations (7-1) and (7-2) used to calculate the flow around the magnetosphere and the cylindrical coordinate system originally presented in figure 6-6. As indicated, the method

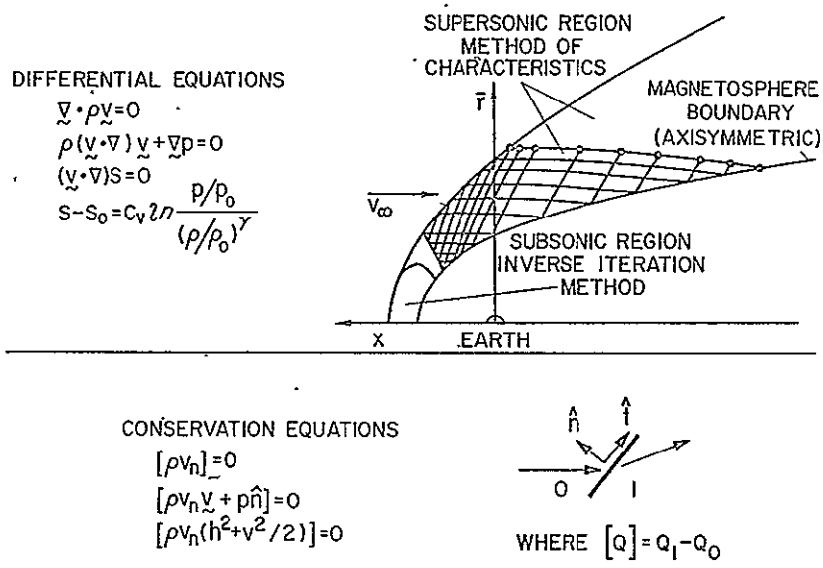

Figure 7-1. Gasdynamic equations for steady flow of a dissipationless perfect gas (Spreiter et al., 1968).

used for the subsonic region near the magnetosphere nose and the immediately adjoining portion of the supersonic region is an indirect one in which the location of the bow-shock wave and the free-streamline conditions are assumed known and the associated flow field and body shape are found as part of the solution. The desired solution for the specified body, either the magnetopause or the ionopause, is then found by iteration following judicious selection of the initial trial shape for the bow wave based on experience with a vast number of cases of aerodynamic interest. The solution for the remainder of the supersonic region is accomplished directly by using as indicated the method of characteristics in the manner described explicitly for this application by Inouye et al. (1965). As a background to our later modification of these schemes and discussion of the computed results, it is appropriate to present at this time a detailed review

of the mathematical and numerical aspects, such as convergence, stability, and accuracy for both of these methods. The following discourse is essentially repeated from Lomax and Inouye (1964) and Inouye et al. (1965).

1. Method for subsonic-transonic region

In forming difference equations from equations (7-1), a more useful form of the energy equation can be developed from the fact that entropy is constant along streamlines. For a gas in equilibrium, the pressure is determined from the equation of state using any two thermodynamic variables, say $p = p(\rho, S)$.[1] Then using the chain rule of differential calculus we find

$$\frac{Dp}{D\tau} = \left(\frac{\partial p}{\partial \rho}\right)_S \frac{D\rho}{D\tau} + \left(\frac{\partial p}{\partial S}\right)_\rho \frac{DS}{D\tau}$$

but since $\frac{DS}{D\tau} = 0$, we finally obtain

$$\frac{Dp}{D\tau} - a^2 \frac{D\rho}{D\tau} = 0 \qquad (7\text{-}5)$$

where $a = \left(\frac{\partial p}{\partial \rho}\right)^{1/2}$ is the local speed of sound. In terms of the cylindrical coordinate system $(x, \bar{r})$ described above, the components of the first two vector equations of (7-1) and scalar equation (7-5) are

$$v\frac{\partial \rho}{\partial \bar{r}} + \rho\frac{\partial v}{\partial \bar{r}} + u\frac{\partial \rho}{\partial x} + \rho\frac{\partial u}{\partial x} + \frac{\rho v}{\bar{r}} = 0$$

$$\rho u\frac{\partial u}{\partial x} + \rho v\frac{\partial u}{\partial \bar{r}} + \frac{\partial p}{\partial x} = 0$$

---

[1] Although we have already specified the equation of state to be that of a perfect gas, the explicit form of that equation is independent of both the form of the difference schemes and the numerical procedures. We therefore use the more general expression for the thermodynamic equation of state $p = p(\rho, S)$.

$$\rho u \frac{\partial v}{\partial x} + \rho v \frac{\partial v}{\partial \bar{r}} + \frac{\partial p}{\partial \bar{r}} = 0 \tag{7-6}$$

$$u \frac{\partial p}{\partial x} + v \frac{\partial p}{\partial \bar{r}} - a^2 u \frac{\partial \rho}{\partial x} - a^2 v \frac{\partial \rho}{\partial \bar{r}} = 0$$

where u and v are respectively the velocity components in the x and $\bar{r}$ directions. These four partial differential equations must be solved simultaneously for the four dependent variables p, ρ, u, and v. The thermodynamic relationship

$$a = a(\rho, p) \tag{7-7}$$

which is derived from the definition of a by using the equation of state provides the fifth equation connecting the five unknowns p, ρ, u, v, and a.

In the subsolar region of the planetary boundary, equations (7-6) exhibit different character; namely, the equations are elliptic in the subsonic region, parabolic on the sonic line, and hyperbolic in the supersonic region. Despite these complications, Lomax and Inouye (1964) have perfected an inverse method in which a shock shape is assumed and the equations are integrated numerically by a finite-difference method to determine the corresponding body shape. Their particular scheme has proven to be accurate and efficient in solving such flow fields, and we have used the computer program which is comprised of a main program and 26 subroutines written by them at Ames Research Center.

The complexity in the details of programming difference equations with more than one independent variable depends critically both on the nature as well as the manner of treating the boundary conditions. For this reason the governing equations (7-6) are transformed to a coordinate system that provides the simplest application of the boundary values. Because the initial-boundary conditions are specified along the shock, the axis of one set of coordinates coincides as shown in figure 7-2 with the shock, and the coordinates are those lines

placement of the shock in the free-stream direction. The other set of coordinates is parallel to the free-stream direction. This coordinate system is obviously convenient for starting the inverse problem although not optimum for studying body shapes. The coordinates are equally spaced in both directions, and their intersections define the points for the difference mesh. If the analytic expression for the shock shape is $x = X(\bar{r})$, then these new coordinates s and t are defined by

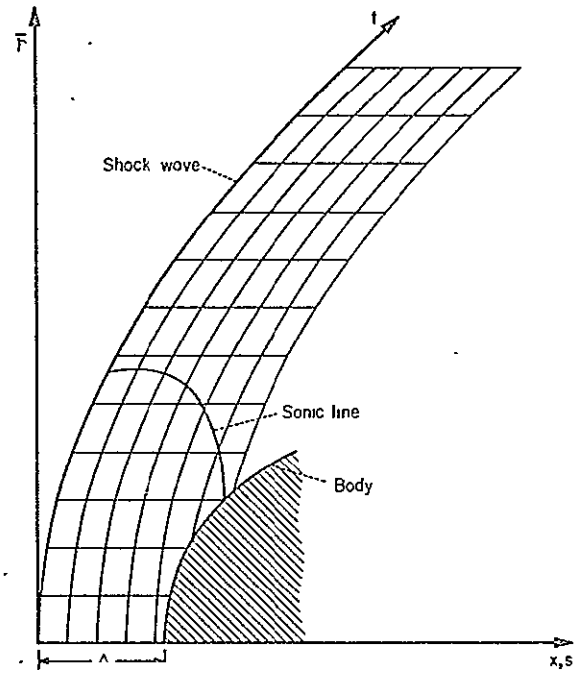

Figure 7-2. Sketch of flow field around blunt-nosed body and coordinate system (Lomax and Inouye, 1964).

$$s = x - X(\bar{r}) \qquad (7\text{-}8)$$

$$t = \bar{r}$$

and by the usual application of calculus, the x and $\bar{r}$ partial differential operators with respect to x and $\bar{r}$ become

$$\frac{\partial}{\partial x} = \frac{\partial}{\partial s} \qquad \frac{\partial}{\partial \bar{r}} = -X' \frac{\partial}{\partial s} - \frac{\partial}{\partial t}$$

Equation (7-6) can then be transformed and expressed in matrix form

$$[A] \cdot [B] = [C] \qquad (7\text{-}9)$$

where

$$[A] = \begin{bmatrix} 0 & u - \bar{X}'v & \rho & \rho\bar{X}' \\ 1 & 0 & \rho(u-\bar{X}'v) & 0 \\ -\bar{X}' & 0 & 0 & \rho(u-\bar{X}'v) \\ u-\bar{X}'v & a^2(u-\bar{X}'v) & 0 & 0 \end{bmatrix}$$

$$[B] = \begin{bmatrix} \frac{\partial P}{\partial s} \\ \frac{\partial \rho}{\partial s} \\ \frac{\partial u}{\partial s} \\ \frac{\partial v}{\partial s} \end{bmatrix} \qquad (7\text{-}10)$$

$$[C] = \begin{bmatrix} -\left(\frac{\rho v}{t} + v\frac{\partial \rho}{\partial t} + \rho\frac{\partial v}{\partial t}\right) \\ -\rho v \frac{\partial u}{\partial t} \\ -\left(\frac{\partial P}{\partial t} + \rho v \frac{\partial v}{\partial t}\right) \\ -\left(v\frac{\partial P}{\partial t} + a^2 v \frac{\partial \rho}{\partial t}\right) \end{bmatrix}$$

Equation (7-9) can be inverted, and the partial derivatives with respect to S of the four dependent variables can be expressed as

$$\frac{\partial P}{\partial S} = f_1\left(t, P, \rho, u, v, \frac{\partial P}{\partial t}, \frac{\partial \rho}{\partial t}, \frac{\partial u}{\partial t}, \frac{\partial v}{\partial t}\right)$$

$$\frac{\partial \rho}{\partial S} = f_2\left(t, P, \rho, u, v, \frac{\partial P}{\partial t}, \frac{\partial \rho}{\partial t}, \frac{\partial u}{\partial t}, \frac{\partial v}{\partial t}\right)$$

$$\frac{\partial u}{\partial S} = f_3\left(t, P, \rho, u, v, \frac{\partial P}{\partial t}, \frac{\partial \rho}{\partial t}, \frac{\partial u}{\partial t}, \frac{\partial v}{\partial t}\right) \qquad (7\text{-}11)$$

$$\frac{\partial v}{\partial S} = f_4\left(t, P, \rho, u, v, \frac{\partial P}{\partial t}, \frac{\partial \rho}{\partial t}, \frac{\partial u}{\partial t}, \frac{\partial v}{\partial t}\right)$$

where f_1 , f_2 , f_3 , and f_4 represent complicated expressions involving the indicated variables and are the four elements of the matrix derived by performing the operation $\left[A\right]^{-1}\left[C\right]$.

For a given shock shape and free-stream conditions, the values of P , ρ , u , and v just behind the shock wave are calculated from the discontinuity relations (7-2). Lomax and Inouye (1964) then divide the numerical calculations into two parts. First, the derivatives with respect to t of P , ρ , u , and v are calculated numerically from their known values along a t coordinate. They are determined by a standard five-point central difference method except at the upper end of a t coordinate where a skewed five-point difference scheme is used. This information together with equation (7-11) is then used to advance the solution in the S direction by a predictor-corrector procedure. A second-order method is used and is illustrated for a typical flow variable P as follows:

(1) Numerically differentiate the flow properties for the i th step to obtain $\left(\frac{\partial P}{\partial t}\right)_i$

(2) Calculate $\left(\frac{\partial P}{\partial S}\right)_i$ from equations (7-11)

(3) Predict new value $\bar{p}_{i+1} = p_{1+1} + 2\Delta s\left(\frac{\partial p}{\partial s}\right)_i$

(4) Numerically differentiate new value to obtain

$$\left(\frac{\partial \bar{p}}{\partial t}\right)_{i+1} \qquad (7\text{-}12)$$

(5) Calculate $\left(\frac{\partial \bar{p}}{\partial s}\right)_{i+1}$ from equation (7-11)

(6) Correct new value $p_{i+1} = p_i + \frac{1}{2}\Delta s\left[\left(\frac{\partial p}{\partial s}\right)_i + \left(\frac{\partial \bar{p}}{\partial s}\right)_{i+1}\right]$

In this manner the known values of the flow properties are advanced by marching step-by-step towards the body.[2] The stream function ψ is calculated for each point, and a body is determined as the locus of points where the stream function vanishes. This body shape is then compared with the desired shape, and if the fit is not satisfactory, then the shock shape $X(t)$ is varied slightly, and the whole procedure is repeated. In practice several such iterations yield the desired body shape to a very accurate degree.

a. Convergence and stability. The question of convergence is considered by Lomax and Inouye (1964) in two parts. First, as the mesh size is reduced, do the difference equations converge to the differential equations, and second, if they do, does the calculation procedure itself converge throughout the region of application? The complexity of the governing equations makes the answer to these questions impossible from a purely mathematical approach. From a physical viewpoint, however, some insight to them can be achieved.

With regard to the first question, if the difference equations do not reduce to the specified differential equations, then they

---

[2]The solution is started by a first-order predictor followed by two second-order correctors.

must reduce to some set of differential equations which violate one or more of the conservation laws. To check whether or not these laws have been violated, however, can be done independently of a mathematical analysis of the difference equations. For example, the body surface is located by the condition of mass conservation and if either momentum or energy is not conserved, the entropy and total enthalpy calculated at the body location would not be constant. These conditions were checked, and for the solutions presented here, the entropy along streamlines was constant to an accuracy consistent with the calculations, and the total enthalpy was constant throughout the flow. These are independent checks because entropy and enthalpy are not used in calculating the flow field, and they insure that the results of the finite difference methods employed do correctly represent solutions to equations (7-6) and (7-7). The second question of whether or not the calculation procedure itself converges is treated by the following argument. If the calculations give answers that are physically consistent i.e., satisfy the independent physical checks and are not significantly affected by changes in either the mesh size or mesh ratio, then we assume they have converged and represent the correct answer.

However, considerable difficulty is encountered in the study of the flow properties behind a prescribed shock with the flow properties ahead of it known. The difficulty arises because analytically our approach is only well-posed for an initial-value or Cauchy-type problem, and we are attempting, in mathematical terms, to solve a boundary-value problem by an approach suitable for an initial-value problem. The difficulties arising from such an attempt lead to some of the most fundamental problems in the numerical treatment of both partial and total differential equations.

In the solution of equations (7-6) and (7-7) by means of equations (7-12), numerical instabilities are easy to detect once they have started. A convenient demarcation of their onset is the locus that separates regions where the variables are at least physically possible from regions where they fluctuate beyond all reason predicting negative pressures, densities, etc. Unfortunately, the

complexity of the problem makes complete mathematical rigor in these studies practically impossible, and one is forced to rely on experience with linearized equations and familiarity with the physical problem for help in making the arguments plausible. Nevertheless, Lomax and Inouye (1964) have been able to classify all the difficulties encountered in this study with one of the following categories (see Fox [1962] for terminology and further background):

i. Inherent instabilities
   (a) Due to ill conditioning (nonessential)
   (b) Due to singularities (essential)
ii. Induced instabilities

Inherent instabilities are brought about because (a) the differential equations themselves contain an unstable (exponentially growing) solution in the direction of one independent variable while remaining bounded in the other, or (b) because the differential equations contain a solution that is singular. Such instabilities are not caused by the finite differencing. Induced instabilities are brought about by the particular numerical techniques employed, mesh size, degree of truncation, implicit or explicit methods, etc., and can lead to implications quite spurious with regard to true solutions to the partial differential equations.

Following Lomax and Inouye (1964) we will refer to the two different kinds of inherent instabilities mentioned above as essential and nonessential. The terminology is, perhaps, not apt because what is referred to as an essential instability is actually caused by the appearance of a singularity or group of singularities in the flow region between the shock and body. The singularities are invariant to coordinate transformations and represent the locations of sources or sinks that would appear in an exact analytic solution behind an analytic shock. Nevertheless, they refer to the numerical behavior caused by them as an instability because of its similarity in appearance to other numerical phenomena which are identified by that term. The important distinction between an essential and a nonessential instability is that the latter would not occur in an exact analytic solution. Nonessential instabilities are started by round-off,

truncation, or end-of-array inaccuracies due entirely to the fact that numerical methods are employed. In most of the literature pertaining to the stability of partial differential equations, the statement is made or implied that initial-value data are always unsuitable for elliptic equations (see Hadamard [1923]). In the present terminology it is the existence of nonessential instabilities that leads to this conclusion, a conclusion that is valid if such instabilities cannot be controlled.

A great deal has been written on the effect and control of what we call nonessential instabilities. So far as we know, most of the reported discussion attempting to identify these instabilities with the local form of the governing equations (elliptic, parabolic, or hyperbolic) have been limited to the elliptic or subsonic region. Although nonessential instabilities could be detected in the subsonic portion of the flow field if the numerical differentiation in the † direction was of very low order and no smoothing was used, Lomax and Inouye (1964) encountered no difficulties in this area. According to them the really critical area for stability was located in the supersonic portion of the flow, roughly in the shaded region of figure 7-3. In fact, in this region they were able to isolate all three of the major types of instabilities listed above. And although the difficulties inherent in the asymmetric differentiation formulas used at the upper end of the arrays often accentuate the breakdown, they are not the cause of these instabilities.

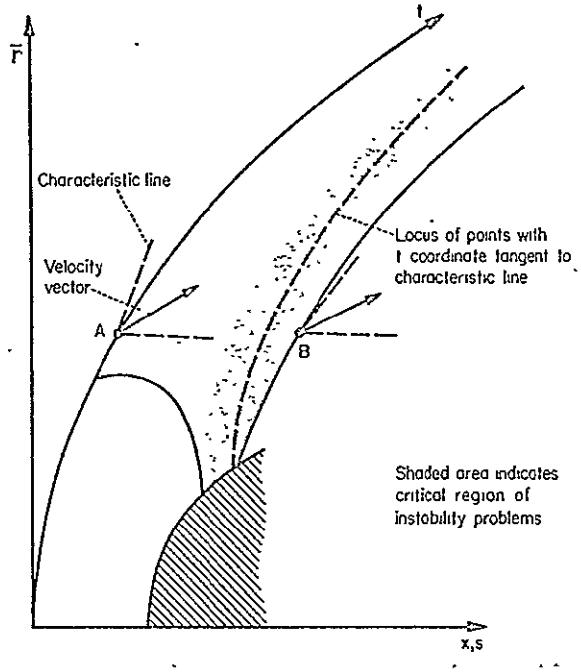

Figure 7-3. Sketch of flow field showing critical region of instability problems (Lomax and Inouye, 1964).

Consider the flow behind the shock in the area where it is supersonic. As we march inward from one $\dagger$ coordinate to the next, we are perpetrating an initial-value problem. We use the term "properly set" in the usual way; that is, Cauchy data (function and derivative) are properly set for the wave equation along the $\dagger = 0$ axis, and Neumann or Dirichlet data (function or derivative) are properly set for Laplace's equation. Usually, stability proofs for hyperbolic equations stem from the assumption that initial-value or Cauchy data are properly set. Hadamard (1923) pointed out, and it is well known in studies of supersonic wing theory, that according to how the line carrying the initial data cro.,s each characteristic, Cauchy data may or may not be properly set for a hyperbolic equation. By Hadamard's terminology, a data line is "duly inclined" if Cauchy data are properly set, and "nonduly inclined" if they are not. One can easily show that a shock is a nonduly inclined surface in the region where the flow is supersonic behind it (see point A, figure 7-3), and Cauchy data are, therefore, nowhere properly set along it. In fact, the $\dagger$ coordinate continues to be nonduly inclined until the upgoing characteristics lie to its right as is shown at point B in figure 7-3.

The principal point made by Lomax and Inouye (1964) in this regard is that the nonlinear equations governing the flow field may have inherent instabilities in the supersonic as well as in the subsonic regions. In fact much of the numerical discussion, as well as most of the criticism, of the inverse method concerns the existence and manner of treatment of the nonessential instabilities. The defense usually invoked by those who use the inverse method is, simply, that the gas layer between the shock and the body is thin enough that the errors caused by numerical calculations cannot grow sufficiently large to invalidate the first few significant digits in the results. We adopt the hypothesis of Lomax and Inouye (1964), that this argument is sufficient to validate those cases for which the solution passes the consistency checks on total enthalpy and entropy as discussed above.

Absolute reliance upon this hypothesis is not always

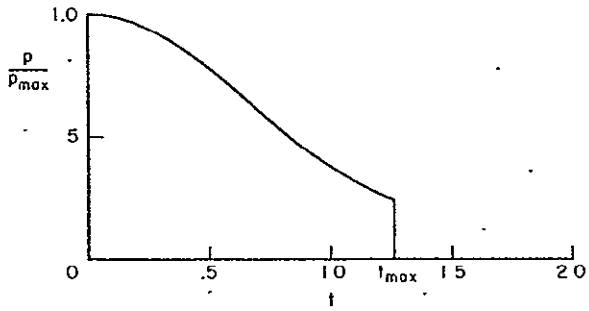

(a) Pressure distribution.

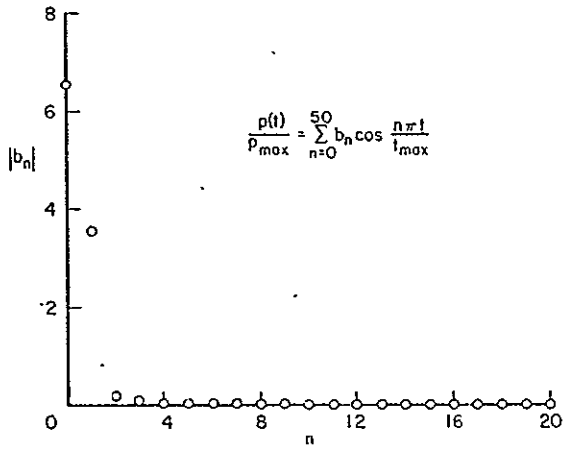

(b) Fourier coefficients.

Figure 7-4. Harmonic analysis of pressure distribution just behind bow shock wave (Lomax and Inouye, 1964).

satisfactory in application, and is certainly not satisfactory from a theoretical point of view. Basically, the validity of such a hypothesis is coupled with the word size (number of significant digits carried in each arithmetic operation and stored in memory) available in the computing machine. It is not always wise to demand larger computing capacity merely to push ahead a few more steps before exponentially growing instabilities started by numerical truncations swamp the first few significant digits in the calculations. A more sensible approach is to face the problem with analysis and attempt to suppress non-essential instabilities by appropriate numerical methods. One such method that has been used by several authors (Fuller, 1961; Lomax and Inouye, 1964) is to "smooth" or filter the data along each † coordinate as the computations proceed. Because of the important role this method plays in controlling instabilities, we shall present some of the discussion of Lomax and Inouye (1964).

A representative variation of pressure along a † coordinate and behind a curved chock is shown in figure 7-4(a). If we expand the pressure distribution in a Fourier series between the maximum absolute values of † used in the calculations, we obtain

$$\frac{P(t)}{P_{max}} = \sum_{n=0}^{\infty} b_n \cos \frac{n\pi t}{t_{max}} \qquad -t_{max} < t < t_{max} \quad (7\text{-}13)$$

The magnitudes of the coefficients are shown in figure 7-4(b). We see that the first few terms dominate the expansion, and higher-order terms, corresponding to higher frequencies, are negligible. Next we assume that a Fourier expansion for any of the dependent variables over the same interval along any t coordinate between the shock and the body would exhibit the same general behavior, that is, could be expressed with acceptable error by the first few terms in a Fourier expansion.

That assumption certainly warrants some discussion. However, to attack it simply on the basis that it arbitrarily prohibits high-frequency terms in the true solution is not justifiable, since any method using finite-difference techniques is subject to such a criticism per se. In fact, as pointed out by Lomax and Inouye (1964) it is a fundamental theorem in communication theory (Shannon and Weaver, 1949) that the highest resolvable frequency in any finite trigonometric series to be represented by a discrete number of points is related to the number of points themselves. Consequently, they reasoned that if more points are used than are required to resolve the highest frequency, the remaining points carry redundant information. The real assumption, then, is not that high-frequency terms are arbitrarily excluded, which is the case for numerical calculations in any event, but rather that enough mesh points are taken to make data contained in them largely redundant in the sense just mentioned. Under these circumstances high-frequency terms, appearing from more or less random errors brought about by numerical truncation in calculations made at discrete points, fall above the frequency range required to express the true solution and can be excluded if the proper numerical filter is applied. The following discussion briefly describes such a filter used by Lomax and Inouye (1964).

Consider an even function $F(x)$ that can be represented by a Fourier cosine series in the interval $0 \leq x \leq L$ as

$$F(x) = \sum_{m=0}^{\infty} a_m \cos \frac{m\pi x}{L} \tag{7-14}$$

and define the operator f_j by the equation

$$f_j(F) = \left[F(x + jd_o) + F(x - jd_o)\right] \tag{7-15}$$

where d_o is the spacing of the points in the X direction. With W_j defined as arbitrary weighting factors, the sequence of operations $\sum_{j=0}^{J} W_j f_j$ applied to equation (7-14) results in the expression

$$F^{(1)}(x) = \sum_{j=0}^{J} W_j f_j(F) = \sum_{m=0}^{\infty} A_m \cos \frac{m\pi x}{L} \tag{7-16}$$

where

$$A_m = a_m \sum_{j=0}^{J} W_j \cos \frac{jm\pi d_o}{L}$$

If we define a polynomial P_f by

$$P_f = \sum_{j=0}^{J} W_j \cos \frac{jm\pi d_o}{L} \tag{7-17}$$

then equation (7-16) becomes

$$F^{(1)}(x) = \sum_{m=0}^{\infty} P_f \, a_m \cos \frac{m\pi x}{L}$$

And n repetitions of the operation yield the expression

$$F^{(n)}(x) = \sum_{m=0}^{\infty} P_f^n a_m \cos \frac{m\pi x}{L} \qquad (7\text{-}18)$$

Thus, Lomax and Inouye (1964) concluded that if the function $F(x)$ is replaced by certain weights of its average at equally spaced intervals to the right and left of x (i.e., applying the operator $\sum_{j=0}^{J} W_j f_j$), the coefficients in its Fourier expansion are multiplied by P_f which is independent of x and depends only on the arbitrarily assigned weights W_j and the factor $\frac{m\pi d_o}{L}$. Furthermore, if the operator is applied n times, each coefficient is multiplied by the n th power of P_f .

If the terms j , W_j , and $\frac{d_o}{L}$ can be chosen such that P_f is near unity for values of m less than some arbitrary frequency M_1 , and close to zero for higher values of m greater than some M_2 and falls in the range $0 < P_f < 1$ for intermediate m where $M_1 \leq m \leq M_2$, then P_f will be suppressing the higher-frequency terms and be acting like a filter. We can therefore easily see that the corresponding weighted-average operation will leave the low harmonics for which $0 \leq m \leq M_1$ unchanged and will destroy all the higher harmonics for which $m > M_2$. Harmonics for which $M_1 < m < M_2$ will be distorted according to the nature of the polynomial P_f . To illustrate that P_f actually does possess such filtering properties, consider equation (7-17). An examination of this equation reveals it to be a truncated Fourier cosine series with summation index j . If we choose $W_o = 1/2$ and $W_j = \frac{2 \sin j\pi/2}{j\pi}$ for $j = 1, 2, 3\ldots$, then P_f is simply a finite-term Fourier expansion in variable $m d_o$ approximating a positive square wave which clearly has the desired characteristics of a filter. To improve the approximation and make the filter sharper, either more terms of the series can be taken, or, as in our case, higher powers of P_f corresponding to repeated averaging can be used.

In our application, d_o is unknown. We simply assume that

an L exists for which our numerical results can be represented with acceptable error by harmonics below M_1 and for which our numerical procedures will introduce errors consisting of harmonics above M_2 (but below those very high frequencies for which $m > \frac{3}{2}\frac{L}{d_o}$). By numerical experimentation with the spacing d_o and the weights W_j , Lomax and Inouye (1964) have verified that this is so. The actual polynomial which they found appropriate and which we have used in our calculations is

$$P_f^* = \frac{17}{35} + \frac{24}{35}\cos\frac{m\pi d_o}{L} - \frac{6}{35}\cos\frac{2m\pi d_o}{L} \qquad (7\text{-}19)$$

Each application of P_f^* amounts to moving the central point in a group of five to the curve obtained by a fitting a least-squares quadratic to them.

The use of numerical filters of this type can be contrasted to the use of higher-order numerical differentiating processes. Consider, as shown in figure 7-5(a), a set of data all zero except for one "bad" point. These data were numerically differentiated by Lomax and Inouye (1964) using central-difference schemes and the results harmonically analyzed. Their results given in figure 7-5(b) show that with higher-order difference methods the amplitudes of higher-frequency terms are increased and the over-all maximum amplitude itself is increased. On the other hand, a five-point difference scheme followed by repeated filtering, of the type just described, has the opposite effect. This does not mean, of course, that relative to low-order schemes, high-order differentiating processes are inferior. Their value comes in reducing the initial error. But once this error has been committed, the higher-order methods are of no value in controlling its effect on the stability.

To demonstrate the growth of an inherent instability and the effect of numerical filtering, we present some results from the study by Lomax and Inouye (1964). Four curves are shown in figure 7-6, one corresponding to each of the four possible combinations of two spacings

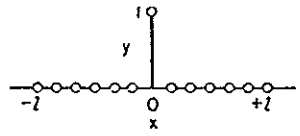

(a) Set of data with one "bad" point.

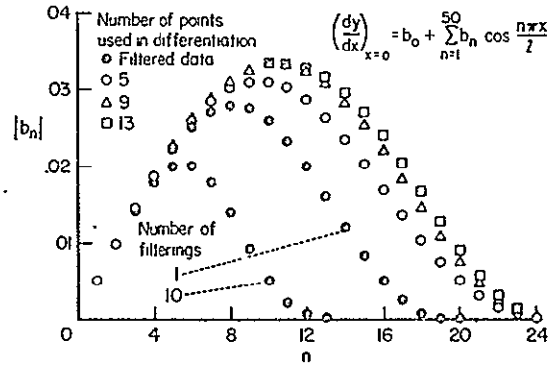

(b) Harmonic analysis of data after differentiation and filtering.

Figure 7-5. Effect of differentiation and filtering on data (Lomax and Inouye, 1964).

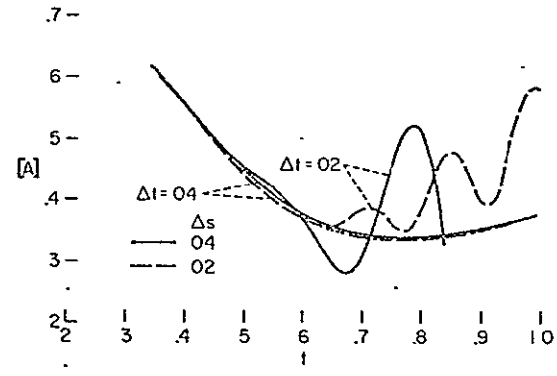

Figure 7-6. Effect of interval size on determinant [A] in equation (7-10) (Lomax and Inouye, 1964).

for ΔS and $\overline{\Delta t}$. The quantity plotted is the magnitude of the determinant of [A] from equation (7-10), the value of which is, of course, critical in evaluating the S derivatives of the dependent variables. (Actually, any one of the dependent variables could be used to display the same result.) Plotted along the abscissa are the points located along a t coordinate in the supersonic region above the body and downstream from the shock. Notice that the instabilities have no correlation with the ratio of $\Delta t/\Delta S$ (all other conditions were held constant), but rather with the absolute value of Δt. For the larger Δt no fluctuations at all are observed, whereas, for the smaller Δt, unstable oscillations begin at a t of around 0.6, and the distance between successive maxima and minima is about five times the Δt interval size. Lomax and Inouye (1964) explained this behavior by estimating the magnitude of the polynomial P_f^*. With the smaller t spacing corresponding to a smaller value for

d_o , equation (7-19) indicates that P_f^* is about 0.99 for one application of the filter and about 0.90 for 10 successive applications. Hence, the amplitude of a term with the frequency corresponding to the oscillating curves presented in figure 7-6 is only slightly damped by the filter represented by P_f^* . A similar study for the larger $\dagger$ spacing in figure 7-6 shows that the same frequency would be heavily damped, especially for multiple applications of the filter. The extent of the curves shown in figure 7-6 is well within the region where the $\dagger$ coordinates in the supersonic flow are nonduly inclined, a region defined by the inequality $\det[A] > 0$. This example illustrates a typical case of a nonessential instability and the manner by which it can be controlled.

In their report Lomax and Inouye (1964) also examine and discuss an example of an essential instability which is caused by a line singularity in the flow field. They found that this singular behavior corresponding to mass absorption was directly caused by the use of an elliptic shock-wave shape $X(\bar{r})$ and that exactly elliptic shocks in the nose region simply do not occur ahead of blunt bodies in source-free flow. The difficulty is easily overcome, however, simply by starting with an analytic shock shape that is not elliptic and never becomes tangent to a free-stream Mach line. Actually, the shock shape used in their work asymptotically approaches twice the slope of a free-stream Mach line, and with its use, essential instabilities such as they discuss disappear.

The question of just how close the shock can come to the free-stream Mach line and just how it should behave at infinity does not have to be settled for most bodies, because we need only to enter the supersonic region far enough to provide information which can be successfully continued by the method of characteristics. Usually this means that the body shape need conform to its desired value only up to a point where the local Mach number is around 1.05 . Past this point the given body shape can then be used explicitly because the method of characteristics is a direct method. The exact shape of the body past this point, however, does not affect the solution in the nose region because no disturbance in the supersonic region can propagate upstream

into the subsonic part. Thus, the solution in the nose region is quite independent of the details of the flow further downstream in the supersonic part. The real importance of this whole concept lies only in the fact that analytic shock equations for such bodies with source-free flow ahead of the limiting characteristic are not difficult to construct.

The instabilities discussed so far existed because of the nature of the differential equations. They would actually have existed in a frictionless flow if the boundary conditions were exactly reproduced. Another kind of instability arises which is caused by the particular choice of numerical procedure. This kind of instability is referred to as an induced instability, and it can presumably be eliminated by the proper choice of coordinates, mesh size, and differencing technique. Lomax and Inouye (1964) examined this aspect of the problem as follows.

The study of the stability of difference methods, as they apply to hyperbolic equations, usually pertains to the continuation of Cauchy data given along a duly inclined line. The criterion given for the stability of the simplest explicit difference scheme in application to the linear two-dimensional wave equation (Fox, 1962) is illustrated in figure 7-7. The scheme is based on a three-point central-difference formula written about the point m,n for the first derivatives in both directions. Given equally spaced data along column n, the method is stable if, as the calculation proceeds from point a to point b in figure 7-7(a), the columns are spaced by Δx_1, and unstable if spaced by Δx_2. The condition for stability is related, simply, to whether the point at the m th row and $(n+1)$ th column does or does not lie in the shaded area bounded

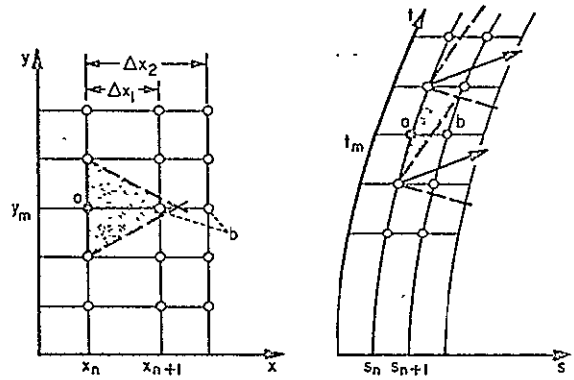

Figure 7-7. Sketch of conditions for stability (Lomax and Inouye, 1964).

by the characteristics shown. If this criterion were to apply to our case (when the n th column became duly inclined), point b in figure 7-7(b) would have to fall in the shaded region shown. Actually our case is much more complicated. A five-point difference scheme is used along the columns and, after smoothing, a second-order corrector equation is applied.

Coupled with the ever present nonlinear form of our basic equations, these complications make a stability analysis of the situation quite involved. However, Lomax and Inouye (1964) have observed that whenever the flow crosses into a region where a $\dagger$ coordinate is duly inclined, the calculation becomes unstable. When the $\dagger$ coordinate changes from a nonduly to a duly inclined line, the value of det [A] in equation (7-10) passes through zero. Since det [A] is the denominator in the equation for the forward-marching derivatives, this can lead to difficulties in numerical methods even though, of course, the numerators also must vanish. As was the case for the end-of-array, asymmetric, numerical differentiation, this occurrence may help start the growth of instability, but it is not the cause of it. In their solutions, this crossing only occurs in the high supersonic region so no attempt was made by Lomax and Inouye (1964) to control it. The line along which the crossover occurs simply becomes a boundary past which calculations were not continued. This way of treating such an instability is only an expedient. Blunter bodies and solutions at lower Mach numbers demand that these instabilities be controlled. Consequently, at the present time, this particular computer program is incapable of solving such cases. Fortunately, however, the bluntness of the magnetopause and ionopause shapes and the high free-stream Mach number that characterize our applications fall within the range for which accurate solutions can be computed by this program so that further development is not required.

b. Relating the shock and body shapes. Even with all the stability and convergence problems controlled where necessary, the real success of the inverse method still depends upon the ability to find some relationship between families of shock and body equations. In other words, it depends upon the ability to formulate a shock

equation that can be systematically modified to a point where it yields a given body to a prescribed accuracy.

The fruition of the shock-shape iteration requires an efficient way of comparing the calculated body shape with the desired shape of the magnetosphere or ionosphere boundary and a means of minimizing the difference. However, the fact that the magnetopause and ionopause shapes were numerically calculated and are not expressed by an analytic expression makes a systematic comparison very complicated. To reduce these complexities, it was found that the nose of both the magnetopause and the ionopause can be represented extremely accurately by a fitted ellipsoid. This simplification made the comparison straight forward. The following method was then used to relate the associated bow shock wave with this boundary.

As Lomax and Inouye (1964) pointed out, elliptical or spherical shock shapes introduce singularities into the flow field which can cause essential instabilities to occur in the low supersonic region near the body. In order to avoid these difficulties, they attempted to represent the general shock shape $\bar{X}(\bar{r})$ by a simple ratio of polynomials in $\bar{r}$. Since the body shape and size corresponding to the given shock are not known at the start of the computation, they found it convenient to reference the x and $\bar{r}$ coordinates to the radius of curvature R_s of the shock wave at $\bar{r} = 0$.

The general equation for an ellipsoid, which is to be fitted to the subsonic region of the given planetary boundary, can be written in terms of the present coordinate system as

$$\frac{\left(\frac{\bar{r}}{R_s}\right)^2}{2\left(\frac{x-\Delta}{R_s}\right)} + \frac{1}{2} B_b \left(\frac{x-\Delta}{R_s}\right) = \frac{R_b}{R_s} \qquad (7\text{-}20)$$

The symbol Δ is the shock-standoff distance, R_b is the radius of curvature of the body at $\bar{r} = 0$, and B_b is the body bluntness parameter obtained from the fit to the specific planetary boundary under consideration and defined by $B_b = (b/R)^2$ where b and R are

ellipsoidal dimensions illustrated in figure 7-8.

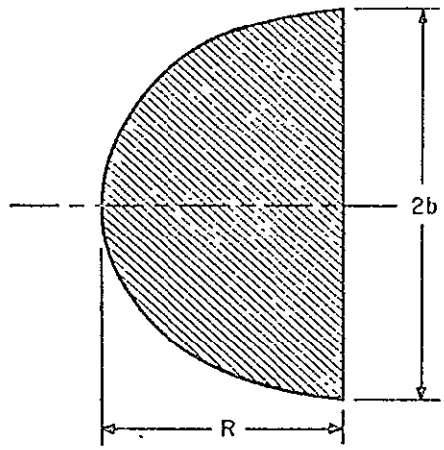

Figure 7-8. Sketch of ellipsoid (Lomax and Inouye, 1964).

In relating the body shape to the shock shape, two factors must be considered. First, the ratio R_b/R_s which relates the size of the calculated body to the shock shape must be determined, and, second, the closeness of fit of the calculated body points to the desired body shape characterized by B_b must be determined. The procedure devised by Lomax and Inouye (1964) and used in the present application is to first assume values for the shock shape parameters and then calculate the flow field including the body shape. The body coordinates for surface Mach numbers between 0.5 and about 1.05 are then substituted into the left side of equation (7-20) and plotted against $(x-\Delta)/R_s$.[3] These points are fitted with a horizontal straight line that minimizes the sum $\sum_o$ of the absolute differences between the points and the line. The ordinate of the line is the ratio R_b/R_s, and the sum of the absolute differences is a measure of the closeness of fit to the desired planetary boundary. If necessary, any given parameter in the shock equation can be changed by a specified increment, and this entire procedure is then repeated until $\sum_o$ is minimized. Each iteration requires approximately 15 seconds on an IBM 7094 computer.

Lomax and Inouye (1964) have experimented using the above procedure with a polynomial ratio for $\overline{X}(\overline{F})$. After extensive

---

[3]The body coordinates for Mach numbers less than 0.5 are ignored because they generally lie on a circular arc and because of the scatter introduced by small values of the denominator $x-\Delta$ in the first term of equation (7-20).

investigation they have discovered the rather remarkable fact that ellipsoidal bodies are produced to a high degree of accuracy for values of the body bluntness parameter up to 2.25 by the simple, one-parameter equation

$$\frac{X(\bar{r})}{R_S} = \frac{\frac{1}{2}\left(\frac{\bar{r}}{R_S}\right)^2 + A_5\left(\frac{\bar{r}}{R_S}\right)^4}{1 + \frac{2A_5}{\sqrt{M_\infty^2 - 1}}\left(\frac{\bar{r}}{R_S}\right)^3} \qquad (7\text{-}21)$$

where A_5 is the shock-wave parameter (illustrated in figure 7-9). This equation is valid for free-stream Mach number greater than 5. The denominator provides that for large distances from the nose, the shock shape is twice the Mach line slope. This condition was imposed to avoid essential instabilities although it does not necessarily prevent the shock angle from becoming smaller than the Mach angle in some intermediary region. The use of the one-parameter equation (7-21) greatly simplifies the body-optimization procedure. In our planetary applications, the body parameter B_b is always less than one and the corresponding shock-wave parameter A_5 is between 0.2 and 0.7 as illustrated in figure 7-9. For these values equation (7-21) yields body shapes that match the magnetopause and the ionopause to a very high degree of accuracy. The typical value for the total absolute error $\sum_o$ in the body coordinates is less than 0.1% .

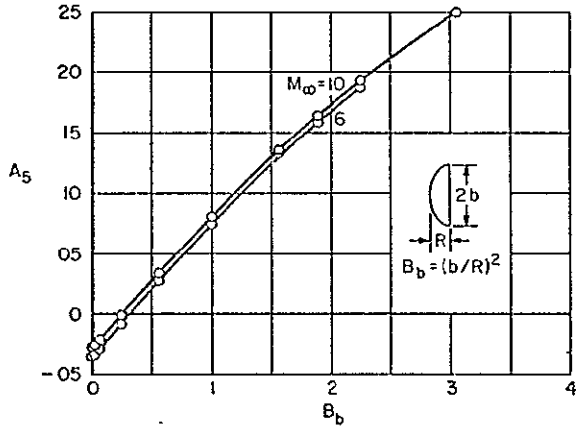

Figure 7-9. Shock-wave parameter A_5 for ellipsoidal bodies (Lomax and Inouye, 1964).

Values of A_5 which Lomax and Inouye (1964) found for ellipsoids of

varying bluntness and for Mach numbers $M_\infty = 6$ and 10 are illustrated in figure 7-9.

For our purposes the inverse method just outlined satisfactorily computes the solution for the flow field in the subsonic-transonic region. The computed flow properties are interpolated along a line joining the shock and body in the supersonic region. These data are then used as input for the method of characteristics program to continue the calculation downstream.

2. Method for supersonic region

A computer program developed by Inouye et al. (1965) at Ames Research Center and based on the method of characteristics is used to determine the flow field in the supersonic region. This program is comprised of a main program and 33 subroutines, for which Inouye et al. (1965) have described and also displayed flow charts. Since this method is both analytically and numerically stable for supersonic flow and since specific accounts of the method of characteristics are given in numerous textbooks (see, e.g., Courant and Hilbert [1962], Garabedian [1964], Hayes and Probstein [1966]), we do not present a detailed discussion of this method, but rather only outline the general procedure for the calculations.

Along the characteristic or Mach lines defined by $\frac{d\bar{r}}{dx} = \tan(\theta \pm \mu)$, the first three partial differential equations of (7-6) reduce to the following ordinary differential equations (Hayes and Probstein, 1966)

$$\frac{\cot\mu}{\rho V^2} dp + d\theta = -\frac{\sin\theta}{M\sin(\theta+\mu)} \frac{d\bar{r}}{\bar{r}} \qquad (7\text{-}22a)$$

on the left-running characteristic line $\frac{d\bar{r}}{dx} = \tan(\theta + \mu)$ and

$$\frac{\cot\mu}{\rho V^2} dp - d\theta = -\frac{\sin\theta}{M\sin(\theta-\mu)} \frac{d\bar{r}}{\bar{r}} \qquad (7\text{-}22b)$$

on the right-running characteristic line $\frac{d\bar{r}}{dx} = \tan(\theta - \mu)$ where θ denotes the angle between the streamline and the free-stream direction x, and $\mu = \sin^{-1}\frac{1}{M}$ is the local Mach angle. Equations (7-22) are solved in conjunction with the energy equation in integrated form (see chapter IX for derivation)

$$h + \frac{1}{2}V^2 = \text{constant} \tag{7-23}$$

the conservation of entropy along streamlines

$$S = S(\psi) \tag{7-24}$$

and the equation of state in the form

$$h = h(p,S) \tag{7-25}$$

Briefly, the method consists of starting with flow properties along a non-characteristic line between the body and the shock wave, as determined from the solution for the subsonic-transonic region, and then integrating the equations downstream along the Mach lines. The stepwise procedure is illustrated by the typical characteristic mesh shown in figure 7-10. Beginning with known data on the starting

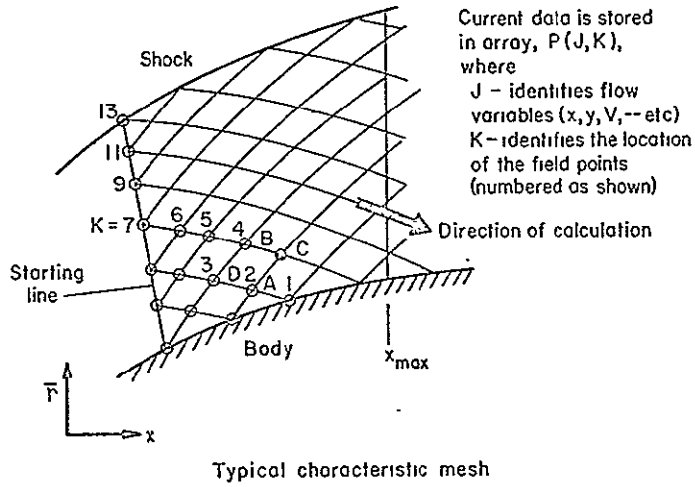

Figure 7-10. The characteristic mesh used in the supersonic region (Inouye et al., 1965).

line the calculation proceeds to the body along a right-running characteristic, and then back to the next starting point or shock point as the calculations advance downstream (see Inouye et al. [1965] for a flow chart which illustrates this part of the program logic.) In figure 7-10 the previously calculated (or input) data points are identified by small circles, and the point currently being calculated is identified by the shaded symbol. Only the numbered points are available in computer memory at this time since the remaining circled points have been written out previously. The stored data points are contained in a two-dimensional array, P (J,K), in which the index J identifies the various flow variables, and the index K identifies the location of the point.

For the calculation of an interior mesh point C in figure 7-10, the flow properties at three adjacent points are required. These points are labeled A, D, and B in figure 7-10, and correspond, in the example shown, to the points K = 2, 3, and 4 in the P array. The calculation of data at the new point is carried out with the use of equations (7-22) through (7-25) and a standard predictor-corrector procedure which averages the coefficients of the differentials. The procedure is started with a crude predictor (i.e., that conditions at C equal those at B) and is followed, therefore, by at least two correctors. This is in contrast to the method used for the subsonic-transonic solution which makes use of only one corrector, but which uses a second-order predictor.

For the calculation of a mesh point located on the shock wave, the flow properties at only two mesh points, the adjacent upstream shock point and the nearest interior point, are required because the upstream segment of the right-running characteristic line does not exist at this point due to the presence of the shock wave. The calculation of data at the new shock point proceeds with the use of equations (7-22a) through (7-25) along with the shock discontinuity equations (7-2) which have replaced equation (7-22b). The procedure is then started and refined in the same manner as for an interior point. In this way the shock shape and location in the supersonic region is calculated as part of the solution and is no longer determined by

equation (7-21) as was the case in the nose region.

For the calculation of a mesh point located on the body, again the flow properties at only two mesh points, the adjacent upstream body point and the nearest interior point, are required because the upstream segment of the left-running characteristic line does not exist at this point due to the presence of the body. For this case, the calculation of data at the new body point is carried out with the use of equations (7-22b) through (7-25) along with the specification of the flow angle θ which is determined for that point from the known shape of the planetary boundary around which the flow is being computed. This procedure is also started and refined in the same manner as was done for an interior point. This method thus allows the direct use of the previously calculated magnetopause and ionopause shapes and contrasts with the inverse method which requires that these boundary shapes be fitted with an analytic equation for an ellipsoid. Consequently, this method computes the shock shape and flow properties for boundary shapes exactly as they are displayed in figure 6-6.

In calculating rotational supersonic flow by the method of characteristics, Inouye et al. (1965) found it convenient to introduce entropy as a flow property since it remains constant on streamlines. Their particular version of this method which we used assumes that the entropy varies quadratically between streamlines. To illustrate this procedure, consider four points in the flow field (see figure 7-10), A, D, and B where the flow properties are known and C where they are to be determined. The entropy at C can be calculated using the flow properties at A, D, and B along with the assumption that the entropy varies quadratically along the normal to the streamlines between A and B . This assumption is valid provided that the higher-order derivatives of entropy between A and B remain small. Although serious errors may occur in the flow-field calculations if this condition is not realized, Inouye et al. (1965) have found that these errors are the order of the cube of the mesh size and, for not-too-coarse meshes, that this scheme computes accurate solutions.

As in the case of the inverse method, a check on the overall accuracy of the method of characteristics is based on physical rather

than mathematical arguments. In the subsonic-transonic region the conservation of total enthalpy everywhere and entropy along streamlines were adopted as independent checks on the physical consistency of the solution. However, for the present method these two requirements are used in the numerical calculations and therefore are not independent and cannot be adopted as checks on the overall accuracy. For the method of characteristics, instead, Inouye et al. (1965) calculate the mass-flow balance between the shock and the body at several positions along the body. This calculation is independent of the numerical computation of the flow field and can be adopted as an independent check on the overall accuracy. For the results presented in this thesis, the mass-flow balance was constant to an accuracy consistent with the calculations throughout the entire supersonic flow region. This check helps to insure us that our computed results do correctly represent solutions to equations (7-6) and (7-7).

CHAPTER VIII

FEATURES OF THE APPROXIMATE SOLUTION

A. Results of the Computed Solution

With the specification of a value for the free-stream Mach number $M_\infty \gg 1$, the location of the bow wave and the properties of the flow field can be computed for either the magnetopause or any of the ionopause shapes shown in figure 6-6 by application of the two highly developed computer programs described in the preceding chapter. Although we have only carried out these calculations for solar-wind flow past Mars and Venus, we present some of the calculated results for flow past the Earth achieved by Spreiter et al. (1966a, 1968) and Spreiter and Alksne (1969, 1970) in order to provide a background for a later discussion about the similarities and differences between these two cases.

1. Flow past the Earth

Figure 8-1 shows the position and shape of the bow shock wave generated by the solar wind's interaction with the magnetosphere boundary and calculated by Spreiter et al. (1966a) using the computer programs just described. These results, which are presented in terms of cylindrical coordinates x and $\bar{r}$, normalized by the distance D as originally denoted by Spreiter et al. (1966a) but exactly equivalent to our r_0, are for $\gamma = 5/3$ and $M_\infty = 8$, a representative value for the free-stream Mach number M_∞. Also included on this figure are several additional solid lines representing streamlines, and dashed lines representing characteristic or Mach lines of the flow which correspond to standing compression or expansion waves of infinitesimal amplitude. As indicated by equation (5-18) with $A = 0$, Mach lines cross the streamlines at such angles that the local velocity component normal to the wave is always exactly equal to the local speed of sound a. Mach lines thus exist only where the flow is supersonic and, consequently, are absent from the vicinity of the

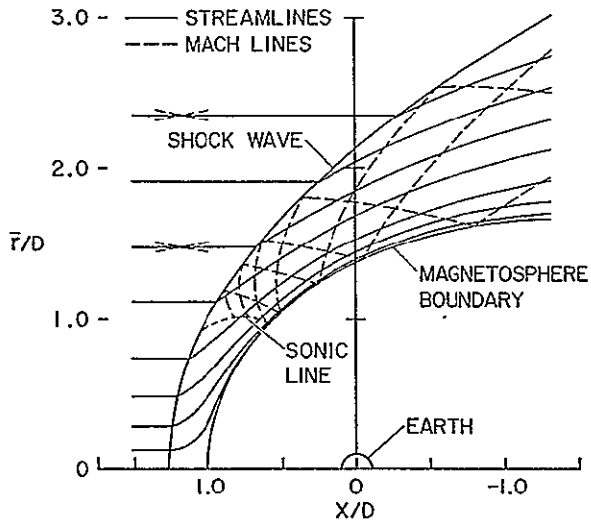

Figure 8-1. Streamlines and wave patterns for supersonic flow past the magnetosphere. $M_\infty = 8$, $\gamma = 5/3$ (Spreiter et al., 1968).

magnetopause nose because the flow there is subsonic. This plot also shows that the angle between the shock wave and the incident stream is much larger along the entire length of the shock wave included in the illustration than the asymptotic angle which is just the angle between the streamlines and Mach lines of the incident undisturbed flow upstream from the bow shock wave. We can thus see that knowledge of the asymptotic direction of weak shock waves is of limited usefulness in the estimation of the location of the bow shock wave, except at extremely great distances from the planet.

Contour maps showing lines of constant density ratio ρ/ρ_∞ , velocity ratio V/V_∞ , and temperature ratio T/T_∞ which were obtained from the computed solution of equation (7-1) and (7-2) and originally presented by Spreiter et al. (1966a) are shown in figure 8-2 for the same conditions of $M_\infty = 8$ and $\gamma = 5/3$ as in figure 8-1. These results show that the density ratio ρ/ρ_∞ remains near the maximum value $(\gamma+1)(\gamma-1) = 4$ for a strong shock wave in a gas with $\gamma = 5/3$ along nearly the entire length of the portion of the bow wave shown. The gas undergoes a small additional compression as it approaches the stagnation point at the magnetosphere nose and then expands to less than free-stream density as it flows around the flank of the magnetosphere. The velocity remains less than in the free stream, however, throughout the same region. As indicated, a single set of contour lines, although with different labels, serves for both V/V_∞ and T/T_∞ because, as Spreiter et al. (1966a) pointed out,

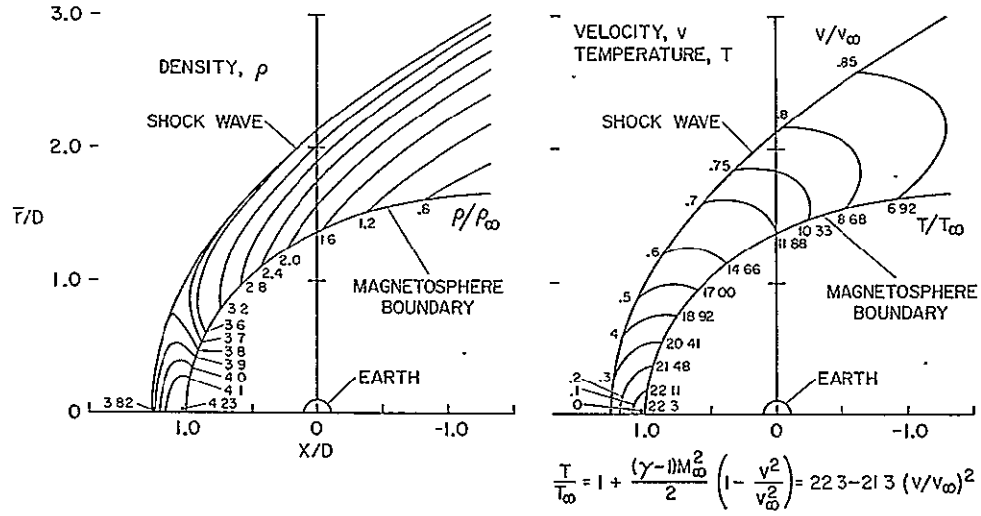

Figure 8-2. Density, velocity, and temperature fields for supersonic flow past the magnetosphere. $M_\infty = 8$, $\gamma = 5/3$ (Spreiter et al., 1966a).

the temperature ratio T/T_∞ is closely related to the velocity ratio through the expression

$$\frac{T}{T_\infty} = 1 + \frac{(\gamma - 1) M_\infty^2}{2} \left[1 - V^2/V_\infty^2 \right] \qquad (8\text{-}1)$$

derived by integrating equation (5-3) with $\underset{\sim}{B} = 0$, combining with relations for enthalpy h and speed of sound a given in equation (5-2), and rearranging. If values for γ and M_∞ are given, it is then a straightforward and simple calculation to determine T/T_∞ as a function of V/V_∞ . The results presented in figure 8-2 show that the temperature is substantially higher than in the free stream throughout the entire region illustrated. Particularly noteworthy is the large increase in temperature of the solar wind in the region of the magnetosphere nose. If, for example, the temperature of the incident solar wind is 10^5 °K , then the temperature at the stagnation point is calculated to be 2.23×10^6 which is of the same order of magnitude as the temperature of the gas in the solar corona before it is accelerated to the high velocities characteristic of the solar

wind. This result simply demonstrates that the energy content of the solar wind is, to a large extent, dependent on the temperature of the solar corona. Although the gas cools considerably as it flows around the magnetosphere, it is still about one million degrees K as it passes the Earth ($X/D = 0$) and about three-quarters of that farther downstream at $X/D = 1$.

Spreiter et al. (1966a) also showed that the constant-velocity contours of figure 8-2 can also be used to represent, with a suitable relabeling, lines of constant local Mach numbers $M = V/a$ Their conclusion follows from equation (5-2) and (8-1) which show that a is proportional to $T^{1/2}$ for a given pair of values for γ and $\bar{m}$ and that T/T_∞ depends only on V/V_∞ for given M_∞ and γ There exists, therefore, for flow characterized by given M_∞ , γ and $\bar{m}$, a unique value for M associated with every value for V/V_∞ . Contours for constant local Mach number are thus identical to those for constant-velocity ratio. Similarly, since the mean velocity of the particles is proportional, but not equal, to the speed of sound according to the simple kinetic theory of a gas, contours of constant ratio of directed to random velocity are also identical to those for constant V/V_∞ .

Figure 6-1 and the accompanying discussion show that the value of 8 for the free-stream Mach number is well centered in the range of values to be expected in the incident solar wind. However, since both the velocity and the temperature, and hence the speed of sound, of the solar wind vary substantially in the course of time, it is of interest to review some of the results given by Spreiter et al. (1966a, 1968) for other Mach numbers. Figure 8-3 shows their plots of contours of constant-density ratio ρ/ρ_∞ for free stream Mach numbers of 5 and 12 . Although differences in the density ratio are clearly evident, they remain sufficiently small to be of only secondary importance for most purposes. It should be noticed, however, that the bow wave recedes from the magnetosphere as the Mach number diminishes although the change is small as the Mach number decreases from 12 to 8 The entire portion of the bow wave shown for $M = 12$ is, in fact, very near its asymptotic position for infinite Mach number, and further

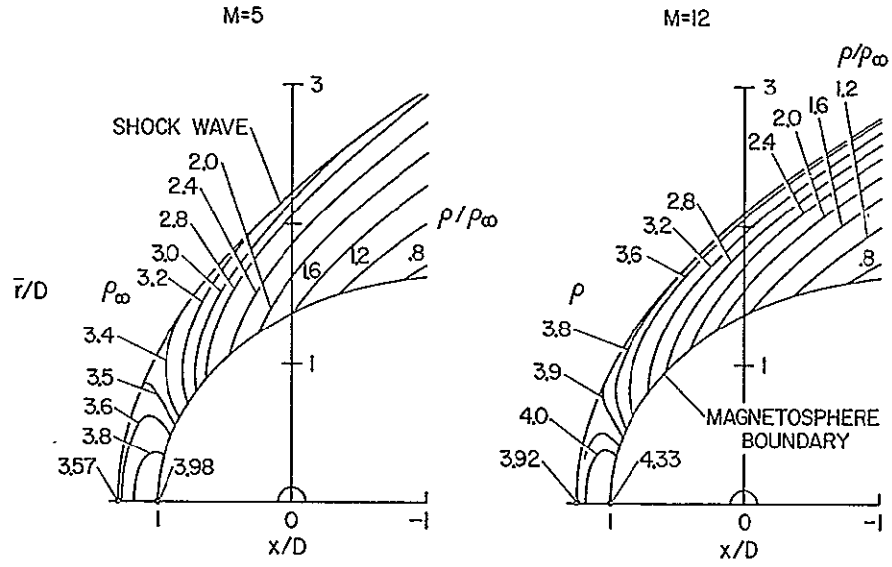

Figure 8-3. Effect of Mach number on density field for flow past the magnetosphere, $\gamma = 5/3$ (Spreiter et al., 1968).

increases in Mach number produce virtually no effect. This lack of dependence on Mach number does not apply, however, far downstream of the planet where the bow wave approaches alignment with the asymptotic direction of weak discontinuities in the undisturbed incident solar wind.

The corresponding results for the velocity and temperature are shown in figure 8-4. Like the density, the velocity field is hardly affected by the change from Mach number 5 to 12 . However, the temperature fields for these two Mach numbers differ substantially, the temperatures for Mach number 12 being about five times larger than for Mach number 5 . Such strong effects on the temperature can be easily explained by an examination of equation (8-1) for T/T_∞ . Although we do not display the results graphically here, Spreiter et al. (1968) showed that the temperature contours can also be put into a form relatively independent of M_∞ by normalizing the temperature by V_∞^2 rather than T_∞ . The explicit form they chose was the ratio $2c_p(T - T_\infty)/V_\infty^2$ of the change of the enthalpy $c_p(T - T_\infty) = \gamma c_v(T - T_\infty)$ to the kinetic energy and derived the expression $2c_p(T - T_\infty)/V_\infty^2 = 1 - V^2/V_\infty^2$ by combining the equation

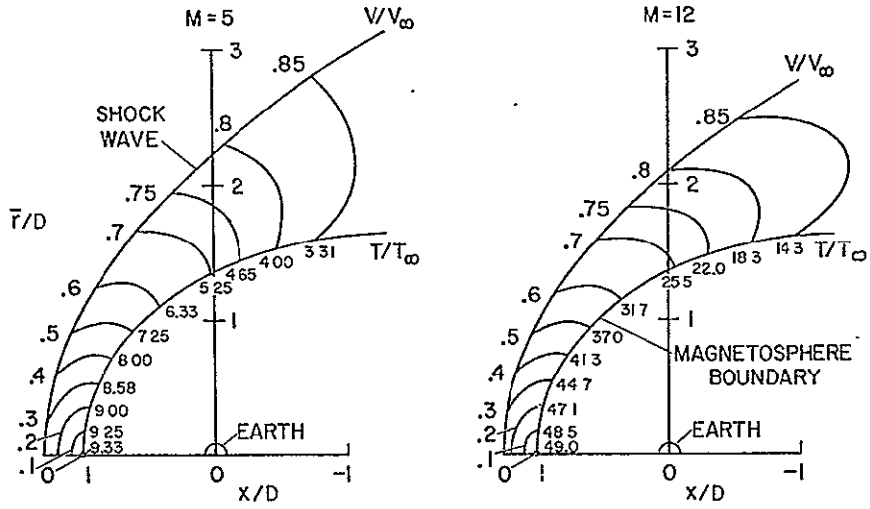

Figure 8-4. Effect of Mach number on velocity and temperature fields for flow past the magnetosphere, $\gamma = 5/3$ (Spreiter et al., 1968).

$(T - T_\infty)/T_\infty = \frac{\gamma-1}{2} M_\infty^2 (1 - V^2/V_\infty^2)$, the relation $h = c_p T$ defining the enthalpy per unit mass, and the expression $M_\infty = V_\infty/(2\gamma R T_\infty)^{1/2}$ for the free-stream Mach number of fully ionized hydrogen. Since V^2/V_∞^2 tends to be independent of Mach number at large M_∞, as illustrated in figure 8-4 for $M_\infty = 5$ and 12, and T_∞ in the same region is very much smaller than T, they concluded that the ratio $2c_p(T - T_\infty)/V_\infty^2$ also tends to be invariant with changes in Mach number at large M_∞.

a. Distortion of the interplanetary field. The results presented in the preceding paragraphs represent solutions of equations (7-1) and (7-2). As described previously, once the dynamic flow properties are numerically computed from these gasdynamic equations and the orientation for the magnetic field in the incident stream is specified, the deformation of the interplanetary magnetic field $\underset{\sim}{B}$ by the flow around the planet can be determined by numerically integrating equations (7-3), or, equivalently, equations (7-4) which indicate that magnetic-field lines deform in exactly the same manner as do fluid lines. Spreiter et al. (1966a) have demonstrated that these

equations lead to a straightforward, but tedious calculation in which the vector distance from each point on an arbitrarily selected field line to its corresponding point on an adjacent field line in the downstream direction is determined by numerically integrating $\int \underset{\sim}{V}\, d\tau$ over a fixed time interval $\delta\tau$. This procedure in general results in field lines that are curved in space.

The intensity of the magnetic field at any point may then be determined from the relation $|\underset{\sim}{B}|/|\underset{\sim}{B}_\infty| = (\rho|\Delta\ell|)/(\rho_\infty|\Delta\ell_\infty|)$ in which $\Delta\ell$ is the length of a small element of a flux tube. Figure 8-5 shows the results of such calculations performed for three different angles between $\underset{\sim}{B}_\infty$ and $\underset{\sim}{V}_\infty$ by Alksne (1967) and

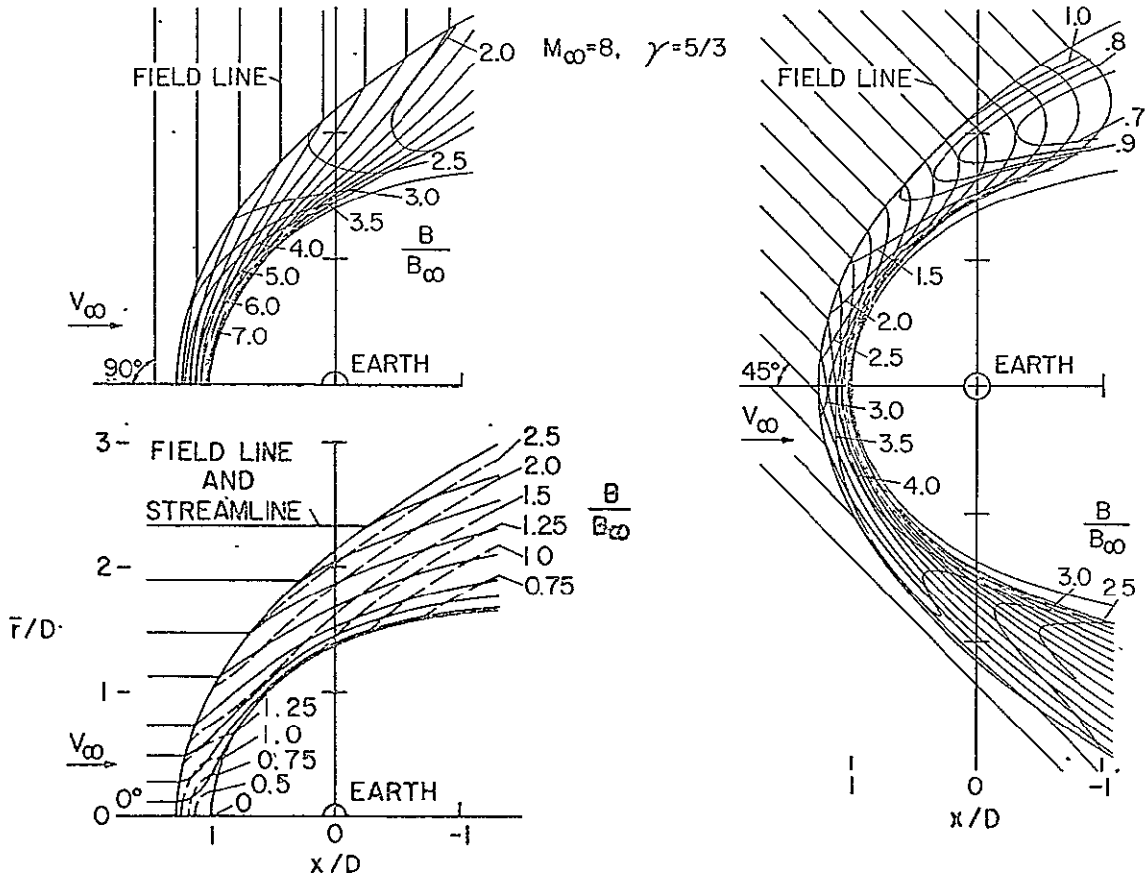

Figure 8-5. Direction and intensity of the magnetic field in the plane of symmetry for three different angles between $\underset{\sim}{B}_\infty$ and $\underset{\sim}{V}_\infty$, $M_\infty = 8$, $\gamma = 5/3$ (Spreiter and Alksne, 1969).

Spreiter and Alksne (1969) for the plane that passes through the center of the Earth and contains both the $\underset{\sim}{V}_\infty$ and $\underset{\sim}{B}_\infty$ vectors. Because of the assumed axial symmetry of the magnetosphere and surrounding flow, all these field lines are planar, rather than spatial, curves. While the calculation of the results for the case shown in the upper left must be carried out in more or less the method just described, the results for the other cases displayed in figure 8-5 can be obtained more easily. Those in the lower left for $\underset{\sim}{B}_\infty$ parallel to $\underset{\sim}{V}_\infty$ can be obtained immediately from the gasdynamic calculations because Imai (1960) found that $\underset{\sim}{B}$ is proportional to $\rho\underset{\sim}{V}$ throughout the entire flow field for this case. The field lines thus coincide with the streamlines, and the contours of constant $\underset{\sim}{B}$ coincide with those of constant $\rho\underset{\sim}{V}$. The results shown on the right for 45° angle between $\underset{\sim}{B}_\infty$ and $\underset{\sim}{V}_\infty$ were originally calculated by Alksne (1967) in the lengthy manner described above, but recently Alksne and Webster (1970) have shown that the linearity of the equations (7-4) for $\underset{\sim}{B}$, with ρ and $\underset{\sim}{V}$ already specified by the axisymmetric gasdynamic calculations, permits the magnetic field at any point in the plane of symmetry to be determined by addition of the $\underset{\sim}{B}$ vector for 0 and 90 degree orientations. Furthermore, results for any angle between $\underset{\sim}{B}_\infty$ and $\underset{\sim}{V}_\infty$ can be obtained by decomposing $\underset{\sim}{B}_\infty$ into components $(B_\infty)_\parallel$ and $(B_\infty)_\perp$ parallel and perpendicular to $\underset{\sim}{V}_\infty$, and superposing the contributions.

Figure 8-6(a) shows the magnetic-field direction and intensity for the more complex case in which the set of field lines considered in the incident solar wind is contained in a plane parallel to the plane of symmetry but offset from it by a distance $D/3$. The lines of intersection of the offset plane with the bow wave and the magnetosphere boundary are indicated by the solid and dotted lines. Since the field lines are no longer confined to a plane behind the bow wave, the results are presented in the form of a pair of projections. These and related results for other cases were originally calculated by Alksne (1967) and Spreiter et al. (1968) in the laborious manner described at the beginning of the preceding paragraph. Alksne and Webster (1970) have shown that the magnetic field at any point in

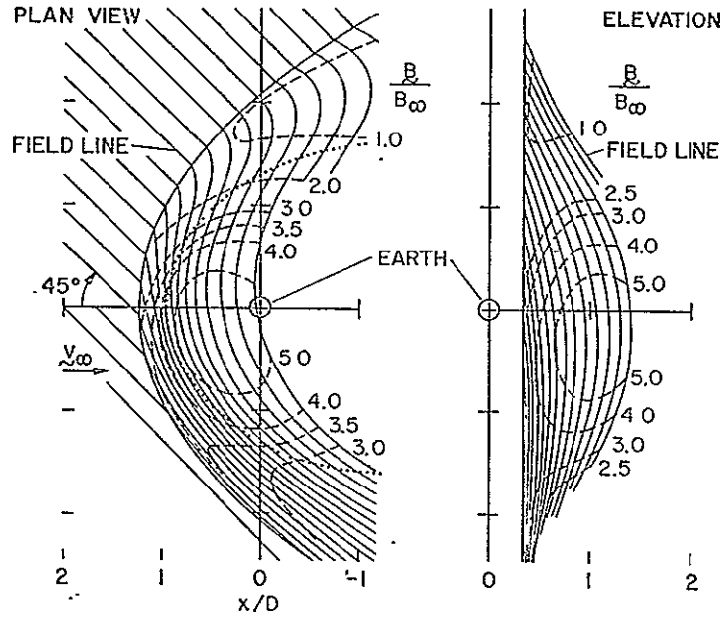

(a) Magnetic-field direction and intensity, $M_\infty = 8$.

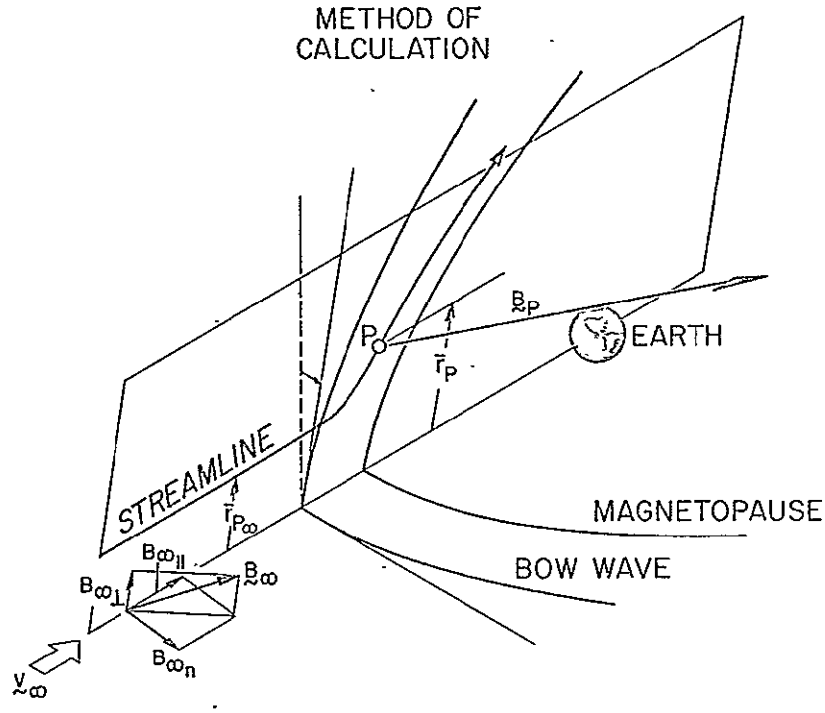

(b) Method of calculation.

Figure 8-6. Direction and intensity of the magnetic field out of the plane of symmetry, and illustration of components of interplanetary magnetic field used in equation (8-2) (Spreiter and Alksne, 1970).

the flow field can be calculated more simply, however, by vectorially summing the contributions of the three component fields indicated in figure 8-6(b). At any point P, the magnetic field $\underset{\sim}{B}_P$ is thus

$$\underset{\sim}{B}_P \quad \left(\frac{\underset{\sim}{B}_P}{B_\infty}\right)_{\parallel} B_{\infty\parallel} + \left(\frac{\underset{\sim}{B}_P}{B_\infty}\right)_{\perp} B_{\infty\perp} + \hat{n}\left(\frac{B_P}{B_\infty}\right)_{n} B_{\infty n} \qquad (8\text{-}2)$$

In this equation, the three ratios with subscripts $\parallel$, $\perp$, and n refer to the contributions associated with the components of $\underset{\sim}{B}_\infty$ parallel to $\underset{\sim}{V}_\infty$; perpendicular to $\underset{\sim}{V}_\infty$ in the plane that contains the point P, the center of the Earth, and the vector $\underset{\sim}{V}_\infty$; and the normal to the that plane. From the previous discussion, we see that $(\underset{\sim}{B}_P/B_\infty)_{\parallel} = (\rho_P \underset{\sim}{V}_P)/(\rho_\infty |\underset{\sim}{V}_\infty|)$ and $(\underset{\sim}{B}_P/B_\infty)_{\perp}$ is as illustrated in the upper left part of figure 8-5 for $M_\infty = 8$ and $\gamma = 5/3$. Since the remaining ratio $(B_P/B_\infty)_n$ can be shown equal to $(\bar{r}_P \rho_P)/(\bar{r}_{P\infty} \rho_\infty)$ where $\bar{r}$ is the radial cylindrical coordinate of the streamline, as indicated in the sketch of figure 8-6(b), values for it can be determined directly from the gasdynamic solution for the flow.

The results displayed in figure 8-5 clearly show how the magnetic-field lines bend discontinuously as they pass through the bow wave at any angle except a right angle, and then curve in a continuous manner throughout the entire region between the bow wave and the magnetosphere. The discontinuous bend at the shock wave is, moreover, always in the direction that preserves the sign of the tangential component of the field, as is required for all physically relevant hydromagnetic shock waves. Interestingly, the field lines illustrated in figure 8-5 are all draped around the nose of the magnetosphere. This is characteristic of the results for all relative orientations, except perfect alignment, of the magnetic-field and velocity vectors for the special plane for which these results are presented. Outside of this plane, however, the field lines drift around the nose with the flow and deform as illustrated in figure

8-6(a) into three-dimensional curves.

The results shown in figures 8-5 and 8-6 indicate that the intensity of the magnetic field is usually a few times larger near the magnetosphere nose than in interplanetary space, except when the magnetic field is aligned or nearly aligned with the flow direction, and that it may be either larger or smaller than the incident-stream value along the flanks of the magnetosphere. They also show that the direction of the field in the region between the bow wave and the magnetosphere is highly distorted by the flow and bears little direct relation to the direction of the field in the incident solar wind.

The results in these figures are for a free-stream Mach number of 8 , but no qualitative changes are anticipated if a somewhat different value is selected since the velocity field is only slightly influenced by variation of Mach number.

2. Flow past Mars and Venus

In exactly the same way as was done for the Earth, once a value for the free-stream Mach number is specified, the location of the bow wave and the properties of the flow field can be computed for any of the Martian or Venusian ionopause shapes shown in figure 6-6 by application of the numerical gasdynamic programs.

Results for the location of the bow wave for flow with $M_\infty = 8$ and $\gamma = 5/3$ are presented in figure 8-7 for each value for H/r_0 for which the coordinates of the ionopause are illustrated in figure 6-6. Although these results are for a specific M_∞ , it has been shown in the previous section relating to the Earth that the shape of the bow wave, and also the associated distributions of ρ/ρ_∞ , $\underset{\sim}{V}/V_\infty$, and $\underset{\sim}{B}/B_\infty$ for any given direction for $\underset{\sim}{B}_\infty$ are relatively independent of free-stream Mach number for all M_∞ greater than about 5 (Spreiter et al., 1966a, 1968).

In figure 8-8 are shown contour maps for the density ratio ρ/ρ_∞ , velocity ratio V/V_∞ , and temperature ratio T/T_∞ for flow with $H/r_0 = 0.2$. Such a value is appropriate, for example, for a Venusian ionosphere composed primarily of atomic hydrogen at

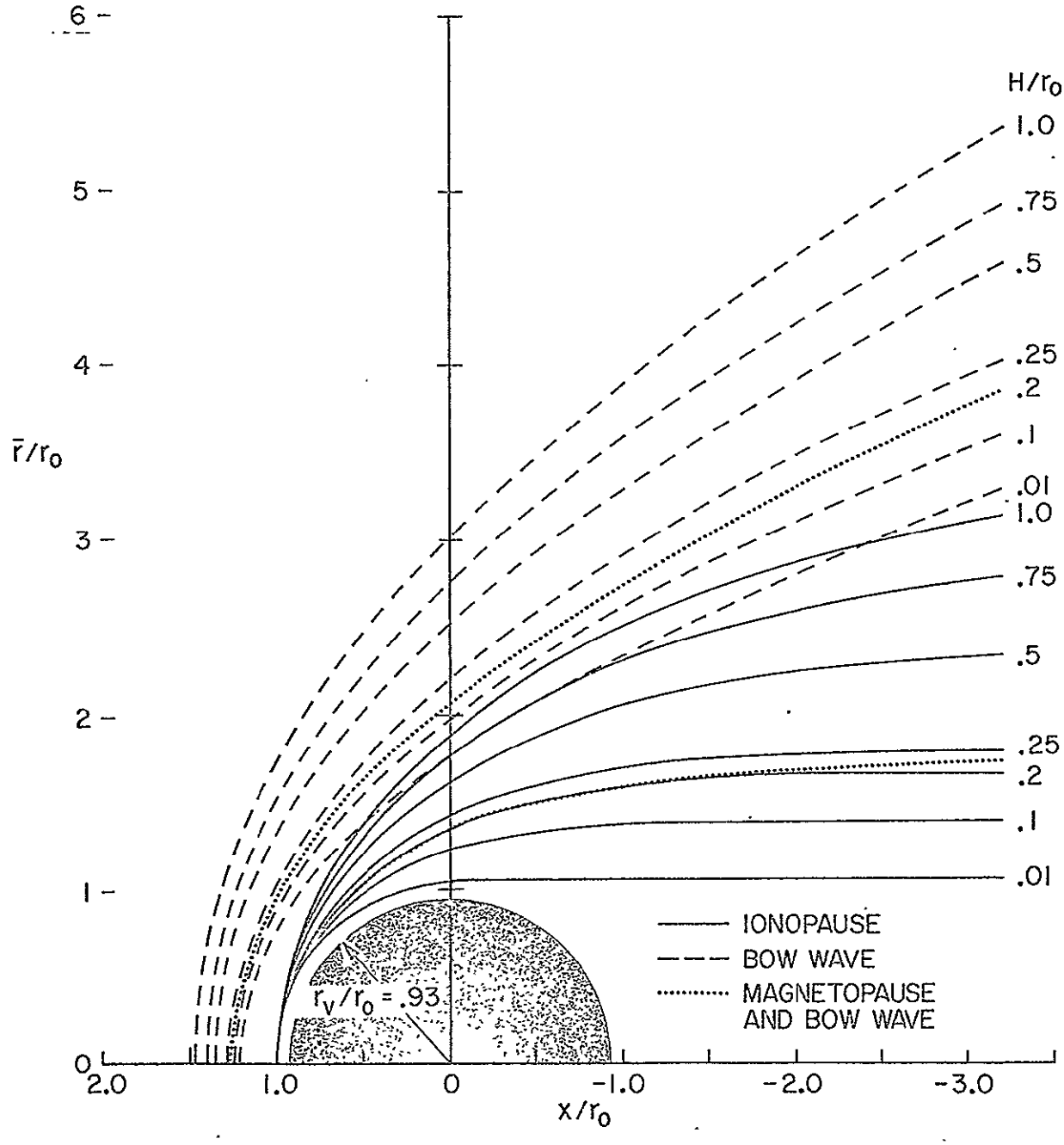

Figure 8-7. Calculated location of ionopause for various H/r_o, and associated location of bow wave for $M_\infty = 8$, $\gamma = 5/3$. The corresponding results for the shape of the Earth's magnetopause and bow wave, nondimensionalized so that the magnetopause nose is at $x/r_o = 1$, is included for purposes of comparison. The dashed line for the bow wave for $H/r_o = 0.2$ has been omitted because it is indistinguishable from the dotted line representing the Earth's bow wave (Spreiter, Summers, and Rizzi, 1970b).

about 600°K.

In view of the current tendency for some to interpret the Mariner-5 results as indicating that the primary constituent in the Venusian atmosphere is molecular hydrogen, or even heavier ions, we have also made a set of calculations for the density, velocity, and temperature in the flow field for $H/r_0 = 0.1$. The results are shown in figure 8-9. Corresponding plots for other quantities of interest, such as the magnetic-field strength and direction, or Maxwellian proton-velocity distribution, can also be calculated in the same way as has been done previously for the Earth by Spreiter and Alksne (1969, 1970) and Spreiter et al. (1966b). Such calculations have not been carried through, however. This is partly because they are time consuming to do and require considerable space to display the results for even a minimum number of cases, but principally because an approximate correspondence rule to be described in the next section makes it possible to convert quickly any of the numerous contour plots already available for the properties of the flow around the Earth's magnetosphere into that for the flow around an ionosphere having any H/r_0 between 0.01 and 1 by a simple relabeling of the coordinate axes.

a. Correspondence rule. The close relationship between the shape of the magnetopause and that of the ionopause for $H/r_0 = 0.2$, and the general similarity of the ionopause shapes for all H/r_0 , suggests the possibility that a correspondence rule relating ionopause shapes for H/r_0 other than 0.20 to an appropriately scaled magnetopause may be found if the coincidence between the Earth and planetary centers be relinquished. Great practical utility would result from the availability of such a correspondence rule, because it would enable a substantial body of results already calculated for solar-wind flow past the Earth to be applied with minor change to nonmagnetic planets having a wide range of ionospheric parameters.

The results displayed in figure 8-10 show that it is indeed possible to achieve a fit that is probably sufficiently good for most purposes relating to the interpretation of data obtained in space.

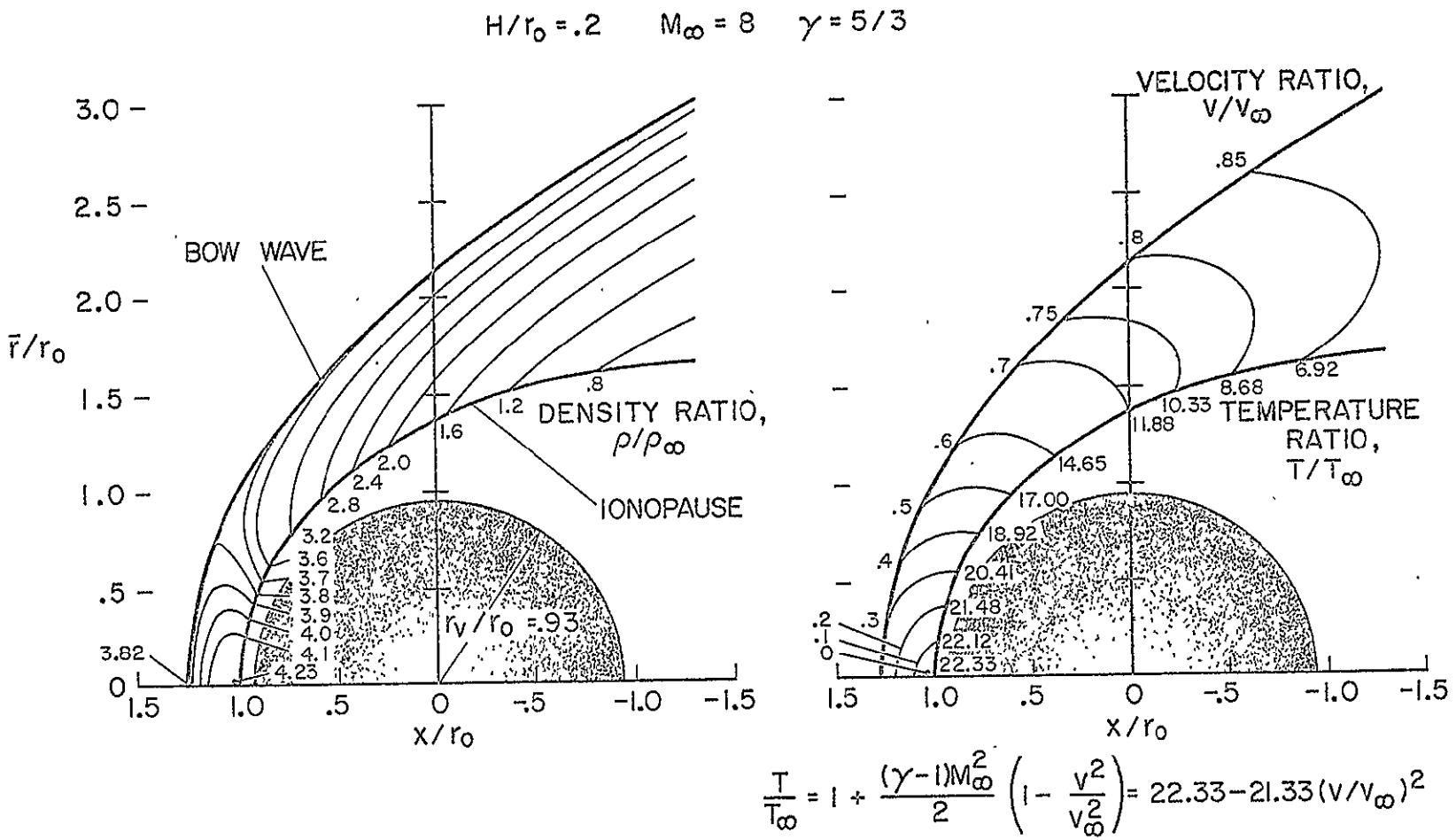

Figure 8-8. Density, velocity, and temperature fields for supersonic flow past the ionosphere; $H/r_0 = 0.2$, $M_\infty = 8$, $\gamma = 5/3$ (Spreiter, Summers, and Rizzi, 1970b).

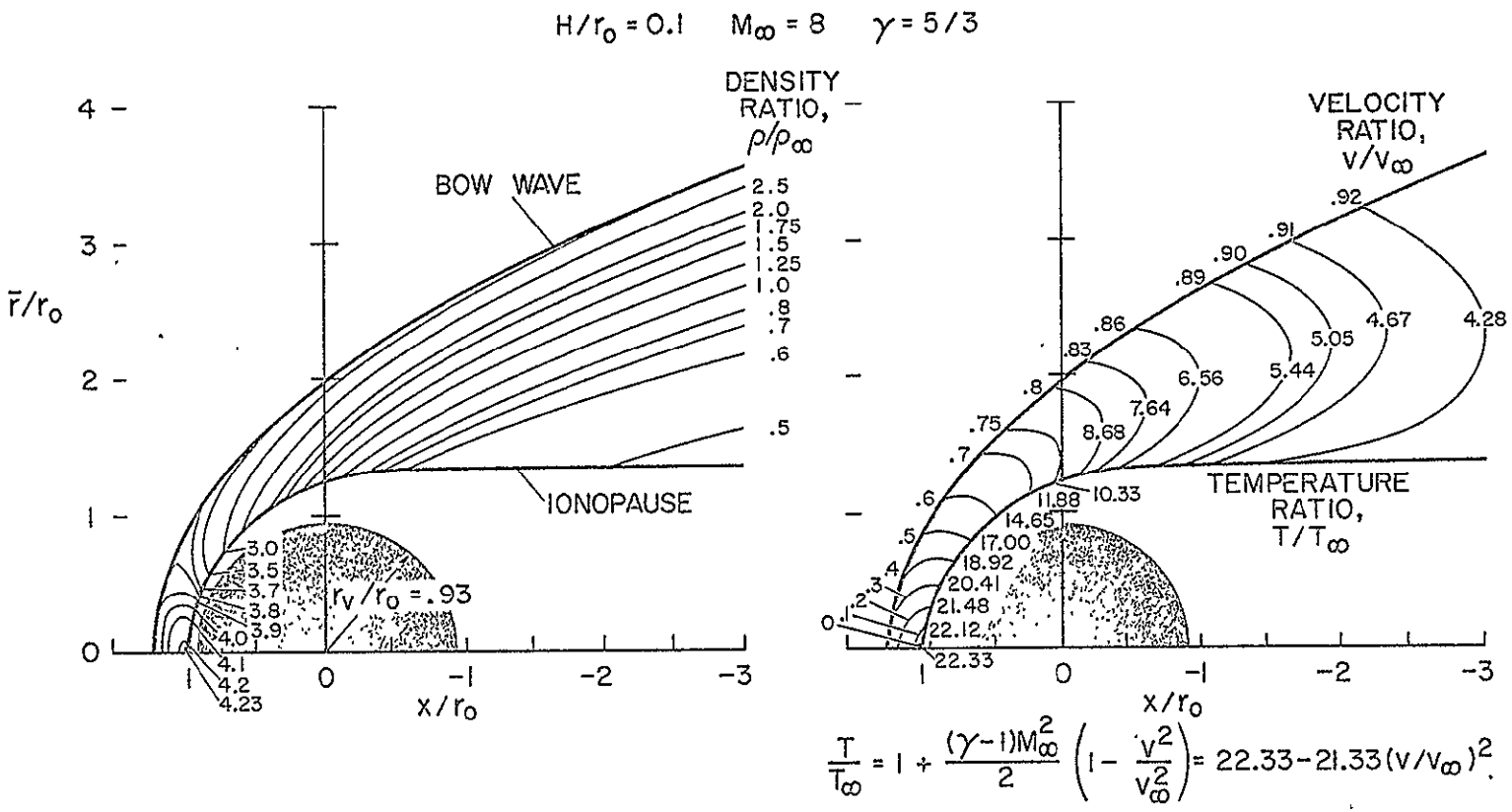

Figure 8-9. Density, velocity, and temperature fields for supersonic flow past the ionosphere; $H/r_o = 0.1$, $M_\infty = 8$, $\gamma = 5/3$ (Spreiter, Summers, and Rizzi, 1970b).

This figure is basically that given originally by Spreiter et al. (1966a) for the magnetosphere boundary and shock wave for the Earth, and the associated characteristic or Mach line pattern, for $M_\infty=8$ and $\gamma = 5/3$. Superposed on it are the ionopause curves from figure 8-7 each with its nose retained at $x/r_0=1$, $\theta = 0$, but with its scale adjusted so that its ordinate coincides with that for the magnetopause curve at $\theta=\pi/2$. The center of the nonmagnetic planet is, in general, no longer at the origin of coordinates, but at the points x_c/r_0 indicated along the axis of symmetry for each value for H/r_0 . The coordinates of these points are listed on figure 8-10 for accuracy and convenience in applications of the correspondence rule. To convert the nondimensional shape for the magnetopause into that for the ionopause for a given H/r_0 , we must thus place the center of the planet at x_c/r_0 and change the labeling of the scales so that $x/r_0 = 0$ at x_c/r_0 , and $x/r_0 = 1$ at the ionopause nose.

It follows from the close correspondence between the coordinates of the ionopause and the magnetopause that the coordinates of the bow wave should also display a similar relationship. It may be seen from figure 8-10 that this is indeed true. A similar degree of correspondence may be anticipated for the coordinates of contour lines for constant values of the flow parameters, such as those for the density, velocity, and temperature shown in figures 8-8 and 8-9.

Although some of the ionopause curves depart significantly from the curve for the magnetopause somewhat downstream of the planet, the effects of these differences have no influence upstream of the rearwardly inclined characteristic line emanating from the point on the boundary where the differences first become significant. It may be seen from figure 8-10 that this is sufficiently far downstream for ionospheres having H/r_0 between 0.01 and 1 that nearly all of the results we have presented previously for the properties of the flow field about the magnetosphere can be carried over with no other change than relabeling the scales to obtain a good approximation for the conditions around Mars and Venus.

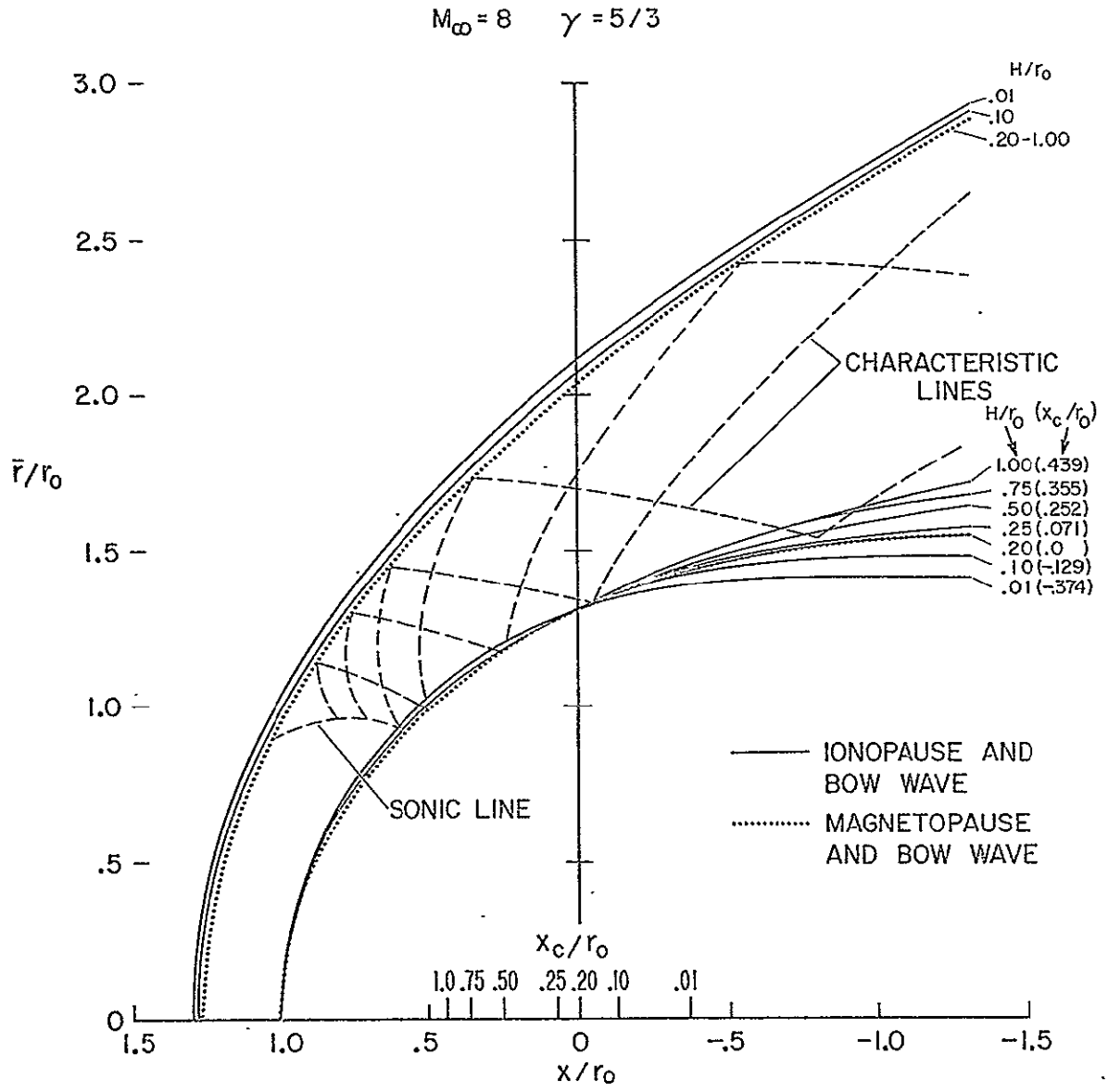

Figure 8-10. Illustration of degree of coincidence of curves representing the ionopause and bow waves for various H/r_0 obtained by application of correspondence rule. The solid lines have been omitted where they are indistinguishable from the dotted lines (Spreiter, Summers, and Rizzi, 1970b).

B. Evaluation of the Theory

Since all of the foregoing theoretical results are founded on the numerical solution of the gasdynamic equations which, we argued, approximate the hydromagnetic equations in this application, it is informative and important to examine these theoretical calculations for internal consistency. This examination should assay the three principal postulates of our theory; namely, do the numerical calculations represent accurate solutions of the gasdynamic equations, how precisely do these equations approximate the complete hydromagnetic equations, and finally, how accurately does the Newtonian pressure predict the flow pressure on the boundary.

The accuracy of the numerical solution has been verified theoretically by the consistency checks built into the computer programs. As discussed in chapter VII, in the subsonic region the conservation of entropy along streamlines and total enthalpy everywhere provides an independent theoretical check on the programs internal consistency whereas the constancy of mass flow furnishes a similar check in the supersonic region. All of the numerical calculations presented in this report accurately satisfies these checks. In addition, Inouye and Lomax (1962), Spreiter et al. (1966a), and others have found that these computer programs provide solutions to the gasdynamic equations that do compare very well with actual aerodynamic measurements obtained experimentially. On this question then, we are assured that out numerical results do indeed accurately represent the solution of the gasdynamic equations.

One of the simplifications fundamental to the attainment of the numerical results presented in the foregoing sections of this chapter assumes that the Alfvén Mach number M_A is sufficiently greater than unity so that the gasdynamic equations satisfactorily approximate those of hydromagnetic theory, and subsequently that the magnetic field can be calculated by application of the concept of the magnetic-field lines moving with the fluid. Comparison of the values for the Alfvén speed displayed in figure 6-1 with representative values for the velocity of the solar wind assures that this condition is easily met in the free-stream. A similar comparison for the conditions

behind the bow wave is more difficult to make a priori because both the flow velocity and the Alfvén velocity vary considerably throughout the flow field. Once the velocity, density, and magnetic-field intensity have been calculated for any point, however, the Alfvén Mach number is easily evaluated, and we can therefore determine to what extent the postulate of large M_A is fulfilled. The findings of such an examination carried out by Spreiter et al. (1968) are presented in figure 8-11 for two orientations of the interplanetary magnetic field both with $M_\infty = 8$. The results are given in the form of a ratio of the local Alfvén Mach number M_A to the free-stream Alfvén

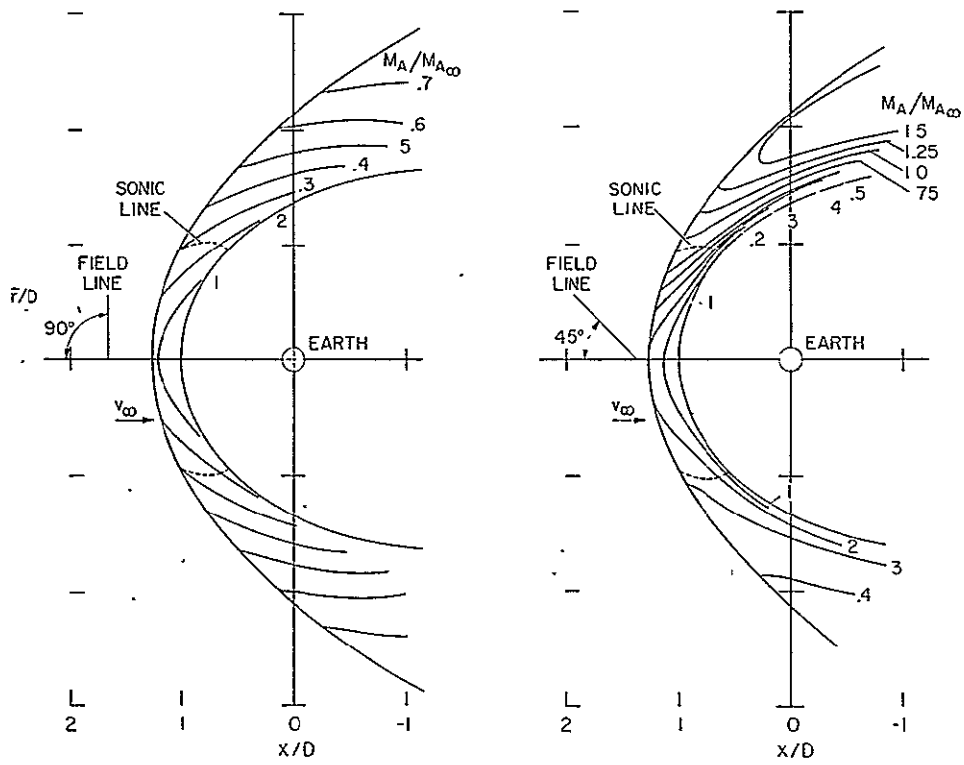

Figure 8-11. Alfvén Mach number distribution, $M_\infty = 8$ and $\gamma = 5/3$ (Spreiter et al., 1968).

Mach number $M_{A\infty}$ in order to take advantage of the simple proportionality between the two quantities at any point in the flow field. If $M_{A\infty} = 10$, as is usual for the incident solar wind, the results show that M_A is greater than unity everywhere except in a small

region near the magnetosphere nose. Although, as predicted by Lees (1964), some localized departures from the calculated results might be anticipated in this region, it would seem that the larger-scale features of the flow should be quite adequately represented by the gasdynamic and frozen-field calculations. Moreover, although this case is not displayed here, as the magnetic-field orientation approaches alignment with the flow direction, this region shrinks even smaller, and the validity of the numerical results becomes even more assured. As $M_{A\infty}$ decreases below 10 , however, the critical regions expand significantly for all orientations, and increasing differences between the approximate numerical results and more exact theoretical or observational results should be anticipated. When $M_{A\infty}$ becomes as small as 2 or 3 , which it does only infrequently, the critical region of small local Alfvén Mach number would become so extensive that substantial departures from the results so far presented must be expected. (This interesting behavior at low Alfvén Mach number will later be more thoroughly discussed in chapter X.)

Lastly, there remains the question of how accurately does the simple Newtonian pressure formula $p = p_{st}\cos^2\psi$ approximate the variation of pressure along the magnetosphere boundary. The answer to this question for the present applications is easily arrived at by comparing the Newtonian pressure on the magnetopause with the pressure derived from the detailed gasdynamic calculations. The results of such a comparison, originally presented by Spreiter et al. (1966a), are shown in figure 8-12 for several values of M_∞ and γ . We can easily see that the simple Newtonian expression does indeed provide a generally good approximation over most of the magnetosphere boundary of interest in the present studies. The agreement is particularly good over the portion of the magnetosphere along which the flow is subsonic. No significant changes are expected, therefore, in the shape of the nose portion of the bow wave if a more accurate and necessarily more complicated calculation of the pressure is carried out. The Newtonian pressure formula does, however, underestimate the pressure somewhat along the flanks of the magnetosphere which indicates that a more exact calculation using the gasdynamic

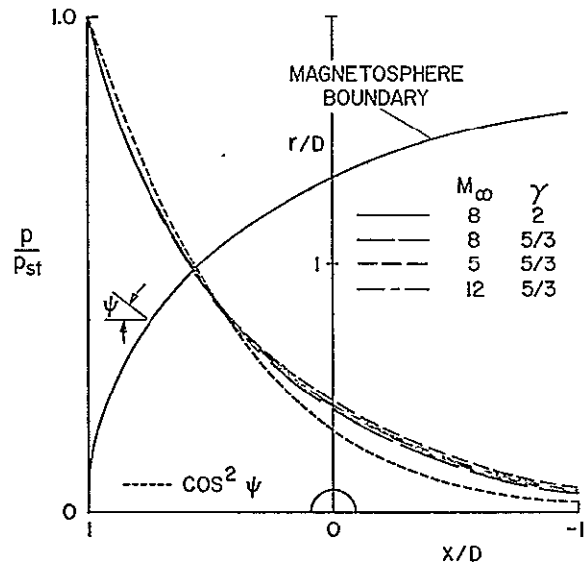

Figure 8-12. Comparison of exact and approximate pressure distributions on magnetosphere boundary (Spreiter et al., 1968).

pressure distribution would yield a slightly slimmer shape. This change in shape along the flanks of the magnetopause should nevertheless be small because the geomagnetic pressure. $B_\oplus^2/8\pi$ which balances the gas pressure p is nearly proportional to the inverse sixth power of the distance from the center of the Earth. A point of equal interest displayed by these results is the lack of significant variation of the pressure distribution with changes in M_∞ and γ over the range of cases presented.

Although we do not display the results here, we have performed a corresponding examination of the accuracy of the modified Newtonian pressure formula

$$p = (p_{st} - p_\infty - B_\infty^2/8\pi)\cos^2\psi + p_\infty + B_\infty^2/8\pi$$

for the ionopause of either Mars or Venus and found the results similar to those presented in figure 8-12. For this case, too, agreement is particularly good in the nose region, but the modified pressure formula

partially underestimates the pressure along the flanks of the ionopause. The resulting slimmer ionopause shape which a more exact calculation using the gasdynamic pressure distribution would indicate, however, would also not differ very much from the present shapes because the ionosphere pressure which balances the gas pressure p varies exponentially with distance from the center of both Mars and Venus.

C. Comparison with Observations in Space

Although a number of checks on the internal consistency of the fluid theory and its subsequent results are given in the original references, some of which we have reviewed in the previous section, the final test of any theory of solar-wind flow past these planets must be based on comparisons with observations actually made in space. Such comparisons have been made by several different authors on several levels of detail. These range from simple comparisons of gross features, such as the existence and location of the magnetosphere boundary and bow wave, to more detailed comparisons of the velocity, density, and temperature of the flowing plasma and the intensity and direction of the magnetic field. Here, rather than review in detail the enormous amount of space observations made in the vicinity of the Earth, we shall restrict ourselves to only a brief account of near-Earth data intended to show the actual validity of one of the fluid assumptions and then concentrate on a more thorough comparison between the appropriate theoretical results presented so far and the data observed near Mars by Mariner spacecraft 4, 6, and 7 and near Venus by Mariner 5. In addition, several extensive summaries of the comparison between Earth-related space observations and theoretical fluid calculations have been given recently by Spreiter *et al.* (1968) and Spreiter and Alksne (1969, 1970).

A key point in the hydromagnetic theory of the steady-state interaction of the solar wind and both the magnetic field of the Earth and ionospheres of Mars and Venus is that the magnetopause must be represented by a tangential discontinuity. Sonnerup and Cahill (1967, 1968) have investigated this by examining the magnitude of the magnetic-field component normal to the magnetopause in the data of

Explorer 12 satellite. Although the accuracy of those data is marginal for the task, and the orientation of the magnetopause is uncertain, they conclude that this quantity is sufficiently small for most of the crossings to be compatible with the theoretical requirement given in equations (5-10) that $B_n = 0$. Fairfield (1967) has also investigated this question using data obtained simultaneously by the IMP 1 and IMP 2 satellites when they were on opposite sides of the bow wave. Within the accuracy of the determination, the results showed that the magnetic field is tangential to the magnetopause, which satisfies the condition $B_n = 0$, and also that the orientation of the magnetic-field vectors throughout the entire region between the bow wave and magnetopause is consistent with the theoretical predictions provided by the simplified hydromagnetic model. This conclusion has been recently confirmed and strengthened by the results of a more extensive study by Behannon and Fairfield (1969) using 1661 hours of data from four spacecraft, Explorers 28, 33, 34, and 35.

1. Comparison with Mariner 5 data for Venus

Due to insufficient data, a similar examination of the fulfillment of the tangential discontinuity conditions cannot be carried out for the ionopause of either Mars or Venus. We can, however, make a general assessment of the relation between the theoretical results shown in figures 8-7 to 8-9 and those observed by Mariner 5 as it flew past Venus. Figure 8-13 shows the time variation of the bulk velocity V, ion number density n, and intensity $|B|$ and direction α and β of the magnetic field together with a plot of the trajectory giving the position of the spacecraft as a function of time (Bridge et al., 1967). The angles α and β are in spherical coordinates in which α is the longitude measurement, in the $\underset{\sim}{R}\underset{\sim}{T}$ plane, and from the $\underset{\sim}{R}$ direction, where $\underset{\sim}{R}$ is a unit vector in the antisolar direction and $\underset{\sim}{T}$ is an orthogonal vector which is parallel to the Sun's equatorial plane and points in the direction of the planet's orbital motion; and β is the latitude angle of the magnetic-field vector, considered positive when northward. For ease of

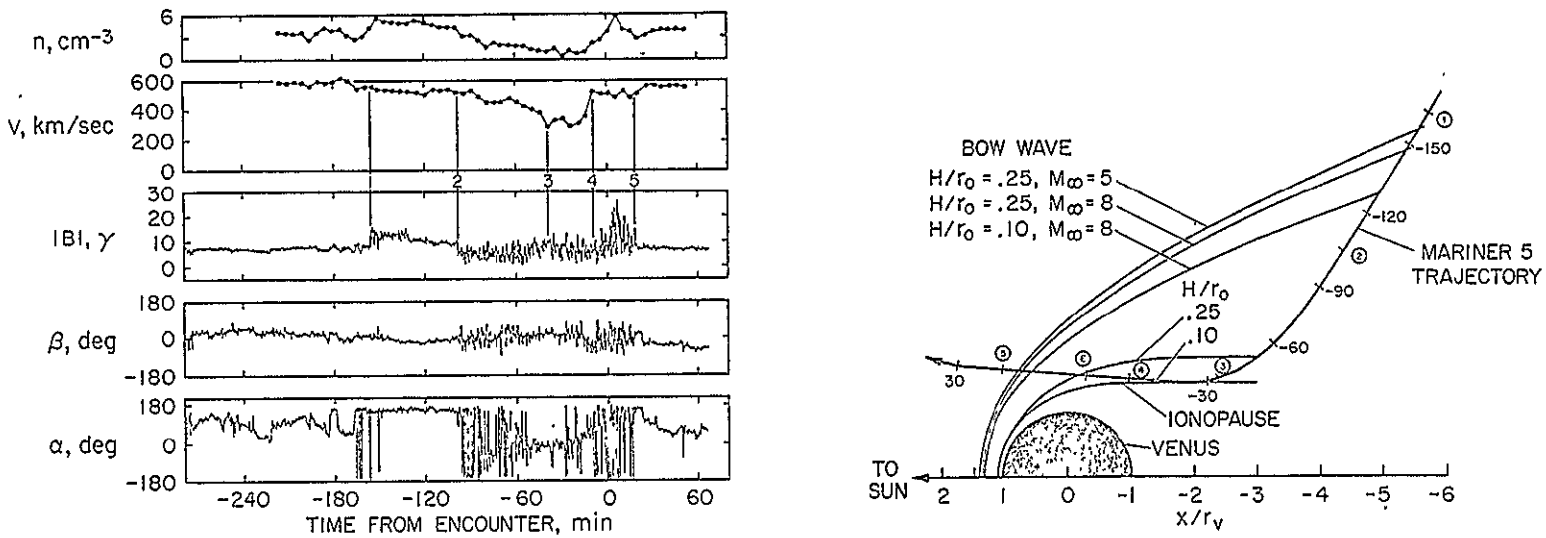

Figure 8-13. Plasma and magnetic data measured by Mariner 5 in its encounter with Venus on 19 October 1967 (Bridge et al., 1967). The indicated trajectory has been projected into a plane by rotation about the Sun-Venus line. Times are in minutes relative to the encounter time E of closest approach to the planet (Spreiter, Summers, and Rizzi, 1970b).

reference, lines indicating the theoretical location of the ionopause and bow wave for $H/r_o = 0.1$ and 0.25, for $M_\infty = 8$, $\gamma = 5/3$, and $r_o = 6500$ km are superposed on the plot of the trajectory. The corresponding location of the bow wave for $M_\infty = 5$ and H/r_o 0.25 is also included in order to better assess the consequences of the fact that the values of about 590 km/sec and 300,000°K reported for the velocity and temperature in the solar wind before and after Mariner 5's encounter with Venus indicate a value of about 6.5 for M_∞.

The magnetometer and plasma probe experimenters have concluded from the presence of abrupt and easily recognizable changes in their data that Mariner 5 crossed the bow wave at the points labeled (1) and (5). These points are reasonably close to the theoretical locations of the shock wave for $H/r_o = 0.25$ for $M_\infty = 5$, and somewhat farther from Venus than indicated by the theoretical results for $M_\infty = 8$, or for $H/r_o = 0.10$. On the other hand, the theoretical results for $H/r_o = 0.25$ indicate that Mariner 5 should have crossed the ionopause, whereas those for $H/r_o = 0.10$ indicate that it should have just skimmed along this surface. Although the data display decreases in n/n_∞ and V/V_∞ that are at least qualitatively similar to those for either $H/r_o = 0.10$ or 0.25, there is no certain evidence that Mariner 5 actually penetrated the ionopause. In particular, the intensity of the magnetic field remained of the order of that for interplanetary space, and V diminished to only a modest fraction of V_∞ rather than to a value comparable with the speed of the spacecraft relative to Venus. On the other hand, the observations made when the spacecraft was near the theoretical location of the ionopause indicate values for n/n_∞ and V/V_∞ that are only about one-half of those indicated by the theory for the flow exterior to the ionosphere.

A possible explanation for these discrepancies is that the tail of the ionosphere might taper inward toward the axis of symmetry rather than extend straight downstream. The theoretical results give no indication of such a trend, but they are of low reliability for this feature of the flow because of the deterioration of the quality of the modified Newtonian approximation for the pressure of the solar

wind as ψ approaches 90°, and the substantial departures from a constant scale height of a planetary atmosphere at great heights caused by the diminished gravitational acceleration, and also by probable increase in temperature. In addition, it is virtually certain that the ionosphere in an extended tail would be supported partially by dynamical interaction with the flowing solar wind instead of entirely by the simple hydrostatic means assumed in the present analysis. Although neither theoretical nor observational evidence is as yet sufficient to provide a definitive statement regarding the nature of the ionosphere tail, we are inclined to explain the discrepancy between the theoretical and Mariner-5 results in terms of an extended tail with a relatively thick boundary layer between the planetary ionosphere and the solar wind. The latter may be contrasted with the thin boundary between the solar wind and the Earth's magnetosphere that is becoming increasingly evident as the time resolution of the observations is improved. That the ionopause might be thick well back from the nose, whereas the magnetopause is usually thin, is plausible in view of the fundamentally different nature of the two boundaries. For the Earth, the magnetopause is essentially a boundary between the flowing solar plasma and a relative vacuum, and would be somewhat like the boundary formed by a free streamline in a water flow with embedded air cavity. For Venus or Mars, the ionopause is essentially a boundary between two different bodies of plasma. As such, a significant boundary layer would be anticipated which would provide an increasingly thick transition between the ionosphere and the solar wind with increasing distance from the stagnation point at the nose of the ionopause. It would spread, moreover, both into the outer part of the ionosphere and outward into the surrounding flow, broadening the transition region in which all properties of the plasma including the density, velocity, and magnetic field change from their values for the flowing solar plasma to those of the planetary ionosphere. At the location of the ionosphere boundary indicated by the present dissipationless theory, the plasma velocity might be expected to be substantially less than indicated by the theory. Since the plasma velocities observed by Mariner 5 in the vicinity of the

theoretical location of the ionopause display such a trend, it is tempting to conclude that Mariner 5 entered the boundary layer separating the ionosphere and the flowing plasma, but did not enter the ionosphere proper. A more detailed examination is clearly required before a definitive statement can be made, however.

2. Comparison with Mariner 4, 6, and 7 data for Mars

As described in less detail previously, data from the magnetometer (Smith et al., 1965), plasma probe (Lazarus et al., 1967), and energetic-particle detectors (Van Allen et al., 1965 and O'Gallagher and Simpson, 1965) on Mariner 4 displayed no effects attributable to the presence of Mars as it flew past that planet. Although such a negative finding does not provide much material for comparison, Spreiter et al. (1970b) found it at least consistent with the indication of the present theory for the conditions measured at the time of the encounter that Mariner 4 did not cross the bow wave into the region influenced by Mars at any time when signals were being received from the spacecraft.

More recently, however, it has been reported by Smith (1969) and Kavanagh et al. (1970) that a closer examination of the magnetometer data indicates that Mariner 4 may have detected a Martian bow wave, although its effects are weak and its presence could not be confirmed by the other instruments. In figure 8-14 are reproduced 16 hr of the Mariner-4 magnetometer record (Smith, 1969) showing the intensity $|B|$ of the field as the spacecraft passed Mars. This quantity is plotted as a function of the time that the data was received at Earth, and is 12 min later than the time at which the measurements were made and transmitted by the spacecraft. The distance of the spacecraft from the center of Mars is indicated by the aerocentric-distance scale at the top of the plots. The point of closest approach to Mars is denoted by CA . The two abrupt changes in $|B|$ signify crossings of the proposed Martian bow wave. Those authors see fit, however, to repeat the cautioning of the experimenters (Smith et al., 1965 and Smith, 1969) that the field disturbances seen while the spacecraft was near Mars could have been interplanetary-field

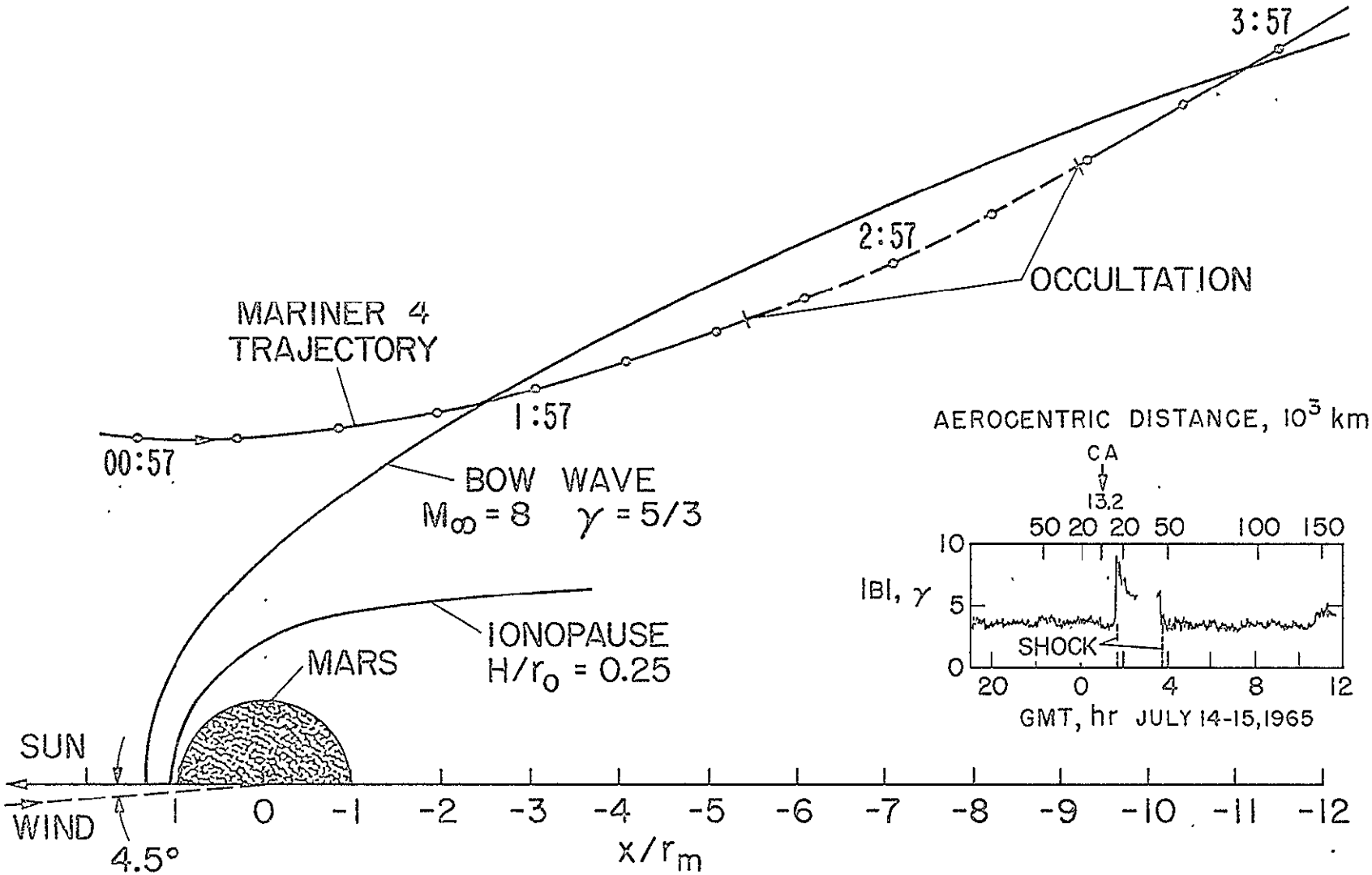

Figure 8-14. Trajectory of Mariner 4 past Mars, projected into a plane by rotation about the Sun-Mars line; calculated location of the ionopause and bow wave for $M_\infty = 8$, $\gamma = 5/3$, and $H/r_o = 0.25$ rotated 4.5 to allow for aberration effects arising from Mars' orbital motion as viewed along the trajectory of Mariner 4 (Smith, 1969); and magnetic record from the latter source showing abrupt changes at virtually the precise times that Mariner 4 crossed the calculated position of the bow wave (Spreiter and Rizzi, 1971).

fluctuations bearing no relation to the planet. Although data from the plasma detector reported by Lazarus (1967) show a slightly broader than average energy spectrum from about 300 to 100 eV when the spacecraft was inside the proposed bow wave, these indications were considered indecisive for the confirmation of the shock wave's presence because failure of the instrument's high voltage supply made the lower energy data unreliable. If, however, it is assumed that the magnetic discontinuities do, in fact, signify crossings of the bow wave, the locations of the crossings can be interpreted (Dryer and Heckman, 1967) as indicating the existence of a Martian magnetic field having a dipole moment about 2.1×10^{-4} that of the Earth.

The alternate interpretation, presented by Spreiter and Rizzi (1971) that the Martian bow wave results from the presence of an ionosphere, and may develop even in the absence of a planetary field, gains substantial support from the remainder of the results shown in figure 8-14. These consist of a plot of the trajectory of Mariner 4 near Mars projected onto the Sun-Mars-spacecraft plane (Van Allen et al., 1965) and superposed on a plot of the calculated position of the bow wave for $M_\infty = 8$ and $\gamma = 5/3$ resulting from interaction with the indicated ionopause drawn for $r_M/r_o = 0.95$ and $H/r_o = 0.25$ The distance r_o was calculated to be 5 percent greater than the 3.4×10^8 cm radius of Mars from the electron density profiles for the Martian ionosphere determined from the Mariner 4, 6, and 7 observations together with the present theory. The value $H/r_o = 0.25$ is representative of conditions that would prevail if the dominant molecule were atomic hydrogen at a temperature T of about 200°K as is indicated by Kliore et al. (1965) and Fjeldbo and Eshleman (1968) to be the case in the upper ionosphere, the region of greatest importance to the interaction with the solar wind. The associated bow wave is drawn for $M_\infty = 8$, but results of similar calculations for the Earth's bow wave have shown that it would be in virtually the same location for higher Mach numbers. Significantly lower Mach numbers would lead to more remote locations for the bow wave, but are considered to be unlikely for Mars in view of extensive knowledge of solar-wind properties in the vicinity of the Earth's orbit and the

prediction of solar-wind theory that M_∞ increases monotonically with increasing distance from the Sun. These theoretical calculations displayed in figure 8-14 are identical to the results presented by Spreiter et al. (1970b) for the same conditions except that (a) the direction of the solar wind has been rotated 4.5° from the Sun-Mars line to allow for the aberration effects of the motion of Mars about the Sun, in the same way as done previously by Smith (1969) in a similar-appearing plot made using a scaled-down drawing of the Earth's bow wave and magnetopause, and (b) the calculated shock-wave location has been indicated for greater distances downstream of the planet. To facilitate comparison with the magnetometer record, markers have been added to the trajectory to indicate the time at which measurements at each point were received at Earth. The times at which the trajectory crossed the calculated bow wave are indicated on the magnetometer record by the vertical dashed lines labeled shock. Their near-perfect coincidence with the times of abrupt changes in $|B|$ supports the proposition that these data do indeed provide the signature of a Martian bow wave and, since Mars almost certainly possesses an ionosphere having a ratio H/r_o of the order of .25 in its upper levels, that its existence arises from the interaction between the solar wind and the planetary ionosphere along the lines described by Spreiter et al. (1970b).

A corollary is that there is no need to postulate a planetary magnetic field to account for the observations. The value proposed by Dryer and Heckman (1967) may still be regarded as an upper limit for the strength of a dipole field, but the actual existence of such a Martian field should not be inferred from the Mariner 4 observations.

Mariners 6 and 7 subsequently approached within 2000 km of the Martian surface, but neither spacecraft carried a magnetometer, plasma probe, or energetic-particle detectors. As a result, the only observation of relevance to the present study is the confirmation of the previous determination of the ionospheric density by Mariner 4.

The data from these experiments, and also those of Mariner 5 for Venus, are of considerable significance to the present theory, however, because they demonstrate that the ionospheres of both Mars and Venus are sufficiently dense to stop the solar wind at the subsolar

point and to deflect it around the ionosphere. Since the margin in the product $\rho_\infty V_\infty^2$ is only about 6 for Mars and 10 for Venus, considering the ionospheric properties to remain fixed, the known variability of the solar wind suggests that it may be sufficiently enhanced at times to proceed directly through the ionosphere at the subsolar point and into the lower atmosphere where it would be absorbed by collisions. Under such conditions, the interaction would be quite different from that described here, and would probably tend toward that described by Spreiter et al. (1970a) for the Moon. Since such conditions can be expected to occur only occasionally, if at all, particularly if the ionospheric density and temperature are enhanced by a strong solar-wind flow, we conclude that the theory given here is both plausible and capable of providing a reasonably accurate description of the conditions that prevail most of the time at Venus and Mars.

CHAPTER IX

NUMERICAL SOLUTION OF THE EXACT EXTERIOR FLOW

All of the results presented so far in this thesis have been based on solutions of the gasdynamic equations which for large Alfvén Mach number only approximate the complete magnetohydrodynamic equations (5-1) of hydromagnetic theory. We have showed in the preceding chapter that these gasdynamic equations provide a satisfactory approximate solution for most cases, but the decoupling of the dynamic and magnetic properties which results from this simplification does represent a loss of the magnetic character of the solar-wind interaction. In the gasdynamic simplification not only do the terms representing the magnetic force in the flow equations disappear, but even the number of parameters required to characterize the flow is reduced.

For the numerical gasdynamic solution we needed to specify the Mach number and velocity direction upstream of the bow wave while for the full hydromagnetic solution, in addition to those two parameters, we must also specify the free-stream Alfvén Mach number and magnetic-field direction. However, because of the combined effects of $M_A \ll 1$ and the strong interaction nature of the flow, the dynamic terms in the momentum equation of (5-1) will dominate, and therefore, for $M_{A\infty}$ at a value of 10 or above the differences between our approximate solution and a more exact one are expected to be small. Nevertheless, as the magnetic field becomes stronger and $M_{A\infty}$ decreases, figure 8-11 shows that these differences will grow.

At the present time the general solution of equations (5-1) through (5-5) representing the fluid description of the solar-wind interaction with the planets Earth, Mars, and Venus has not yet been worked out. This solution is of considerable interest because it would express the interdependent dynamic and magnetic interaction and consequently be a more consistent fluid theory for representing these phenomena. Since equations (5-1) through (5-5) represent a more refined theory, the general solution would also provide a good check

on the accuracy and applicability of the simpler gasdynamic one already presented. Furthermore, a comparison between the exact solution based on magnetohydrodynamics and the approximate one based on gasdynamics would determine whether Dryer's (1970) suggested use of the free-stream magnetoacoustic Mach number M_∞^* in an attempt to include the effects of both M_∞ and $M_{A\infty}$ in the gasdynamic solution actually improves the accuracy of that theory.

A. Equations for Aligned Hydromagnetic Flow

In our fluid formulation the hydromagnetic equations (5-1) through (5-5) represent the flow of the solar wind past the planets Earth, Mars, and Venus. Now, instead of simplifying these equations to those of gasdynamics as we did before, we attempt to determine the general solution to them. The completely general solution is, however, still intractable at this time, but we are able to find the solution for the particular case of aligned velocity and magnetic-field vectors. Although this hydromagnetic solution is for a particular orientation of the upstream magnetic field and cannot show the effect of variation of that direction, it will demonstrate, what the approximate gasdynamic solution did not, the role that the magnetic field $\underset{\sim}{B}$ and the parameter $M_{A\infty}$ plays in determining the character of the flow downstream of the bow wave. Moreover, study of the Friedrichs, or phase and group velocity, diagrams illustrated in figure 5-1 for hydromagnetic flow with any orientation of the flow direction relative to the magnetic-field direction shows that perfect alignment of the $\underset{\sim}{V}_\infty$ and $\underset{\sim}{B}_\infty$ vectors is not essential so that qualitatively similar effects may be anticipated for other alignments as well. This solution, therefore, should be representative of the character of the general hydromagnetic solution and provide some insight to the influence that the magnetic field bears on the flow properties.

Compare the second equation of (7-4) and the expression $\frac{D}{D\tau}(\underset{\sim}{V}) = (\underset{\sim}{V}\cdot\nabla)\underset{\sim}{V}$ for the rate of change of velocity for a fluid particle in steady flow. Imai (1960) originally pointed out that the rate of change of the vectors $\underset{\sim}{B}/\rho$ and $\underset{\sim}{V}$ are given by identical

equations and concluded that if these two vectors are initially in the same direction they will remain parallel everywhere and their lengths along a given streamline will remain in the same ratio. Mathematically, this result is expressed by

$$\frac{\underset{\sim}{B}}{\rho} = \lambda(\Psi)\underset{\sim}{V}$$

or (9-1)

$$\underset{\sim}{B} = \lambda(\Psi)\,\rho\,\underset{\sim}{V}$$

where $\lambda(\Psi)$ is a constant along streamlines but can differ on different streamlines. Thus, if the velocity and magnetic-field vectors once become aligned, then they will remain aligned throughout the entire flow field, and the magnetic-field lines will coincide with the streamlines of the flow. Looking at it from a more physical viewpoint, we see that this result is just a consequence of the frozen-field property of these perfectly conducting hydromagnetic flows.

By following and extending the work of Imai (1960) and Spreiter et al. (1970a), we can derive the explicit form of the general equations for aligned hydromagnetic flow and then specialize them for our application. The conditions which $\lambda(\Psi)$ must satisfy are easily derived by substituting equations (9-1) into the third of equations (5-1) which yields the expressions $(\underset{\sim}{V}\cdot\nabla)\lambda = 0$ and $[\lambda] = 0$ requiring $\lambda(\Psi)$ to be constant along streamlines even passing through a shock wave. In our application upstream conditions are uniform, and λ is therefore a global constant. For this situation equations (5-1) and (5-3) reduce to (Spreiter et al., 1970a)

$$\nabla \cdot \rho \underset{\sim}{V} = 0$$

$$\rho(\underset{\sim}{V}\cdot\underset{\sim}{\nabla})\underset{\sim}{V} + \underset{\sim}{\nabla}p = -\frac{\lambda^2}{4\pi}\rho\underset{\sim}{V} \times \underset{\sim\sim}{\mathrm{curl}}(\rho\underset{\sim}{V}) = -\frac{\lambda^2}{4\pi}\left[\underset{\sim}{\nabla}(\rho V)^2 - \rho(\underset{\sim}{V}\cdot\underset{\sim}{\nabla})\rho\underset{\sim}{V}\right]$$

$$(\underset{\sim}{V}\cdot\underset{\sim}{\nabla})S = 0 \qquad\qquad S - S_\infty = c_v \ell n \frac{p/p_\infty}{(\rho/\rho_\infty)^\gamma} \tag{9-2}$$

$$\nabla\cdot\left[\rho\underset{\sim}{V}\left(\tfrac{1}{2}V^2+h\right)\right] = \rho(\underset{\sim}{V}\cdot\underset{\sim}{\nabla})\left(\tfrac{1}{2}V^2+h\right) = 0$$

and the discontinuity conditions (5-5) to

$$\left[\rho V_n\right] = 0$$

$$\left[\rho V_n \underset{\sim}{V} + \left(p + \frac{\lambda^2(\rho V)^2}{8\pi}\right)\hat{n} - \frac{\lambda^2\rho^2}{4\pi}V_n\underset{\sim}{V}\right] = 0 \tag{9-3}$$

$$\left[\rho V_n\left(\tfrac{1}{2}V^2 + h\right)\right] = \left[\tfrac{1}{2}V^2 + h\right] = 0$$

Equations (9-2) and (9-3) along with the auxiliary relations (5-2) and (5-4) are the equations of nondissipative aligned hydromagnetic flow which in our fluid theory represents solar-wind flow with parallel velocity and magnetic fields. They show that aligned flow past any of the boundary shapes for either the Earth, Mars, or Venus illustrated in figure 6-6 is axisymmetric about a line through the center of the planet and parallel to the direction of the solar wind. This is so because the azimuthal components of all the terms vanish identically for flows that are uniform at infinity and disturbed only by an obstacle that is axisymmetric about a line parallel to the direction of flow in the undisturbed stream. Nonaligned flows past

these planets are not axisymmetric, however, because the azimuthal components of the magnetic terms in equations (5-1) and (5-5) are, in general, not zero. In the latter case, nevertheless, mirror symmetry still remains about the plane through the center of the planet that contains the $\underset{\sim}{V}_\infty$ and $\underset{\sim}{B}_\infty$ vectors.

Since $(\underset{\sim}{V}\cdot\underset{\sim}{\nabla})S = 0$ indicates that entropy is constant along a streamline, except where derivatives cease to exist as at a shock wave, and $S = S_\infty$ far upstream of the shock, the flow is isentropic until the shock wave is crossed. Equations (9-2) show that $\frac{1}{2}V^2 + h$ is also a constant along a streamline equal to $\frac{1}{2}V_\infty^2 + h_\infty = h_{st}$ where subscript st refers to conditions at a stagnation point anywhere in the isentropic part of the flow field. Since equations (9-3) show, in addition, that $\frac{1}{2}V^2 + h$ is conserved across a shock wave in aligned flow, h_{st} is an absolute constant throughout the entire flow field. We should note that the constancy of h_{st} everywhere in aligned flow also holds in the corresponding gasdynamic flow. This equivalence results because the Lorentz force $\underset{\sim}{B}\times\underset{\sim}{\text{curl}}\,\underset{\sim}{B}$ is everywhere normal to the streamlines in aligned flow, and hence the energy equation (5-3) reduces to that of gasdynamics. Moreover, the continuity and energy equations of (9-2) are in fact exactly equivalent to those corresponding equations (7-1) of gasdynamics. Equations (9-2) actually differ from the gasdynamic equations (7-1) only by the Lorentz-force term standing on the right-hand side of the momentum equation. A corresponding examination of equations (9-3) and (7-2) reveals a similar comparison for the discontinuity relations.

However, the numerical solution to equations (9-2) and (9-3) remains formidable because of their nonlinear nature and complicated regions of mixed elliptic, parabolic, and hyperbolic character. Furthermore, the partial derivatives representing the Lorentz force in the momentum equation prevents making direct use of any of the vast amount of work already carried out in developing the two gasdynamic computer programs described in chapter VII because their finite-difference schemes approximate the gasdynamic momentum equation and do not correspond to the momentum equation for aligned flow. Consequently, to compute the solution of equations (9-2) and (9-3) we would

have to begin anew and develop entirely different programs for which extensive analyses of the stability and convergence would have to be carried out in much the same way as was done for the gasdynamic programs in chapter VII. The magnitude of such a task is formidable.

This problem is very much simplified, however, by introducing a transformation of the flow properties which reduces the aligned-hydromagnetic-flow equations to those of gasdynamics for a fictitious gas obeying a peculiar equation of state. This reduction of the aligned-flow equations to those of gasdynamics has been known for sometime (Cowley, 1960). For example, the details of this correspondence has been worked out for the case of two-dimensional flow by Grad (1960) for linearized motion, by Imai (1960) and Iuriev (1960) for irrotational motion, and more recently Spreiter et al. (1970a) have developed the transformation for axisymmetric, shock-free rotational flow. In our application we have extended this concept and developed the transformation for more general aligned flow which admits shock waves in the flow region.

For our purposes, then, a mathematical transformation of the aligned-flow properties is introduced, and the resulting transformed variables are defined as pseudoproperties, indicated by $*$ and related to the actual physical properties by the transformation equations

$$\underset{\sim}{V}^* = \underset{\sim}{V}\left(1 - \frac{\lambda^2\rho}{4\pi}\right)$$

$$\rho^* = \rho\left(1 - \frac{\lambda^2\rho}{4\pi}\right)^{-1} \tag{9-4}$$

$$p^* = p + B^2/8\pi$$

$$h^* = h + (\lambda^2\rho V^2/4\pi)(1 - \lambda^2\rho/4\pi)$$

$$s^* = s$$

From equations (5-4) and the definition for λ given by equations (9-1) we easily derive

$$\frac{\lambda^2 \rho}{4\pi} = \frac{1}{M_A^2} = \frac{\rho}{\rho_\infty M_{A\infty}^2} \tag{9-5}$$

Substitution of equations (9-4) into the aligned-flow equations (9-2) and (9-3) yields

$$\begin{aligned} \underset{\sim}{\nabla} \cdot \rho^* \underset{\sim}{V}^* &= 0 \\ \rho^* (\underset{\sim}{V}^* \cdot \underset{\sim}{\nabla}) \underset{\sim}{V}^* + \underset{\sim}{\nabla} p^* &= 0 \\ (\underset{\sim}{V}^* \cdot \underset{\sim}{\nabla}) S^* &= 0 \\ \underset{\sim}{\nabla} \cdot \left[\rho^* \underset{\sim}{V}^* (\tfrac{1}{2} V^{*2} + h^*) \right] = \rho^* (\underset{\sim}{V}^* \cdot \underset{\sim}{\nabla}) (\tfrac{1}{2} V^{*2} + h^*) &= 0 \end{aligned} \tag{9-6}$$

and the discontinuity relations

$$\begin{aligned} \left[\rho^* V_n^* \right] &= 0 \\ \left[\rho^* V_n^* \underset{\sim}{V}^* + p^* \hat{n} \right] &= 0 \\ \left[\tfrac{1}{2} V^{*2} + h^* \right] &= 0 \end{aligned} \tag{9-7}$$

which are identical in form to the equations of ordinary gasdynamics. The definition of $\underset{\sim}{V}^*$ and h^* shows that $h^*_{st} = \frac{1}{2}V^{*2} + h^* = \frac{1}{2}V^2 + h = h_{st}$ which for uniform upstream conditions is constant everywhere and is the integrated form of the pseudoenergy equation.

An equation of state relating the variables ρ^*, p^*, and S^* is needed to complete the system of equations (9-6) and (9-7). Although the equation of state relating p, ρ, and S is the same as in ordinary gasdynamics for a perfect gas, the corresponding relation between p^*, ρ^*, and S^* is substantially different. Explicitly equations (7-1) show that

$$p = \frac{p_\infty}{\rho_\infty}\rho^\gamma \exp\left[(S - S_\infty)/c_v\right] \tag{9-8}$$

The derivation of the corresponding relation for the pseudovariables begins by using equations (9-1) to eliminate $B^2/8\pi$ from the definition of p^* given in equation (9-4) and by introducing the enthalpy in place of V through the relation $h + \frac{1}{2}V^2 = h_{st}$ = constant. There thus results

$$p^* = p + \lambda^2\rho^2(h_{st} - h)/4\pi = p + \rho^2(h_{st} - h)/\rho_\infty M_{A\infty} \tag{9-9}$$

in which the stagnation enthalpy $h_{st} = \frac{1}{2}V_\infty^2 + c_pT_\infty$ is given by

$$h_{st} = \frac{1}{2}V_\infty^2 + \frac{\gamma}{\gamma-1}\cdot\frac{p_\infty}{\rho_\infty} = V_\infty^2\left[\frac{1}{2} + \frac{1}{(\gamma-1)M_\infty^2}\right] \tag{9-10}$$

Substituting $h = \frac{\gamma}{\gamma-1}\frac{p}{\rho}$ and equation (9-8) into equation (9-9) and rearranging, we finally express p^* in terms of density ρ and pseudoentropy S^* by

$$p^*(\rho, S^*) = \left(1 - \frac{\gamma}{\gamma-1}\frac{\rho}{\rho_\infty M_{A\infty}}\right) p_\infty \left(\frac{\rho}{\rho_\infty}\right)^\gamma \exp\left(\frac{S-S_\infty}{c_v}\right) + \frac{h_{st}\,\rho^2}{\rho_\infty M_{A\infty}^2} \tag{9-11}$$

valid for $0 < \rho \leq \rho_{max}$ where the upper limit

$$\rho_{max} = \left\{\frac{\frac{\gamma-1}{2}M_\infty^2 + 1}{\exp\left(\frac{S^*-S_\infty^*}{c_v}\right)}\right\}\rho_\infty$$

arises from the substitution into equation (9-9) of $V^2 = 2(h_{st} - h)$ $= 2\left(h_{st} - \frac{\gamma}{\gamma-1}\frac{p}{\rho}\right) \geq 0$. From equation (9-11) we can proceed to obtain the desired relation between p^* , ρ^* , and S^* by using equation (9-10) and the following relation derived from equation (9-4) to express ρ in terms of ρ^* :

$$\rho = \rho^*\left(1 + \frac{\lambda^2\rho^*}{4\pi}\right)^{-1} = \rho^*\left(1 + \frac{\rho^*}{\rho_\infty M_{A\infty}^2}\right)^{-1} \tag{9-12}$$

Thus the correspondence between the aligned-flow equations and those of gasdynamics for a hypothetical gas obeying an unusual equation of state is complete. A significant advantage results from applying these equations because now the partial differential equations (9-6) for the pseudogas are exactly equivalent to those of gasdynamics, and therefore we can make use of much of the numerical analysis and program development that has been carried out for gasdynamic applications.

What these transformation equations (9-4) have accomplished, in effect, is to absorb the Lorentz-force term of equations (9-2) into the inertial and pressure-gradient terms while leaving the form of the continuity and energy equations unchanged. However, this simplification of the momentum equation by the effective elimination of the Lorentz force comes at the expense of a more complicated equation of state. Nevertheless, the net result remains a significant advantage because we have reduced the number of partial derivatives which must be approximated by finite-difference expressions while only increasing the complexity of an alegebraic equation which is simply used in an auxiliary step to relate flow variables.

B. Adaptation for Numerical Solution

Once the foregoing transformation is introduced and the aligned-flow equations (9-2) and (9-3) are reduced to the gasdynamic equations (9-6) and (9-7) for a pseudogas obeying the equation of state $p^* = p^*(\rho^*, S^*)$, the two computer programs described in chapter VII and originally designed for gasdynamics can be modified to the flow field for aligned hydromagnetic flow. We have indicated in the foregoing section that the basic numerical approach (inverse iteration method for the subsonic region and method of characteristics for the supersonic region) as well as the finite-difference schemes all remain intact, the only changes required are to the auxiliary relations derived from the properties of the pseudogas. Thus, the explicit forms of the auxiliary equations which are used in each of the two computer programs must now be derived.

1. Inverse iteration method

For the inverse iteration program which computes the flow in the subsonic region, the dependent pseudovariables are the two pseudovelocity components u^* , v^* along with the pseudo pressure and density p^* and ρ^* . In precisely the same way as outlined in chapter VII, the derivation of the alternate form of the pseudoenergy equation

$$(\underset{\sim}{V}^* \cdot \underset{\sim}{\nabla})\, p^* - a^{*2}(\underset{\sim}{V}^* \cdot \underset{\sim}{\nabla})\, \rho^* = 0 \tag{9-13}$$

follows from the constancy $(\underset{\sim}{V}^* \cdot \underset{\sim}{\nabla})S^* = 0$ of pseudoentropy along streamlines and the definition of the pseudosound speed

$$a^{*2}(\rho^*, p^*) = \left(\frac{\partial p^*}{\partial \rho^*}\right)_{S^*} \tag{9-14}$$

By performing the indicated differentiation of expression (9-14) on equation (9-11) by means of the chain rule and equation (9-12), we obtain

$$a^{*2}(\rho^*, p^*) = \left[\left(\frac{1}{\rho^*} + \frac{2}{\rho_\infty M_{A_\infty}^2}\left(\frac{\gamma-2}{\gamma-1}\right) - \left(\frac{\gamma-5}{\gamma-1}\right)\frac{\rho^*}{\rho_\infty M_{A\infty}^2} - \frac{2}{\gamma-1}\,\frac{\rho^{*2}}{(\rho_\infty M_{A\infty}^2)^3}\right)\gamma p^* + \right. \tag{9-15}$$

$$\left. \frac{h_{st}}{\rho_\infty M_{A\infty}^2}\left((2-\gamma)\rho^* - \frac{2}{\rho_\infty M_{A\infty}^2}\rho^{*2}\right)\right]\left[\left(1 + \frac{\rho^*}{\rho_\infty M_{A\infty}^2}\right)^3\left(1 - \frac{\rho^*}{(\gamma-1)\rho_\infty M_{A\infty}^2}\right)\right]^{-1}$$

or, equivalently, by a similar operation on the definition of p^* given in equations (9-4) we obtain

$$a^{*2} = \left(1 - \frac{1}{M_A^2}\right)^2\left[a^2\left(1 - \frac{1}{M_A^2}\right) + A^2\right] \tag{9-16}$$

where $a = \left(\frac{\partial p}{\partial \rho}\right)^{1/2}$ is the actual speed of sound and $A = \left(\frac{B^2}{4\pi\rho}\right)^{1/2}$ is the Alfvén speed of sound. Therefore, the continuity equation and the two components of the momentum equation from equations (9-6)

together with the energy expression in the form of equation (9-13) supplemented by the auxiliary relation $a^* = a^*(\rho^*, p^*)$ provide the four partial differential equations required to determine the four unknowns u^*, v^*, p^*, and ρ^*. In this form we see that the pseudogas transformation has in effect transported the Lorentz force from the momentum equation to the energy equation (9-13) through the influence of the auxiliary relation for a^*.

Although it is not intrinsically required for the numerical solution of these equations, an explicit form for $h^* = h^*(\rho^*, p^*)$ can also be derived from the definition $h^* = h + \frac{\lambda^2 V^2 \rho}{4\pi}\left(1 - \frac{\lambda^2 \rho}{8\pi}\right)$ of h^* or, from what is easily derived from that by use of equations (9-5), $h^* = h + A^2\left(1 - \frac{1}{2M_A^2}\right)$. In a manner similar to the derivation of p^*, we replace V by means of the relation $h + \frac{1}{2}V^2 = h_{st}$ = constant, h by its calorically perfect form $\frac{\gamma}{\gamma-1}\frac{p}{\rho}$, and ρ by equation (9-12), and after considerable rearranging, obtain

$$h^*(\rho^*, p^*) = \left[\frac{\gamma}{\gamma-1}\frac{p^*}{\rho^*} - \frac{h_{st}}{1 + \frac{\rho^*}{\rho_\infty M_{A\infty}^2}}\right]\left[1 - \frac{1}{\gamma-1}\frac{\rho^*}{\rho_\infty M_{A\infty}^2}\right]^{-1} + h_{st} \tag{9-17}$$

It should also be pointed out now that the conservation of entropy S along streamlines and of stagnation or total enthalpy h_{st} everywhere in the aligned flow carries over and is maintained for the pseudoentropy S^* and pseudo total enthalpy h_{st}^* in the pseudogas flow. This is an important result because the internal consistency checks built into the computer program of Lomax and Inouye (1964) will remain valid independent checks on the accuracy of the computed solution of the pseudogas. Furthermore, since $\underset{\sim}{V}^*$ and $\underset{\sim}{V}$ are parallel vectors, the streamlines for both flows will coincide, and similarly the definition of the stream function $\psi = \int \bar{r}(\rho u\, dx - \rho v\, d\bar{r}) = \int \bar{r}(\rho^* u^*\, dx - \rho^* v^*\, d\bar{r})$ is equivalent for both flows. In this way the criterion of ψ vanishing, which is used to determine the calculated body shape in the subsonic region, can still be maintained.

2. Method of characteristics.

This close equivalence between the actual aligned flow and the pseudogas also extends into the supersonic region of flow where the pseudo Mach number M^* has a value greater than unity. The relation between the pseudo Mach number and the two Mach numbers M and M_A of the aligned hydromagnetic flow is derived from the definition $M^* = \frac{V^*}{a^*}$ and equation (9-16) and rearranged into the form

$$M^{*2} = \frac{M^2 M_A^2}{M^2 + M_A^2 - 1} \tag{9-18}$$

From this relation we can readily see that when $M = 1$ M^* also has a value of unity, and consequently the sonic line and transition region from subsonic to supersonic flow coincide for both these flows (see next section for further discussion about this transition). Because of this equivalence we can use the method-of-characteristics program to compute the pseudoflow in the supersonic region.

Since the flow equations (9-6) for the pseudogas are exactly the same as ordinary gasdynamics, the equation derived from them and applicable along characteristic lines is exactly equivalent to the corresponding equations (7-22) for ordinary gasdynamics although the shape and location of the characteristic lines will be different. To compute the pseudoflow by use of the present characteristic program, in addition to the pseudoenergy equation in integrated form $\frac{1}{2}V^{*2} + h^* = h_{st} = \text{constant}$, and the constancy of pseudoentropy S^* along streamlines, an auxiliary equation $h^* = h^*(p^*, S^*)$ is required to complete the mathematical description. This relation, however, cannot be obtained in explicit form from the relation $h^* = h^*(\rho^*, S^*)$ because the equation of state $p^* = p^*(\rho^*, S^*)$ cannot be inverted analytically to yield $\rho^* = \rho^*(p^*, S^*)$. This finding causes no difficulty, however, because given numerical values for p^* and S^* in the computer algorithm, it is a simple matter to compute the corresponding value for ρ^* from equations

(9-11) and (9-12) by a standard root-finding technique. Then with $h^* = h^*(p^*, S^*)$ effectively determined, the mathematical description for the pseudogas corresponds exactly to that for gasdynamics and has precisely the form required for the method-of-characteristics computer program. Furthermore, since $\rho \underset{\sim}{V} = \rho^* \underset{\sim}{V}^*$, the independent mass-balance check on the accuracy of this program is still maintained.

Although the discontinuity conditions (9-7) relating pseudogas properties across a shock wave have exactly the same form as those of gasdynamics, they do not reduce to the simplified relations of ordinary gasdynamics for a perfect gas because of the unusual pseudo equation of state. This result stems from the fact that even though the aligned hydromagnetic flow is a perfect gas, the bow wave in that flow is a fast hydromagnetic shock wave and not a gasdynamic one. Therefore, because both of the above numerical programs require explicit equations relating the flow conditions across the shock wave, the discontinuity relations (9-7) for the pseudogas must be expressed in such a way that the pseudoflow variables u_1^*, v_1^*, ρ_1^*, and p_1^* on the downstream side of the shock wave can be determined from the conditions u_∞^*, v_∞^*, ρ_∞^* and p_∞^* upstream. For this purpose the four equations of the discontinuity conditions (9-7) together with equation (9-17) provide a determinate system to calculate the five downstream unknowns u_1^*, v_1^*, ρ_1^*, p_1^*, and h_1^*. By combining equations (9-7) and (9-17) and rearranging, we form the more convenient expressions

$$(\rho_1^* - \rho_\infty^*)\left[b_3\left(\frac{\rho_1^*}{\rho_\infty^*}\right)^3 + b_2\left(\frac{\rho_1^*}{\rho_\infty^*}\right)^2 + b_1\left(\frac{\rho_1^*}{\rho_\infty^*}\right) + b_0\right] = 0$$

$$p_1^* = p_\infty^* + \rho_\infty^* V_{n\infty}^{*2} - (\rho_\infty^* V_{n\infty}^*)^2/\rho_1^* \qquad (9\text{-}19)$$

$$V_{n_1}^* = V_{n\infty}^*/\rho_1^*$$

$$V_{t_1}^* = V_{t\infty}^*$$

where

$$b_3 = -\frac{1}{2(\gamma-1)(M_{A\infty}^2-1)^2}\left(\frac{V_{t\infty}^*}{V_\infty^*}\right)^2$$

$$b_2 = \frac{1}{2(M_{A\infty}^2-1)}\left[1 - \frac{1}{\gamma-1}\left(1 + \frac{1}{M_{A\infty}^2-1}\right)\right]\left(\frac{V_{t\infty}^*}{V_\infty^*}\right)^2 \tag{9-20}$$

$$b_1 = \frac{\left(1+\frac{1}{2}\gamma\right)}{(\gamma-1)(M_{A\infty}^2-1)}\left(\frac{V_{n\infty}^*}{V_\infty^*}\right)^2 - \left[\frac{\gamma}{\gamma-1}\frac{p_\infty^*}{\rho_\infty^* V_\infty^{*2}} - \left(\frac{V_{n\infty}^*}{V_\infty^*}\right)^2\right]$$

$$b_0 = \left(\frac{\gamma}{\gamma-1} - \frac{1}{2}\right)\left(\frac{V_{n\infty}^*}{V_\infty^*}\right)^2$$

The first equation of (9-19) is a quartic in ρ_1^* which can be solved numerically if the upstream conditions and shock angle are specified. Once ρ_1^* is determined, then p_1^* and $\underset{\sim}{V}_1^*$ are easily calculated from the remaining three equations of (9-19). This quartic equation in ρ_1^* has four roots, the trivial solution $\rho_1^* = \rho_\infty^*$ and three others which must be determined by numerically solving the remaining cubic equation for ρ_1^*. Over the range of values for parameters $V_{n\infty}^*$, $V_{t\infty}^*$, p_∞^*, and $M_{A\infty}$ in our application, we found the solution of this cubic to consist of one real and two complex conjugate roots. Since equations (5-14) state that a hydromagnetic shock wave must satisfy the condition $\frac{1}{\rho_1} < \frac{1}{\rho_\infty}$, we find that the nontrivial real root is the physically relevant solution. With ρ_1^* determined, the calculation of the remaining downstream properties follows directly from equations (9-19).

3. Identification of flow regimes

In the preceding paragraphs we have shown that except for the equation of state the analogy between the pseudogas equations and those of gasdynamics is exact. However, if we expect to solve these pseudogas equations by use of the inverse-iteration and method-of-

characteristic computer programs, then the character of these equations must also correspond, that is, the pseudogas equations must be elliptic in the subsonic region and hyperbolic in the supersonic one.

The approach to gasdynamics as $\underset{\sim}{B}_\infty \to 0$ and hence $M_{A\infty} \to \infty$ is clearly evident from equations (9-4), (9-5), (9-15), and (9-18). But although the mathematical analog holds for all M_A, it becomes less suitable when $\underset{\sim}{B}_\infty$ increases and $M_A < 1$ since ρ^* then becomes negative and the two velocity vectors $\underset{\sim}{V}^*$ and $\underset{\sim}{V}$ are of opposite sign. As in the corresponding gasdynamic case, an examination of the local pseudo Mach number M^* indicates the character of the pseudogas equations and in turn the aligned hydromagnetic equations also. From an investigation of equations (9-18) we determine the following relationship between the actual Mach number M and the pseudo one M^* :

$$\text{if } M_A > 1 \text{ then } M \gtrless 1 \text{ implies } M^* \gtrless 1 \qquad (9\text{-}21)$$

and $M^* = 1$ for all M when $M_A = 1$. Thus for $M_A > 1$ throughout the flow field the aligned hydromagnetic equations are elliptic in the subsonic flow region and hyperbolic in the supersonic region. This situation corresponds exactly to that for ordinary gasdynamics, and therefore the application of our two computer programs to the fictitious flow is possible. A closer inspection of equations (9-18) reveals, however, some unusual behavior when $M_A < 1$ and consequently when ρ^* becomes negative and $\underset{\sim}{V}^*$ has the opposite sign of $\underset{\sim}{V}$. For the case when both $M_A < 1$ and $M < 1$, equation (9-18) shows that $M^* > 1$ when $M^2 + M_A^2 > 1$ and $M^{*2} < 0$ when $M^2 + M_A^2 < 1$. The first of these results indicates that even though the aligned hydromagnetic flow is subsonic and subAlfvénic, the flow equations are hyperbolic when $M^2 + M_A^2 > 1$ while the latter indicates that the wave speed becomes imaginary and the equations are elliptic when $M^2 + M_A^2 < 1$! For the case when $M^2 + M_A^2 > 1$, subsonic aligned hydromagnetic flow is related to supersonic ordinary gasdynamic flow in the opposite direction. As indicated by the Friedrichs diagrams

in figure 6-2, hydromagnetic disturbances would then propagate along upstream rather than downstream characteristics, and slow hydromagnetic shock waves would extend upstream from the body rather than downstream as in ordinary gasdynamics. For $M_A < 1$ and $M > 1$ ρ^* is negative, $\underset{\sim}{V}^*$ has the opposite sign of $\underset{\sim}{V}$, and supersonic aligned hydromagnetic flow is related to subsonic ordinary gasdynamic flow in the opposite direction past a similar body. With this peculiar behavior we cannot expect our numerical programs which were designed for ordinary gasdynamics to successfully compute the pseudogas flow. Nevertheless, some applications for $M_A < 1$ flows past obstacles have been carried out by Seebass (1961), Tamada (1964), Geffen (1965, 1966) and others.

This behavior of M^* is illustrated in figure 9-1 which shows the range of values for M^* for various pairs of values for M and M_A. Also included in that figure is an isentrope (dashed line) indicating variation of M_A as a function of M along a streamline. The explicit form of that function is given by the expression

$$\frac{M_A}{M_{A\infty}} = \left[\frac{(M^2 + \frac{2}{\gamma-1})}{2 h_{st} M_\infty^2} V_\infty^2 \exp\left(-\frac{S-S_\infty}{c_v}\right)\right]^{\frac{1}{2(\gamma-1)}} \qquad (9\text{-}22)$$

derived from the definition of Mach number M, equations (9-5) and (9-8), and the relation $\frac{1}{2}V^2 + h = h_{st}$. From this equation it is clearly evident that along a given streamline M_A is a monotonically increasing function of M. Since entropy reaches a maximum value and M a minimum value at the stagnation point, equation (9-22) indicates that M_A also reaches its minimum value $M_{A\min}$ there. The value of $M_{A\min}$, which depends on M_∞ and $M_{A\infty}$, therefore, determines whether the condition $M_A \leq 1$ will occur in any region of the flow. For example, as illustrated in figure 9-1 if $M_{A\min} \geq 1$ then both M_A and M^* increase monotonically from the stagnation point to the free stream along the stagnation streamline just as for

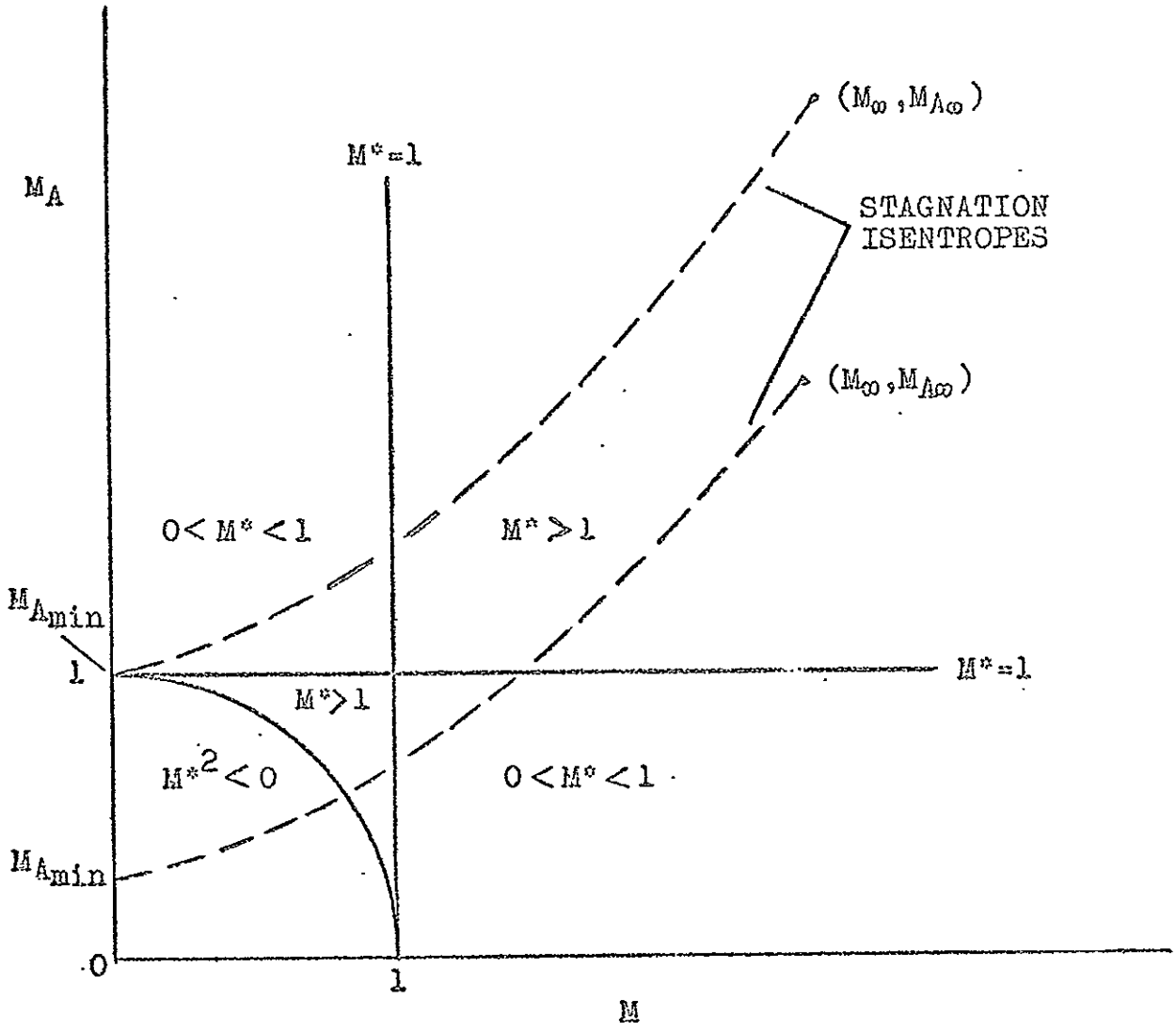

Figure 9-1. Variation of M^* for various ranges of values for M and M_A . The isentropes display the behavior of M_A as a function of M according to equation (9-21) along the stagnation streamline.

ordinary gasdynamics, and M_A never becomes less than unity at any point in the flow field. On the other hand if $M_{A_{min}} < 1$, M_A still increases monotonically, but M^* varies in a complicated manner: it is imaginary at the stagnation point, then decreases to $-\infty$, jumps up to $+\infty$, and then decreases down to a minimum which is less than 1 , and finally increases monotonically up to the free-stream value. The condition, then, that M^* increases monotonically and that the pseudogas equations have the same character as those of ordinary gasdynamics is easily determined from equations (9-5) to be

$$M_{A\infty}^2 \geq \rho_{st}/\rho_\infty \tag{9-23}$$

which for hypersonic flow would usually be satisfied if $M_{A\infty} > 2$. If condition (9-23) is satisfied, then both the supersonic and subsonic regions of the pseudogas flow will correspond directly with those of ordinary gasdynamic flow, and therefore the inverse-iteration-method and method-of-characteristics computer programs will be suitable for computation of the pseudoflow.

Actually, difficulties arise even before the free-stream Alfvén Mach number $M_{A\infty}$ reaches its lower limit. An examination of equation (9-15) for a^* and (9-17) for h^* reveals that when input values for $M_{A\infty}$ become lower than about $\sqrt{10}$, the denominators of both these equations vanish at some point in the flow field, and both a^* and h^* would be infinite at that point unless the numerators also vanish simultaneously. If the critical values for the flow properties at this point are designated by the subscript cr , we see from the denominators of those equations that $\rho_{cr}^* = (\gamma - 1) M_{A\infty}^2 \rho_\infty$ or equivalently after use of equation (9-12) that $\rho_{cr} = (\gamma-1)/\gamma\, M_{A\infty}^2 \rho_\infty$. A similar analysis of the numerators yields $p_{cr}^* = h_{st}(\gamma-1)/\gamma)^2 M_{A\infty}^2 \rho_\infty$, and they also vanish. Both quantities a^* and h^* , then, are of indeterminate form at this point. This situation actually stems from the fact that if the pseudoentropy S^* is considered as a surface described by equations

(9-11) and (9-12) over the $p^*-\rho^*$ plane, then S^*_{cr} is multivalued at the critical point p^*_{cr}, ρ^*_{cr}. However, an analysis of the limit process for these equations shows that as the point p^*_{cr}, ρ^*_{cr} is approached in the $p^*-\rho^*$ plane, a continuous and finite limit for S^*_{cr} which depends on the direction of approach to that point is also reached, and in addition, that the indeterminate form of equations (9-15) and (9-17) actually leads to a continuous finite value for a^* and h^* at the critical point. Some limit values for S^*_{cr} corresponding to certain approach directions in the $p^*-\rho^*$ plane, however, are not physically realistic and incite the growth of instabilities in the numerical computation of the flow field. To control the instability we have developed an algorithm that restricts the path of approach to the critical point to only those that lead to a physically realistic limit for S^*_{cr} and were able to get sufficiently smooth values for S^*, a^*, and h^* in the vicinity of the critical point so that the computation scheme was stable.

Even with these added procedures the lowest value of $M_{A\infty}$ for which we could compute an accurate solution was for $M_{A\infty} = 2.5$ Uncontrollable numerical instabilities associated with the $\dagger$ coordinate line becoming duly inclined and consequent deterioration of accuracy as indicated by the consistency checks on the conservation of S^* and $h^*_{S\dagger}$ as well as increasing discrepancy between the calculated and desired body shape prevented solutions being computed for lower $M_{A\infty}$. In fact in retrospect it appears rather remarkable that even for values of $M_{A\infty}$ of 2.5 and higher, the shock-shape equation (7-21) which produced ellipsoidal body shapes to a high degree of accuracy for gasdynamic flow of a perfect gas also produces similar body shapes to the same accuracy for aligned hydromagnetic flow.

CHAPTER X

FEATURES OF THE EXACT SOLUTION

We have shown in the last chapter that with the introduction of the pseudogas transformation the equations for aligned hydromagnetic flow can be reduced to those of gasdynamics supplemented by an unusual equation of state. Once the required auxiliary relations derived from the pseudo equation of state have been determined and written into the inverse iteration and method of characteristics computer programs, all that remains is the specification of the input parameters M_∞ and $M_{A\infty}$, and then the solution to the pseudogas equations (9-6) and (9-7) can be computed. It is then a simple matter to invert the transformation equations (9-4) and convert the pseudoflow properties back to the actual aligned-flow properties which satisfy equations (9-2) and (9-3). As discussed before this solution now depends on the two input parameters M_∞ and $M_{A\infty}$, instead of the single parameter M_∞ as was the case in the gasdynamic theory. Thus, once we specify $M_{A\infty} \geq 2.5$ and $M_\infty >> 1$, we can compute the hydromagnetic solution to equations (9-2) and (9-3), and therefore determine what effect variation of the parameters $M_{A\infty}$ and M_∞, representing different conditions in the oncoming flow, has on the aligned-flow properties. And even though this investigation is based on the solution to the aligned hydromagnetic flow equations, study of the Friedrichs diagrams suggests that qualitatively similar effects may be anticipated for other alignments as well.

A. Broad Features of the Aligned-Flow Solution

Together with the input Mach numbers, we must also specify an axisymmetric planetary boundary. For all the calculations presented in this chapter, we have chosen to compute these hydromagnetic solutions for aligned-flow interaction with the magnetosphere boundary of the Earth partly because of the interest in and enormous amount of data

measured in near-Earth space, but mainly because application of the correspondence rule quickly converts any of the properties of the flow around the Earth's magnetosphere into those for flow around the ionosphere of either Mars or Venus by a simple relabeling of the coordinate axes. Using the magnetopause shape illustrated in figure 6-6 for the magnetosphere boundary, we have computed aligned-flow solutions for various sets of input Mach number M_∞ and Alfvén Mach number $M_{A\infty}$ in the range $5 \leq M_\infty \leq 20$ and $2.5 \leq M_{A\infty} \leq 20$. A comparison of the different solutions obtained for differing values of input Alfvén Mach number $M_{A\infty}$ but the same value of Mach number M_∞ immediately reveals qualitative variations in these solutions. The most apparent distinction noticed among these solutions for differing values of $M_{A\infty}$ is the large diversity in the shapes and locations of the fast hydromagnetic shock wave that forms upstream of the planet. To illustrate this effect we have plotted in figure 10-1 the calculated bow-wave positions derived in the computed solutions for aligned hydromagnetic flow using values for $M_{A\infty}$ of 2.5, 3, 5, 10, and 20 but while maintaining $\gamma = 5/3$ and the Mach number M_∞ constant at a value of 10, which is representative of normal conditions in the solar wind. For ease of comparison the corresponding bow-wave position determined by using $M_\infty = 10$ in the approximate gasdynamic theory described in chapter VII is also included in figure 10-1. Easily noticed in this figure is the trend that as $M_{A\infty}$ decreases the position of the bow wave for aligned flow further departs from that for the gasdynamic bow wave. The departure is such that as $M_{A\infty}$ diminishes the hydromagnetic shock-wave location becomes closer to the magnetosphere boundary in the nose region than does the gasdynamic one but moves substantially further away from the magnetosphere tail downstream from the Earth. The nature of this variation in bow-wave position as $M_{A\infty}$ decreases is almost as if the bow wave were rotated counterclockwise about the point of intersection of all the bow waves illustrated in figure 10-1. No particular significance, however, is attributed to this point. For $M_{A\infty} = 20$ the hydromagnetic and gasdynamic shock waves nearly coincide, and the approach to gasdynamics as $M_{A\infty}$ further increases is clearly

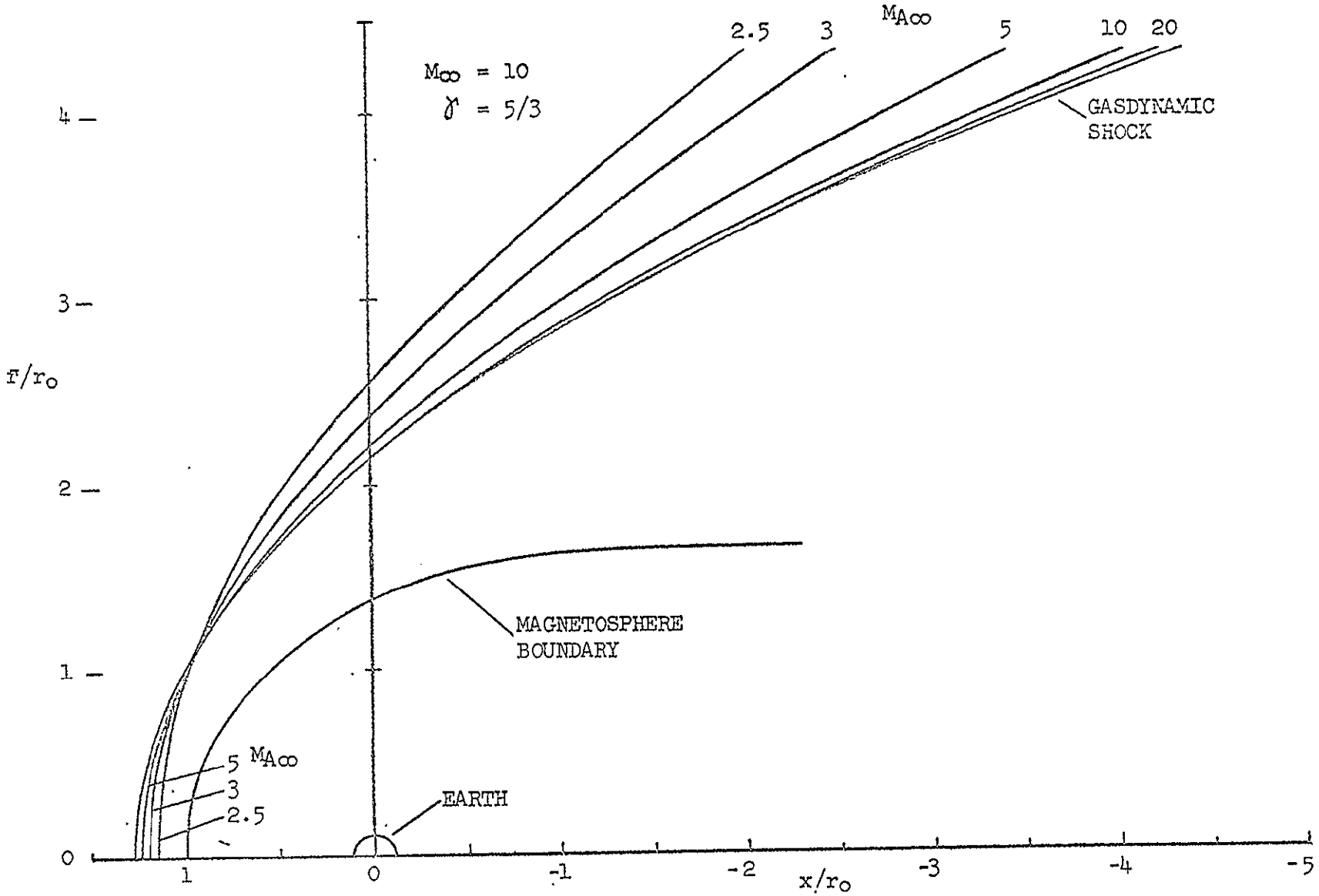

Figure 10-1. Various calculated positions of the hydromagnetic bow wave which develops in aligned flow upstream of the Earth's magnetosphere for several $M_{A\infty}$, $M_\infty = 10$, and $\gamma = 5/3$. The corresponding bow wave determined by gasdynamic theory is included for purposes of comparison.

evident.

This migration of the hydromagnetic bow wave from the position of the gasdynamic bow wave as $M_{A\infty}$ decreases can be understood by comparing the relative values for the pseudosound speed a^* in the hydromagnetic solution and the speed of sound a in the gasdynamic one. Such a comparison was carried out, and it revealed that throughout the flow a^* was greater than a except in the nose region of the magnetosphere where a^* was less than a . These relative differences become greater as $M_{A\infty}$ diminished. Since the pseudovelocity V^* and the gasdynamic velocity V are also about the same magnitude, the higher value of a^* means that infinitesimal disturbances in all regions of the aligned flow except near the nose of the magnetosphere travel faster, relative to the flow speed V^* , than do similar disturbances in gasdynamic flow and, consequently, propagate further upstream in a given time interval before coalescing into the bow wave. Conversely, in the nose region of the magnetosphere the lower value of a^* indicates that these disturbances travel slower relative to V^* than do corresponding ones in gasdynamics and, therefore, do not propagate as far before coalescing into the bow wave. As $M_{A\infty}$ diminishes, this propagation effect increases, and in this way the aligned hydromagnetic shock wave reaches the positions illustrated in figure 10-1 for the various values of $M_{A\infty}$.

In relation to the magnetopause the position of the hydromagnetic bow wave in the nose region is best characterized by the standoff distance defined as the distance along the axis of symmetry between the magnetopause and bow wave. Not only does figure 10-1 distinctly show that this distance diminishes with decreasing $M_{A\infty}$ but also the numerical calculations indicate that the extent of the subsonic-flow region likewise contracts with a diminution of $M_{A\infty}$ We should point out that a decrease in $M_{A\infty}$ has just the opposite effect as does a corresponding decrease in the Mach number M_∞ in ordinary gasdynamic flow. However, this behavior connected with diminishing $M_{A\infty}$ actually aided the stability of the computation scheme because a decrease in the standoff distance means fewer steps in the marching technique and a shrinking subsonic region aided

control of the associated numerical difficulties in the neighboring transonic region.

All of the hydromagnetic shock-wave shapes presented in figure 10-1 have been computed for varying values of input parameter $M_{A\infty}$ while holding the other input parameter M_∞ fixed at a constant value. The combination of the definition of Mach number and the calorically perfect relation for internal energy e leads to the equation

$$M_\infty = \frac{V_\infty}{a_\infty} = \left(\frac{V_\infty^2}{\frac{\gamma R T}{\bar{m}}}\right)^{1/2} = \left(\frac{V_\infty^2}{\gamma(\gamma-1)e_\infty}\right)^{1/2}$$

which indicates that the square of the Mach number expresses the ratio of the directed energy to the internal energy. Thus, the free-stream Mach number specifies the relative gasdynamic energy in the fluid of the oncoming flow but not its magnetic energy. Heretofore, in gasdynamic theory the shock-wave position for a given magnetopause shape was solely determined by the free-stream Mach number M_∞, which in turn is set by the values of V_∞ and T_∞. Figure 10-1 shows that for $M_{A\infty} > 10$ this is still true for hydromagnetic shock waves. However, since for $M_{A\infty} < 10$ this figure indicates that the observed variation in bow-wave positions is also a function of $M_{A\infty}$, the definition $M_{A\infty} = \left[\left(\frac{1}{2}\rho_\infty V_\infty^2\right)/\left(B_\infty^2/8\pi\right)\right]^{1/2}$ for input parameter $M_{A\infty}$ suggests that it is the ratio of the kinetic to the magnetic energy of the incoming flow as well as its relative gasdynamic energy that determines the hydromagnetic shock-wave position for low values of $M_{A\infty}$. For a given free-stream velocity V_∞ this ratio, and hence $M_{A\infty}$, can only be made small by either unusually small values of density ρ_∞ or unusually high values of magnetic field B_∞ in the undisturbed flow. If we hold the free-stream velocity V_∞ and temperature T_∞ constant, and hence specifying M_∞, we conclude on the basis of the results presented in figure 10-1 that either a low value of ρ_∞ or a high value of B_∞ or a

combination of these two effects can cause the position of the hydromagnetic shock wave to substantially differ from that of the corresponding gasdynamic shock wave calculated for the same value of M_∞ .

Although most of the time the flow properties of the solar wind are steady and are approximately the values indicated in figure 2-3, several instances of unusually low density or high field strength have been observed. For example, for nearly the entire day of July 31, 1967 Lyon et al. (1968) reported that Explorer 35 in the vicinity of the Moon observed an anomalously low solar-wind flux of about 0.2 protons/cm^3 flowing at 200 km/sec and that these results are corroborated by data from Mariner 5 in flight to Venus at 0.84 a.u. Both magnetometers on Explorer 35 (Colburn et al., 1967; Ness et al., 1968) show that the intensity of the interplanetary magnetic field was about 7 γ during this time. Substitution of these values into equations (5-4) leads to a value for $M_{A\infty}$ of about 0.6 . Unfortunately, no data on the Earth's bow wave was reported on this date so that the effect on the position of the bow wave remains unknown.

However, Ungstrup (1971) has recently analyzed data that show a very strong correlation between increasing magnetic-field strength in the solar wind and shock-wave movement out from the magnetosphere tail. He has examined magnetometer and plasma-detector data measured simultaneously by the satellites OGO 5, Pioneer 9, and Explorer 33 and 35 covering a wide region of near-Earth space during a 36-hour period spanning November 17-18, 1968. The magnetometer data from Explorer 33 revealed the remarkable occurrence of the satellite following the movement of a segment of the bow wave downstream from the Earth for a distance of more than 18 Earth radii during the 36-hour period. From these data and simultaneous observations made by the three other satellites, Ungstrup (1971) was able to determine that not only did the density of the solar wind remain at a practically constant value of about 2 protons/cm^3 but the velocity and temperature, and hence the Mach number, also remained relatively constant throughout the entire 36-hour period. The data indicated that the only varying flow property of the solar wind was the magnetic field which linearly

decreased from 13 to 3.5 γ during that 36-hour time interval. Since the magnetometer data from Explorer 33 indicated that the rear portion of the bow wave downstream of the Earth traveled steadily inward from its unusually large distance from the magnetosphere tail towards its more usual position as predicted by gasdynamic theory during that same time interval, Ungstrup (1971) concluded that the large magnetic-field strength in the solar wind was responsible for the unusual position of the bow wave and that the decreasing field strength brought about the movement of the bow wave back towards its usual position. Since a linear decrease in magnetic-field strength from 13 to 3.5 γ corresponds, for the steady plasma conditions of the solar wind reported by Ungstrup (1971), to a linear increase in Alfvén Mach number $M_{A\infty}$ from about 2 to around 8 , the space observations which he analyzed as well as his conclusions are in complete agreement with the trend displayed in the theoretical curves presented in figure 10-1 for varying positions of a hydromagnetic shock wave for differing values of $M_{A\infty}$. Such space observations confirm the validity of our hydromagnetic fluid model and the conclusions which are drawn from it.

With the applicability of this refined model substantiated, we can now proceed to examine the effects of input Alfvén Mach number on the aligned-flow properties which are calculated as part of the numerical solution. For each individual solution using a given set of input parameters M_∞ and $M_{A\infty}$, the main flow properties of interest are the density ratio ρ/ρ_∞ , velocity ratio V/V_∞ , and magnetic-field-strength ratio B/B_∞ as well as the streamlines of the flow which indicate the direction of both the magnetic-field and velocity vectors throughout the flow. The temperature ratio is also of interest, and since the energy equation for aligned hydromagnetic flow integrated to exactly the same form as in gasdynamics, equation (8-1), which is derived from it and relates velocity to temperature, still holds. Thus the contours of constant-temperature ratio T/T_∞ coincide with those for velocity ratio V/V_∞ , and specific values for T/T_∞ can be determined by a simple application of equation (8-1). We present in figures 10-2 through 10-5 these flow

properties of four individual solutions for aligned hydromagnetic flow computed with input conditions of $M_\infty = 10$ and $\gamma = 5/3$ for each of the four values for $M_{A\infty}$ of 2.5 , 5 , 10 , and 20 . For each of the four solutions presented in figure 10-2 to 10-5 four subfigures have been drawn to illustrate lines of constant-property contours for (a) density ratio ρ/ρ_∞ , (b) velocity V/V_∞ and temperature T/T_∞ ratios, and (c) magnetic-field-strength ratio B/B_∞ , as well as (d) direction of magnetic-field and velocity vectors.

A comparison between constant density and velocity contours from the hydromagnetic solution for $M_{A\infty} = 20$ presented in figures 10-5 (a) and (b) and the corresponding contours from the gasdynamic solution in figure 8-2 shows that the differences between these two solutions are practically indistinguishable, and clearly indicates that the hydromagnetic solution approaches that of gasdynamics as $M_{A\infty}$ further increases. A similar comparison between these gasdynamic properties and the corresponding hydromagnetic properties in figures 10-4 (a) and (b) computed for $M_{A\infty} = 10$ shows that the differences between these two solutions are also relatively small. However, an examination of all four solutions presented in figures 10-2 to 10-5 reveals some general qualitative trends in these flow properties as the free-stream Mach number decreases to the value 2.5 For example, figures 10-2 (a) to 10-5 (a) show that as $M_{A\infty}$ diminishes the zone of high-density ratio in the nose region of the magnetosphere shrinks while in the remaining part of the flow the density ratio approaches unity. Hence the overall effect of decreasing $M_{A\infty}$ is a decrease in both the compression and expansion of the flowing plasma. Meanwhile, figures 10-2 (b) to 10-5 (b) indicate that a decrease in $M_{A\infty}$ produces a slight increase in the velocity ratio, and consequently a small decrease in the temperature ratio, uniformly throughout the entire flow field. On the other hand, figures 10-2 (c) to 10-5 (c) manifest that diminishing $M_{A\infty}$ causes the magnetic-field-strength ratio to increase slightly in the flow region near the nose of the magnetosphere but to approach unity in the remaining part of the flow. Finally, figures 10-2 (d) to 10-5 (d) show that as

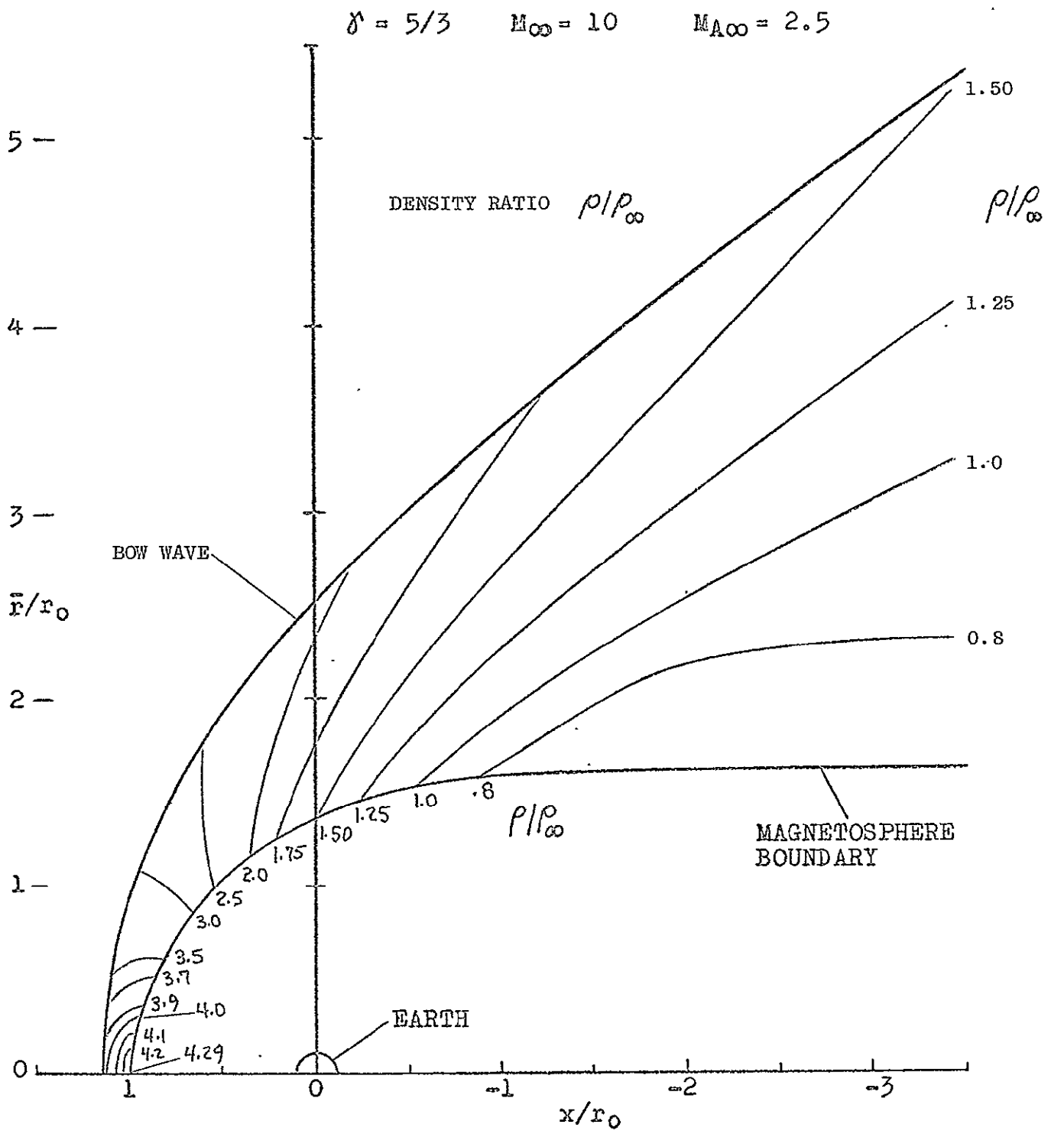

Figure 10-2. Various field properties for aligned hydromagnetic flow past the magnetosphere for $M_{A\infty} = 2.5$, $M_\infty = 10$, and $\gamma = 5/3$ represented by lines of constant-property contours for:

(a). Density ratio ρ/ρ_∞.

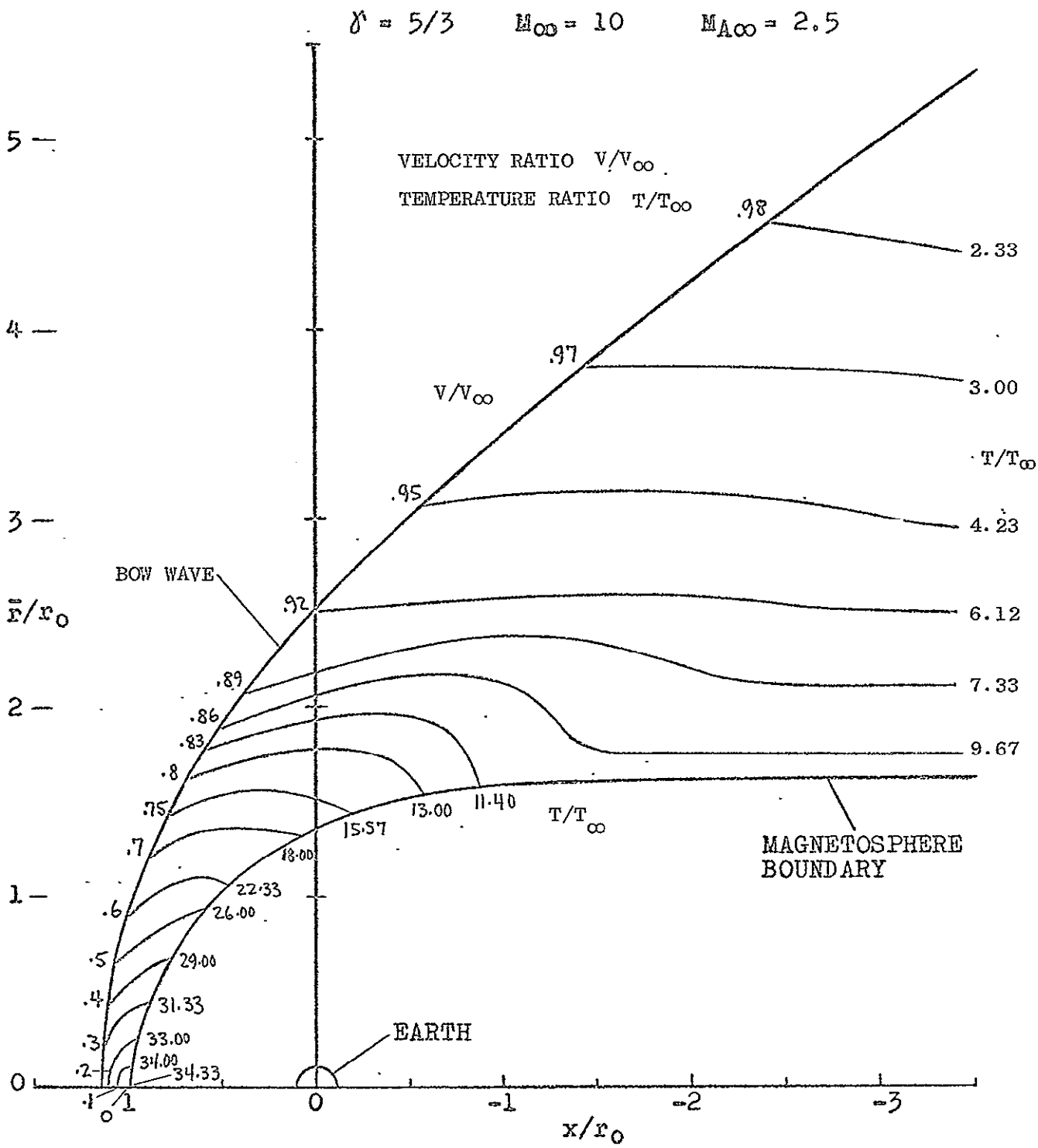

Figure 10-2 (b). Velocity V/V_∞ and temperature T/T_∞ ratios.

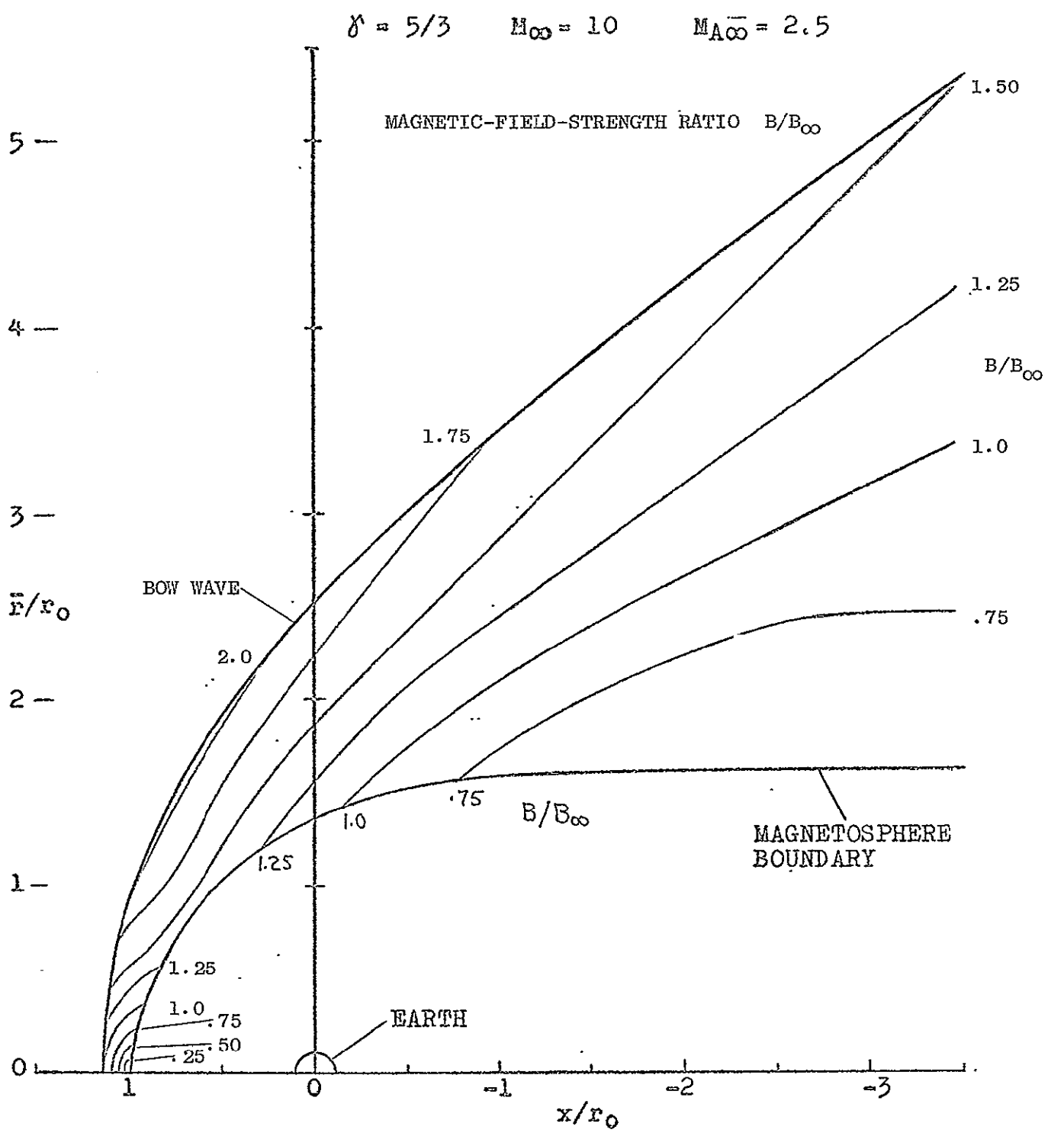

Figure 10-2 (c). Magnetic-field-strength ratio B/B_∞ .

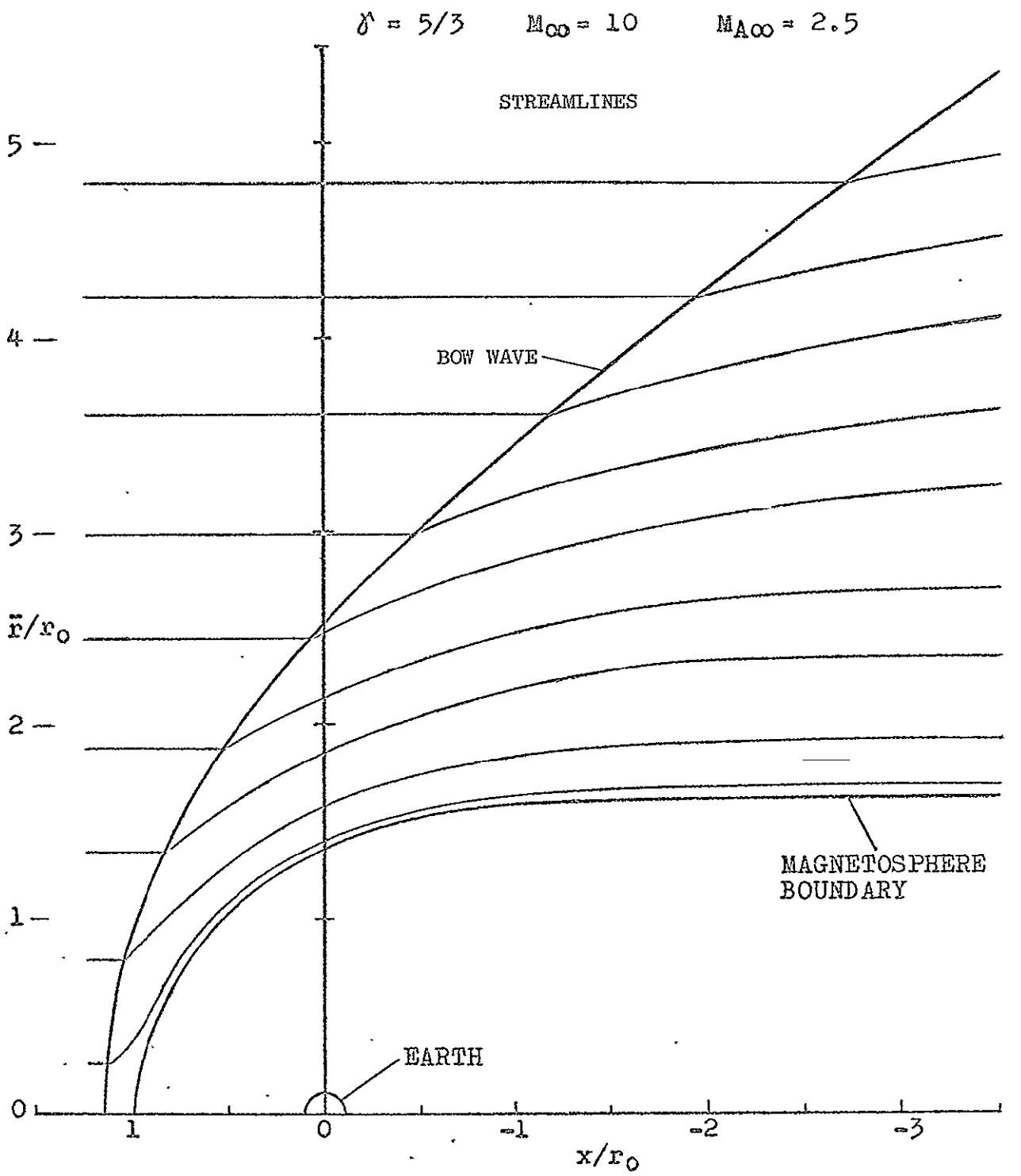

Figure 10-2 (d). Direction of magnetic-field and velocity vectors.

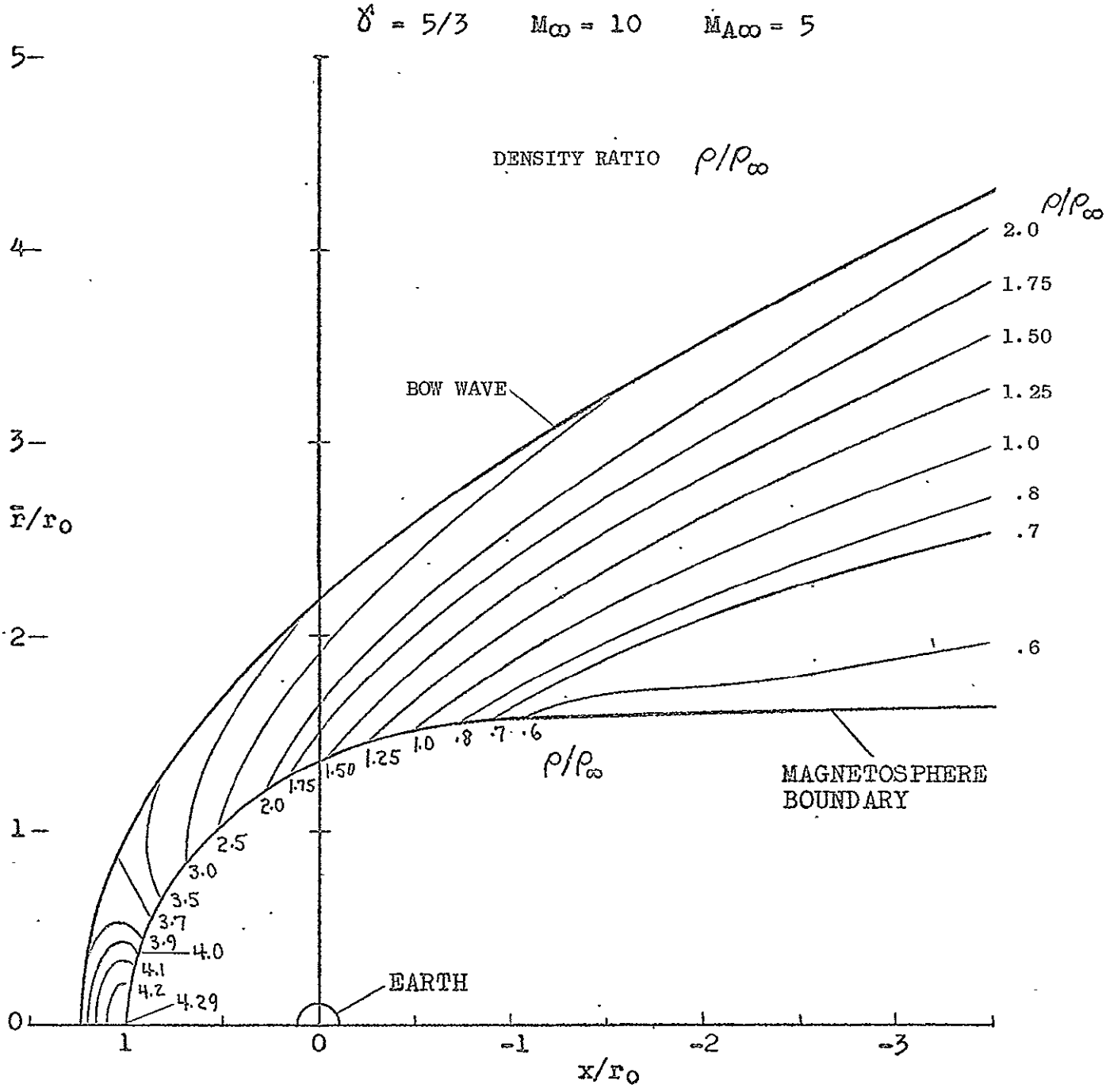

Figure 10-3. Various field properties for aligned hydromagnetic flow past the magnetosphere for $M_{A\infty} = 5$, $M_\infty = 10$, and $\gamma = 5/3$ represented by lines of constant-property contours for:

(a). Density ratio ρ/ρ_∞.

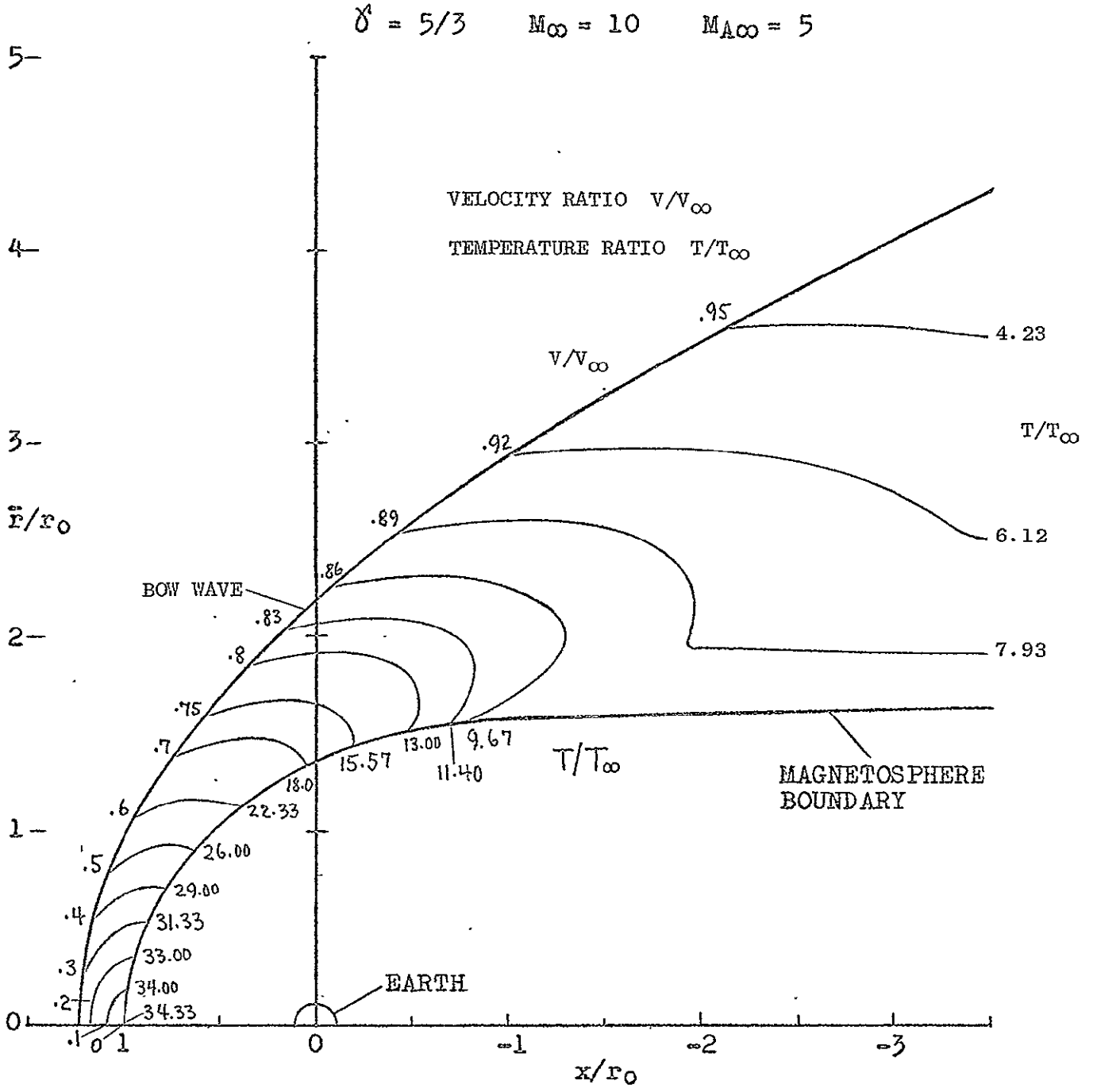

Figure 10-3 (b). Velocity V/V_∞ and temperature T/T_∞ ratios.

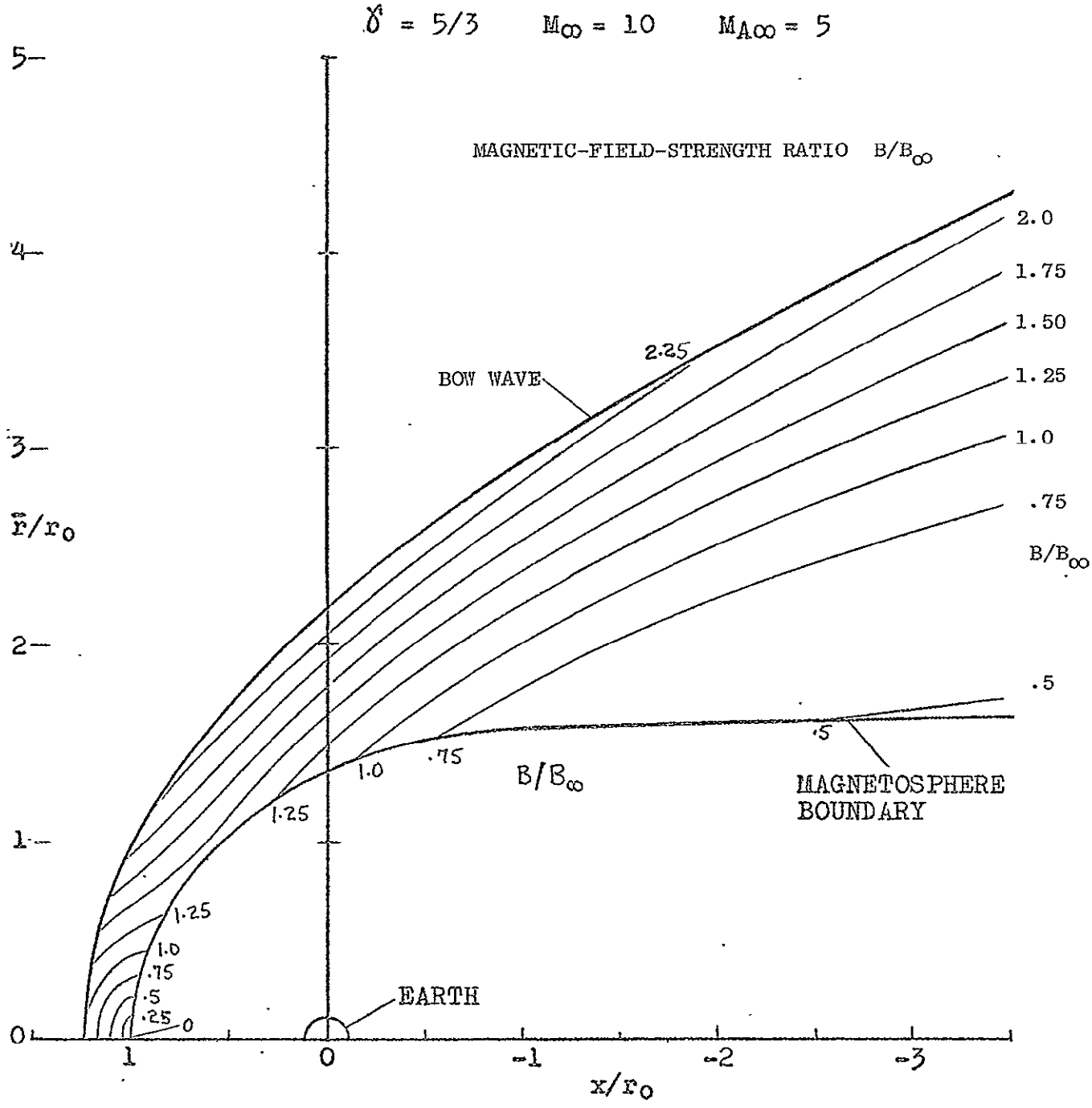

Figure 10-3 (c). Magnetic-field-strength ratio B/B_∞.

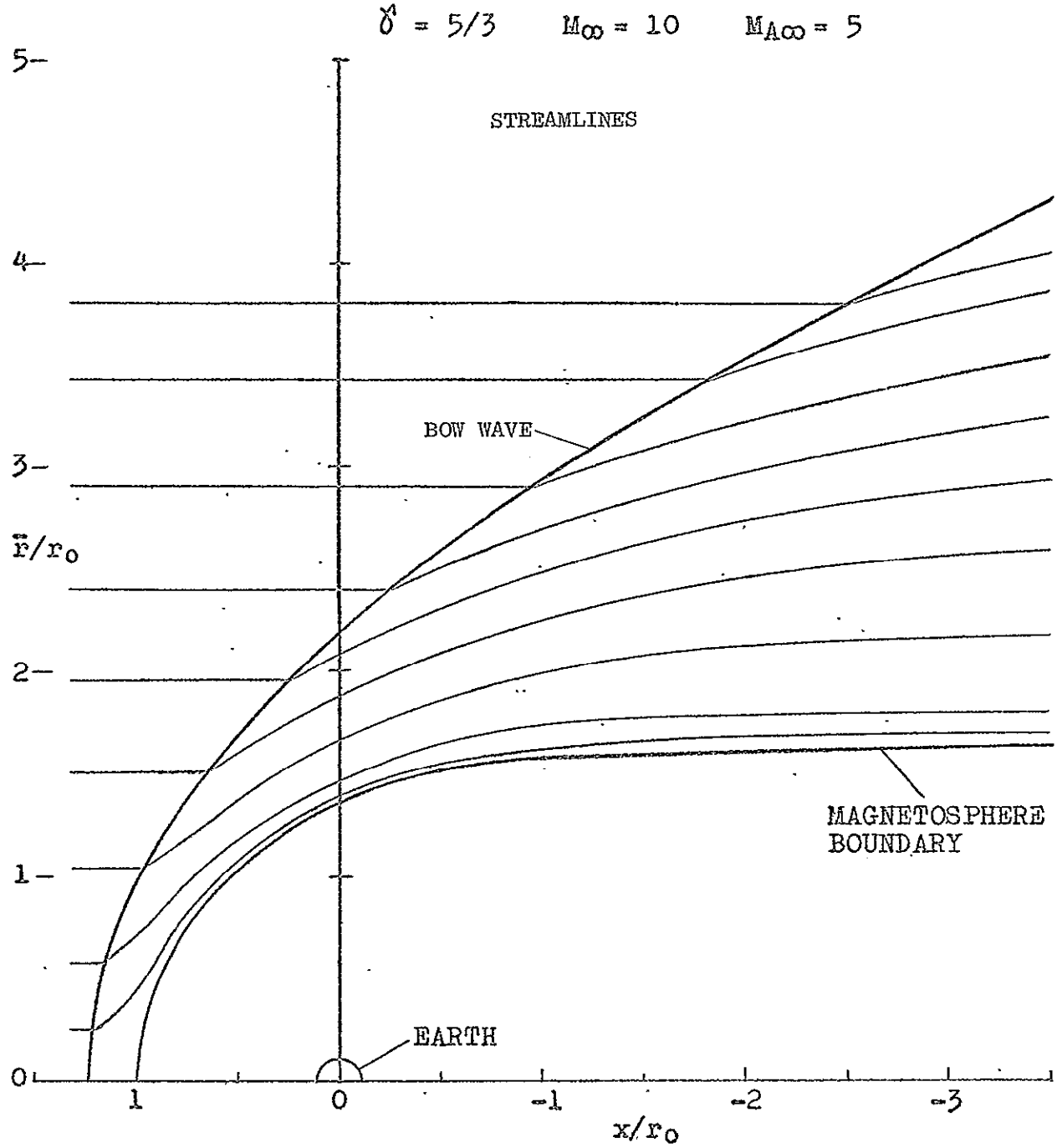

Figure 10-3 (d). Direction of magnetic-field and velocity vectors.

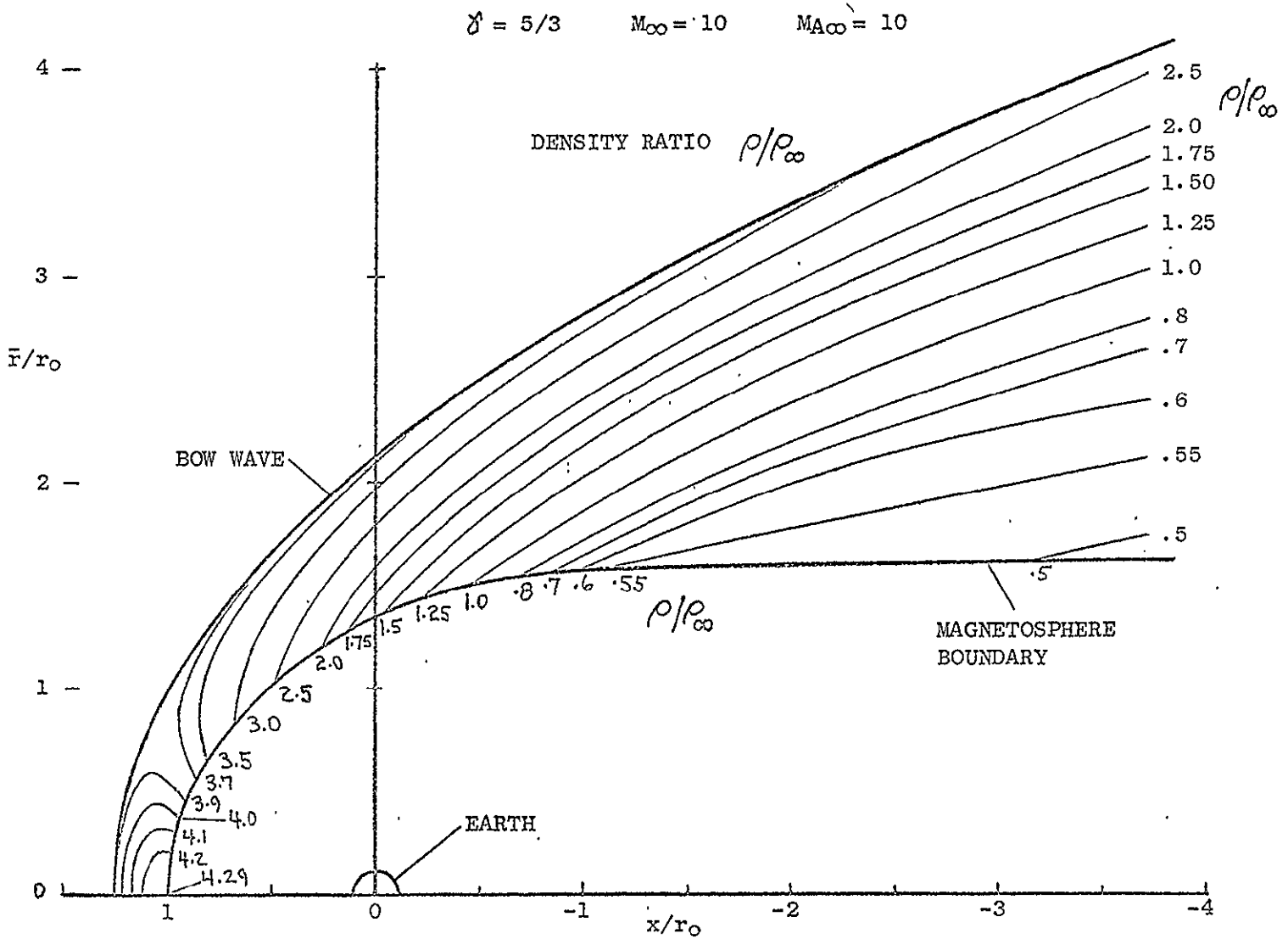

Figure 10-4. Various field properties for aligned hydromagnetic flow past the magnetosphere for $M_{A\infty} = 10$, $M_{\infty} = 10$, and $\gamma = 5/3$ represented by lines of constant-property contours for:

(a) Density ratio ρ/ρ_{∞}

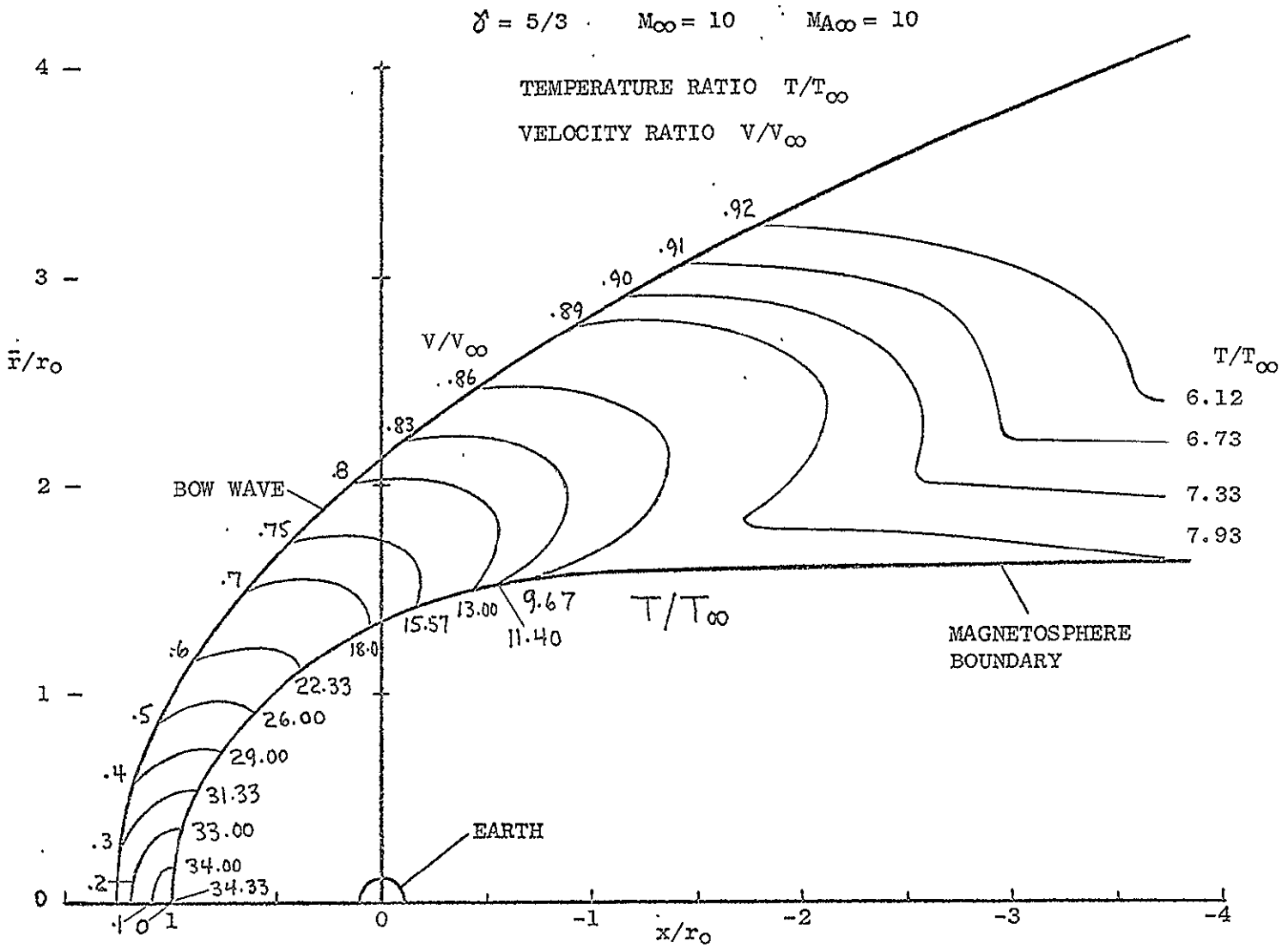

Figure 10-4 (b). Velocity V/V_∞ and temperature T/T_∞ ratios.

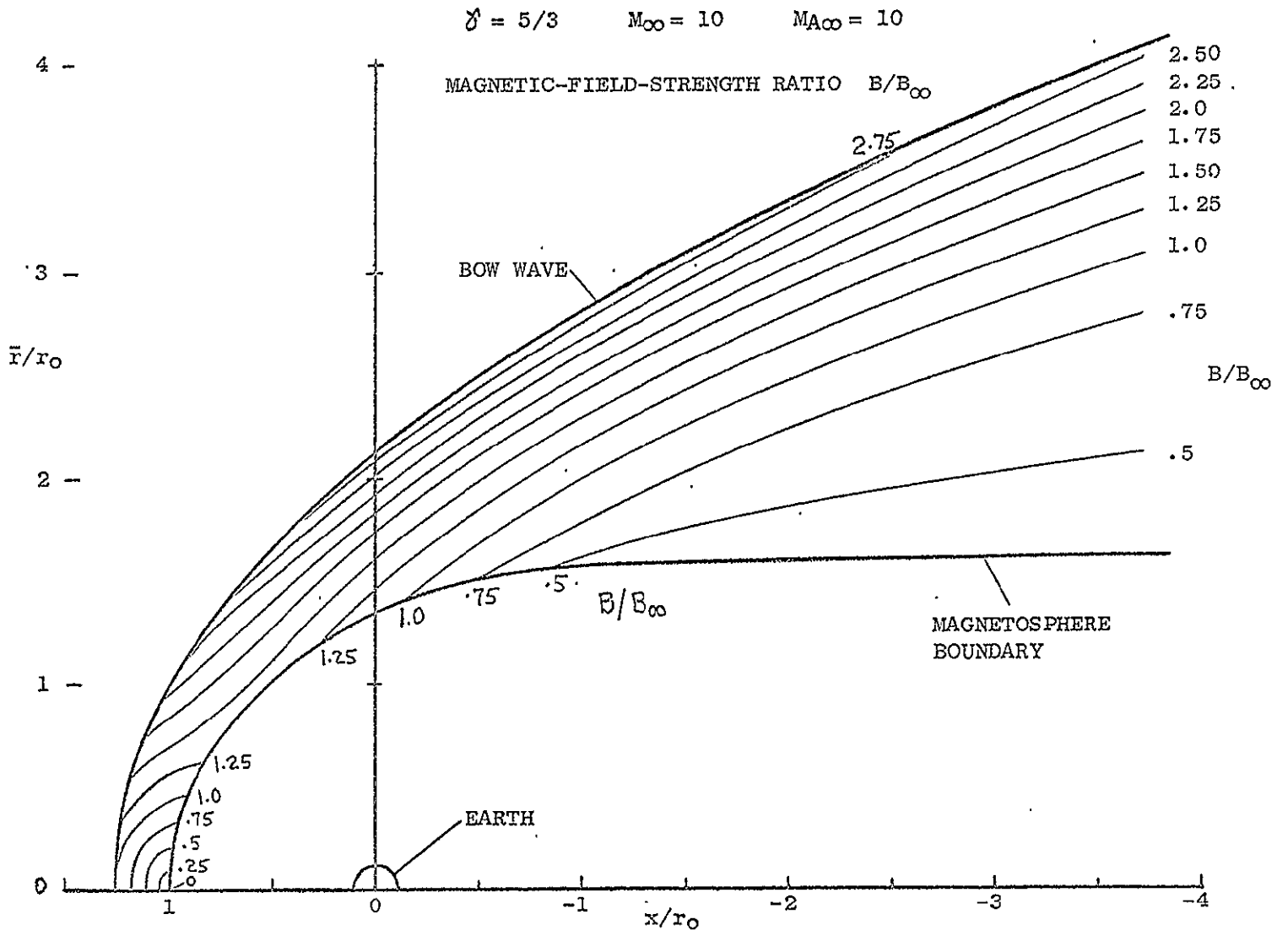

Figure 10-4 (c). Magnetic-field-strength ratio B/B_∞ .

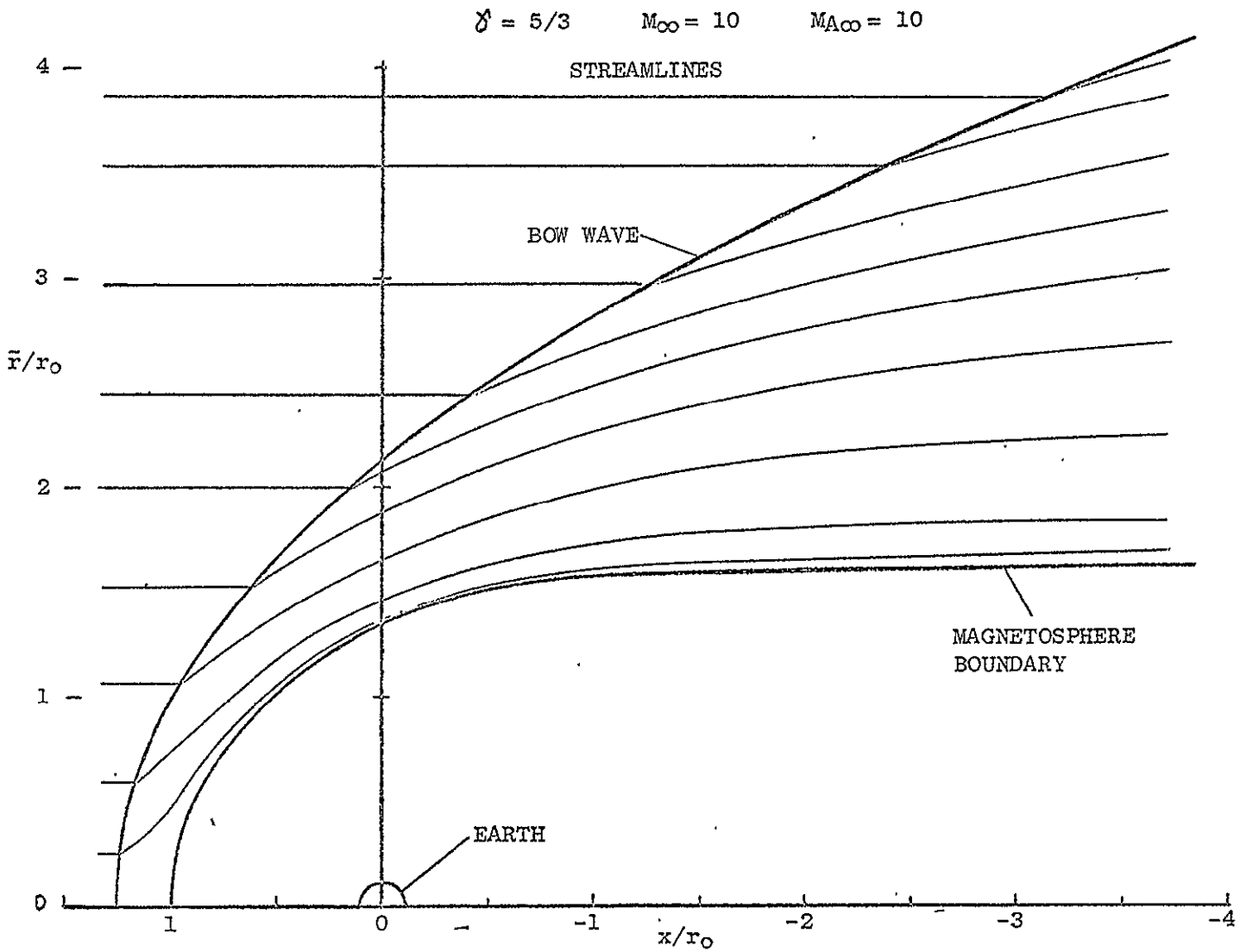

Figure 10-4 (d). Direction of magnetic-field and velocity vectors.

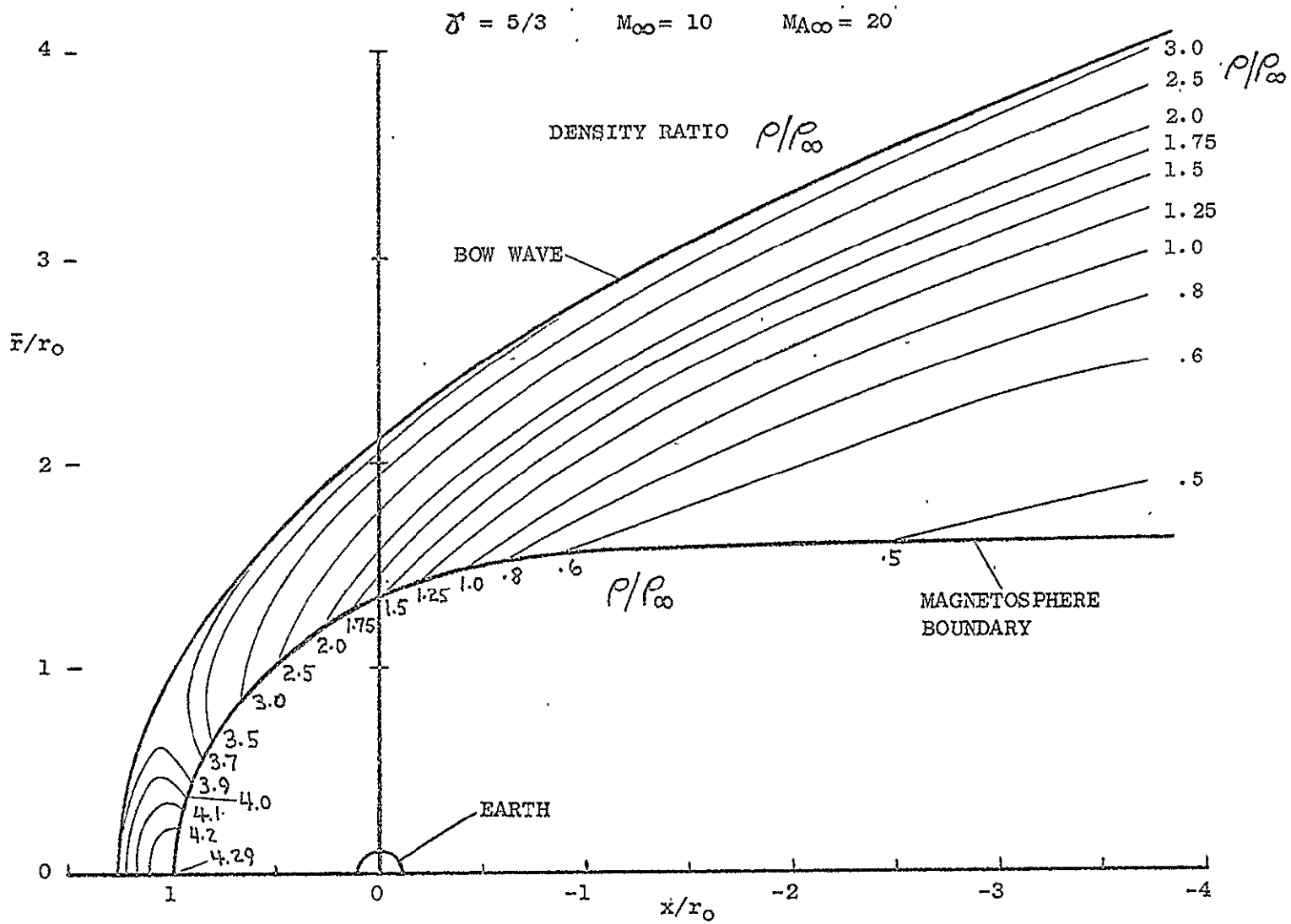

Figure 10-5. Various field properties for aligned hydromagnetic flow past the magnetosphere for $M_{A\infty} = 20$, $M_\infty = 10$, and $\gamma = 5/3$ represented by lines of constant property contours for:

(a). Density ratio ρ/ρ_∞.

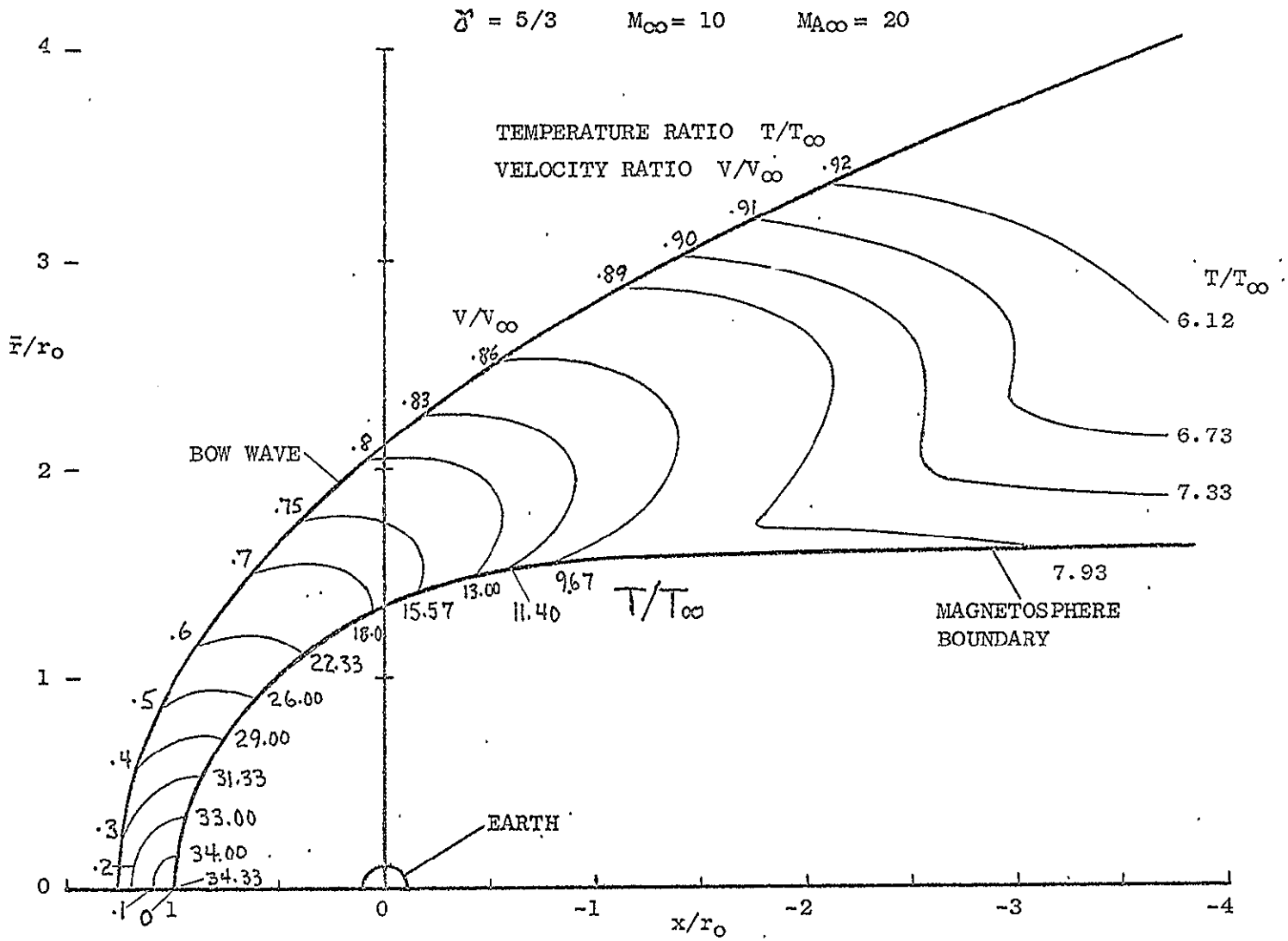

Figure 10-5 (b). Velocity V/V_∞ and temperature T/T_∞ ratios.

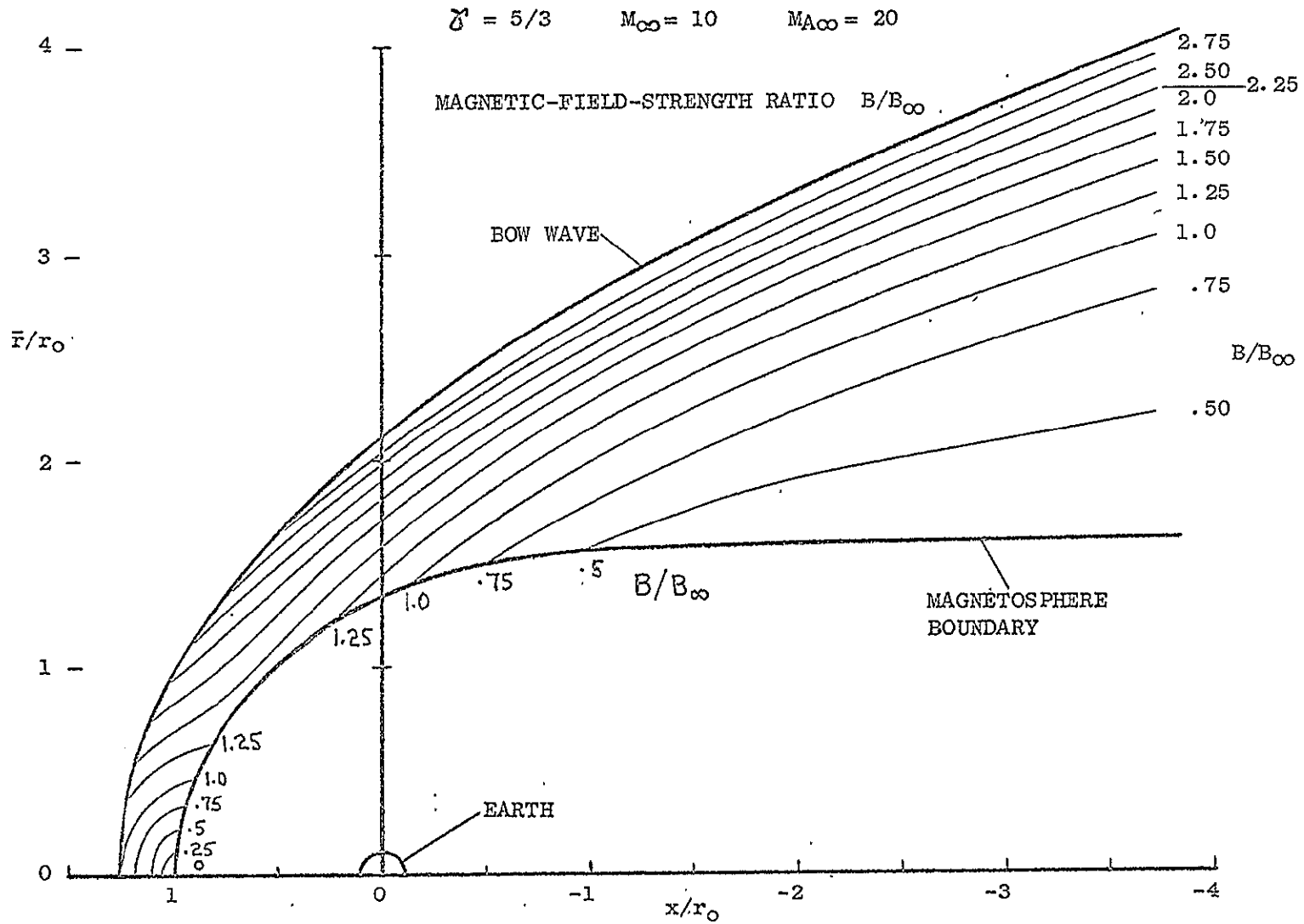

Figure 10-5 (c). Magnetic-field-strength ratio B/B_∞.

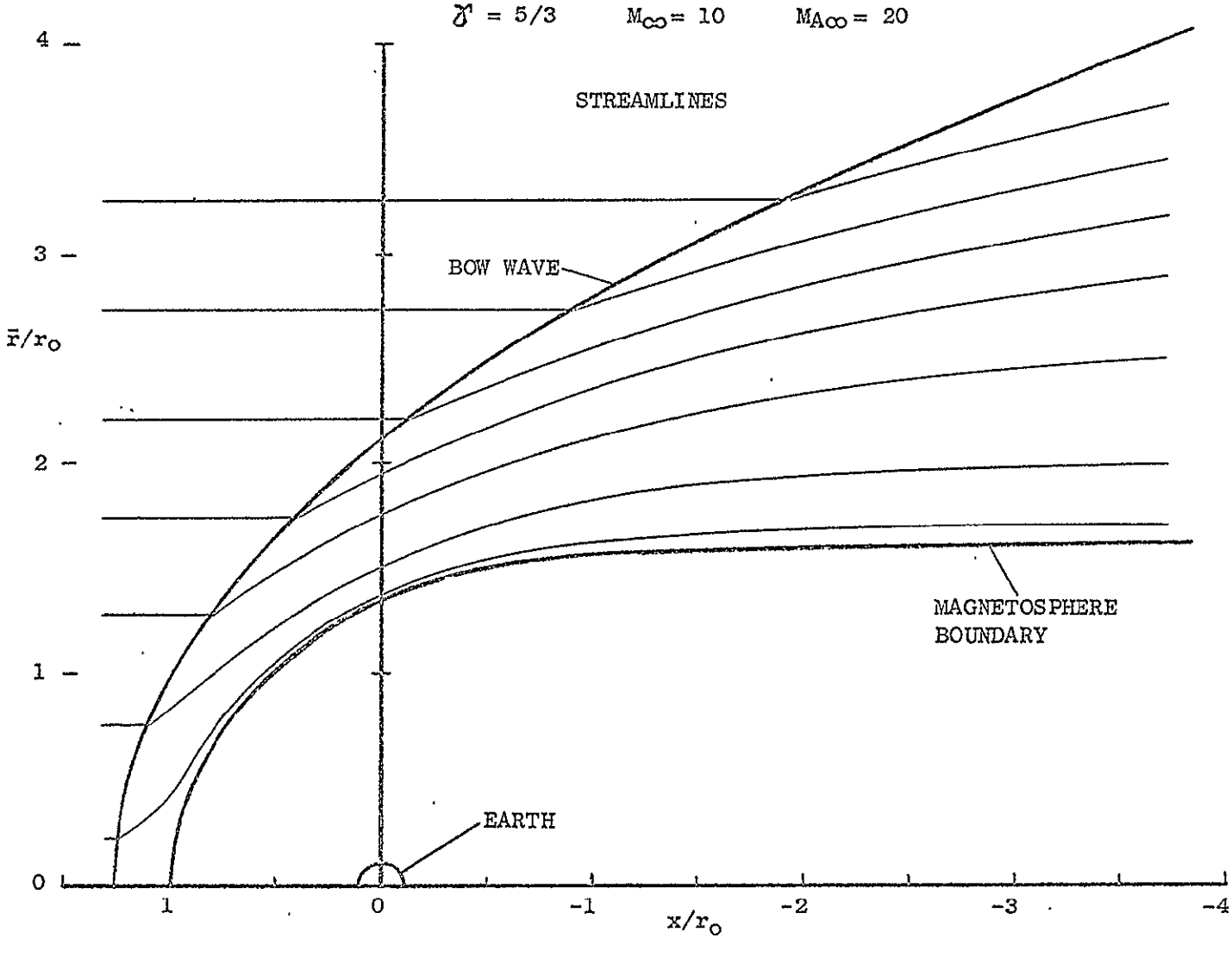

Figure 10-5 (d). Direction of magnetic-field and velocity vectors.

$M_{A\infty}$ decreases the angles that the streamlines make with the axis of symmetry also decrease somewhat throughout the entire flow except for that portion of the nose region where they remain relatively constant. Since a decrease in $M_{A\infty}$ implies an increase in the magnetic-energy content of the oncoming flow relative to its kinetic energy, we thus conclude from the foregoing results that as $M_{A\infty}$ decreases it becomes increasingly more difficult for the flow to stretch and distort magnetic-field lines. Consequently, the density and field strength are less disturbed and tend to remain closer to their free-stream values while the velocity tends to increase somewhat because of the smaller flow deflection. Although these four solutions presented in figures 10-2 through 10-5 are all for the same value of Mach number, we have also computed similar solutions for this same set of values for $M_{A\infty}$ but for different values of M_∞ and found the same variation in flow properties for decreasing $M_{A\infty}$ as we did for the case with $M_\infty = 10$. These effects, then, appear to be controlled by the value for $M_{A\infty}$, and hence ρ_∞ and B_∞ and to be relatively independent of M_∞ .

B. Comparison Between Approximate and Exact Solutions

In the foregoing section we have discussed in a rather qualitative way some of the broad features of the aligned hydromagnetic solution and its behavior for decreasing $M_{A\infty}$. At this point it is appropriate to carry out a more thorough comparison of these solutions for varying $M_{A\infty}$ and ultimately a collation of them with the more approximate gasdynamic results.

A quantitative comparison of the shock-wave position is most easily and adequately performed by plotting characteristic distances of the shock position from the planetary boundary. The two measurements we chose are the shock standoff distance x_s to characterize the nose region and the radial coordinate $\bar{r}_s$ measured from the axis of symmetry to the shock wave at a distance $2.5\, r_o$ downstream of the Earth. Since, for $M_{A\infty}$ approaching infinitely large values, the hydromagnetic solution reduces to that of gasdynamics, we have plotted in figure 10-6 two groups of curves depicting the two

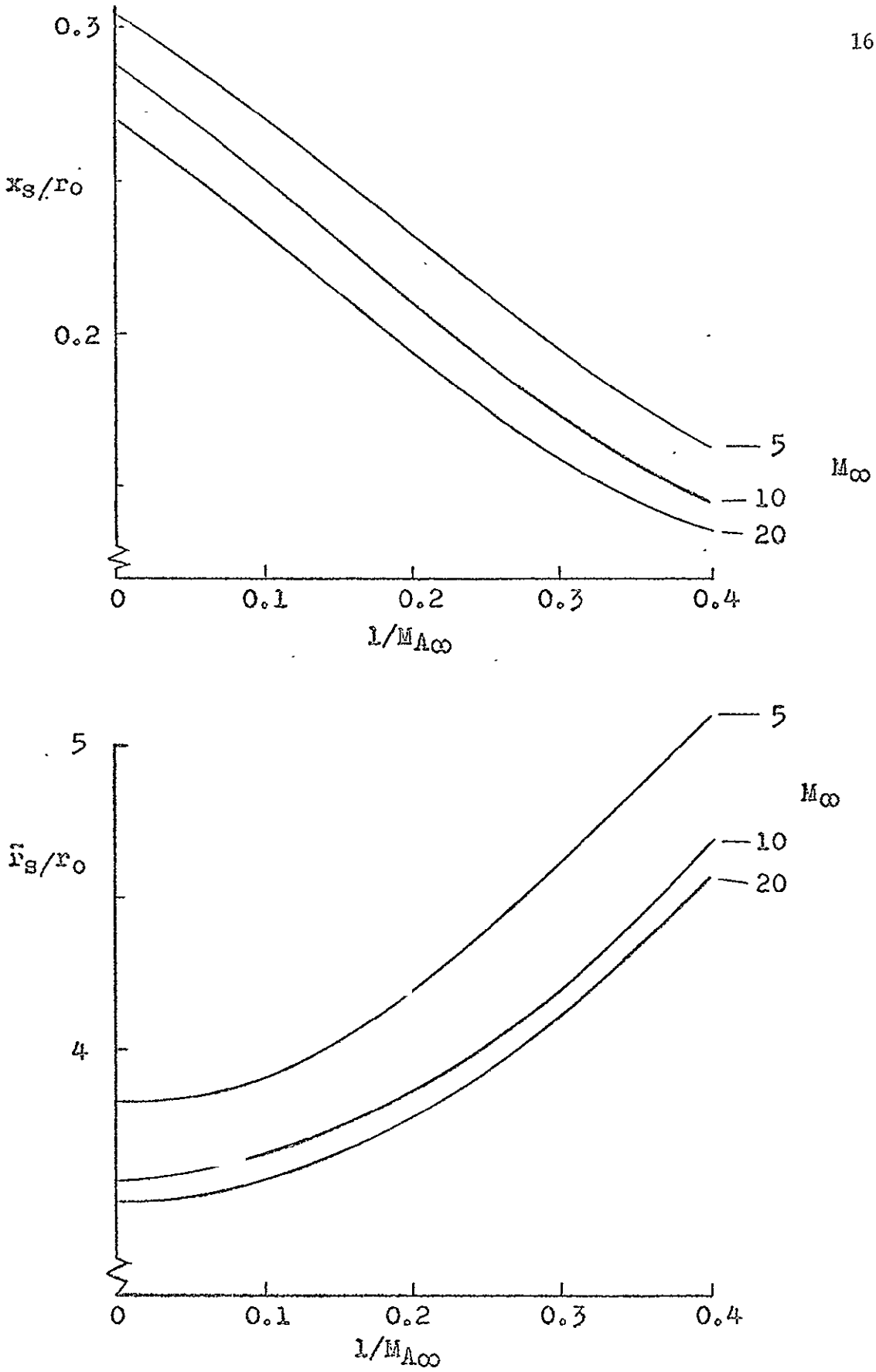

Figure 10-6. Variation with $M_{A\infty}$ and M_∞ of standoff distance X_s and downstream radial coordinate $\bar{r}_s$ of bow shock in aligned hydromagnetic flow; $\gamma = 5/3$.

40

distances x_s and $\bar{r}_s$ versus $1/M_{A\infty}$ in order that values on the ordinate represent the distances for a gasdynamic shock wave. In this figure three curves in each group are drawn representing three sets of solutions over the given range of $M_{A\infty}$ for values 5 , 10 and 20 for M_∞ . For decreasing values of $M_{A\infty}$ both these curves clearly indicate a decrease in x_s as the bow wave moves closer towards the nose of the magnetosphere and an increase in the shock coordinate $\bar{r}$ as the downstream segment of the shock moves farther from the magnetosphere tail. Furthermore, the similarity of these curves for different values of M_∞ shows that the relative shock movement for decreasing $M_{A\infty}$ is independent of the value of M_∞ although the absolute shock position does vary with M_∞ . Finally, we should point out that these curves indicate the smooth approach to gasdynamics for increasing $M_{A\infty}$, but that as the value of $M_{A\infty}$ decreases below 10 the position of the hydromagnetic shock departs significantly from that of the gasdynamic shock.

To compare this effect with the variance of position of the gasdynamic bow shock for differing values of M_∞ , in figure 10-7 we have plotted versus $1/M_\infty$ the corresponding values for x_s and $\bar{r}_s$ for the shock calculated in the gasdynamic solution. This figure indicates that the distance $\bar{r}_s$ for the gasdynamic shock varies with M_∞ in roughly the same manner as the corresponding distance $\bar{r}_s$ for the hydromagnetic shock does with $M_{A\infty}$ in figure 10-6. This equivalence, however, does not carry over to the shock standoff distance x_s . For this distance figure 10-7 shows that x_s varies with M_∞ in just the opposite sense that the corresponding x_s for the hydromagnetic shock does with $M_{A\infty}$. That is, decreasing M_∞ causes the gasdynamic shock standoff distance to increase while decreasing $M_{A\infty}$ brings about a decrease in the hydromagnetic x_s . This result is just another manifestation of the differing natures of the two input parameters M_∞ and $M_{A\infty}$.

Figure 10-7 further provides a suitable examination of the effect of using, as advocated by Dryer (1970) in an attempt to include some effect of the second input parameter $M_{A\infty}$, the value of the free-stream pseudo Mach number M^*_∞ for the input Mach

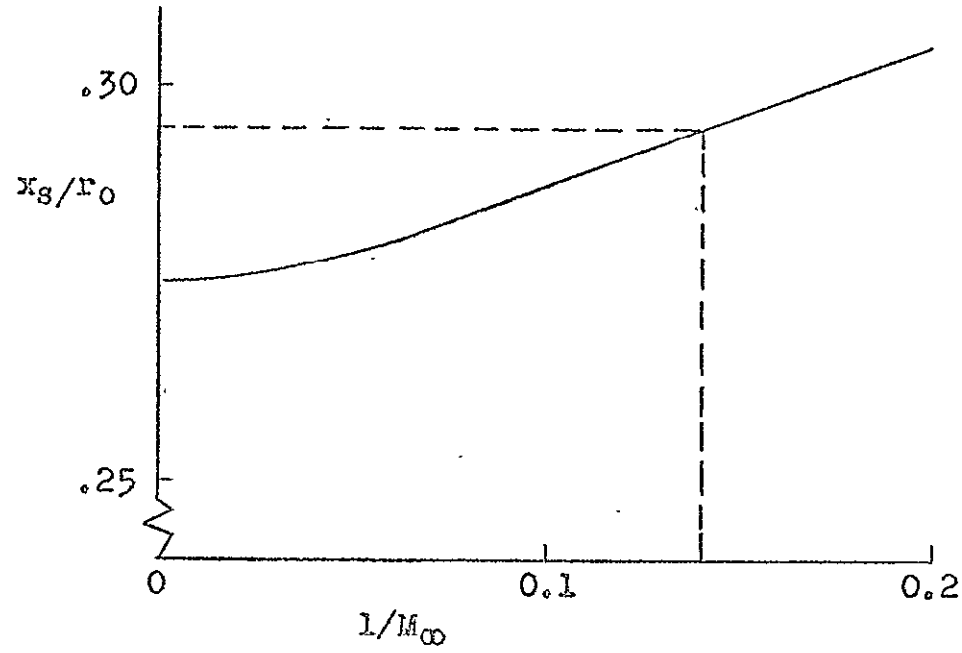

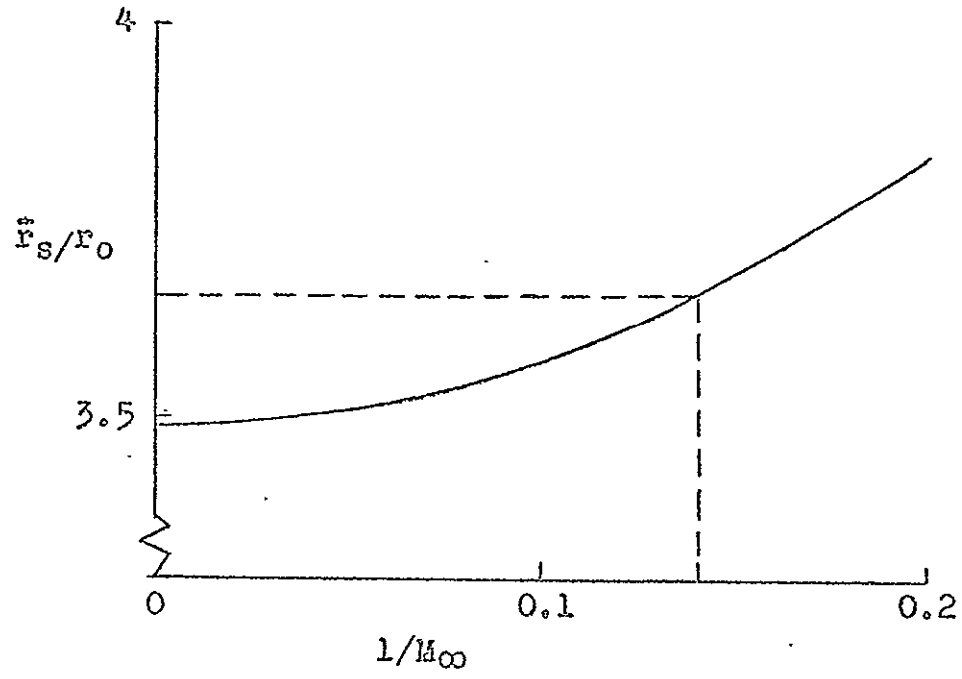

Figure 10-7. Variation with M_∞ of standoff distance x_s and downstream radial coordinate $\bar{r}_s$ of bow shock in gasdynamic flow; $\gamma = 5/3$. Dashed lines indicate values for $M^* = 7.09$ corresponding to $M_\infty = 10$ and $M_{A\infty} = 10$.

number in the gasdynamic theory. For example, if the free-stream parameters M_∞ and $M_{A\infty}$ in the aligned flow both have a value of 10 , then equation (9-18) determines M^*_∞ to be about 7.09 . With dashed lines we have indicated this value on the abscissa for the curves in figure 10-7 so that the values for x_s and $\bar{r}_s$ resulting from the gasdynamic solution using M^*_∞ instead of M_∞ as the input parameter can be easily read off. The dashed lines in this figure show that for this case the standoff distance would have a value about $x_s = 0.29\, r_0$ while the shock ordinate would be about $\bar{r}_s = 3.7\, r_0$. These values together with those obtained by using the gasdynamic theory in the usual way with M_∞ instead of M^*_∞ can now be compared to the exact values determined by the hydromagnetic solution. For $\bar{r}_s$ figure 10-7 shows that gasdynamic theory using $M_\infty = 10$ calculates a value $\bar{r}_s = 3.57\, r_0$ as compared to $3.7\, r_0$ obtained from the same theory using $M^*_\infty = 7.09$. Comparing these two values with the exact value $\bar{r}_s = 3.66\, r_0$ displayed in figure 10-6 for $M_\infty = 10$ and $M_{A\infty} = 10$, we see that use of M^* in the gasdynamic theory does improve the accuracy of the shock ordinate $\bar{r}_s$ calculated downstream from the Earth by that theory. However, in a similar comparison of the value for x_s figure 10-7 indicates the value to be $x_s = 0.26\, r_0$ for the gasdynamic theory using $M_\infty = 10$ and $x_s = 0.29\, r_0$ using $M^*_\infty = 7.09$ while figure 10-6 shows the exact value to be $x_s = 0.25\, r_0$. Therefore, the use of M^*_∞ in place of M_∞ actually lessens the accuracy of the gasdynamic theory in calculating the standoff distance. Because such use of M^*_∞ in the gasdynamic theory increases the accuracy of that theory only for that part of the flow downstream from the Earth while reducing it for the flow upstream, M_∞ appears to be the best overall choice of input parameter to use in the gasdynamic theory for approximating the hydromagnetic solution.

C. Synopsis of the Foregoing Results and Conclusions

The comparison between the solution of the gasdynamic equations and the solution to the more exact aligned hydromagnetic equations representing our fluid model of the solar-wind interaction has

been presented in this chapter, and it has verified the accuracy and applicability of the simpler gasdynamic theory for modelling the solar-wind interaction for conditions in the solar wind when $M_{A\infty}$ has a value around 10 or higher. When this provision is fulfilled, all of the previous theoretical results based on gasdynamic theory that has been derived in an analysis of the solar-wind interaction with the Earth, Mars, and Venus remain accurate and valid. However, when the value of $M_{A\infty}$ becomes lower than 10., the aligned-flow solution indicates that substantial discrepancies exist between the exact hydromagnetic theory and the simpler gasdynamic one. These differences manifest themselves in not only the values of the flow properties but even the gross features of the theory such as the shape and location of the bow shock wave. This result shows that the position of the bow wave is not only determined by the values of V_∞ and T_∞ in the undisturbed flow as is the case in gasdynamic theory, but also by the values of ρ_∞ and B_∞ which fix the value of $M_{A\infty}$. And indeed the validity of this conclusion based on the aligned-flow solution has been supported by the satellite measurements made in space and reported by Ungstrup (1971). For the conditions in the solar wind at that time, he concluded that the unusual position of the bow wave was determined by the strong magnetic field and that it varied with decreasing field strength in precisely the manner indicated by our theoretical hydromagnetic analysis.

Finally, we should point out that although these results and conclusions are all based on the solution of the hydromagnetic equations (9-2) and (9-3) for aligned flow, the study of the Friedrichs, or phase and group velocity, diagrams in figure 5-1 as well as the good agreement with space observations shows that perfect alignment of the $\underset{\sim}{V}_\infty$ and $\underset{\sim}{B}_\infty$ vectors is not essential, and qualitatively similar effects can be anticipated for other alignments as well.

CHAPTER XI

COMPARISON WITH ALIGNED-FLOW OBSERVATIONS MADE IN SPACE

In the last two chapters we have developed the nondissipative hydromagnetic theory for the case of parallel velocity and magnetic fields and presented a numerical procedure for solving the resulting aligned-flow equations and determining the position of the bow shock wave and the hydromagnetic flow properties of the shocked plasma. In the previous chapter we have qualitatively examined these computed results for a variety of free-stream conditions, compared them with corresponding results from gasdynamic theory, and have recognized trends in the general character of the hydromagnetic solution for decreasing free-stream Alfvén Mach number $M_{A\infty}$. Since this preliminary comparison indicated very encouraging agreement with previous theoretical and experimental investigations for large $M_{A\infty}$ and with measurements observed in space for low $M_{A\infty}$, it is now appropriate to carry out a more detailed, quantitative comparison with space observations in order to further verify the accuracy and validity of this aligned hydromagnetic model.

For such a comparison space observations made at a time when the velocity and magnetic-field directions in the solar wind were reasonably aligned is obviously most suitable. One instance of such experimental data is the measurements of the plasma and magnetic-field properties of the solar wind made by Mariner 5 as it flew past Venus. The magnetometer and plasma-probe experimenters (Bridge et al., 1967) found that the interplanetary plasma conditions in the solar wind were quite steady, and although the direction of the magnetic field showed some fluctuations its magnitude was nearly constant. They do not attribute these fluctuations in field direction to changes in overall interplanetary conditions, but rather to a series of local solar-wind structures, perhaps filaments, which were convected past the spacecraft. For our purposes this localized character can be disregarded. The nature of the average magnetic field encountered along the spacecraft's trajectory is illustrated in figure 11-1 as originally

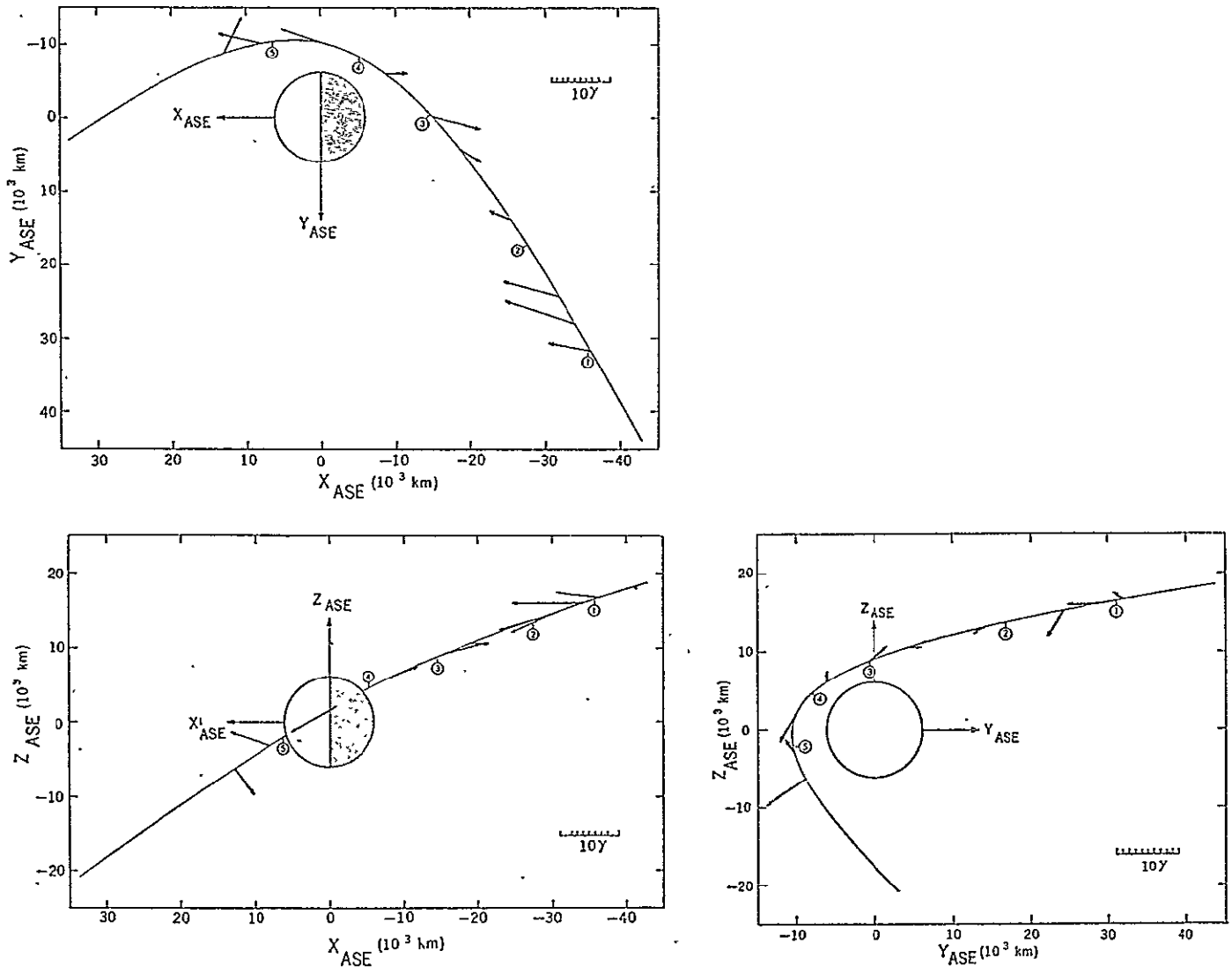

Figure 11-1. Mariner-5 trajectory and magnetic-field vectors. The three panels contain aphrodiocentric-solar-ecliptic projections of the Mariner trajectory and of the average, measured field at specific points. (Bridge et al., 1967).

presented by Bridge et al. (1967). The three parts of this figure show the usual orthographic projections of both the Mariner trajectory and the measured fields. The aphrodiocentric-solar-ecliptic (ASE) coordinates are defined by a plane parallel to the ecliptic passing through the center of Venus and by X_{ASE}, the projection in this plane of the direction to the Sun. The axis Z_{ASE} points toward the north ecliptic pole, and Y_{ASE} completes the orthogonal, right-handed system. The circled numbers ① through ⑤ correspond to the labels added by the experimenters to the plasma and magnetic-field data in figure 8-13 and denote features of special significance. The field vectors are not shown at equally spaced intervals but at times that best illustrate the character of the average magnetic field within the various regions along the spacecraft's trajectory.

That the magnetic-field direction is reasonably parallel to the velocity direction which is radially outward from the Sun can be determined by study of the orthographic projections in figure 11-1. The X_{ASE} - Z_{ASE} projection, which is viewed from the cross-section edge of the plane parallel to the ecliptic passing through the center of Venus and along the line between the Sun and Venus, shows that the magnetic field remains nearly parallel to the Sun-Venus line throughout the time interval displayed. Furthermore, the small components of the magnetic field illustrated in the Y_{ASE} - Z_{ASE} projection, which is viewed from the Sun toward the planet, also indicate that the field direction is primarily parallel to the ecliptic and in a radial direction from the Sun during the interval. And finally, the X_{ASE} - Y_{ASE} projection, viewed from the north ecliptic pole, confirms that the magnetic field lies in the ecliptic plane, and a comparison with the theoretically calculated field direction displayed in figure 10-3(d) for aligned flow downstream of a shock wave shows that the observed direction of the field is indeed consistent with that for aligned flow. We then conclude that at the time these data were measured the average magnetic-field direction was reasonably aligned with the velocity direction, and thus these data are very appropriate for comparison with the theoretical calculations made with our aligned-flow model.

Although there have been other examples of measurements made in space which show the solar wind to be more steady and the velocity and magnetic-field directions to be more perfectly aligned, we choose to make a detailed comparison with these near-Venus data from Mariner 5 for two particular reasons. The first is that in chapter VIII we have already carried out a comparison between these data and the theoretical positions of gasdynamic shocks arising from interaction with several of the ionopause shapes illustrated in figure 6-6 and found general agreement. An additional comparison of these same data with the calculated results of a more refined interaction model would therefore enable us to also contrast the theoretical results calculated using the simpler gasdynamic theory with those from the more refined hydromagnetic theory with reference to these Mariner-5 observations. But the primary reason is, however, that the values of about 590 km/sec , 4 protons/cm^3 , and 8 γ reported by Bridge et al. (1967) for the velocity, ion number density, and magnetic-field strength in the solar wind before and after Mariner 5's encounter with Venus indicate a value of about 6.75 for $M_{A\infty}$; and our analysis of the aligned hydromagnetic theory presented in chapter IX showed that when $M_{A\infty} < 10$ substantial differences between the theoretically calculated hydromagnetic and gasdynamic results begin to appear. Thus on this theoretical argument alone we should expect better agreement to exist between the hydromagnetic results and the observations of Mariner 5 than existed for the corresponding gasdynamic results. In fact at this point we can already predict better agreement with the hydromagnetic theory on the basis of the following argument. Figure 8-13 shows that the gasdynamic shock wave calculated for $M_\infty = 5$ and associated with the ionopause shape for $H/r_o = 0.25$ indicates that the theoretical shock is positioned somewhat closer to Venus than was observed. However, since we have learned in chapter X that for $M_{A\infty} < 10$ the position of a hydromagnetic shock wave is, in all regions except near the nose, somewhat farther away from the planet than the corresponding position for a gasdynamic shock, hydromagnetic theory will predict a shock position that better agrees with the observations than did the gasdynamic theory. This good agreement

between the calculated position of the shock wave associated with the ionopause shape for $H/r_o = 0.25$ and that observed by Mariner 5 suggests that the upper ionosphere consists primarily of ionized atomic hydrogen at a temperature of about 700 °K corresponding to a scale height of around 1500 km . On the other hand, however, the theoretical results displayed in figure 8-13 for $H/r_o = 0.25$ indicate that Mariner 5 should have then crossed the ionopause, but there is no certain evidence that Mariner 5 actually did penetrate the ionopause. As discussed in chapter VIII, a possible explanation for this discrepancy is that the tail of the ionosphere might taper inward toward the axis of symmetry rather than extending straight downstream. The theoretical ionopause shapes displayed in figure 6-6 give no indication of such a trend, but they are of low reliability for this feature of the flow because of the deterioration of the quality of the Newtonian approximation for both the gas and magnetic pressure of the solar wind as ψ approaches 90 degrees. This aspect of our model can be refined, however, by using the exact pressure of the solar wind calculated in the numerical solution instead of the approximate Newtonian expression and thus determining the exact shape of the ionopause as part of the solution. Such a calculation would then accurately represent the shape of the ionopause tail for the model presented.

A. Calculation of the Exact Ionopause Location

The ionopause shape is defined as the locus of those points at which the tangential discontinuity conditions (6-12) are exactly satisfied. For all the boundary shapes illustrated in figure 6-6, the calculated results presented in figure 8-12 imply that although the discontinuity relations (6-12) are not satisfied exactly on any of these shapes the discrepancy is larger on the flanks than on the nose section of each boundary. In fact we found that the necessary increment in the radial coordinate $\bar{r}$ of the present ionopause shapes needed to satisfy the discontinuity relation

$$p^*_{EXT} = (p + B^2/8\pi)_{EXT} = p_{INT} = (p_{st} - p_w) \exp\left(-\frac{\bar{r} - r_o}{H}\right) + p_w \qquad (11\text{-}1)$$

on the forward part of the boundary is imperceptibly small on the scale of figure 8-12 and would not change the calculated results for the exterior flow in this region. On the other hand a similar procedure for the coordinates of the ionopause flanks shows that large increments are necessary, thus indicating serious errors in the present shape of the ionosphere tail. This error can be corrected by calculating a new shape for the ionopause. Since the error lies in the region where the flow is supersonic and the equations hyperbolic, the position of the boundary is not required to be specified a priori, but rather can be calculated by the method of characteristics as part of the solution of the exterior flow. A simple numerical procedure to calculate the position of these new boundary points as well as the exterior-flow properties such that equation (11-1) is satisfied at those points was developed. A representative boundary point C is indicated in figure 11-2, and the unknown flow properties at point C are to be determined from the known flow properties at points B and D by using the aligned-flow equations (7-22) to (7-25) in the following way. We use a crude predictor and assume that the ionosphere boundary and right-going characteristic lines are straight and then solve for the location $\bar{r}$ of the point C. With this value of $\bar{r}$ the ionosphere pressure p_{INT} can be calculated by equation (11-1) and then $(p + B^2/8\pi)_{EXT} = p^*_{EXT}$ can therefore be determined at point C by use of equation (6-12). Thus with p^*_B and p^*_C now known, we then solve the right-going characteristic equation (7-22b) for the flow angle θ_C at point C. Finally, using this value of θ_C, we can compute the average of the flow angles at points C and D and the average of the angles $(\mu - \theta)$ at points C and B, and then correct the position of point C using these averaged angles to specify straight lines from points B and D. This corrector process can be repeated till the new position of point C differs from the old by less than 0.01 percent. (For all of our solutions this procedure always converged in less than 20 iterations.) In this way, then, the precise shape of the ionopause, on which the tangential discontinuity conditions (6-12) are satisfied exactly, is determined simultaneously as part of the solution for the exterior flow. We

can thus solve the exact free-boundary problem and no longer need to decouple the calculation of the ionopause shape from the exterior-flow solution as was done before.

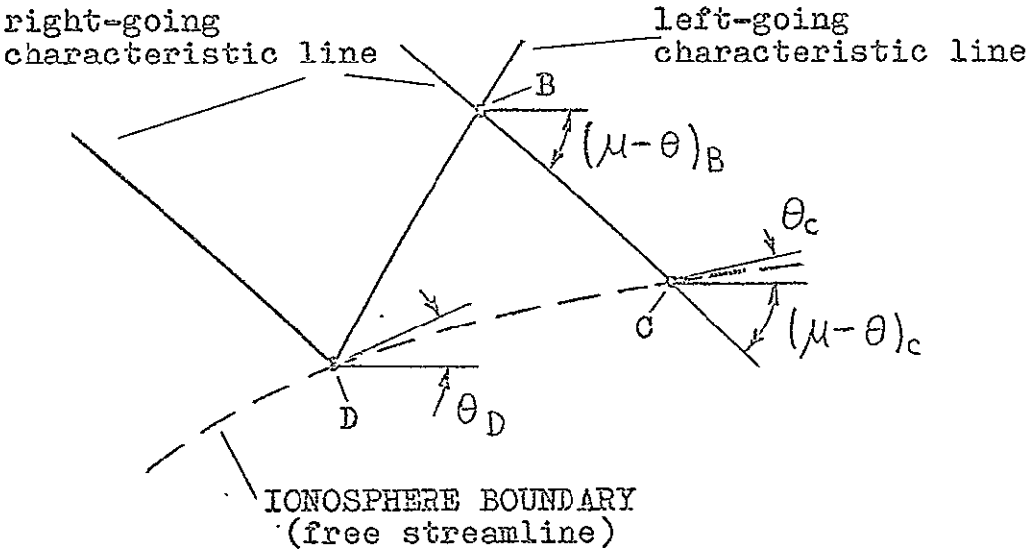

Figure 11-2. Sketch of characteristic lines for determination of the location of, and flow properties at, a representative mesh point C on the ionosphere boundary.

B. Comparison with Mariner-5 Data

Since the pressure of the external hydromagnetic flow is balanced by the ionosphere pressure at the interface, the exact shape of the ionopause depends on the input parameters of the exterior flow and the expression (6-11) for the ionosphere pressure. In order to make a comparison of the calculated aligned-flow properties around this new ionopause shape with those observed by Mariner 5, values for these input parameters which correspond to conditions in the solar wind at the time of observation must be determined. For the exterior flow we have already found $M_{A\infty} = 6.75$ while values of about 590 km/sec and 300,000 °K reported for the velocity and temperature

in the solar wind before and after Mariner 5's encounter with Venus indicate a value of about 6.47 for M_∞ . For the interior pressure we choose a value for H/r_0 of 0.2 corresponding to a Venusian ionosphere composed primarily of atomic hydrogen at about 600 °K because it agrees reasonably well with both the dual-frequency-occultation and Lyman-alpha measurements made by Mariner 5 on the dayside as well as nightside ionosphere. Similarly, the pressure in the ionosphere wake $p_w = p_\infty + B_\infty^2/8\pi = p_\infty^*$ is about 5×10^{-10} dyne/cm^2 which, in view of the uncertainties attendant with these measurements made in space, approximately agrees with the value of 800 electrons/cm^3 at a temperature of about 675 °K for the electron density and temperature in the ionosphere tail reported by Fjeldbo and Eshleman (1969).

Figures 11-3(a) to (d) illustrate the aligned hydromagnetic solution for the exterior flow represented by lines of constant-property contours for (a) density ratio ρ/ρ_∞ , (b) velocity ratio V/V_∞ , (c) magnetic-field-strength ratio B/B_∞ , and (d) the direction of the velocity and magnetic-field vectors as well as the bow-wave position and the exact ionopause shape all of which were computed for $M_\infty = 6.47$, $M_{A\infty} = 6.75$, $\gamma = 5/3$, and $H/r_0 = 0.2$. The exact ionopause shape illustrated in these figures is seen to be somewhat slimmer than the approximate shape for $H/r_0 = 0.2$ presented in figure 6-6. The ionosphere tail in the exact calculation also tapers slightly inward toward the axis of symmetry rather than extending straight downstream as did the approximate shape. This inward tapering just indicates that the solar wind closes in behind the ionosphere plasma some distance downstream from the planet as might be expected since the pressure in the ionosphere decreases with increasing altitude and Venus is a nonmagnetic planet. Also included in figures 11-3 is a plot of Mariner 5's trajectory near Venus. The plotted trajectory has been obtained by transforming the ASE coordinates of the trajectory given in figure 11-1 by Bridge et al. (1967) to a second cartesian coordinate system having its x axis along the Sun-Venus line, its y axis pointing in the direction of Venus's motion, and its z axis completing the right-handed system. To take

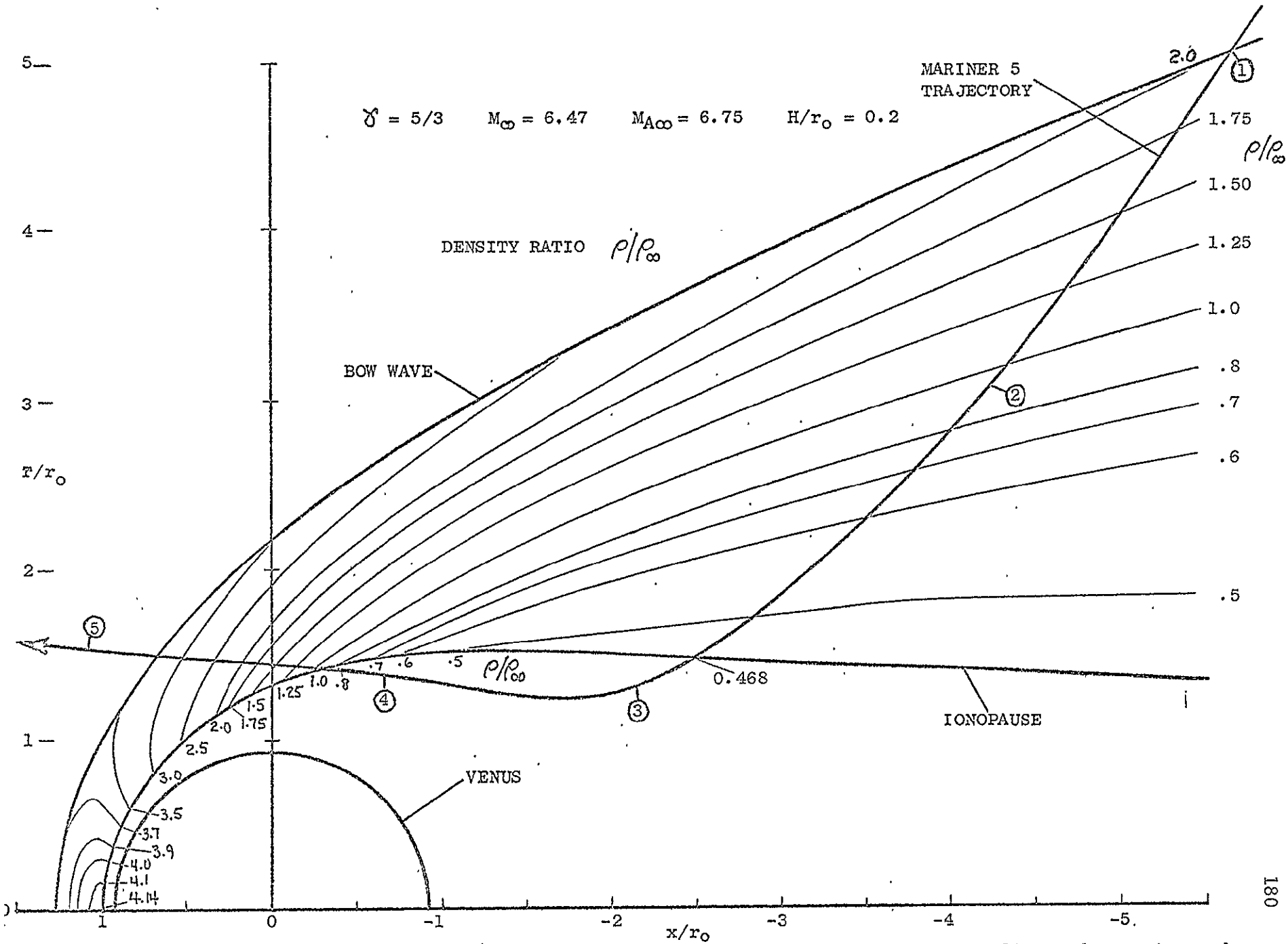

Figure 11-3. Trajectory of Mariner 5 past Venus rotated into a plane about the wind-Venus line and superimposed on the theoretical location of the ionopause and bow wave as well as various field properties for aligned hydromagnetic flow represented by lines of constant-property contours for: (a) Density ratio ρ/ρ_∞.

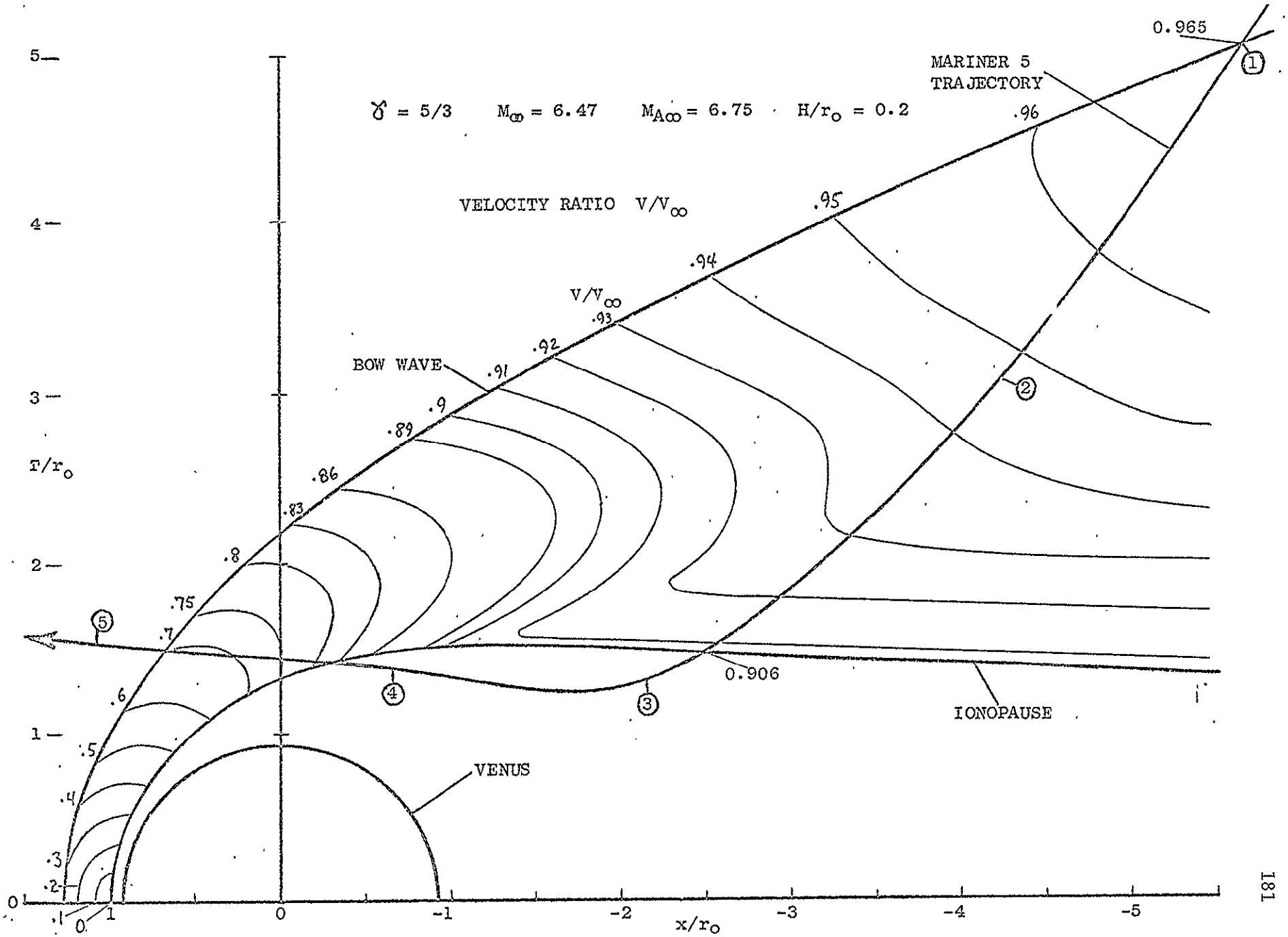

Figure 11-3 (b). Velocity ratio V/V_∞.

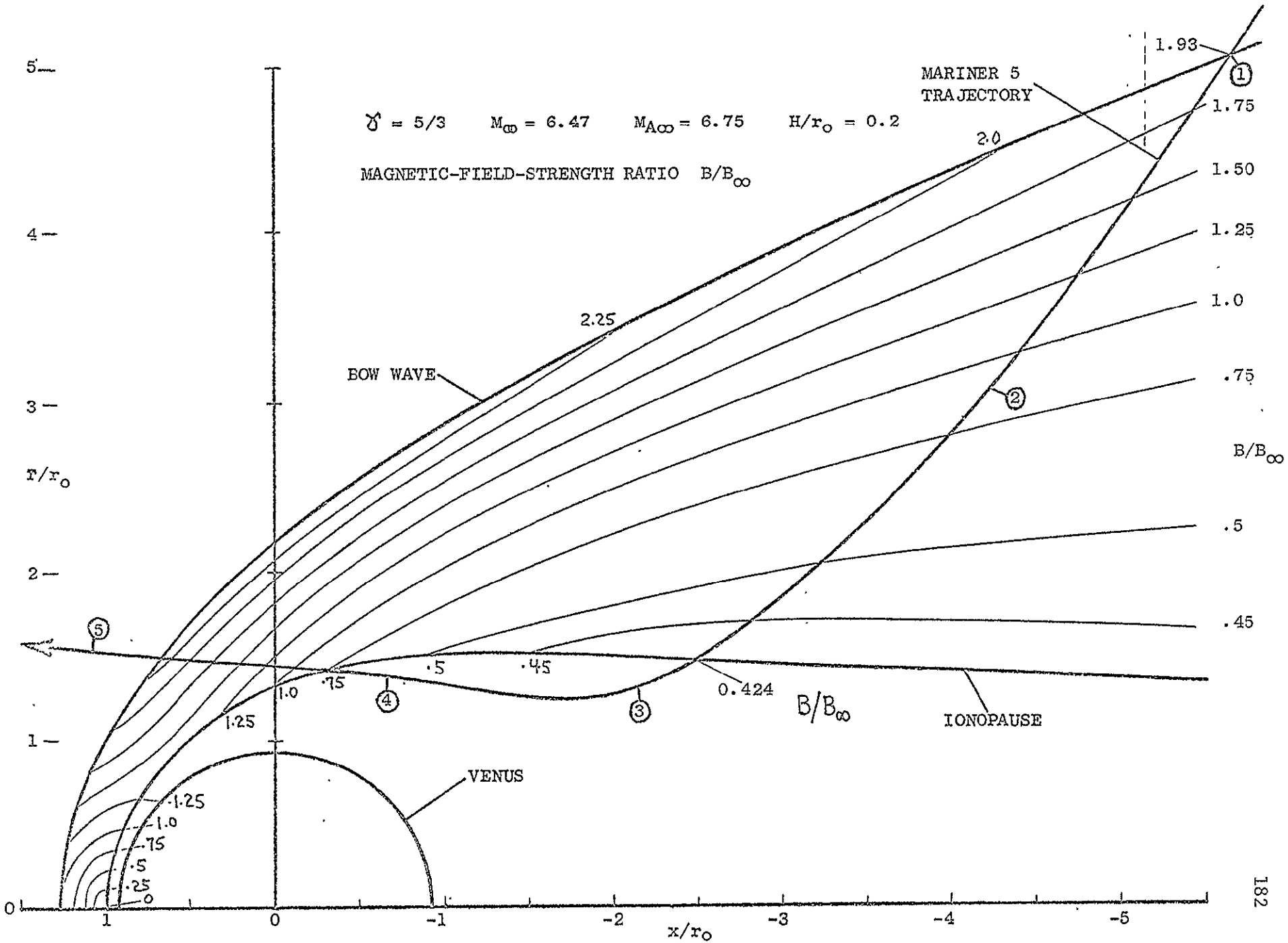

Figure 11-3 (c). Magnetic-field-strength ratio B/B_∞ .

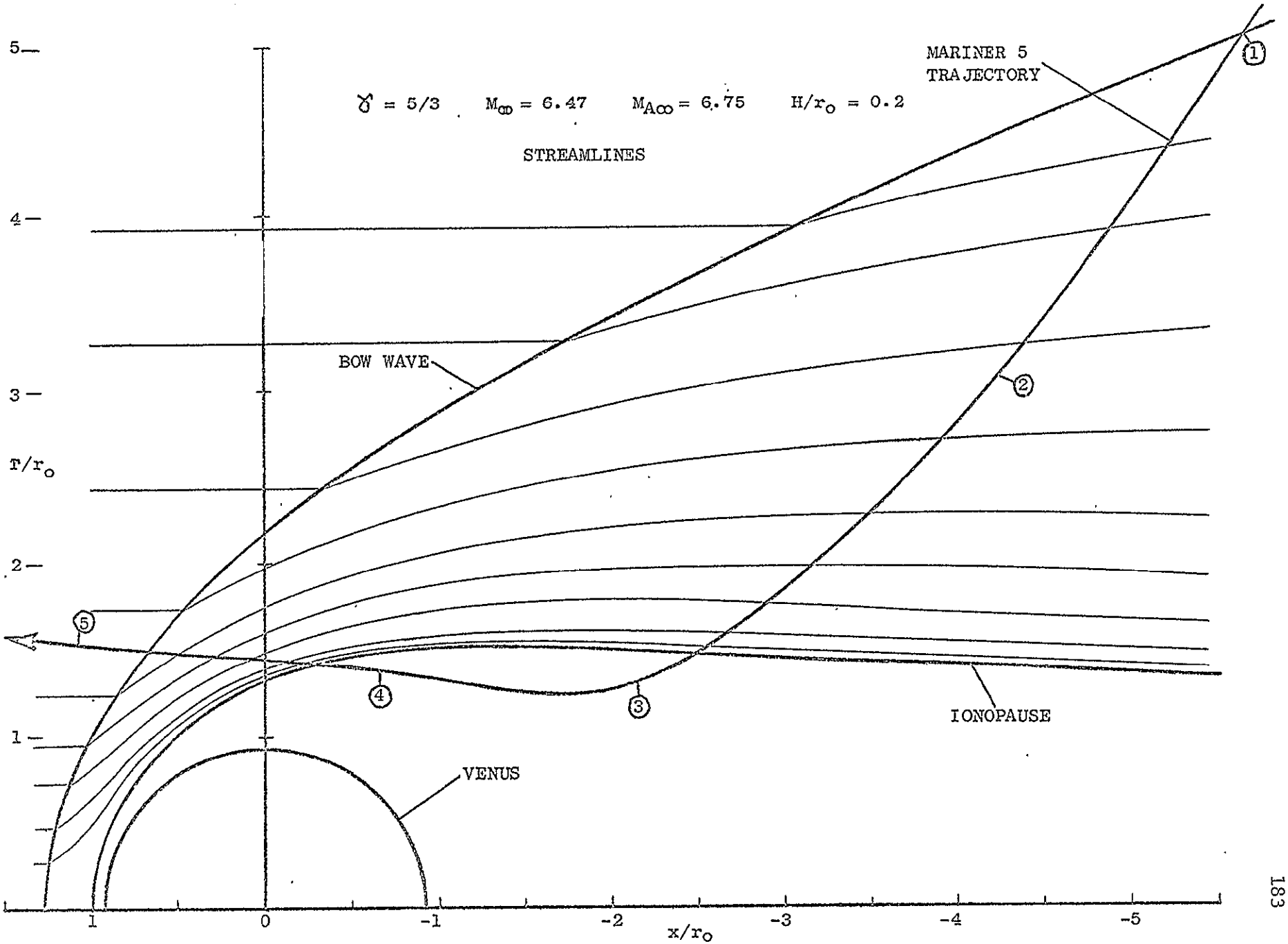

Figure 11-3 (d). Direction of magnetic field and velocity vectors.

into account the effect of the aberration angle of 3.4 degrees arising from the relative motion of Venus in its orbit about the Sun, this new system was then rotated 3.4 degrees about its Z axis. Finally, since our flow solution possesses axial symmetry, the Y and Z coordinates were formed into a radial coordinate $\bar{r} = (Y^2 + Z^2)^{1/2}$, and these X and $\bar{r}$ coordinates of the trajectory were then plotted in figures 11-3.

The magnetometer and plasma-probe experimenters have concluded from the presence of abrupt and easily recognizable changes in their data that Mariner 5 crossed the bow wave at the points of the trajectory labeled (1) and (5) (Bridge et al., 1967). Point (1) is in virtually perfect agreement with the theoretical location of the hydromagnetic shock wave although point (5) is somewhat farther upstream from the theoretical results. But figures 11-3 also indicate that Mariner 5 should have crossed the ionopause. These results, however, are best interpreted by comparing the observed density, velocity, and field strength of the solar wind with the corresponding calculated properties. Figure 11-4 shows the time variation of the bulk velocity V, ion number density n, and field intensity $|B|$ observed by Mariner 5 as it flew past Venus originally as presented in figure 8-13 only now enlarged. Superposed on this plot are dashed lines representing the flow properties theoretically calculated at the position of the spacecraft's trajectory illustrated in figures 11-3(a) to (c).

Although conditions in the solar wind were reasonably steady, study of figure 11-4 shows that all the data presented display some fluctuations just before time 1. After a discontinuous increase at time 1, the agreement between the theoretical and observed value of the intensity as they both decrease somewhat up to time 2 is quite good. Agreement is also good between the theoretical and observed velocities as they likewise decrease slightly to time 2. The observed ion density, however, does not rise discontinuously through the shock as does the theoretical density, but the agreement is nearly perfect from then till just before time 3 when the spacecraft passed through the calculated ionopause and out of the theoretical flow field.

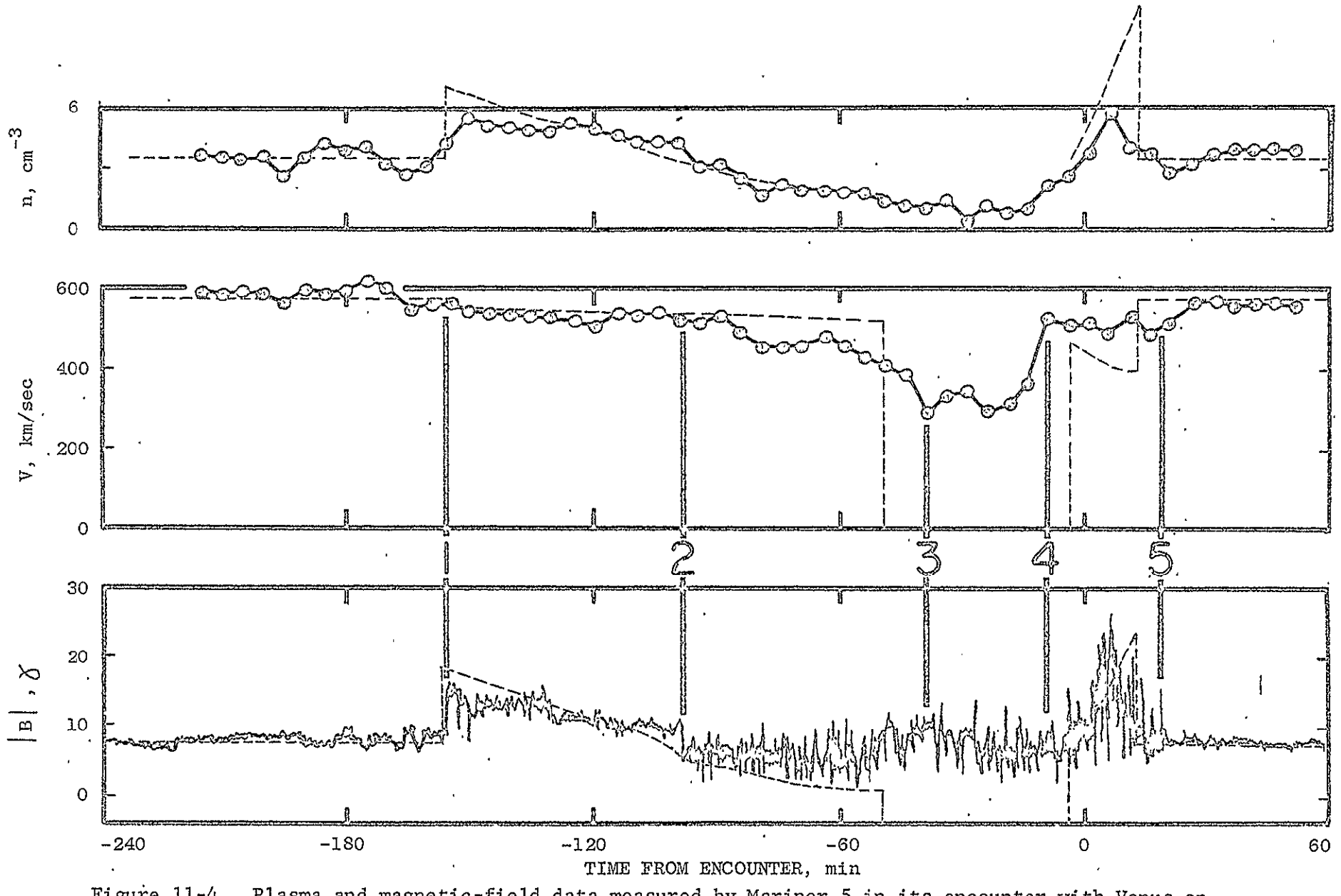

Figure 11-4. Plasma and magnetic-field data measured by Mariner 5 in its encounter with Venus on 19 October 1967 (Bridge et al., 1967). Superposed on these are dashed lines representing the theoretically calculated flow properties that occur along the Mariner 5 trajectory as illustrated in figures 11-3 (a) to (c).

Meanwhile after time 2 the measured velocities begin to be somewhat lower than their calculated counterparts as they both decrease to just before time 3 when the spacecraft entered the theoretical ionosphere and the computed value falls discontinuously to zero in our hydrostatic model of the ionosphere. The observed values also decrease sharply but only to a value about one-half the interplanetary level. At the same time fluctuations in the field intensity have substantially increased after time 2 , although the average intensity remains at about interplanetary level till after time 4 , while the theoretically calculated intensity continues to decrease slightly until falling discontinuously to zero just before time 3 at the ionopause calculated in our theory for a nonmagnetic planet. After emerging from the theoretical ionosphere after time 4 , the spacecraft observed a rapid and large increase in field intensity which corresponds fairly well with the displayed theoretical values. Just before time 5 the theoretical intensity falls discontinuously across the shock wave to the interplanetary value while at nearly the same time the observed intensity also decreases sharply to the interplanetary value. Similarly, after the spacecraft re-enters the theoretical flow field after time 4 , it observed a sharp increase in density closely corresponding to the large compression in the theoretical density which then falls discontinuously through the shock wave to interplanetary values just before time 5 . Although during this interval the calculated solution indicates a discontinuous drop following a larger rise in density than that observed, this discrepancy is not serious since it involves only one data point which is a 5-minute average and cannot sharply represent such a large compression rapidly followed by a discontinuous decrease. Just after time 4 the theoretical velocity returns to about three-fourths of the interplanetary value and roughly agrees with the measured velocities. At the theoretical shock position the calculated velocity jumps discontinuously to its full interplanetary value while the observed velocity continuously increases up to that level.

Overall the theoretically calculated flow properties agree with those observed by Mariner 5 very well indeed. In particular,

this good agreement appears to suggest that the upstream crossing of the bow wave was encountered by Mariner about 5 minutes sooner than the experimenters had originally indicated with their label (5). Support for this belief increases if the fluctuations superposed on the interplanetary value of intensity just before time 5 are disregarded and the time-averaged nature of the plasma data is taken into account. If so, the observed bow-wave crossings and the calculated position of the bow wave are in virtually perfect agreement. These theoretical results also indicate that Mariner 5 should have crossed the ionopause into the ionosphere where the plasma velocity and magnetic-field intensity would be zero and the density would be that of the ionosphere plasma. However, although the data display decreases in n/n_∞ and V/V_∞ that are at least qualitatively similar to the theoretical values, there is no certain evidence that Mariner 5 actually penetrated the ionosphere. In particular, the intensity of the magnetic field remained of the order of that for interplanetary space, and V diminished to only a modest fraction of V_∞ rather than to a value comparable with the speed of the spacecraft relative to Venus.

These results for the more refined hydromagnetic solution using the improved calculation for the tapering ionosphere tail give further support to the concept, originally suggested in chapter VIII as an explanation of a similar discrepancy with the simpler gasdynamic model, that a relatively thick boundary layer grows along the ionopause shape between the planetary ionosphere and the solar wind. Because the ionopause is essentially a boundary between these two fundamentally different bodies of plasma, it is highly probable that the ionopause would provide an increasingly thicker transition between the ionosphere and the solar wind with increasing distance from the stagnation point at the nose of the ionopause. As such, it would spread both into the upper part of the ionosphere and outward into the surrounding flow, broadening the transition region in which all properties of the plasma including the density, velocity, and magnetic field change from their values for the flowing solar plasma to those of the planetary ionosphere. Thus at the location of the ionosphere

boundary indicated by the present dissipationless hydromagnetic theory, the plasma velocity would probably be substantially less than indicated by the theory. Since the plasma velocities observed by Mariner 5 at the times when it penetrated the theoretical location of the ionopause display such a trend, we conclude that just before time 3 Mariner 5 entered the boundary layer separating the ionosphere and the flowing plasma, but did not enter the ionosphere proper, and finally emerged from it shortly after time 4 .

One peculiar aspect of these data is the substantial increase in fluctuations of the magnetic-field intensity at time 2 . Even though there is little change in average field intensity, the experimenters (Bridge et al., 1967) chose to interpret these fluctuations as changes in the interplanetary medium. Another possible interpretation is that these fluctuations are generated by disturbances in the ionosphere boundary, possibly caused by turbulence in the boundary layer. To give some idea as to the location of such boundary disturbances, we have plotted in figure 11-5 solid lines representing characteristic lines of the flow which correspond to standing hydromagnetic compression or expansion waves of infinitesimal amplitude. Also included in this figure is a dashed line representing the characteristic line passing through point (2) of the spacecraft's trajectory. The segment of the ionosphere boundary downstream from the intersection point A of this line with the ionopause is then a possible region for the generation of disturbances which propagate out to point (2) . We might thus infer that a turbulent boundary layer exists downstream of point A . Actually, though, the fluctuations in the magnetic-field data measured by Mariner 5 persist after emerging from the theoretical boundary layer near point (4) , which suggests that this boundary layer may be turbulent much farther upstream than point A . Such interpretations, however, must be regarded as purely speculative at the present time.

The overall good agreement between the observations made by Mariner 5 near Venus and the corresponding calculated properties of our hydromagnetic model offers excellent support for the validity of our hydromagnetic theory for the interaction of the solar wind with

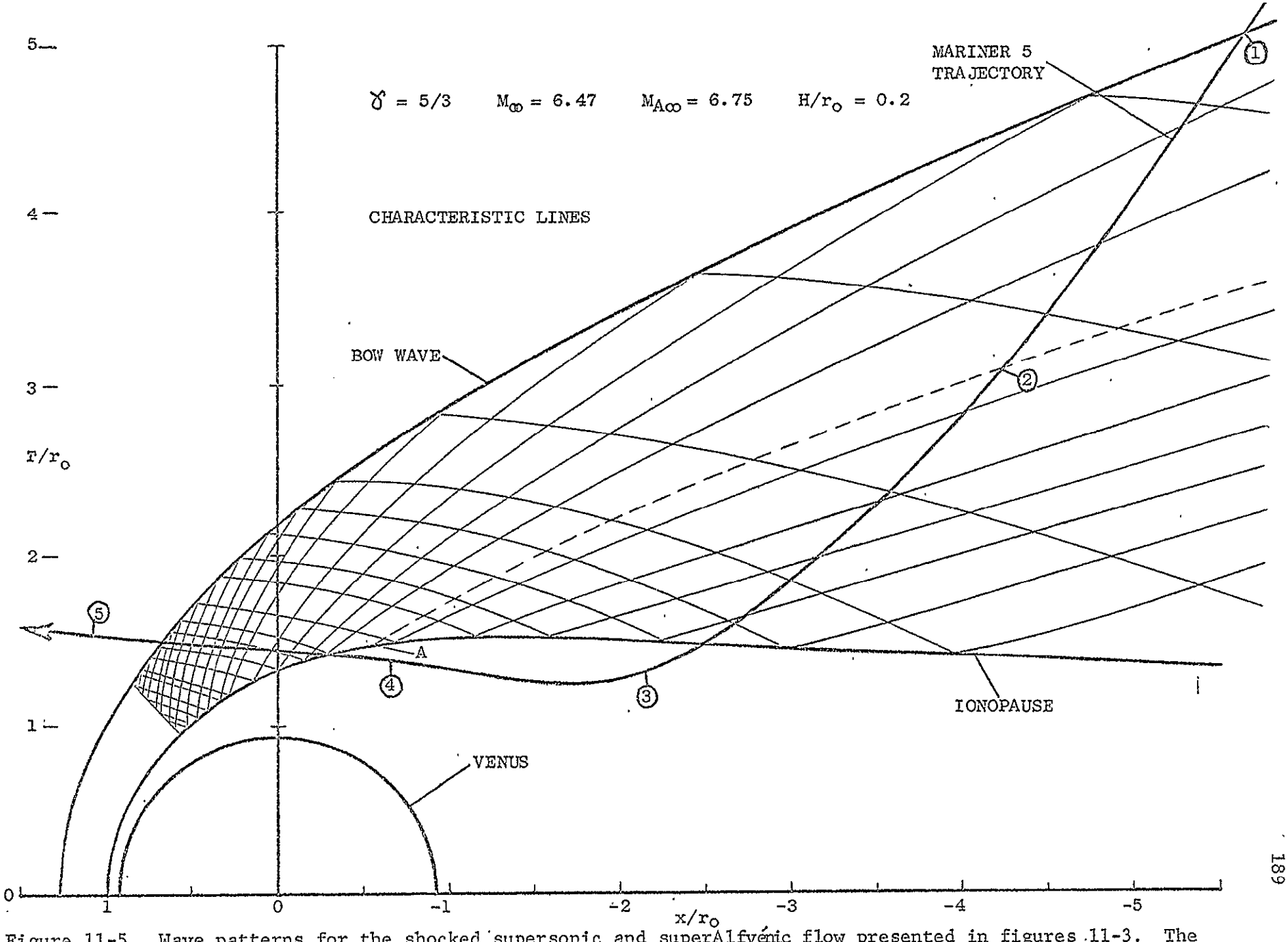

Figure 11-5. Wave patterns for the shocked supersonic and superAlfvénic flow presented in figures 11-3. The dashed line represents the standing wave of infinitesimal amplitude which passes through point ② of the superposed trajectory of Mariner 5.

nonmagnetic planets, such as Mars and Venus, which have a sufficient ionosphere to deflect the solar plasma around the planet and its atmosphere. In particular, it has verified the supposition that the current sheath which bounds the solar wind away from the planet is formed by interaction with the ionosphere rather than with a planetary magnetic field as in the case of the Earth and that continuum hydromagnetic theory sufficiently represents this interaction of the solar plasma with the ionosphere and the consequent development of a shock wave as well as the variation of the average plasma and magnetic-field properties throughout the surrounding flow. Furthermore, the comparison of these theoretical results with spacecraft observations also demonstratesthe validity of treating the subsolar segment of the boundary between the solar wind and the upper planetary ionosphere as a tangential discontinuity even though on the remaining segment of this theoretical boundary certain differences suggest the presence of a thick transition region or boundary layer.

We therefore conclude that the theory given here is both plausible and capable of providing a reasonably accurate description of the conditions that prevail at Mars and Venus.

CHAPTER XII

COMPENDIUM

To provide a basis for the theoretical approach of the major topic of this thesis, we have reviewed the data acquired in recent years in the vicinity of the Earth, Moon, Mars, and Venus that have disclosed three essentially different types of interaction with the solar wind. In addition, the basic properties and idealizations of the solar wind itself, which have been predicted theoretically and also actually observed in space, were outlined in some detail in order to illustrate the basic unity of the entire theoretical description of the solar wind and its interaction with these planets.

The fundamental assumption underlying our theoretical analysis of the large-scale features of the interaction of the solar wind with the Earth, Mars, and Venus is that the average bulk properties of the flow can be adequately described by a continuum-fluid theory. Although this assumption has not been theoretically justified, we remarked that the presence of a weak and irregular magnetic field in the incident solar-wind plasma appears to couple the motions of particles even in the absence of collisions. More convincingly, we argued that the real support for the use of the continuum-fluid model is provided by the outstanding agreement between results calculated in this way and those actually measured in space.

Our fluid model is based on the differential equations of magnetohydrodynamics for the steady flow of a perfect gas having infinite electrical conductivity as well as both zero viscosity and thermal conductivity. Study of these equations reveals five classes of discontinuities that can exist in the flow because of the omission of dissipative terms from the differential equations. Two of these, the fast hydromagnetic shock wave and the tangential discontinuity, are of concern in our analysis. The first is relevant for relating conditions on the two sides of the bow wave which forms in the solar wind upstream of the planets, and the latter is the only one that has properties compatible with those required to describe a boundary

surface that deflects the solar wind around the planet. For non-magnetic planets which have a highly conducting ionosphere, such as Mars and Venus, this boundary is formed by interaction of the solar wind with the ionosphere rather than with the geomagnetic field as in the case of the Earth.

With the problem so formulated, there follows an account of the manner in which these equations can be simplified to obtain a tractable mathematical problem without undue loss of realism or accuracy of representation of principal features of the interaction. First, by using the Newtonian pressure formula the approximate shape and location of the ionosphere boundary is calculated for selected values of the parameters that characterize the ionosphere just as in the analogous problem of the Earth. Following that, the magneto-hydrodynamic equations are then simplified to those of gasdynamics by dropping the magnetic terms on the basis of the large magnitude of the Alfvén Mach number. The location of the bow wave and the properties of the flow field are then determined for a substantial range of values for the parameters describing conditions in the solar wind by solving these simpler gasdynamic equations using numerical techniques specifically developed for that purpose. It is found that the results for a wide range of ionospheric parameters can be brought into close correspondence with those for flow past the Earth's magnetosphere by application of a simple geometric transformation of the coordinates. This correspondence rule enables a substantial body of theoretical results available for solar-wind flow past the magnetosphere to be applied to Mars or Venus with only minor modification. Finally, these approximate theoretical results are compared with the observations made by Mariner 5 as it flew past Venus, and implications of the points of agreement and disagreement are discussed. A similar comparison with data from Mariners 4, 6, and 7 indicates that Mars has a sufficient ionosphere for the theory to be applicable and that the observed position of the Martian bow wave is exactly predicted by the theory.

A more refined solution is carried out for the complete magnetohydrodynamic equations for the special case of parallel velocity and magnetic-field vectors. The explicit hydromagnetic equations for

aligned flow are derived, and the numerical procedures developed originally for gasdynamics are modified so that solutions to these equations are able to be computed for a substantial range of values for the parameters describing conditions in the solar wind. Study of these exact hydromagnetic solutions discloses a strong dependence on the content of the magnetic energy relative to the kinetic energy in the solar wind. When this ratio is low, or equivalently when the Alfvén Mach number is high, this refined solution shows that the bow-wave location and flow-field properties are very similar to those of the simpler gasdynamic solution. However, when this ratio is high, the bow-wave location and flow properties are strikingly different. This unusual phenomena for low-Alfvén-Mach-number flow past the Earth has recently been confirmed by spacecraft measurements. A detailed comparison of these two models is also carried out to determine the accuracy and usefulness of the simpler gasdynamic model.

The calculation of the exact shape of the ionopause is also performed by determining as part of the flow solution the points at which the tangential discontinuity relations are satisfied exactly. Lastly, these refined theoretical results are found to agree better with the observations made by Mariner 5 as it flew past Venus than do the simpler gasdynamic results. However, certain differences near the theoretical location of the ionopause suggest the presence of a thick boundary layer.

Overall, we conclude that the theory presented here is both plausible and capable of accurately describing the phenomena associated with the interaction of the solar wind with the Earth, Mars, and Venus.

LITERATURE CITED

Alksne, A. Y. 1967. The steady-state magnetic field in the transition region between the magnetosphere and bow shock. Planet. Space Sci. 15: 239-45.

Alksne, A. Y., and Webster, D. L. 1970. Magnetic and electric fields in the magnetosheath. Planet. Space Sci. 18: 1203-12.

Anderson, J. E. 1963. Magnetohydrodynamic Shock Waves. M.I.T. Press.

Barth, C. A.; Pearce, J. B.; Kelly, K. K.; Wallace, L., and Fastie, W. G. 1967. Ultraviolet emissions observed near Venus from Mariner V. Science. 158: 1675-78.

Barth, C. A. 1968. Interpretation of the Mariner 5 Lyman alpha measurements. Jour. Atmospheric Sci. 25: 564-67.

Barth C. A.; Wallace, L.; and Pearce, J. B. 1968. Mariner 5 measurements of Lyman-alpha radiation near Venus. J. Geophys. Res. 73: 2541-45.

Bauer, S. J. 1969. Diffusive equilibrium in the topside ionosphere. Proc. of the IEEE. 57: 1114-18.

Beard, D. B. 1960. The interaction of the terrestrial magnetic field with the solar corpuscular radiation. J. Geophys. Res. 65: 3559-68.

Behannon, K. W., and Fairfield, D. H. 1969. Spatial variations of the magnetosheath magnetic field. Planet. Space Sci. 17: 1803-16.

Belton, M. J. S.; Brandt, J. C.; and Hodge, P. W. 1963. On the characteristics of distant comets. Ann. Astrophys. 26: 250-52.

Biermann, L. 1951. Kometenschweife und solare korpuskular Strahlung. Z. Astrophys. 29: 274-86.

Biermann, L. 1957. Solar corpuscular radiation and the interplanetary gas. Observatory. 77: 109-10.

Binsack, J. H. 1968. Shock and magnetopause boundary observations with IMP 2, in Physics of the Magnetosphere (Eds. R. L. Carovillano, J. F. McClay, and R. H. Radoski). Reidel, Dordrecht, Holland.

Binsack, J. H., and Vasyliunas, F. M. 1968. Simultaneous IMP 2 and OGO 1 observations of bow shock compression. J. Geophys. Res. 73: 429-33.

Brandt, J. C. 1962. A model of the interplanetary medium. Icarus 1: 1-6.

Brandt, J. C. 1967. Interplanetary gas XIII. Gross plasma velocities from the orientations of ionic comet tails. Astrophys. J. 147: 201-19.

Bridge, H. S.; Lazarus, A. J.; Snyder, C. W.; Smith, E. J.; Davis Jr., L.; Coleman, P. J.; and Jones, D. E. 1967. Mariner V: Plasma and magnetic fields observed near Venus. Science. 158: 1669-73.

Briggs, B. R., and Spreiter, J. R. 1963. Theoretical determination of a boundary and distortion of the geomagnetic field in a steady solar wind. NASA Tech. Rep. No. TR R-178.

Chapman, S., and Ferraro, V. C. A. 1931. A new theory of magnetic storms. Terr. Magnetism Atmos. Elect. 36: 77-97, 171-86.

Chapman, S., and Bartels, J. 1940. Geomagnetism, Vol. I and II. Oxford: Oxford University Press.

Colburn, D. S.; Currie, R. G.; Mihalov, J. D.; and Sonett, C. P. 1967. Diamagnetic solar wind cavity discovered behind moon. Science. 158: 1040-42.

Courant, R.; and Hilbert, D. 1962. Methods of Mathematical Physics, Vol. II. New York: Interscience.

Cowley, M. D. 1960. A magnetogasdynamic analogy. Jet Propulsion. 30: 271-73.

Dessler, A. J. 1967. Solar wind and interplanetary magnetic field. Rev. Geophys. 5: 1-41.

Donahue, T. M. 1969. Deuterium in the upper atmosphere of Venus and Earth. J. Geophys. Res. 74: 1128-37.

Dryer, M., and Heckman, G. R. 1967. Application of the hypersonic analog to the standing shock of Mars. Solar Phys. 2: 112-20.

Fairfield, D. H. 1967. The ordered magnetic field of the magnetosheath. J. Geophys. Res. 72: 5865-77.

Faus, A. A. 1966. Solar wind beyond the earth's orbit. The transition zone. Planet. Space Sci. 14: 143-54.

Fjeldbo, Gunnar, and Eshleman, V. R. 1968. The atmosphere of Mars analyzed by integral inversion of the Mariner IV occultation data. Planet. Space Sci. 16: 1035-59.

Fjeldbo, Gunnar, and Eshleman, V. R. 1969. Atmosphere of Venus as studied with the Mariner 5 dual radio-frequency occultation experiment. Radio Sci. 4: 879-97.

Fjeldbo, G.; Kliore, A.; and Seidel, B. 1970. The Mariner 1969 occultation measurements of the upper atmosphere of Mars. Radio Sci. 5: 381-86.

Fox, L. 1962. Numerical Solution of Ordinary and Partial Differential Equations. New York: Pergamon Press.

Friedrichs, K. O., and Kranzer, H. 1958. Non-linear wave motion in magnetohydrodynamics. Institute of Mathematical Sci., New York Univ. Rep. No. MH-8.

Fuller, F. B. 1961 Numerical solutions for supersonic flow of an ideal gas around blunt two-dimensional bodies. NASA Tech. Note No. TN D-791.

Garabedian, P. R. 1964. Partial Differential Equations. New York: John Wiley & Sons.

Geffen, N. 1965. Magnetogasdynamic hypocritical flows with shocks. Israel J. Tech. 3: 82-87.

Geffen, N. 1966. Four simple examples of related hydrodynamic and magnetohydrodynamic flows. Israel J. Tech. 4: 70-76.

Grad, Harold. 1960. Reducible problems in magneto-fluid dynamic steady flows. Rev. Mod. Phys. 32: 830-47.

Hadamard, J. S. 1923. Lectures on Cachy's problem in linear partial differential equations. New Haven: Yale Univ. Press.

Hayes, W. D., and Probstein, R. F. 1966. Hypersonic Flow Theory, Vol. I. New York: Academic Press.

Hirshberg, J.; Alksne, A.; Colburn, D. S.; Bame, S. J.; and Hundhausen, A. J. 1970. Observation of a solar flare induced interplanetary shock and helium-enriched driver gas. J. Geophys. Res. 75: 1-17.

Hundhausen, A. J. 1968. Direct observations of solar-wind particles. Space Sci. Rev. 8: 690-749.

Hundhausen, A. J. 1970. Composition and dynamics of the solar wind plasma. Rev. Geophys. Space Phys. 8: 729-811.

Imai, I. 1960. On flows of conducting fluids past bodies. Rev. Mod. Phys.

Inouye, M., and Lomax, H. 1962. Comparison of experimental and numerical results for the flow of a perfect gas about blunt-nosed bodies. NASA Tech. Note No. TN D-1426.

Inouye, M.; Rakich, J. V.; and Lomax, H. 1965. A description of numerical methods and computer programs for two-dimensional and axisymmetric supersonic flow over blunt-nosed and flared bodies. NASA Tech. Note No. TN D-2970.

Iuriev, I. M. 1960. On a solution to the equations of magnetogas-dynamics. J. Appl. Math. and Mech. 24: 233-37.

Jeffrey, A., and Taniuti, T. 1964. Non-linear Wave Propagation. New York: Academic Press.

Jeffrey, A. 1966. Magnetohydrodynamics. London: Oliver and Boyd.

Kantrowitz, A. R., and Petschek, H. E. 1964. Avco-Everett Res. Lab. Res. Report No. 185. Everett, Mass.

Kaplan, S. A. 1966. Interstellar Gasdynamics. Oxford: Pergamon Press.

Kavanagh, Jr., L. D.; Schardt, A. W.; and Roelof, E. C. 1970. Solar wind and solar energetic particles: Properties and interactions. Rev. Geophys. Space Phys. 8: 389-460.

Kliore, A.; Cain, D. L.; Levy, G. S.; Eshleman, V. R.; Fjeldbo, G.; and Drake, F. 1965. Occultation experiment: Results of the first direct measurement of Mars' atmosphere and ionosphere. Science. 149: 1243-48.

Landau, L. D., and Lifshitz, E. M. 1959. Fluid Mechanics. London: Pergamon Press.

Landau, L. D., and Lifshitz, E. M. 1960. Electrodynamics of Continuous Media. London: Pergamon Press.

Lazarus, A. J.; Bridge, H. S.; Davis, J. M.; and Snyder, C. W. 1967. Initial results from the Mariner 4 solar plasma experiment. Space Res. 7: 1296-1305.

Lees, L. 1964. Interaction between the solar plasma wind and the geomagnetic cavity. AIAA J. 2: 1576-82.

Levy, R. H.; Petschek, H. E.; and Siscoe, G. L. 1964. Aerodynamic aspects of the magnetospheric flow. AIAA J. 2: 2065-76.

Liepmann, H. W., and Roshko, A. 1957. Elements of Gasdynamics. New York: John Wiley & Sons.

Lomax, H., and Inouye, M. 1964. Numerical analysis of flow properties about blunt bodies moving at supersonic speeds in an equilibrium gas. NASA Tech. Rep. No. TR R-204.

Lüst, R. 1963. Interplanetary plasma. Space Sci. Rev. 1: 522-52.

Lüst, R. 1965. Interplanetary plasma in Introduction to Solar Terrestrial Relations (Eds. J. Ortner and H. Maseland). New York: Gordon and Breach.

Lyon, E. F.; Bridge, H. S.; and Binsack, J. H. 1967. Explorer 35 plasma measurements in the vicinity of the moon. J. Geophys. Res. 72: 6113-17.

Lyon E. F.; Siscoe, G. L.; and Bridge, H. S. 1968. Explorer 35 observations of the solar wind-moon interaction. CSR Tr-68-7.

MacDonald, G. J. F. 1964 in Space Physics (Eds. D. P. LeGalley and A. Rosen). New York: John Wiley & Sons.

McElroy, M. B., and Strobel, D. F. 1969. Models for the nighttime Venus ionosphere. J. Geophys. Res. 74: 1118-27.

Mariner Stanford Group 1967. Venus: Ionosphere and atmosphere as measured by dual-frequency radio occultation of Mariner V. Science. 158: 1678-83.

Mead, G. D., and Beard, D. B. 1964. Shape of the geomagnetic field solar wind boundary. J. Geophys. Res. 69: 1169-79.

Ness, N. F.; Scearce, C. S.; Seek, J. B.; and Wilcox, J. M. 1966. Summary of results from IMP-1 magnetic field experiment. Space Res. 6: 581-628.

Ness, N. F.; Behannon, K. W.; Scearce, C. S.; and Contarano, S. C. 1967. Early results from the magnetic field experiment on lunar Explorer 35. J. Geophys. Res. 72: 5769-78.

Ness, N. F.; Behannon, K. W.; Taylor, H. E.; and Whang, Y. C. 1968. Perturbations of the interplanetary magnetic field by the lunar wake. J. Geophys. Res. 73: 3421-40.

O'Gallagher, J. J., and Simpson, J. A. 1965. Search for trapped electrons and a magnetic moment at Mars by Mariner IV. Science. 149: 1233-39.

Olson, W. P. 1969. The shape of the tilted magnetopause. J. Geophys. Res. 74: 5642-51.

Parker, E. N. 1958. Dynamics of the interplanetary gas and magnetic fields. Astrophys. J. 128: 664-76.

Parker, E. N. 1963. Interplanetary Dynamical Processes. New York: Interscience.

Parker, E. N. 1965. Dynamical theory of the solar wind. Space Sci. Rev. 4: 666-708.

Scarf, F. L. 1964. The solar wind and its interaction with magnetic fields, in Space Physics (Eds. D. P. LeGalley and A. Rosen). New York: John Wiley & Sons.

Scarf, F. L. 1970. Microscopic structure of the solar wind. Space Sci. Rev. 11: 234-70.

Sears, W. R. 1960. Some remarks about flow past bodies. Rev. Mod. Phys. 32: 701-05.

Seebass, R. 1961. On transcritical and hypercritical flows in magnetogasdynamics. Quart. Appl. Math. 19: 231-37.

Shannon, C. E., and Weaver, W. 1949. The Mathematical Theory of Communication. Urbana: Univ. of Illinois Press.

Smith, E. J.; Davis, Jr., L.; Coleman, Jr., P. J.; and Jones, D. E. 1965. Magnetic measurements near Mars. Science. 149: 1241-42.

Smith, E. J. 1969. Planetary magnetic field experiments, in Advanced Space Experiments (Eds. O. L. Tiffany and E. M. Zaitzeff). American Astronautical Soc., Tarzana, Calif.

Smith, S. M.; Henderson, M. E.; and Torrey, R. A. 1967. Coronal photographs, isophates, and a flash spectrum from the solar eclipse of May 30, 1965. NASA Tech. Note No. TN D-4012.

Sonnerup, B. U. O., and Cahill, Jr., L. J. 1968. Explorer 12 observations of the magnetopause current layer. J. Geophys. Res. 73: 1757-70.

Spreiter, J. R., and Briggs, B. R. 1961. Theoretical determination of the form of the hollow produced in the solar corpuscular stream by the interaction with the magnetic dipole field of the earth. NASA Tech. Rep. No. TR R-120.

Spreiter, J. R., and Briggs, B. R. 1962. Theoretical determination of the form of the boundary of the solar corpuscular stream produced by interaction with the magnetic dipole field of the earth. J. Geophys. Res. 67: 37-51.

Spreiter, J. R., and Summers, A. L. 1965. Dynamical behavior of magnetosphere boundary following impact by discontinuity in the solar wind. J. Atmospheric Terrest. Phys. 27: 357-65.

Spreiter, J. R.; Summers, A. L.; and Alksne, A. Y. 1966a. Hydromagnetic flow around the magnetosphere. Planet. Space Sci. 14: 223-53.

Spreiter, J. R.; Alksne, A. Y.; and Abraham-Shrauner, B. 1966b. Theoretical proton velocity distributions in the flow around the magnetosphere. Planet. Space Sci. 14: 1207-20.

Spreiter, J. R., and Summers, A. L. 1967. On conditions near the neutral points on the magnetosphere boundary. Planet. Space Sci. 15: 787-98.

Spreiter, J. R.; Alksne, A. Y.; and Summers, A. L. 1968. External aerodynamics of the magnetosphere, in Physics of the Magnetosphere (Eds. R. L. Carovillano, J. F. McClay, and H. R. Radoski). Reidel, Dordrecht, Holland.

Spreiter, J. R., and Alksne, A. Y. 1969. Plasma flow around the magnetosphere. Rev. Geophys. 7: 11-50.

Spreiter, J. R., and Alksne, A. Y. 1970. Solar-wind flow past objects in the solar system. Ann. Rev. Fluid Mech. 2: 313-54.

Spreiter, J. R.; Marsh, C. M.; and Summers, A. L. 1970a. Hydromagnetic aspects of solar wind flow past the moon. Cosmic Electrodynamics. 1: 5-50.

Spreiter, J. R.; Summers, A. L., and Rizzi, A. W. 1970b. Solar wind flow past nonmagnetic planets - Venus and Mars. Planet. Space Sci. 18: 1281-99.

Spreiter, J. R., and Rizzi, A. W. 1971. The Martian bow wave - theory and observation. (submitted to Planet. Space Sci.).

Tamada, Ko. 1964. Two-dimensional transonic flow of perfectly conducting gas with aligned magnetic field, in Symposium Transsonicum (Eds. K. Oswatitsch), Springer-Verlag, Berlin.

Ungstrup, Eigil. 1971. Movements of the Earth's bow shock wave under control of the solar wind magnetic field. (to be published).

Van Allen, J. A.; Frank, L. A.; Krimigis, S. M.; and Hills, H. K. 1965. Absence of Martian radiation belts and implications thereof. Science. 149: 1228-33.

Van Dyke, M. D. 1958. The supersonic blunt-body problem - review and extension. J. Aerospace Sci. 25: 485-96.

Van Dyke, M. D., and Gordon, H. D. 1959. Supersonic flow past a family of blunt axisymmetric bodies. NASA Tech. Rep. No. TR R-1.

Wallace, L. 1969. Analysis of the Lyman-alpha observations of Venus made from Mariner 5. J. Geophys. Res. 74: 115-31.

Whitten, R. C. 1970. The daytime upper ionosphere of Venus. J. Geophys. Res. 75: 3707-14.